Alma Mater Studiorum – Università di Bologna

DOTTORATO DI RICERCA IN

CHIMICA

Ciclo XXXII

Settore Concorsuale: **03/A1**

Settore Scientifico Disciplinare: **CHIM/01**

Design and characterization of Electrochemical Sensors for Organic Bioelectronics

Presentata da: Federica Mariani

Coordinatore Dottorato

Prof.ssa Domenica Tonelli

Supervisore

Prof.ssa Erika Scavetta

Co-Supervisore

Dr. Isacco Gualandi

Esame finale anno 2020

To Lorenzo

wherever you are

Abstract

This Ph.D. Thesis concerns the design and characterisation of functional electrochemical interfaces in organic electronic devices for bioelectronic applications. The Thesis is structured as follows:

Chapter I – Technological context that has inspired the research, introduction to Organic Bioelectronics and literature review concerning Organic Electrochemical Transistors (OECTs) for sensing applications.

Chapter II – Working principle of an all-polymeric OECT and *operando* microscopic characterization using scanning electrochemical techniques.

Chapter III – Dopamine detection with all-polymeric OECT sensors. Development of a potentiodynamic approach to address selectivity issues in the presence of interfering species and design of a needle-type, sub-micrometric OECT sensor for spatially resolved detection of biological Dopamine concentrations.

Chapter IV – Development of an OECT pH sensor. Characterization of the electrochemical transducer and functionalization of the OECT gate electrode with the sensing material. Potentiodynamic and potentiostatic operation modalities are explored and the sensing performances are assessed in both cases. The final device is realized on a flexible substrate and tested in Artificial Sweat.

Chapter V – Study of two-terminal, electrochemically gated sensors inspired by the OECT configuration. Design and characterization of novel functional materials showing a potentiometric transduction of the chemical signal that can be exploited in the realization of electrochemical sensors with simplified geometry for wearable applications.

Chapter VI – Conclusion.

Table of Contents

I. Introduction

1. Context

Especially from the 90s, the advance of the Internet has been a major breakthrough in the establishment of branched digital communication networks. As of July 2019, over 4.33 billion people were active Internet users, encompassing 56% of the global population.[1] Indeed, the Internet somehow deprived the concept of *place* of its meaning by linking people worldwide and revolutionised our societies with unprecedented opportunities and challenges. More recently, the novel concept of the Internet of Things (IoT) is introducing the vision of an interconnected reality of responsive objects and things that are able to interact with each other through unique addressing schemes. Originally intended for radio frequency identification (RFID) network, IoT is today a global infrastructure based on a variety of smart devices that find application, for example, in domotics and assisted living, e-health, enhanced learning and intelligent transportation of people and goods. IoT has been included among the six "Disruptive Civil Technologies" by the US National Intelligence Council[2] and, considering that the next generation mobile connection technology 5G will boost the actualization of IoT in everyday life, 75.44 billion IoT connected devices are expected to be installed worldwide by 2025.[3]

The exchange of information generated by this thick network of interwoven smart objects and delivered through the Internet raises concerns about the IoT applicability and poses significant challenges for the IoT growth. Due to the non-standard architecture of such a heterogeneous system, common protocols adopted for the Internet must be implemented to guarantee security and privacy of IoT users and avoid data leaks and theft. Also,

handling and storage of the huge amount of data streaming out of the IoT call for smart and efficient technologies for cloud computing and Big data management.[4] Interconnecting paths that enable the advanced services of IoT are described using graph theory and Network Science, which makes use of mathematical models to study complex networks' topology. For instance, small-world theory is based on the hypothesis that highly clustered networks in nature can be studied in terms of *nodes* connected by *links* where, despite the complexity of the system, characteristic path lengths are relatively small.[5] Interestingly, the unmatched ability of nature in creating interconnecting paths can be studied from this point of view. Connected proteins, transcriptional networks and brain networks in our body have inspired, for example, the development of artificial neural networks for machine learning. Natural information networks such as photosynthesis or pollination make use of natural built-in sensors in plants and animals to sense the surrounding environment and share information. Typical eco-systems, which rely on the sustainable and balanced organization of beings, processes and sources, embody naturally available models for circular economy design.[6]

With the possibility to interact with the surrounding environment and share information remotely with different degrees of automation, IoT devices can be grouped in four domains including transportation and logistics, healthcare, smart environment and personal/social.[7,8] Actualization of the IoT vision is realisable through the synergic integration of several enabling technologies, including sensing technologies, identification and recognition technologies, hardware and software. In particular, wireless sensor networks play a crucial role in the IoT as they can provide augmented awareness of a certain environment. Applicability of sensor networks holds great potential in several scenarios, such as environmental monitoring, e-health, intelligent transportation systems, military and industrial plant monitoring. Major requirements for IoT sensor networks include reliability, low power consumption, low cost and scalability, appropriate real-time communication capability and data security. At present, physical sensors able to track movement, location, pressure, temperature, moisture and so on dominate in IoT applications with several examples in domotics and fitness that are already on the market.[7,9,10] IoT sensors include smart sensors and actuators, and even wearable sensing devices that can be incorporated into daily clothes or worn as accessories or implants. The possibility of providing people with a tool that monitors body status in real time, tracks environmental parameters and can share information wirelessly would have a dramatic impact on healthcare and personalized medicine, together with safety and risk

management, and so on. For this reason, "soft" and flexible electronics is regarded as one of the key technologies for the IoT era.[11]

2. Introduction to Bioelectronics

Life and electricity are intimately related. Membrane potentials at the cellular level, for instance, are part of an archetypical signaling system. They are essential to control and assist metabolic processes in the case of non-excitable cells (resting potential), or responsible for nerve impulses and muscles' contraction (action potential). The charge carriers of bio-electricity are *ions*, which can diffuse throughout specific channels in the semi-permeable lipid bilayer constituting cell membranes. Interestingly, the cell resting potential can be calculated as the sum of the equilibrium potentials of all ions (typically K^+, Na^+, Ca^{2+} and Cl^-), as determined by the Nernst equation. Not only electrical properties characterize biological matter, but also exogenous electrical stimuli can be applied to drive biological events.[12] While primal awareness of excitation and nerve conduction dates back to the ancient Galenic doctrine, the first electrophysiological experiments came at the end of the 18th century, when Luigi Galvani and Alessandro Volta debated the popular frog's leg muscle twitching upon external connection by two metal electrodes to its spinal cord. Since then, great technological advancements, encompassing patch clamps and microelectrodes development, have revolutionised both research in biology and medicine and our everyday life, with routine clinical tests, such as electrocardiography (ECG), drug-free therapies, bionic interfaces for prosthetics and life-saving implants, like pacemakers.[13]

Interfacing electronics with biological entities is the cornerstone of the field of *Bioelectronics* and a major challenge in modern medicine. It is indeed intuitive that trying to couple a solid, abiotic electronic component with an extremely soft, water- and ion-rich, living biological system is at least complex. First, there is a great mechanical mismatch between the two that originates the so-called *hard to soft challenge* (**Figure 1**). As regards stiffness, for instance, the elastic modulus of hard inorganic solids like silicon or polycrystalline metals is around 100 GPa, while brain tissue has a Young's modulus of 0.1 - 16 kPa.[14,15]

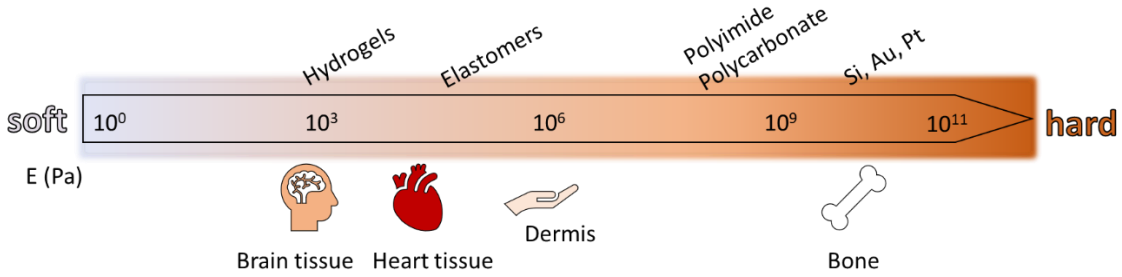

Figure 1. The hard to soft challenge in Bioelectronics.

It must be said that inorganic materials have entered the field of bioelectronics anyway, thanks to the well-established integrated-circuit industry built on a library of well-known inorganic semiconductors. Recent technological breakthroughs including nanotechnology have significantly contributed in the effort to improve bending stiffness and other mechanical properties. For instance, miniaturization of inorganic components has improved their molecular dynamics leading to ultra-thin and flexible devices, such as the nanofabricated 3D mesh electronics, which reduce inflammation due to the reduced strain between tissue and bioelectronic implants.[16,17] However, the nature of charge transport represents the other major dichotomy between biological entities and abiotic inorganic electronics. While the first shuttle information through ionic currents and chemical signaling, electrons and electron-hole pairs are responsible for electrical properties in metals and semiconductors, respectively. This discrepancy in the communication mechanisms hinders efficient transduction of the biological signal. At a bioelectronic interface, the measure of how easily the conversion between electronic and ionic currents is performed is given by the impedance of the electrode.[18] A way to achieve low impedance characteristics per electrode area is the design of materials with high capacitance, i.e. that facilitate the storage of a high amount of charge at the interface, which in turn must be easily accessed by the ions from the electrolyte. Since the higher the effective surface area, the larger the amount of charge that can be stored, a typical strategy used to improve signal transduction across the inorganic/biotic interface include the incorporation of porous structures and nanomaterials.[19,20] Alternatively, the inclusion of redox-active compounds that enable Faradaic charge transfer, such as activated iridium species, yields hybrid electrodes with increased intrinsic injection capacity.[21,22] Further drawbacks of inorganic materials used for bioelectronic applications encompass susceptibility to biofouling and passivation, as well as limited number of biocompatible materials. In this scenario, the

discovery of organic semiconductors and the rise of *Organic Electronics* represent a milestone in the evolution of material science.

3. Organic Conductors

3.1 The rise of Organic Electronics

Although the "*production of a blue substance by the electrolysis of sulphate of aniline*", identified as oxidized polyaniline, was first reported in 1862 and the electrochemical synthesis of *pyrrole black* is known since 1968,[23,24] the birth of *Organic Electronics* is commonly associated to the synthesis of halogen-doped polyacetylene in 1977, recognized as the prototyped conducting polymer.[25] While polyacetylene itself had no commercial application due to air-instability and scarce processability, this research shed light on a unique class of materials and the Nobel Prize in Chemistry 2000 was awarded to Shirakawa, MacDiarmid and Heeger for "the discovery and development of conductive polymers". Since then, the possibility to replace traditional inorganic conductors and semiconductors with carbon-based counterparts has triggered increasing research enthusiasm towards ultra-lightweight, stretchable electronics and low-cost fabrication of printed electronics for flexible displays, lightning, organic photovoltaics, flexible circuitry and sensors. Active organic materials are often divided into two classes: small-molecular materials (or semiconducting molecular solids and salts, including polycyclic aromatic compounds such as pentacene and rubrene) and polymers. Despite fundamental similarities, the main difference relies in the way thin films are prepared.[26] Indeed, while the first ones are typically thermally evaporated in vacuum, polymers are processed from solution, thus allowing straightforward fabrication of small-area thin films by standard deposition techniques like spin-coating, production of laterally structured circuitry by ink-jet printing and even large-volume roll-to-roll fabrication of organic devices. Moreover, ease of structural tailoring and functionalization, together with peculiar features exhibited by electrically conducting polymers, have made them especially suited candidates for interfacing biological substrates and are discussed in the following section.

3.2 Intrinsically Conducting Polymers

An organic polymer that possesses the electrical, electronic, magnetic, and optical properties of a metal while retaining the mechanical properties and processability

commonly associated with a conventional polymer, is called *intrinsically conducting polymer* (ICP). Such materials are also known as "synthetic metals" and their properties are intrinsic to a *doped* form of the polymer.[27] This feature is fundamental to distinguish between ICPs and Extrinsically Conducting Polymers (ECPs), i.e. composite materials of a non-conductive polymer loaded with a conducting material such as metal or carbon powder. Polypyrrole (PPy), Polyaniline (PANi), Polythiophene (PT) and its derivative Poly(3,4-ethylenedioxythiophene) (PEDOT) are by far the most popular and widespread used ICPs (**Figure 2**).

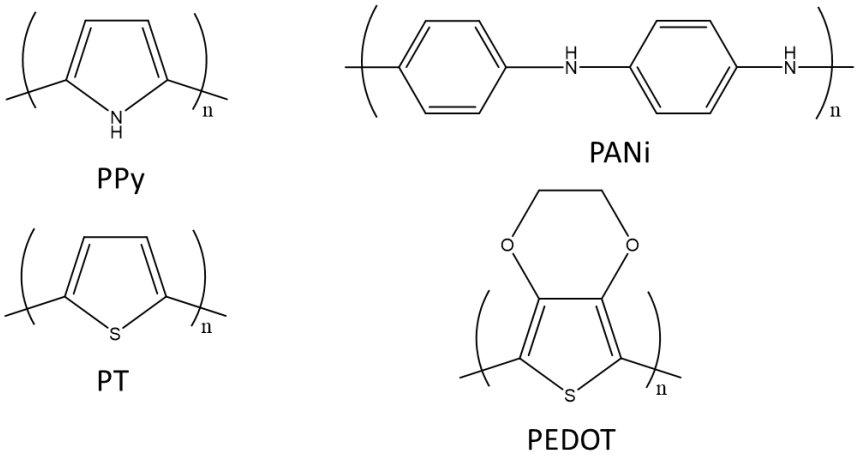

Figure 2. Chemical structures of PPy, PANi, PT and PEDOT.

3.2.1 Electronic properties

According to their electronic structure, all materials can be grouped into three categories i.e. conductors, semiconductors and insulators. For conductors like metals, the band structure follows the "electron sea model", where the lowest energy level in the conduction band and the highest energy level in the valence band are merged. In contrast, the separation between valence and conduction bands is large for insulators like quartz and polystyrene. The valence band is full and the band gap can exceed 9 eV, therefore such materials show conductivities (σ) lower than 10^{-8} S cm^{-1}. Finally, semiconductors like Si and Ge show intermediate conductivity between conductors and insulators and moderate band gap, thus having a slightly thermally populated valence band at room temperature.

Increase of charge carrier concentration (introduction of either electrons or holes) is achieved by doping of inorganic semiconductors, i.e. inclusion of foreign neutral atoms into the host lattice that changes the electronic structure. As for polymers, in molecular orbital theory the last filled molecular orbital is defined as the highest occupied molecular orbital (HOMO), while the vacant lowest anti-bonding molecular orbital is known as the lowest unoccupied molecular orbital (LUMO). The HOMO-LUMO energy difference is the molecular orbital band gap. The presence of a saturated chain as in the case of linear polyolefins, such as polyethylene (PE) or polypropylene (PP), implies large band gaps (typically around 10 eV) and confers insulating properties to the material.[28]

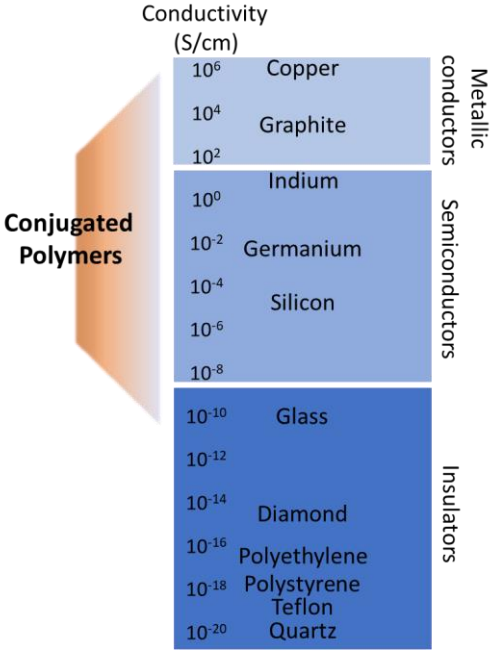

Figure 3. Overview with widely accepted ranges of conductivity for common insulators, semiconductors and conductors compared to that of conjugated polymers.

ICPs in their pristine state typically behave as inorganic semiconductors, since there are no partially filled orbitals at room temperature and conductivity values lie in the lower semiconductor region. It is known that the extension of the conjugation length causes a π-molecular orbitals energy splitting that results in densely packed HOMO and LUMO energy states, thus improving intra-chain conductivity.[29] Generally speaking, disorder leads to charge localization. For instance, stereoregularity contributes to improve the

probability of charge carriers hopping among different chains. On the other hand, owing to the strengthened intermolecular interactions within the backbone, rigidity of the polymeric chains increases, and this leads to low-solubility and mechanical stiffness, eventually worsening the material processability. Alternatively, an organic semiconductor showing weak conductivity in the low semiconductor region can be converted into a semiconductor or ever show a conductor-like behaviour upon doping. Indeed, conductivity in ICPs is intrinsic to a doped state, where π-electrons are delocalized over the whole conjugated polymer backbone with a positive impact on their mobility.

3.2.2 The concept of Doping

The concept of doping is the unique, central, underlying, and unifying theme, which distinguishes conducting polymers from all other types of polymers.[27] During this process, an organic semiconductor, either an insulator or semiconductor having a small conductivity, typically in the range 10^{-10} – 10^{-5} S cm^{-1}, is converted into a conducting species which is in the *metallic* conducting regime (1 to 10^4 S cm^{-1}). Differently from inorganic semiconductors, doping of ICPs implies the occurrence of a chemical reaction, i.e. oxidation or reduction of the polymer backbone, and it is a redox reversible process. Doping can be either performed chemically or electrochemically, to increase the concentration of the major charge carriers, i.e. electrons of holes, thus in a *n-type* or *p-type* fashion, respectively. Concurrently, a counterion is generally addressed as the *doping agent* that stabilizes the doped state by neutralizing the extra charge resulting from electrons extraction or injection during the doping process. For this reason, the doped species is typically classified as a polymeric salt.[28]

The additional charge introduced upon doping is stored in novel electronic states, i.e. polarons and bipolarons.[30,31] Additionally, the rearrangement of the electronic states is accompanied by a lattice distortion. In the case of p-doping (**Figure 4**), a polaron is formed locally when an electron is removed from the conjugated backbone to give a radicalcation. This is consistent with the upward shift of one electronic level from the HOMO and a downward shift of one electronic level from the LUMO into the molecular band gap.

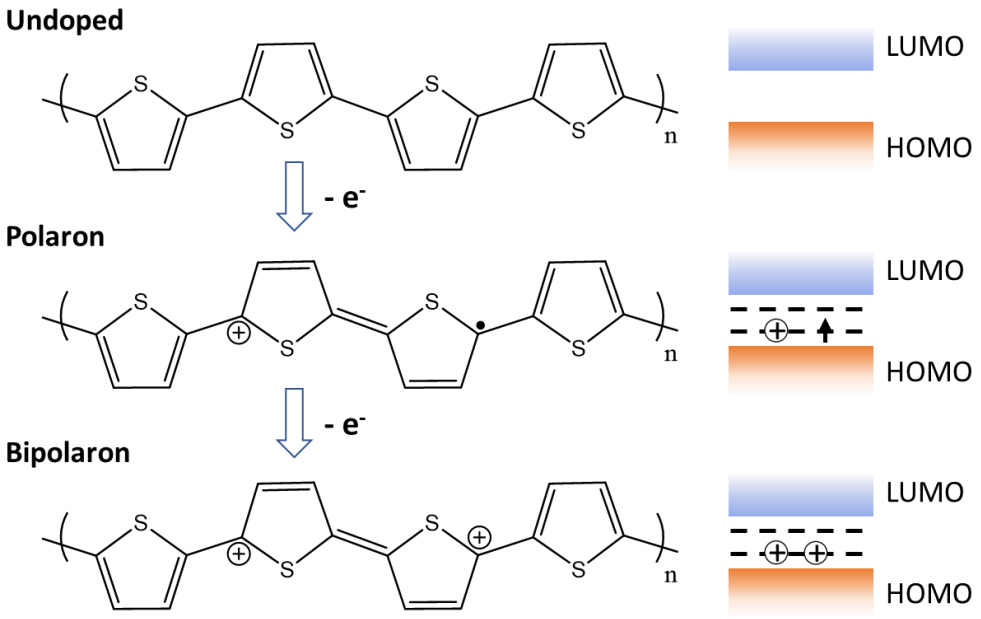

Figure 4. Polythiophene p-doping process and correspondent evolution of the band structure.

The energy difference between the band edge and the newly created states depends on the band gap and the chain length. The electron is then removed from the newly created HOMO-shifted level that results eventually half-filled and localized in the band gap. Therefore, no metal-like character is observed. The polaron formation is associated with a relaxation of the polymer chain that shifts from benzoid to quinoid form. Such a structural rearrangement in polypyrrole, for instance, is shown in **Figure 5** and has been observed experimentally by in situ Raman spectroelectrochemistry.[32]

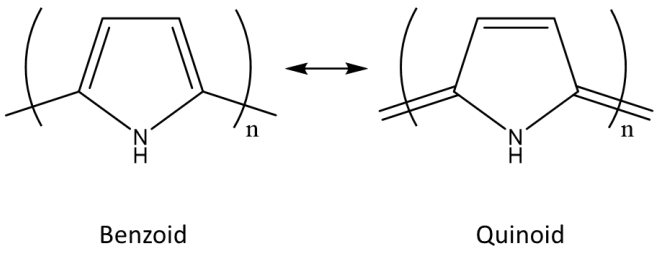

Figure 5. Benzoid and quinoid forms of PPy.

Due to the strong interaction with the counterion, a relatively high amount of dopant is required, with respect to inorganic materials doping, to reach a good carrier mobility in the field of surrounding counterions. Further oxidation leads to the formation of a spinless

charge carrier called bipolaron, which is the thermodynamically favoured combination of two polarons to give a dicationic species: after removal of a second electron from the half-filled level, both shifted levels within the molecular band gap are empty. This phenomenon is associated with a severe local lattice distortion. At high doping levels, newly formed bipolaronic states start to interact with each other and the overlap of their electronic wave functions yields two bands of bipolaronic states within the gap. Therefore, the increase of the polaron density of states creates intermediate band structures that facilitate electronic transport throughout the polymer chain. Energy differences between polaronic/bipolaronic states and the band edges have been reported for polypyrrole by Bredas et al. using tight-binding band-structure calculations, which are in accordance with the evolution of the optical absorption spectrum upon doping.[33] The virtual achievement of a 100% doping level would lead to the extreme broadening of the bipolaron bands until coalescence into the valence and conduction bands. In such case, a metal-like character would arise from the lower half-filled valence/bipolaron band.

Conductivity of ICPs not only varies depending on their chemical nature and degree of doping, but also it is greatly affected by nature of the dopant, synthesis method and physico-chemical properties of the surrounding environment. As regards the effect of temperature, for example, a semiconductor-like behaviour is observed at low doping level, while an increase in the dopant concentration causes a decrease in conductivity with increasing temperature beyond a specific cross-over value. Control of the size, chemical nature and mobility of the dopant counterions is a viable tool for tailoring electrochemical, mechanical and optical properties, as well as processability of the doped system. Electrochemical, chemical and enzymatic syntheses have been reported to impact dramatically on morphology, charge transport properties and electroactivity and they are closely related to the desired final application.

Among polyheterocyclic ICPs, PANi is probably the most prominent example of *non-redox doping* (**Figure 6**). The generalized structural formula consists of alternating *x* benzenoid (reduced) and *(1-x)* quinoid (oxidized) repeating units. The average oxidation state can be varied continuously from x = 1 to give the completely reduced *leucoemeraldine base*, to x = 0.5 to give the half-oxidized *emeraldine base*, to x = 0 to give the completely oxidized *pernigraniline base*. The imine nitrogen atoms can be protonated to give the corresponding salts, with a protonation degree that depends on the oxidation

state and acidity of the solution. Remarkably, the semiconductor emeraldine base subjected to complete protonation by aqueous HCl is doped to its salt form, where delocalized polysemiquinone radical cations determine an increase in conductivity of about 10 orders of magnitude. Conversely, both leucoemeraldine and pernigraniline obtained by emeraldine's reduction and oxidation, respectively, show low electrical conductivity even in their doped forms.[27,34]

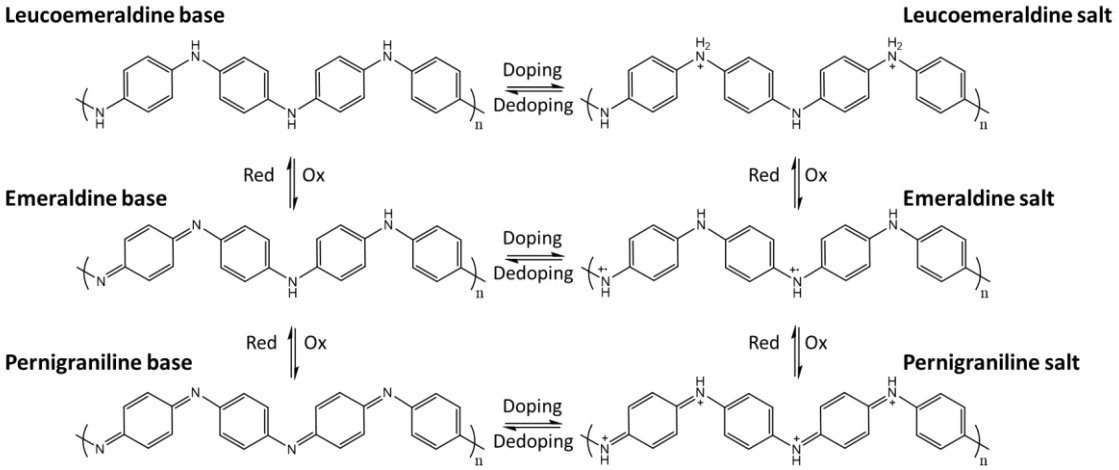

Figure 6. Structures of different oxidation and reduction states of PANi.

3.2.3 Mixed conduction

Among organic electronic materials, ICPs show the capability of transducing ionic fluxes into electronic signals. This feature is addressed as mixed conduction and makes them unique candidates for bioelectronic applications. Indeed, ICPs can shuttle charge through holes/electrons transport in the electronic circuit, together with ionic species via mass transport within an ionic circuit. In disordered semiconductors with localized states in the band gap, conduction occurs by anisotropic intrachain and interchain *hopping* (i.e. phonon-assisted tunnelling between electronic localized states centred at different positions) throughout the conjugated system.[35] In the form of an ion, electrical charges may migrate through an organic solid material if enough cross section (i.e., pore size) and molecular dynamics (e.g., flexibility) are provided by the conducting solid.[18] In the case of conducting polymers, a permeable and soft interface assist ionic transport to occur via the intercalation and drift or diffusion of ions among the flexible polymer chains, with solvent swelling of polymers often increasing the ease of ion motion. However, the capability to

support both ionic and electronic transport by itself is not enough to define a mixed conductor. Crucially, a strong ionic-electronic coupling is needed so that ionic fluxes can induce electronic currents and vice versa. In ICPs this is promoted by the doping process, where ionic species enter the charge balance process that is required to stabilize mobile electronic charges along the polymer backbone.[36] Experimental evidence for mixed conduction has been given for PANi,[37] PPy[38] and PEDOT.[39] The ionic-electronic coupling manifested by ICPs has played a substantial role in the development of organic bioelectronic devices able to bridge the communication gap between biological events and electronic interfaces.

3.2.4 Elements of Biocompatibility

Biocompatibility is not univocally defined and a biomaterial can elicit different responses depending on the local tissue environment and the particular application. The International Organization of Standardization (ISO) has established a framework for such evaluations (ISO 10993; Biological evaluation of medical devices). Feron et al. reviewed in detail the state of the art in organic bioelectronics interfaces and materials' biocompatibility.[40] *In vitro* cytocompatibility, cells adhesion and growth as well as low inflammatory response *in vivo* have been reported for PPy, PANi and PEDOT. However, as properly stressed by Zeglio et al., specific experimental conditions in the synthesis, purification and processing of biomaterials are crucial in determining the biocompatibility of the final device.[41] According to Scopus and despite the relative immaturity of the field with respect to well-established hard microelectronics, about 500 works have been published since 1991 that deal with the use, testing or optimization of conducting polymer-based devices as biointerfaces. Indeed, ICPs possess a unique combination of transducing abilities, chemical and morphological properties that undeniably favours the active interaction of organic bioelectronic devices with biological events. First of all, the already discussed mixed conductivity enables efficient detection and transduction of the bio-information, which is typically shuttled by ions. In addition, films made of ICPs are considered soft solids, with tunable surface roughness and a Young's modulus that is compatible with that of biological tissues. Also, a substantial improvement over the traditional inorganic counterpart is the available 3-D network of ICPs. Indeed, ICPs films swell upon contact with aqueous environments, including biological media, exhibiting a sponge-like behaviour and

providing a 3-dimensional interfacing surface area that is not subjected to corrosion. Ion uptake involves the entire volume of an ICPs film, where the mixed conductor stores charge via reversible and discrete, but overlapping Faradaic events.[42] This aspect determines their pseudocapacitive character and has shed light on ICPs performance as materials for energy storage applications.[43] The ICPs' figure of merit that somehow squares the circle is Volumetric Capacitance (C_V), i.e. a measure of the magnitude of ionic-electronic coupling per unit volume. Therefore, with a high accessible interfacial area and large intrinsic C_V, ICPs based biointerfaces offer significantly lower impedance and better signal transduction with respect to hard-microelectronic materials.[36]

4. PEDOT:PSS

4.1 Polythiophenes

Despite doped polyacetylene is known as the "prototype" and the most highly conductive polymer, intrinsic drawbacks such as its air sensitivity have historically compromised the material processability, leading to a technically useless product. With the aim of stabilizing the sensitive π-electron system, the insertion of heteroatoms in electron-donating substituents or as polymer chain atoms has led to the development of the conjugated heterocycles Polypyrrole and Polythiophene, and of the Polyanilines family, respectively. As a result, a good thermal stability given by aromatic units and high conductivities were achieved in easily synthesizable ICPs.[44] Since 1967, when it was first mentioned as a potential conducting polymer,[45] PT has attracted increasing attention, owing to its favourable characteristics in terms of stability, ease of processability and functionalization. Differently from PPy and PANi, PT and its derivatives do not show intense colours, but rather enough transparency to be extensively employed in a wide range of thin films applications and optoelectronics. Moreover, because of their ease of functionalization, PTs may be nowadays considered the preferred ICPs for electrode systems devoted to amperometric sensing.[46] Due to the great potential in technical applications, a variety of PT derivatives has been synthesised in the last decades by chemical tailoring of the conjugated backbone in order to impart specific features to the resulting material. In this regard, some observations are summarized in the following. First, while PT is almost insoluble in the commonly used organic solvents, the introduction of alkyl substituents facilitates the solubilisation. Moreover, thanks to an electron donor inductive effect, a

significant decrease of the potential required for the oxidation of the monomer is achieved, which is a highly desirable feature when the polymeric film is synthesised by electrochemical methods. Also, regioregularity and coplanar arrangement of the aromatic rings, being closely related to interchain contacts and conjugation, are crucial to ensure high conductivity. Blocking the reactive 3- and 4-positions is necessary to inhibit branching, but mono-substituted derivatives suffer from mixed coupling. While bulky substituents stabilize the polymeric chain, the steric hindrance sharply lowers conductivity. Finally, oxygen substituents at the 3- and 4-positions in the thiophene moiety further stabilize the doped state in polythiophenes, thanks to their electron-donating character. By the development of a PT derivative with two heteroaromatic-fused rings, i.e. the introduction of an ethylenedioxy substituent in the 3- and 4- positions, the goals of high conductivity, long-term environmental stability and processability were combined in poly(3,4-ethylenedioxythiophene) (PEDOT).[44,46]

4.1.1 Synthesis of Polythiophenes

Polythiophene and its derivatives can be readily synthesised through chemical or electrochemical oxidative methods. While the chemical routes consist in mixing the monomer solution with an oxidant, typically $FeCl_3$ or $Na_2S_2O_8$, and the doping agent, during the electrochemical polymerization the supporting electrolyte acts as both doping agent and counterion, which diffuses into the growing chain and allows the polymer formation.[44] As for the electrochemical method, the polymerization is performed through electrodeposition in a three-electrode cell setup, in the presence of a solution containing the monomer, an electrolyte and a solvent. When a suitable potential is applied at the working electrode, the monomer is oxidised leading to the formation of radical cations. Coupling of these species proceeds very fast with respect to the monomer diffusion from the solution, thus promoting further radical-radical coupling nearby the electrode surface. The process goes on until an insoluble oligomer is formed and precipitates above the working electrode.

Chemical synthesis is quite versatile and it yields a bulk product that can be easily solution-processed afterwards. For those reasons, it is particularly suitable for a large-scale production. All ICPs can be synthesized chemically, while electrochemical synthesis is limited to those systems in which the monomer can be oxidized by means of an applied

potential. Electrodeposition benefits from a good time and chemicals economy and, most importantly, it allows the *in-situ* formation of highly conductive thin films.[46] Since the substrate must be conductive, the range of shapes and amounts that can be synthesized is restricted by the geometry and surface area of the electrode.

4.2 PEDOT:PSS

Poly(3,4-ethylenedioxythiophene) was invented in 1988 at the Bayer AG research laboratories (Leverkusen, Germany) and over time it has stood out as the gold star of conductive polymers. Indeed, nowadays it is the only large-scale produced ICP and it finds broad application in plastic electronics, including organic light emitting diodes,[47] organic photovoltaics,[48] supercapacitors,[49] memory storage devices,[50] thin-film transistors,[51] electroactive interface material for bioelectronic applications.[52] In fact, PEDOT exhibits attracting properties and advantages if compared with other ICPs, such as biocompatibility, low oxidation potential, moderate energy band gap (1.6 – 1.7 eV) and stability in the oxidized state. As previously explained, the presence of an ethylenedioxy group in the thiophene moiety yields a resulting polymer with enhanced regioregularity. Additionally, this substituent is responsible for considerably lowering the oxidation potential of both the monomer and the growing polymer, thus stabilizing its conductive form and facilitating the electrochemical synthesis.[46] A massive drawback of PEDOT is its insolubility: to overcome this problem, the water-soluble polyanion poly(styrenesulfonate) (PSS^-) is commonly employed as doping agent and counterion. The resulting PEDOT:PSS (**Figure 7**) is a polyelectrolyte complex that is commercially available as stable dispersion and widely used to fabricate PEDOT:PSS thin films through many deposition techniques, such as spin coating and ink-jet printing. As counterion for PEDOT, PSS^- stabilizes the conducting form of the ICP by maintaining electroneutrality. It is always used in excess and, for this reason, it is addressed as host polyelectrolyte (HPE). The molar ratio of thiophene groups to sulfonic acid groups in standard PEDOT:PSS dispersions is in the range of 1:1.9 to 1:15.2, which corresponds to a weight ratio range of 1:2.5 up to 1:20. Since only one charge is found for every three to four thiophene rings, the charge excess of PSS is between 6-fold and 46-fold.[44] Due to the electrostatic interactions between PEDOT and PSS chains, a core–shell structure with a PEDOT core and a PSS shell forms micro-gel particles (10 nm - 1 mm) in water, with minimal interactions between PEDOT

and water. The non-stoichiometric ratio of PSS to PEDOT also results in a scrambled egg conformation of PEDOT:PSS in water, which remains as colloidal particles at dilute concentrations (<0.1 mg mL^{-1}).[53]

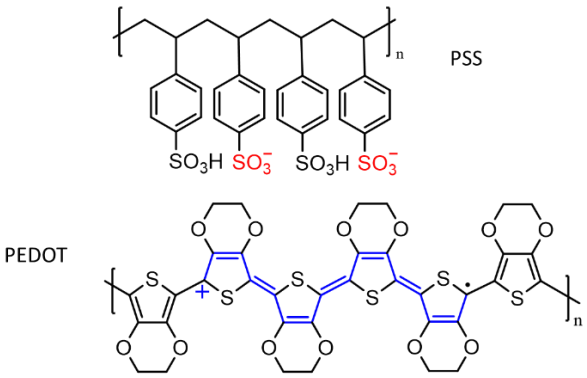

Figure 7. Chemical structure of PEDOT:PSS.

4.2.1 Thin films deposition techniques

It is well known that the properties of materials significantly change when they are in the form of thin films. Like most of the functional materials, PEDOT:PSS is commonly employed in thin film applications due to its peculiar morphological, electrical and optical properties, which will be discussed in following paragraph 4.2.2. Plenty of solution processable methods that yield polymeric thin films are currently available and, among them, the choice is driven by both the processability of the raw starting material and the specific requirements related to the final application. The ideal process involves as few steps as possible, with high throughput, low environmental impact and efficient chemicals economy. Several ink formulations optimized for specific applications and deposition techniques are commercially available, the most popular being produced by Heraeus GmbH (Clevios), Sigma-Aldrich and Agfa Gevaert N.V..

In this section, a brief overview of the most popular film-forming techniques applied to solution processable polymers is given.[44,54,55]

- Casting: probably the simplest film-forming technique available, no equipment is needed apart from a very horizontal work surface. The procedure simply consists in casting a solution onto a substrate followed by solvent evaporation. While it is possible to prepare

films of good quality, the technique suffers from poor reproducibility and a lack of control over the final thickness.

- Spin-coating: this technique typically involves the application of an ink onto a substrate and, after that, the substrate is accelerated to a chosen rotational speed through a suitable equipment. Most of the applied liquid is ejected during rotation, leaving a thin film on the substrate. While closely related to rotational speed, viscosity, volatility, diffusivity, molecular weight and concentration of the solutes, the resulting thickness, morphology and surface topography depend relatively little on the amount of solution deposited, the rate of deposition and the spinning time. Despite the amount of waste produced, spin-coating shows several advantages over other coating techniques and allows the formation of very homogenous films over a large area (the diameter of the substrate can be as high as 30 cm) with remarkable reproducibility.

- Doctor blading: if a well defined film thickness is required, using a doctor blade is a valid alternative to spin coating. The deposition procedure consists in placing a sharp blade at a fixed distance from the substrate surface that is to be coated; then, the coating solution is placed in front of the blade, which is moved linearly across the substrate leaving a thin wet film after the blade. Doctor blading avoids excessive waste production, but is more time-consuming and leads to less homogeneous films if compared to spin-coating.

- Dip coating: the substrate is dipped into the solution and then withdrawn at a controlled speed. The film thickness is determined by the balance of forces at the liquid-substrate interface. Extreme thickness control can be achieved by forming nanostructured systems called Langmuir–Blodgett (LB) films. LB films comprise one or more monolayers that are assembled vertically during immersion/emersion and are usually composed either of amphiphilic molecules or nanoparticles. Despite the quite good uniformity of the resulting film, the possibility of obtaining very thin layers covering large surface areas, this procedure is time consuming and drawbacks include a considerable waste of material.

- Screen printing: also known as serigraphy, it is a printing technique where a mesh is used for the ink transfer. In particular, the solution of the active material is squeezed by a moving blade through a screen mask (stencil) onto the substrate. Generally, micrometric resolution is achieved and the technique is compatible with large area samples, but the waste production is consistent. The main limitation is represented by the need of inks with a certain viscosity to allow a good printing quality.

• Ink-jet printing: it is a relatively novel technique with respect to the other deposition technologies. This process has the major advantage of quite high resolution, ranging from 300 up to 1200 dpi. In contrast to other printing techniques, such as screen printing, it does not require a complex master mould, as the source image to be printed is digitally impressed. In principle, a small droplet is formed either by mechanical compression of the ink through a nozzle (piezoelectric) or by heating the ink. The droplet is then electrostatically charged and accelerated towards the substrate by an electric field. The main advantage is the possibility of creating complex patterns in series of sample with good ink and time economy. However, inks' composition and viscosity strongly affect the printing speed and quality.

• Spray coating: mostly employed in organic photovoltaics, this technique is based on forcing the printing ink through a nozzle, whereby a fine aerosol is formed. A carrier gas and electrostatic charging may be involved to aid in directing the aerosol at the surface that is to be coated. The nozzle is moved at a constant rate over the temperature-controlled substrate and the solution coalesces and spreads over the entire substrate. Once the solvent evaporates, the electrically conducting film is formed. Critical deposition parameters that govern the properties of the cast films are the substrate temperature, solvent composition and additives, volumetric spray rate, lateral nozzle speed, and nozzle-to-substrate distance. Patterning can be done by the use of a shadow mask similar to the stencil employed for screen printing. Spray coating requires a precise temperature control and patterning can be performed with a millimetric-scale resolution. It does not need high quantities of chemicals and the process is scalable to mass production.

4.2.2 Thin films properties

Thanks to their facile integration into various types of devices and their peculiar optical, morphological and electrical properties, thin films of PEDOT:PSS have been utilized in a wide range of applications.

4.2.2.1 Electrochromism

The absorption spectrum of PEDOT:PSS strongly depends on the PEDOT oxidation state (see **Figure 8**). Indeed, it absorbs in the visible region showing a deep-blue colour in the undoped state, while the oxidised form is highly transmissive and its absorption band lies in the NIR region.[56] This behaviour is addressed as *electrochromism.* Thanks to the fact

that PEDOT optical absorption is similar to blue tungsten trioxide and being commercial PEDOT:PSS inks available to the industrial scale, many groups have been investigating this material in electrochromic devices, like smart windows and displays.[57-59] Interestingly, optical properties including color and contrast can be tuned upon chemical modification of EDOT structure to change the absorbance spectrum, design of copolymers comprising another chromophore unit to introduce modified and additional redox and optical states, attachment of electrochromic dyes, use of blends and structured layers.[44]

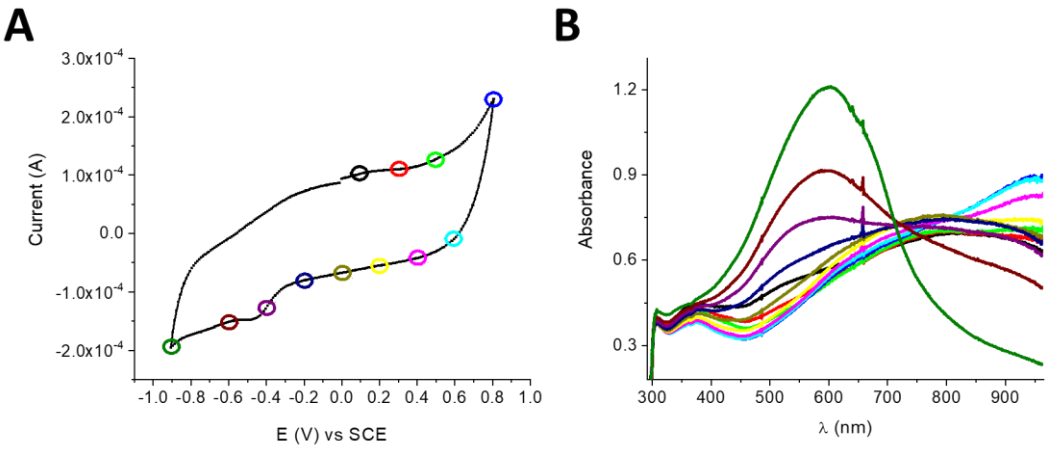

Figure 8. **Spectroelectrochemical analysis of a PEDOT:PSS film deposited on ITO glass**. (**A**) Voltammogram of a PEDOT:PSS/ITO electrode recorded in 0.1M $LiClO_4$ during simultaneous acquisition of UV-Vis spectra (**B**).

4.2.2.2 Morphology

At the nanometre scale, a pancake-like structure comprising flattened, PEDOT rich particles separated by quasi-continuous PSS lamellas has been observed for solid films deposited from aqueous dispersions by atomic force microscopy.[60] Moreover, X-rays scattering analyses have revealed the nanometre-sized crystallization of PEDOT inside hydrophobic core regions of PEDOT:PSS.[61]

As for the meso and microscale, morphological diversity exists among films obtained using different techniques. Electrochemical deposition of PEDOT:PSS produces films with micro-structured texture, where a typical cauliflower-like morphology can be observed by SEM and AFM analyses with slight changes depending on the deposition technique (potentiodynamic, potentiostatic or galvanostatic) and the nature of the substrate. Formation of rod-and fibrous-like structures has been found after potentiodynamic

deposition on stainless steel with anodic potential limit higher than 1.0 V vs SCE.[62,63] Increase in surface roughness upon potentiodynamic deposition cycles has been pointed out.[64] In contrast, a more flattened surface is generally observed for films deposited from PEDOT:PSS dispersions (see **Figure 9**).

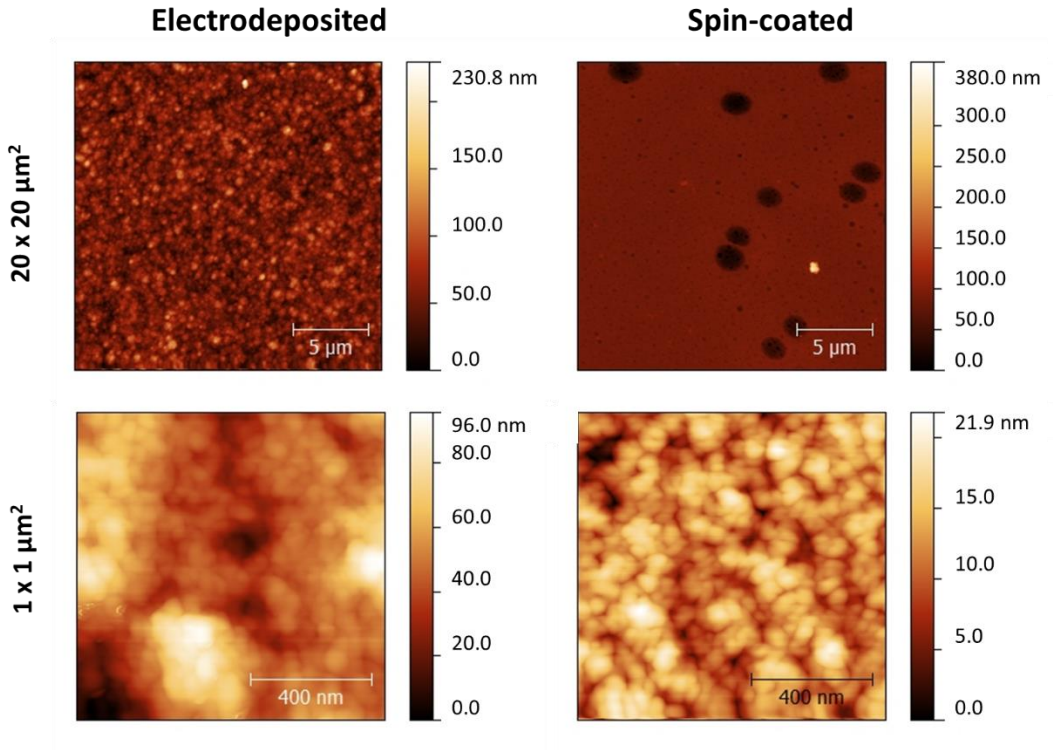

Figure 9. **AFM characterization of electrodeposited and spin-coated PEDOT:PSS films on ITO glass.** For the electrodeposited sample, 5 cycles deposition were carried out from an aqueous solution containing 10 mM EDOT and 0.1 mM PSS in the potential range 0 < E < 1.5 V vs SCE, Scan rate 100 mV s^{-1}; for the spin-coated sample, an ink containing Clevios CPP105D with 20% EG, 0.05% DBSA and 1% GOPS was spin-coated at 1000 rpm for 10 s and annealed at 140°C for 30 minutes.

Phase segregation and a resulting wet film with a PEDOT-rich layer at the bottom and a PSS-rich layer on the top have been observed after spray and spin-coating, in which strong centrifugal forces due to high spinning speed and time is known to promote such phenomenon. Increase of the ink concentration and use of multiple spray passes help to reduce phase segregation and defects formation.[65,66] Also, a library of stabilizing agents, surfactants, film-forming promoters and cross-linkers is available to enrich commercial ink formulations and improve the film quality, with dramatic consequences on the resulting

conductivity and stability. For organic electronic applications, electrical conductivity of the electroactive film is a crucial parameter to consider. Film thickness, lattice dimensions and order, purity and surface roughness are key aspects in defining the type, mechanism and efficiency of the electrical transport.

4.2.2.3 Conductivity

As regards electrical conductivity, values for both chemically and electrochemically prepared PEDOT:PSS films are typically reported at hundreds of S/cm while still transmitting around 80% of visible light. It is known that both excess of PSS in the blend and PEDOT intra/interchain conformation play a key role in the resulting conductivity of PEDOT:PSS. Indeed, charge transport takes place through a hopping mechanism among PEDOT-rich conductive domains, separated by insulating, PSS-rich regions, which represent the main obstacle to transport electric current within the material. It is also known that an increase in the order of the PEDOT segments within the film leads to the formation of highly conductive networks.[67] This positive effect is observed whether a thermally-promoted rearrangement takes place after the deposition, i.e. if the film, for instance, is subjected to an annealing step: the blend of polymeric chains rearranges to a thermodynamic-like form.

Segregation of the PSS excess can be obtained by acid treatments. For instance, sulfuric acid[68,69] and organic acids[70] treatments have been reported to enhance PEDOT:PSS conductivity up to 3000 - 4000 S/cm.[71] However, these approaches raise severe environmental and safety concerns.

More commonly, use of specific additives is a viable tool for film stability and conductivity improvement. For instance, 4-Dodecylbenzenesulfonic acid (DBSA) is an alkyl sulfonate, typically employed as a surfactant to facilitate film processing from PEDOT:PSS dispersions. A beneficial effect has also been reported on conductivity, but concentrations of DBSA higher than 0.5 v/v % induce a phase separation in the ink. Worth of mention is 3-glycidoxypropyltrimethoxysilane (GOPS), the most commonly used cross-linker. Due to the high hydrophilicity of PSS, the exposure of PEDOT:PSS to water can be followed by film delamination. In the presence of GOPS, the assisted formation of covalent bonds between polymer chains and with the substrate improves the film adhesion and stability. Although addressing this issue, increased thickness and lower conductivity of the resulting films are reported as main drawbacks of GOPS use.[72]

Among conductivity enhancing agents, the most popular are glycerol, sorbitol, ethylene glycol (EG) and dimethyl sulfoxide (DMSO).[72-74] Despite the mechanism of conductivity enhancement remains unclarified, the occurrence of a screening effect among the chains that improves the charge carriers hopping rate,[75] a plasticizer effect that promotes reorientation of the polymer chains within the lattice[76,77] and assisted removal of the insulating PSS excess[78] have been proposed as possible explanations.

4.3 Electrochemical sensing and biosensing

Since 1980s[79] electrochemistry at chemically modified electrodes (CMEs) has revolutionized the field of electroanalysis. In particular, the evolution of amperometric sensing from the bare to the modified electrode systems has been triggered by the development of three main electrode modifiers, namely ICPs, self-assembled monolayers (SAMs) and nanostructures,[80] all of them providing an electrocatalytic effect that springs from their inner nature of electron transfer mediators. Commercial availability of precursors, ease of synthesis and functionalization have strongly facilitated the wide diffusion of these materials. Among them, polytiophenes are nowadays flagship surface modifiers for electrode systems devoted to amperometric sensing.[46]

PEDOT has been extensively employed for the realization of CMEs.[81] Thanks to the antifouling properties, it prevents poisoning and insulating layers to form or adsorb onto the electrode surface, providing measurement reliability and expanded linear response range of the sensing device towards the target molecule. Moreover, the capability to activate catalytic charge transfers (electrocatalytic behaviour), similarly to conventional redox mediators, implies two significant benefits for sensing: first, it boosts the redox process by allowing it to take place at lower potentials with respect to those required for bare electrodes, sometimes even avoiding them to occur beyond the solvent discharge; furthermore, catalysis is also responsible for enhancing resolution whether interfering species are present. Thanks to the improved reversibility of the electrochemical process induced by electrocatalysis (**Scheme 1**), the resulting currents are generally higher, thus leading to a lower limit of detection. Additionally, owing to the low oxidative potential at which EDOT polymerizes, PEDOT shows a wide anodic potential window and, since the polymerization is easily run in aqueous media leading to electrochemically stable films, PEDOT:PSS based sensors results noteworthy tools for many electroanalytical

applications. Nevertheless, given the ease of derivatization, selectivity towards the target molecule can be driven up by chemical tailoring and functionalization or design of suited composite materials. Finally, the biocompatible character renders PEDOT particularly suited for the development of bioelectronic devices.

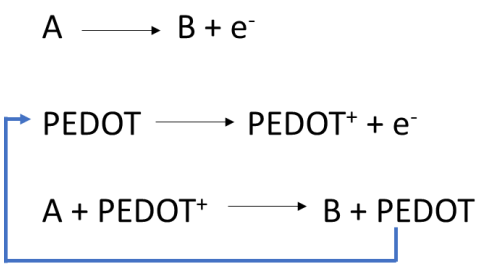

Scheme 1. Electrocatalytic process involving PEDOT and A/B redox couple.

For instance, mixed conductivity of PEDOT:PSS has been exploited to realize a bioelectronic platform to electrically control cells' viability, substrate adhesion and growth.[52] Stretchable, low impedance microelectrodes to record neural activity *in vivo* have been fabricated by electrochemical polymerization of PEDOT:PSS on Au tracks in the presence of the plasticizer polyethylene glycol (PEG)[82] and PEDOT:PSS thin films have been integrated on micro-structured stretchable membranes for Organ-on-a-chip devices.[83]

A number of PEDOT-based sensors and biosensors has been realized for the determination of biologically relevant markers on substrates of different nature.

Interestingly, the ability of conducting polymers to form an ohmic contact to materials with high work function (such as carbon, gold and platinum) and their mixed conductive character have been exploited to develop solid-contact ion-selective electrodes (solid-contact ISEs). These devices can be used for testing ions exchange as well as transport processes that occur across biological membranes and are based either on ICPs as ion-to-electron transducers that can be combined with a library of polymeric ion-selective membranes, or on ICP-based membranes modified to incorporate the ion-recognition sites.[84,85] Solid state PEDOT-based ISEs for K^+ detection[86] have shown less sensitivity to pH with respect to PPy-based counterparts and similar approaches have been applied for the realization of all-plastic, disposable, solid-state K^+ and Ca^{2+} ISEs with near-Nernstian

slope.[87] As sensing membranes, one year stable, heparin-doped PPy and PEDOT, for example, have been used for potentiometric detection of Ca^{2+} and Mg^{2+}, with selectivity in the presence of Na^{+} and K^{+}.[88]

Among the recent literature, enzymatic biosensors for amperometric detection of glucose have been fabricated using PEDOT nanostructures or composites with nanomaterials. For instance, screen-printed carbon electrodes with ferrocene-functionalized PEDOT nanobeads mixed with glucose oxidase (GOx)[89] or coated with a graphene-PEDOT composite with immobilized GOx,[90] PEDOT nanofibers with entrapped GOx[91-93] and hybrid films of PEDOT-containing GOx on nanoporous gold[94] have been reported. Examples of selective amperometric detection of other biologically relevant compounds include a mixed-valent nickel hexacyanoferrate (NiHCF) and PEDOT hybrid film modified sensor for ascorbic acid,[95] a polydopamine/PEDOT composite for dopamine detection,[96] the ascorbic acid and uric acid simultaneous assay at a mixed Diazonium/PEDOT film modified electrode.[97]

As for applications in the field of flexible bioelectronics, PEDOT-based biosensors have been realized on paper, plastic and textiles. Very recently, a disposable, conducting paper-based immunosensing platform with a nanocomposite made of PEDOT:PSS and nanostructured Fe_2O_3 has been reported for the detection of a cancer biomarker,[98] while a fully polymeric, paper-based sensor has been fabricated for the detection of glucose in saliva.[99] With potential in electronic skin applications, a PEDOT:PSS-based biocomposite ink has been micropatterned on flexible Polydimethylsiloxane (PDMS) films to obtain biosensing systems for both redox-active molecules (dopamine, ascorbic acid) and enzyme-catalyzed detection (glucose).[100] As for wearable healthcare applications, PEDOT-based textile electrodes have been developed for electrocardiogram monitoring[101,102] and temperature sensing.[103]

Another class of emerging PEDOT-based bioelectronic devices is that of Organic Thin Film Transistors (OTFTs), and in particular Organic Electrochemical Transistors (OECTs), which will be discussed in the following section.

5. The Organic Electrochemical Transistor (OECT)

ICPs are of great interest in the field of organic bioelectronics as materials that can improve the interface between electronics and biology. Among them, PEDOT:PSS has emerged as the most promising candidate and, in recent years, it has been extensively applied in bioelectronic devices for electrophysiology, biomolecules detection, smart textiles, *in vitro* and *in vivo* cellular recordings. In particular, a special class of electrolyte-gated devices, i.e. Organic Electrochemical Transistors (OECTs), have entered successfully the biomedical arena combining the unique properties of organic conducting materials with the advantages provided by the transistor configuration, such as intrinsic signal amplification and low power consumption. Thanks to their features, OECTs have gained momentum in a number of bioelectronic applications for healthcare and biomedical research, including electrophysiology to record and stimulate the electrical activity of cells,[104,105] drug screening and cell-culture monitoring,[106,107] detection of metabolites and ions[108,109] and neuromorphic devices.[110,111]

The device physics of PEDOT:PSS-based OECTs will be discussed in this section, with particular focus on their use as bioelectronic sensors.

5.1 Working principle of OECTs

In the first papers describing "molecule-based" transistors, Polypyrrole[112] and Polyaniline[113] were electrodeposited to cover Au microelectrodes arrays and the resulting devices were showed to mimic the fundamental characteristics of a solid-state transistor.[114]

An organic electrochemical transistor is a three terminal device where a thin film of an organic semiconductor (channel) is deposited between individually addressable source (S) and drain (D) electrodes. While the source is grounded, a bias (V_d) is applied to the drain electrode that generates a current flowing through the channel (I_d) and collected at the drain. The channel is in direct contact with an electrolyte medium. In the most common configuration, the third electrode, i.e. the gate (G), is electrically separated from the channel, but in contact with the electrolyte solution as well (**Figure 10**).

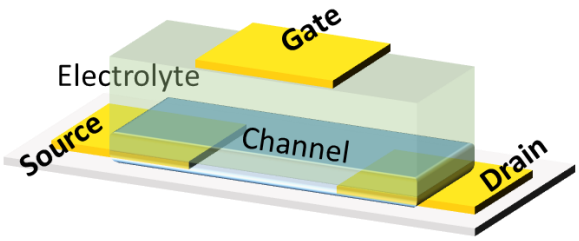

Figure 10. Organic Electrochemical Transistor configuration.

This device exploits the reversible doping process undergone by the polymeric film, which is controlled by the application of a gate voltage, V_g, through the electrolyte solution. Thanks to the high difference in conductivity between doped and dedoped states of conjugated polymers, the polarization of the gate electrode generates an ionic current (I_g) across the medium that is able to induce a pronounced switch between an "on" (conductive) and an "off" (nonconductive) state of the channel. This modulation is caused by the interaction between electronic and ionic charge carriers.[115]

In a PEDOT:PSS-based OECT, following the application of a positive V_g (relative to ground, i.e. the source electrode) at the metal gate electrode, an electric field is generated. Cations in the electrolyte solution are repelled from the gate and injected into the PEDOT:PSS film, causing a depletion of charge carriers while establishing electrostatic interactions with the immobile PSS^- segments (**Figure 11**). The overall result of such a bulk charge accumulation is the dedoping of the polymer channel and thus a decrease in the magnitude of I_d. The opposite occurs in case a negative V_g is applied, and higher I_d values are recorded. Importantly, thanks to the reversibility of the doping process, the modulation upon gating is also reversible and the output current recovers its pristine value whenever a zero-gate bias is applied. If a n-type semiconductor comprises the OECT channel, application of positive or negative V_g values leads to the channel doping or dedoping, respectively. OECTs can work in accumulation or depletion mode. Accumulation-mode transistors are non-conductive at V_g = 0 V and become more conductive in response to a non-zero gate voltage. On the contrary, in depletion-mode transistors the conducting polymer is used in its pristine doped state and is then switched off by the application of a suitable V_g during operation. Since PEDOT:PSS-based OECTs are used in depletion for the applications described in this thesis, only this operation mode

will be analysed. Moreover, dealing with a degenerately p-doped ICP, the nomenclature will be referred to p-type doping.

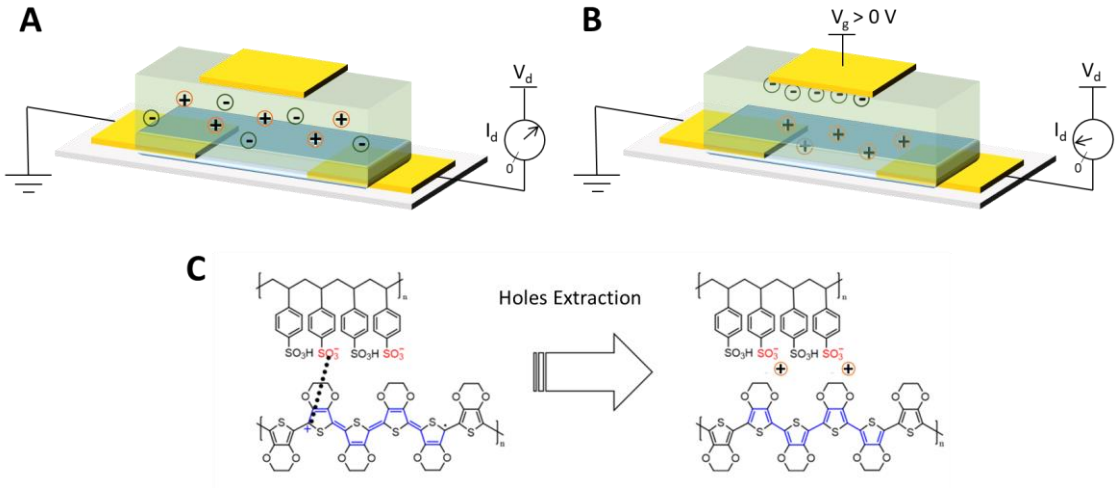

Figure 11. Working principle of a p-type OECT (**A**) without the application of V_g and (**B**) upon application of a positive V_g that causes charge carrier extraction in the channel (**C**).

OECTs are usually characterised through the acquisition of I-V characteristics, where I_d is recorded as a function of the drain (output curve) or the gate voltage (transfer curve). In the output curve (**Figure 12 A**), I_d depends linearly on V_d at low voltages (linear regime) and saturates at higher voltages (saturation regime). The expected modulation upon gate action across the electrolyte can be observed from output curves recorded at different applied V_g. The ability of an OECT to transduce a small V_g input into large changes in the output signal I_d is described by the transfer curve (Figure 12 B). Here, the magnitude of I_d decreases as V_g becomes more positive. The steeper the transfer curve, the larger the I_d variation upon gate action.[116] The amplification capability is provided by the transconductance, expressed as the first derivative of the transfer curve:

$$g_m = \frac{\partial I_d}{\partial V_g} \quad (1)$$

Transconductance is the figure of merit of OECTs, usually reported in the mS range for micrometre-scale devices.[104]

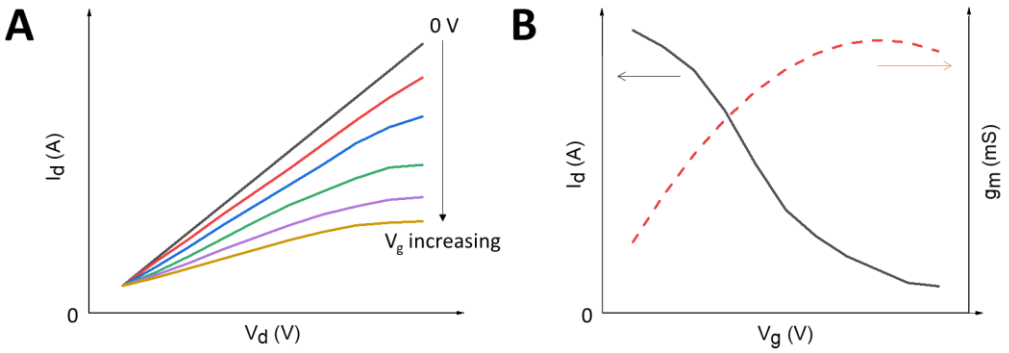

Figure 12. I-V characteristics of the OECT. (**A**) Output curves upon application of positive V_g and (**B**, black solid line) transfer characteristics with correspondent transconductance g_m (red dotted line).

The difference between OECTs and conventional metal-oxide-semiconductor field-effect transistors (MOSFETs) physics is substantial. As already discussed, holes depletion/accumulation involves the entire volume of the semiconductor in a p-type OECT during modulation upon gating. In contrast, in p-type MOSFETs an oxide insulator with immobile dipoles separates the gate from the channel. Upon application of a gate voltage, dipoles are polarized in the insulating layer, thus generating an electric field that induces the accumulation of charge carriers in the channel at the semiconductor/insulator interface.[114,115] Despite this, the I-V characteristics resulting from the two p-type devices in depletion mode show great similarities. For this reason, the first attempt to quantitatively describe OECTs, known as the "Bernards model",[117] was inspired by MOSFETs physics. According to this approach, the behaviour of an OECT can be modeled by considering two complementary circuits: the electronic one, accounting for the hole transport within the channel, i.e. between source and drain, and the ionic one, in which ions are transported through the electrolyte and across the electrolyte/semiconductor interface (**Figure 13**).

The *electronic circuit* is approximated by a resistive element following Ohm's law:

$$J(x) = q\mu p(x)\frac{dV(x)}{dx} \quad (2)$$

where $J(x)$ is the current flux, q is the elementary charge, μ is the hole mobility, p is the hole density and $dV(x)/dx$ is the electric field through the semiconductor. Here, μ is taken as a constant with respect to electrical field and carrier density, while the total charge density is assumed to be uniform within the whole film thickness. By applying a positive

V_g, cations are repelled from the gate electrode into the organic semiconductor and, to maintain charge neutrality, for each ion entering the film a hole extracted from the drain is not replaced by injection at the source electrode (for $V_d < 0$). Therefore, the concentration of hole carriers in a volume v of semiconducting material can be described by:

$$p(x) = p_0 \left(1 - \frac{Q}{q p_0 v}\right) \quad (3)$$

where p_0 is the initial hole density in the organic semiconductor before the application of a gate voltage and Q is the total charge of the cations injected in the organic film from the electrolyte.

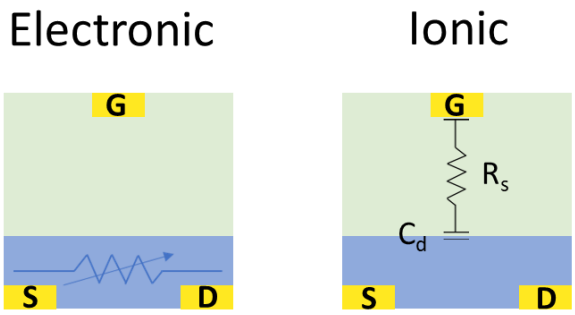

Figure 13. Schemes of the OECT electronic and ionic circuits.

The *ionic circuit*, accounting for the motion of ions through the electrolyte and the charge transfer and accumulation at the gate electrode/electrolyte and channel/electrolyte interfaces, is modeled as a resistor (R_s) and a capacitor (C_d) in series. The resistor stands for the conductivity of the electrolyte and depends on its ionic strength, while the capacitor is the sum of two capacitors in series, which correspond to the polarization occurring at the interfaces just mentioned. If no redox-active species are involved (non-Faradaic regime), the application of a gate voltage is followed by the charging of the capacitor C_d, which refers to the amount of ions that can be stored in the bulk of the ICP. Here, rather than capacitance per unit area, volumetric capacitance has been pointed out as a suitable parameter for describing OECTs operation.[118]

Along with the steady-state behaviour, Bernards et al. also describe the transient behaviour of an OECT. Indeed, the use of the abovementioned equivalent circuit implies that the time

required for the channel current in an OECT to respond to a change in the gate voltage is characterized by an RC time constant defined by the ionic circuit between the gate and channel. The transient behaviour upon the application of a gate voltage exhibits the characteristics of a charging capacitor:

$$Q(t) = Q_{ss}\,[1 - \exp(-t/\tau_i)] \quad (4)$$

where $Q_{ss} = C_d\,\Delta V$ is the total charge that passes through the circuit, ΔV is the voltage applied across the electrolyte, and the ionic transit time is described by $\tau_i = C_d\,R_s$.

The Bernards model provides good fit for the I-V characteristics and allows quantitative predictions of the transconductance.[116,118]
For depletion-mode OECTs:

$$g_m = (W/L)\,d\,\mu\,C_V\,(V_T - V_g) \quad (5)$$

where W, L and d are the channel width, length and thickness, respectively; μ is the charge carrier mobility; C_V is the capacitance per unit volume of the channel and V_T is the threshold voltage. The product $d{\cdot}C_V$ in this expression replaces the capacitance per unit area of the MOS capacitor and defines the major difference between OECTs and MOSFETs.
As pointed out by Friedlein et al.,[115] not only the simplicity of the Bernards model has contributed to its widespread use for describing OECTs in numerous applications, but also it has provided fundamental analytical tools for many more detailed models. The transistor performances, which are affected by the interplay between ionic and electronic currents, can be tuned by varying the material and size of the main transistor elements.[118-121] In this regard, device scaling, geometry optimization and material research are currently focus of great interest among the OECTs community. However, it is evident that OECTs belong to a highly cross-disciplinary domain and micro-scale events, such as mixed conduction and ion uptake, are crucial in the determination of device performances. Therefore, there is an intrinsic complexity in the achievement of unifying theoretical models supported by experiments that can bridge the gap between macro scale observations and micro scale events. This point will be further discussed in Chapter II.

5.1.1 Faradaic and non-Faradaic regimes of operation

According to [122], there are two regimes of operation for OECTs. In particular, the conductivity of the polymer channel can be achieved either involving Faradaic charge transfer processes at the gate/electrolyte interface (Faradaic regime), or by coupling to the charging of an ionic double layer (non-Faradaic or capacitive regime). It is clear that the gate electrode material and the composition of the electrolytic solution are predominant factors in determining the working regime of the device. For instance, it has been pointed out how the I-V curves features of OECTs having Ag or Pt gate electrodes distinguish form each other and exhibit fingerprints of the gate behaviour.[123] On one hand, the transistor I-V characteristics depend on the gate to channel area ratio for the non-Faradaic regime only. While it is generally assumed that the capacitance per unit area in conventional OECTs is bigger at the PEDOT:PSS channel/electrolyte interface than at the polarisable gate electrode/electrolyte interface, the gate to channel area ratio plays a key role in the gating efficiency. Indeed, with a large gate and a small channel area, a significant potential drop arises at the electrolyte/channel interface, resulting in enhanced transconductance. Conversely, with a small gate area, the applied V_g mainly drops at the gate/electrolyte interface and a negligible I_g flows, thus reducing the effective gate voltage acting on the channel. On the other hand, a large steady-state I_g flows due to irreversible redox reaction between ions (halides) in the electrolyte and the Ag gate electrode and leads to improved modulation of I_d. From an electrochemical point of view, a second kind electrode (such as Ag/AgCl) is obtained in the second situation, i.e. a non-polarisable electrode, whose potential is thermodynamically fixed by the halides' activity in the electrolytic solution. Consequently, the applied potential at the gate mainly drops at the channel/electrolyte interface, regardless of the device geometry.

5.2 OECT-based sensors

Since the OECT channel is exposed to an electrolyte solution and PEDOT:PSS exhibits mixed ionic/electronic conductivity, these devices can be used to convert chemical signals into electronic ones with major advantages with respect to conventional electrochemical transducers for bioelectronic application. Indeed, OECT-based sensors combine signal amplification, high transconductance and low power consumption with the ability to operate without a reference electrode, which in most cases hinders sensors' miniaturization

and integration on flexible substrates. Consequently, OECT-based sensors show remarkable design versatility both in terms of geometry and adaptability to unconventional substrates. OECT sensors have two fundamental interfaces, i.e. gate/electrolyte and channel/electrolyte. Typically, analytes detection can be carried out at both transistor elements depending on the detection mechanism and the OECT mode of operation. OECT sensors can be operated in the non-Faradaic and the Faradaic regimes, depending on the desired application. The former case is characterized by the absence of steady-state current flow through the gate circuit: the application of V_g determines exclusively a capacitive current at the gate electrode, the polymer doping is coupled with the charging of an ionic double layer at the gate and the OECT acts purely as an ion-to-electron converter. In the Faradaic regime, the application of V_g determines the occurrence of redox reactions at the gate electrode, with the consequent flow of a steady-state current.[124]

5.2.1 An OECT-based sensor for Glucose detection

From a material research point of view, the strategies used for building selective OECT sensors are generally borrowed from the well-established examples reported for amperometric sensing. In fact, the first works concerning OECT sensors explored the use of redox enzymes as bio-recognition elements, either immobilized within the organic channel or onto the gate electrode or dispersed free-floating in the electrolyte solution, for metabolites' detection.[125-128] Here it was observed that the interaction of the target analyte with the recognition element generates a modulation of I_d, whose variations can be correlated with the analyte concentration, as in a traditional calibration curve. However, the interplay between detection mechanism and current modulation was yet to be understood. The first effort to elucidate the physics underlying OECTs' operation as sensors and connect device response to analyte concentration in OECT-based enzymatic sensors is attributed to Bernards et al.,[129] who chose the enzyme-catalyzed detection of glucose at an OECT as model redox sensing system. For this, a PEDOT:PSS OECT endowed with a Pt gate electrode is considered, where the enzyme GOx is dissolved in the electrolyte solution. The sensor cannot be used for direct electron transfer (DET) detection, and, similarly to a first-generation glucose biosensor, it exploits hydrogen peroxide oxidation. Briefly, in the presence of glucose, GOx catalyzes its oxidation to gluconolactone and the regeneration of GOx cofactor (flavine adenine dinucleotide, FAD)

occurs in a catalytic pathway by reacting with O_2 and production of H_2O_2. Therefore, H_2O_2 is oxidized at the Pt electrode: the number of electron transfers at the electrode surface is directly proportional to the glucose concentration (**Figure 14**).

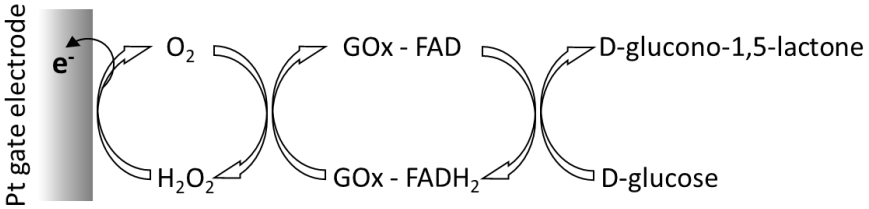

Figure 14. Reaction cycle involved in the detection of glucose.

Upon increase of glucose concentration, enhanced modulation of I_d is observed in the transfer characteristics according to the following equations:

$$I_d = \frac{q\mu p_0 tW}{LV_P}\left(V_P - V_g^{eff} + \frac{V_d}{2}\right)V_d \qquad |V_d| \ll \left|V_P - V_g^{eff}\right| \quad (6)$$

$$V_P = {}^{qp_0 t}/_{c_i} \quad (7)$$

$$V_g^{eff} = V_g + V^{offset} \quad (8)$$

where V_P and V_g^{eff} are the pinch-off voltage and the effective gate voltage, respectively; c_i is the effective gate capacitance per unit area of the transistor and V^{offset} is an offset voltage at the interfaces.

In the presence of a reactive species in the electrolyte solution, the transistor operates in the Faradaic regime. Here, V_g^{eff} represents the gate voltage that is effectively acting on the transistor channel when charge-transfer reactions due to the presence of redox-active species alter the chemical potential equilibrium at the gate/electrolyte interface. The voltage shift V^{offset} accounts for the Faradaic contribution to the effective gate voltage, it is scaled by the capacitance ratio at the channel/electrolyte (C_c) and gate/electrolyte (C_g) interfaces and is linked to the electrochemical potential of the solution, which is in turn

described by the Nernst equation. For this reason, V^{offset} is linearly dependent on the logarithm of analyte concentration.

It is worth to note that in an OECT, where V_g is fixed, the potential shift described by the Nernst equation is manifested by a shift of the electrolyte potential relative to that of the gate. In the absence of charge transfer reactions (non-Faradaic regime), the electrolyte potential (V_{sol}) is determined by the capacitances associated with double layer formation at the gate and the channel:

$$V_{sol} = \frac{V_g}{1+\gamma} \quad (9)$$

with

$$\gamma = \frac{c_c A_c}{c_g A_g} \quad (10)$$

where c_c and c_g are capacitance per unit area of channel and gate, respectively, and A_c, A_g being the correspondent areas. Conversely, due to the occurrence of charge transfer reactions at the gate electrode (Faradaic regime), V_{sol} is shifted by a Faradaic contribution described by the Nernst equation, resulting in:

$$V_{sol} = \frac{V_g}{1+\gamma} + \frac{kT}{ne}\ln[C] + constant \quad (11)$$

where *k* is the Boltzmann constant, *T* the absolute temperature, *n* the number of exchanged electrons, *e* the elementary charge and *[C]* the analyte's concentration.

Based on equation 9, it has been highlighted that, in transistors with a large gate electrode, the electrolyte is nearly at the same potential as the gate, resulting in a large potential drop between the electrolyte and the channel, which, in turn, leads to a strong modulation of the drain current. On the contrary, in transistors with a small gate electrode, the applied potential drops at the gate/electrolyte interface and the resulting modulation of the drain current is weak. It is evident that for both regimes of operation, gate material and transistor geometry play a paramount role in the sensing performances.[119,130-133] For instance, while for OECTs applied as ion-to-electron transducers it is convenient to choose large and/or non-polarizable gate electrodes, in electrochemical sensing a small gate electrode leads to higher sensitivities.

5.2.2 OECT sensors for bioelectronics

Combining the features of a sensor and an amplifier, where small potential changes due to the analyte may lead to a pronounced variation of the output channel current, OECT sensors ensure high sensitivity and improved signal to noise ratio. OECT sensors have been reported for the detection of a variety of biologically relevant analytes with nanomolar and sub-nanomolar detection limits, thus exceeding the performance of conventional electrochemical sensors. These include enzymatic glucose sensing using nanomaterials-modified gate electrodes,[134,135] detection of neurotransmitters, such as epinephrine[136] and dopamine[137] and highly sensitive ions' determination.[109] Integrated with microfluidic systems, OECT sensors have been used for liposome sensing,[138] monitoring of 3D cell cultures membrane integrity[107] and for multianalyte saliva testing.[139] Also, lactate detection in tumour cell cultures has been recently carried out[140] and an OECT sensor capable of attomolar detection of Immunoglobulin G has been reported.[141]

5.2.2.1 All-PEDOT:PSS OECT sensors

A special mention goes to metal-free OECT sensors. First realized by Nilsson et al. in combination with a Nafion membrane as sensitive layer for the determination of air-humidity,[142] this architecture offers remarkable advantages in terms of fabrication and applicability to unconventional substrates. Indeed, since the transistor elements (gate electrode, channel and contacts) can all be patterned from a film of PEDOT:PSS by soft-fabrication techniques in a single step, the device production is considerably simplified, being particularly suited for low-cost and disposable applications.[143] Moreover, the all-plastic, metal-free transistor architecture has unique flexibility and adaptability to supports of different nature, including textiles, with potentiality for wearable applications. Textile, all-PEDOT:PSS OECT sensors have been realized by screen printing on woven cotton and lycra, with no degradation observed after deformation and repetitive hand-washing cycles.[144] In the optimized geometry, the textile OECT sensor was tested for ascorbic acid, dopamine and adrenaline detection.

The working regime of all-PEDOT:PSS devices and the role of the gate in their behaviour have been recently studied for ink-jet printed OECTs.[145,146] In particular, the authors point out that, in contrast to OECTs with metal gate electrodes, in all-PEDOT:PSS OECTs both

gate/electrolyte and channel/electrolyte interface have the same capacitance per unit area. Consequently, it is no longer true that the total capacitance, resulting from the two capacitances combined in series, is dominated by that of the gate/electrolyte interface. In fact, at both interfaces there is a pseudo capacitor material and the device behaviour strongly depends on the gate to channel area ratio. Based on combined I_d-V_g and open circuit potential measurements, it is demonstrated that the all-PEDOT:PSS OECTs behaviour is comparable to the case in which a polarizable metal gate electrode is employed (as long as the overoxidation potential limit of PEDOT:PSS is not reached) and depends on the device geometry. Importantly, it is however stressed that the non-Faradaic-like behaviour originates from electron-transfer processes (doping/dedoping of PEDOT:PSS) involving potential-dependent variation of the polymer's oxidation state at both interfaces, which in turn causes the capacitive effect typical of a pseudo capacitor.

The all-PEDOT:PSS OECT sensors response has been studied in reference to the oxidative detection of the redox benchmark ascorbic acid (AA).[147] AA oxidation at a PEDOT:PSS electrode follows an electrocatalytic pathway (**Scheme 2**) and, at the all-PEDOT:PSS OECT, it can take place at both OECT interfaces. Indeed, V_g not only modulates I_d, but also determines the electrochemical potentials of gate (E_g) and channel (E_{ch}), thus establishing at which OECT element AA oxidation takes place. Indeed, when a positive V_g is applied, E_g is higher than the electrochemical potential of the source (E_s) and AA oxidation is therefore favoured at the gate. Conversely, for negative V_g values, the reaction mainly takes place at the channel because E_g is lower than E_d. While in the former case the charge transfer reaction at the gate boosts the electrocatalytic path and therefore I_g increases, in the latter AA oxidation directly provokes the reduction of PEDOT in the channel. Consequently, the overall result is the depletion of carriers from the channel, with the expected I_d variation. I_d changes until a stationary state is achieved, wherein the rate of holes extraction is equal to the rate of hole injection in the channel. The steady-state I_d scales linearly with the logarithm of AA concentration. Following optimization of device parameters (channel thickness and V_g), the authors report a detection limit of 13 nM, exceeding the performances of OECT sensors endowed with noble metals and nanomaterials-based gate electrodes.

Scheme 2. Electrocatalytic oxidation of ascorbic acid (AA) to dehydroascorbic acid (dAA) at a PEDOT:PSS electrode.

Although all-PEDOT:PSS OECT sensors show remarkable advantages, a selectivity issue must be addressed for real-life applications that has motivated a main part of the research presented in this thesis. Indeed, PEDOT:PSS itself does not show redox affinity to specific molecules, whereas biological fluids contain a number of oxidisable species that act as interferants. Possible solutions are the use of a potentiodynamic V_g and the functionalization of the gate electrode, which will be discussed in Chapters III and IV.

5.2.2.2 Considerations on the sensing response of OECTs

The *intrinsic amplification* provided by OECTs is often invoked as a clear advantage with respect to other devices that has fuelled their successful access in the field of biochemical sensing. It is intuitive that an enhanced output signal is desired to achieve higher sensitivity and has a great impact on the simplification of the readout electronics, both aspects being of paramount importance in bioelectronic applications such as clinical tests or portable/wearable devices. However, the description of such amplifying behaviour is usually limited to the physical characterization of the transistor in terms of transconductance and comparisons with well-assessed technologies, including amperometric sensors, are very rarely provided.

As for the amplification aspects, the sensor response in the detection of the benchmark AA has been discussed for an all-PEDOT:PSS OECT.[133] Importantly, it is shed light on I_g that is related to the rate of both the charge transfer between AA and PEDOT:PSS and the regeneration of charge carriers in PEDOT:PSS by the readout electronics. Indeed, upon increase of AA concentration, I_g increases by a value that is associated to the number of electrons injected in PEDOT:PSS by AA. Therefore, the ΔI_g value is compared to the signal measured in amperometric sensors that exploit AA electro-oxidation. Following this, the chemical gain, G, is introduced, in contrast to the transconductance, to describe the amplification achieved with an OECT sensor:

$$G = \frac{\Delta I_d}{\Delta I_g} \quad (12)$$

Moreover, an attempt in explaining the high amplification observed at low V_g is made. In such conditions, the lowest values of I_g are recorded, meaning that the electrons injected in the channel by AA oxidation are removed more slowly from the channel, exhibiting a longer lifetime. The enduring persistence of electrons in the channel due to slow holes regeneration leads to a stronger action on the output I_d. Despite the fact that low V_g values ensure the highest amplification, they also impact negatively on the response time of the sensor due to the slowered electrochemical kinetics. Consequently, a trade-off is essential to set the working parameters that maximizes both aspects. As pointed out by the authors, a strategy that allows to quickly reach a stable response while maintaining the conditions for maximum amplification is to take advantage of a spontaneous redox reaction for the detection. The research work described in Chapter V has been inspired by this approach.

The use of OECT sensors as quantitative electroanalytical tools has recently been reviewed by Picca et al..[148] In particular, with the aim to encourage a more rigorous approach in the use of transistor-based sensors, the definitions of the figures of merit for performance assessment of a biosensor, including detection (LOD) and quantification limits, sensitivity and so on, are recalled together with the critical description of the two sensing operation conditions exploited for quantitative electroanalytical measurements, i.e. potentiometric and amperometric. The authors argue that the use of OECTs in the detection of redox active species is sometimes difficult to describe unequivocally in these terms when the output I_d is exploited for quantitative purposes. While organic bioelectronic sensors for ions, antigens, DNA, and peptides are generally described as potentiometric devices in similarity with ion-selective electrochemical electrodes, when a redox reaction is involved to selectively detect metabolites, such as glucose, the sensor can be operated either in a potentiometric or amperometric mode. In the first case, an open-circuit potential (relative to a reference electrode) builds at a selective membrane or at an electrode interface functionalized with biological recognition elements that, upon interaction with the analyte, quantitatively correlates to its concentration by the Nernst equation. Such electrochemical potential drop across the sensing interface can be exploited to modulate the output I_d in a transistor configuration. Conversely, the amperometric operating mode involves the measurement of a transient current generated upon application of an external bias that is large enough to trigger the occurrence of the redox reaction used for the detection, i.e.

higher than the electrochemical equilibrium potential of the redox species involved, E_0. The correlation between the measured Faradaic current and the concentration of the analyte in a chronoamperometric measurement is given by the Cottrell equation:

$$I_{ss} = (\pi t)^{-1/2}\, A\, n\, F\, D^{1/2}\, C \quad (13)$$

where I_{ss} is the steady-state current, t is the time, A is the electrode area, n is the moles of exchanged electrons, F is the Faraday constant, D is the diffusion coefficient of the reacting species and C is the analyte's concentration. However, in a transistor configuration that does not comprise a reference electrode, as in the case of OECTs, the quantitative meaning of the analysis is compromised by the impossibility to run the experiment under potentiostatic control. To this regard, alternative analytical uses of OECT and OECT-inspired sensors are presented in this thesis that take into accounts all these aspects for the development of reliable and quantitative bioelectronic devices.

6. References

1. https://www.statista.com/statistics/617136/digital-population-worldwide/
2. National Intelligence Council, Conference Report CR 2008-07, **2008**. http://www.dni.gov/nic/NIC_home.html
3. https://www.statista.com/statistics/471264/iot-number-of-connected-devices-worldwide/
4. A. Al-Fuqaha, M. Guizani, M. Mohammadi, M. Aledhari, M. Ayyash. *IEEE Commun. Surv. Tut.* **2015**, *17*, 2347-2376.
5. I. Sohn. *Mob. Inf. Syst*. **2017**, *2017*, 1-9.
6. A. Pelaez. "The Internet (and the Nature) of Things". https://ubidots.com/blog/the-internet-the-nature-of-things/
7. L. Atzori, A. Iera, G. Morabito. *Comput. Networks* **2010**, *54*, 2787–2805.
8. J. Gubbi, R. Buyya, S. Marusic, M. Palaniswami. *Future. Gener. Comp. Sy*. **2013**, *29*, 1645–1660.
9. G. P. Hancke, B. de Carvalho e Silva, G. P. Hancke Jr. *Sensors* **2013**, *13*, 393-425.
10. R. A. Potyrailo. *Chem. Rev.* **2016**, *116*, 11877−11923.
11. E. K. Lee, M. Y. Lee, C. H. Park, H. R. Lee, J. H. Oh. *Adv. Mater*. **2017**, *29*, 1703638.
12. U. Pliquett. *Proc. 2008 Int. Biennial Baltic Electronics Conference (BEC2008)*, Tallinn, Estonia. **2008**, 11-20.

13. A. Verkhratsky, V. Parpura. *Methods Mol. Biol.* **2014**, *1183*,1-19.
14. D. C. Martin. *MRS Commun*. **2015**, *5*, 131–153.
15. S. Wagner, S. Bauer. *MRS Bull*. **2012**, *37*, 207-213.
16. G. Hong, X. Yang, T. Zhou, C. M. Lieber. *Curr. Opin. Neurobiol*. **2018**, *50*, 33–41.
17. K. Fidanovski, D. Mawad. *Adv. Healthc. Mater*. **2019**, *8*, 1900053.
18. D. T. Simon, E. O. Gabrielsson, K. Tybrandt, M. Berggren. *Chem. Rev*. **2016**, *116*, 13009 −13041.
19. Y. Lu, H. Lyu, A. G. Richardson, T. H. Lucas, D. Kuzum. *Sci. Rep*. **2016**, *6*, 33526.
20. D. J. Carrad, A. B. Mostert, A. R. Ullah, A. M. Burke, H. J. Joyce, H. H. Tan, C. Jagadish, P. Krogstrup, J. Nygård, P. Meredith, A. P. Micolich. *Nano Lett*. **2017**, *17*, 827-833.
21. S. F. Cogan, P. R. Troyk, J. Ehrlich, T. D. Plante. *IEEE Trans. Biomed. Eng*. **2005**, *52*, 1612–1614.
22. C. J. Bettinger. *Bioelectron. Med*. **2018**, *4*, 6.
23. H. Letheby. *J. Chem. Sot*., **1862**, *15*, 161-163.
24. A. Dall'Olio, Y. Dascola, V. Varacca, V. Bocchi, *C. R. Seances Acad. Sci., Ser. C* **1968**, *C267*, 433-435.
25. H. Shirakawa, E. J. Louis, A. G. MacDiarmid, C. K. Chiang, A. J. Heeger. *Chem. Commun.* **1977**, *16*, 578-580.
26. N. Koch. *Chem. Phys. Chem*. **2007**, *8*, 1438–1455.
27. A. G. MacDiarmid. *Angew. Chem. Int. Ed*. **2001**, *40*, 2581-2590.
28. P. Kar. "Doping in Conjugated Polymers". John Wiley & Sons, **2013**.
29. A. Yassar, J. Roncali, F. Garnier. *Macromolecules* **1989**, *22*, 804–809.
30. T.-H. Le, Y. Kim and H. Yoon. *Polymers* **2017**, *9*, 150.
31. P. Chandrasekhar. "Conducting Polymers, Fundamentals and Applications. Including Carbon Nanotubes and Graphene". Springer, **2018**, 2nd edition.
32. M. J. L. Santos, A.G. Brolo, E.M. Girotto. *El. Acta* **2007**, *52*, 6141–6145.
33. J. L. Bredas, J. C. Scott, K. Yakushi, G. B. Street. *Phys. Rev. B* **1984**, *30*, 1023-1025.
34. F. Nastase. "Polyaniline - From Synthesis to Practical Applications". IntechOpen, **2019**.
35. A. B. Kaiser. *Rep. Prog. Phys*. **2001**, *64*, 1–49.
36. B. D. Paulsen, K. Tybrandt, E. Stavrinidou, J. Rivnay. *Nat Mater*. **2020**, *19*, 13–26.
37. J. Stejskal, O. E. Bogomolova, N. V. Blinova, M. Trchová, I. Šeděnková, J. Prokeš, I. Sapurina. *Polym. Int.* **2009**, *58*, 872–879.
38. C. Deslouis, T. El Moustafid, M. M. Musiani, B. Tribollet. *El. Acta* **1996**, *41*, 1343-1349.

39. E. Stavrinidou, M. Sessolo, B. Winther-Jensen, S. Sanaur, G. G. Malliaras. *AIP Adv*. **2014**, *4*, 017127.
40. K. Feron, R. Lim, C. Sherwood, A. Keynes, A. Brichta, P. C. Dastoor. *Int. J. Mol. Sci*. **2018**, *19*, 2382.
41. E. Zeglio, A. L. Rutz, T. E. Winkler, G. G. Malliaras, A. Herland. *Adv. Mater.* **2019**, *31*, 1806712.
42. J. Heinze, B. A. Frontana-Uribe, S. Ludwigs. *Chem. Rev*. **2010**, *110*, 4724–4771.
43. A. M. Bryan, L. M. Santino, Y. Lu, S. Acharya, J. M. D'Arcy. *Chem. Mater.* **2016**, *28*, 5989-5998.
44. A. Elschner, S. Kirchmeyer, W. Lovenich, U. Merker, K. Reuter. "PEDOT: Principles and Applications of an Intrinsically Conductive Polymer". CRC Press, **2010**.
45. M. Armour, A. G. Davies, J. Upadhyay, A. Wassermann. *J. Polym. Sci. Part A-1 Polym. Chem.* **1967**, *5*, 1527–1538.
46. C. Zanardi, F. Terzi, R. Seeber. *Anal. Bioanal. Chem*. **2013**, *405*, 509-531.
47. W. H. Kim, A. J. Mäkinen, N. Nikolov, R. Shashidhar, H. Kim, Z. H. Kafafi. *App. Phys. Lett.* **2002**, *80*, 3844-3846.
48. J.-H. Choi, H.-J. Choi, J.-H. Shin, H.-P. Kim, J. Jang, H. Lee. *Org. Electron.* **2013**, *14*, 3180–3185.
49. G. Cai, P. Darmawan, M. Cui, J. Wang, J. Chen, S. Magdassi, P. S. Lee. *Adv. Energy Mater.* **2016**, *6*, 1501882.
50. J. A. Ávila-Niño, W. S. MacHado, A. O. Sustaita, E. Segura-Cardenas, M. Reyes-Reyes, R. López-Sandoval, I. A. Hümmelgen. Org. Electron. **2012**, *13*, 2582-2588.
51. W. Xu, Z. Hu, H. Liu, L. Lan, J. Peng, J. Wang, Y. Cao. *Sci. Rep*. **2016**, *6*, 29055.
52. F. Amorini, I. Zironi, M. Marzocchi, I. Gualandi, M. Calienni, T. Cramer, B. Fraboni, G. Castellani. *ACS Appl. Mater. Interfaces* **2017**, *9*, 6679−6689.
53. R. Piramuthu Raja Ashok, M. S. Thomas, S. Varughese. *Soft Matter* **2015**, *11*, 8441-8451.
54. O. O. Abegunde, E. T. Akinlabi, O. P. Oladijo, S. Akinlabi, A. U. Ude. *AIMS Mater. Sci.* **2019**, *6*, 174-199.
55. F. C. Krebs. *Sol. Energy Mater. Sol. Cells* **2009**, *93*, 394–412.
56. N. Massonnet, A. Carella, O. Jaudouin, P. Rannou, G. Laval, C. Cellea, J.-P. Simonato. *J. Mater. Chem. C* **2014**, *2*, 1278-1283.
57. P. Andersson, R. Forchheimer, P. Tehrani, M. Berggren. *Adv. Funct. Mater*. **2007**, *17*, 3074–3082.

58. A. W. Lang, Y. Li, M. De Keersmaecker, D. E. Shen, A. M. Österholm, L. Berglund, J. R. Reynolds. *Chem. Sus. Chem*. **2018**, *11*, 854 –863.
59. R. Singh, J. Tharion, S. Murugan, A. Kumar. *ACS Appl. Mater. Interfaces* **2017**, *9*, 19427-19435.
60. A. M. Nardes, M. Kemerink, R. A. J. Janssen, J. A. M. Bastiaansen, N. M. M. Kiggen, B. M. W. Langeveld, A. J. J. M. Breemen, M. M. de Kok. *Adv. Mater*. **2007**, *19*, 1196-1200.
61. T. Takano, H. Masunaga, A. Fujiwara, H. Okuzaki, T. Sasaki. *Macromolecules* **2012**, *45*, 3859-3865.
62. S. Patra, K. Barai, N. Munichandraiah. *Synth. Met.* **2008**, *158*, 430-435.
63. V. Castagnola, C. Bayon, E. Descamps, C. Bergaud. *Synth. Met*. **2014**, *189*, 7-16.
64. M. Marzocchi, I. Gualandi, M. Calienni, I. Zironi, E. Scavetta, G. Castellani, B. Fraboni. *ACS Appl. Mater. Interfaces* **2015**, *7*, 17993−18003.
65. F. Zabihi, Y. Xie, S. Gao, M. Eslamian. *Appl. Surf. Sci*. **2015**, *338*, 163–177.
66. H. J. Snaith, H. Kenrick, M. Chiesa, R. H. Friend. *Polymer* **2005**, *46*, 2573-2578.
67. A. M. Nardes, M. Kemerink, M. M. de Kok, E. Vinken, K. Maturova, R. A. J. Janssen. *Org. Electron.* **2008**, *9*, 727–734.
68. Y. Xia, K. Sun, J. Ouyang. *Adv. Mater*. **2012**, *24*, 2436−2440.
69. N. Kim, H. Kang, J. H. Lee, S. Kee, S. H. Lee, K. Lee. *Adv. Mater.* **2015**, *27*, 2317−2323.
70. J. Ouyang. *ACS Appl. Mater. Interfaces* **2013**, *5*, 13082−13088.
71. Z. Yu, Y. Xia, D. Du, J. Ouyang. *ACS Appl. Mater. Interfaces* **2016**, *8*, 11629−11638.
72. S. Zhang, P. Kumar, A. S. Nouas, L. Fontaine, H. Tang, F. Cicoira. *APL Mater*. **2015**, *3*, 014911.
73. F. M. Tarmidzi, S. B. Sasongko. *Int. J. Appl. Eng*. **2018**, *13*, 10234-10239;
74. A. M. Nardes, R. A. J. Janssen, M. Kemerink. *Adv. Funct. Mater.* **2008**, *18*, 865-871.
75. J. Y. Kim, J. H. Jung, D. E. Lee, J. Joo. *Synth. Met*. **2002**, *126*, 311–316.
76. F. Zhang, T. Nyberg, O. Inganäs. *Nano Lett*. **2002**, *2*, 1373–1377.
77. J. Ouyang, C. W. Chu, F. C. Chen, Q. Xu, Y. Yang. *Adv. Funct. Mater.* **2005**, *15*, 203–208.
78. Y. H. Kim, C. Sachse, M. L. Machala, C. May, L. Müller-Meskamp, K. Leo. *Adv. Funct. Mater.* **2011**, *21*, 1076–1081.
79. R. W. Murray. *Acc. Chem. Res.* **1980**, *117*, 135–141.
80. R. Seeber, F. Terzi. *J. Solid State Electrochem*. **2011**, *15*, 1523–1534.
81. R. Seeber, L. Pigani, F. Terzi, C. Zanardi. *Electrochim. Acta* **2015**, *179*, 350–363.

82. F. Decataldo, T. Cramer, D. Martelli, I. Gualandi, W. S. Korim, S. T. Yao, M. Tessarolo, M. Murgia, E. Scavetta, R. Amici, B. Fraboni. *Sci. Rep*. **2019**, *9*, 10598.
83. W. F. Quirós-Solano, N. Gaio, C. Silvestri, G. Pandraud, P. M. Sarro. *Procedia Eng*. **2016**, *168*, 1184-1187.
84. J. Bobacka. *Electroanalysis* **2006**, *18*, 7–18.
85. J. Bobacka, A. Ivaska, A. Lewenstam. *Chem. Rev.* **2008**, *108*, 329-351.
86. M. Vázquez, J. Bobacka, A. Ivaska, A. Lewenstam. *Sens. Actuators B* **2002**, *82*, 7–13.
87. A. Michalska, K. Maksymiuk. *Anal. Chim. Acta* **2004**, 523, 97-105.
88. B. Paczosa, T. Blaz, J. Migdalski, A. Lewenstam. *Polish J. Chem*. **2004**, *78*, 1543–1552.
89. J.-Y. Wang, L.-C. Chen, K.-C. Ho. *ACS Appl. Mater. Interfaces* **2013**, *5*, 7852–7861.
90. A.Wisitsoraat, S.Pakapongpan, C. Sriprachuabwong, D. Phokharatkul, P. Sritongkham, T. Lomas, A. Tuantranont. *J. Electroanal. Chem*. **2013**, *704*, 208-213.
91. G. Yang, K. L. Kampstra, M. R. Abidian. *Adv. Mater*. **2014**, *26*, 4954–4960.
92. P. Santhosh, K. M. Manesh, S. Uthayakumar, S. Komathi, A. I. Gopalan, K. P. Lee. *Bioelectrochemistry* **2009**, *75*, 61-66.
93. M. Z. Çetin, P. Camurlu. *RSC Adv*. **2018**, *8*, 19724–19731.
94. X. Xiao, M. Wang, H. Li, P. Si. *Talanta* **2013**, *116*, 1054-1059.
95. T.-H. Tsai, T.-W. Chen, S.-M. Chen. *Electroanalysis* **2010**, *22*, 1655-1662.
96. R. Salgado, R. del Rio, M. A. del Valle, F. Armijo. *J. Electroanal. Chem*. **2013**, *704*, 130-136.
97. W. Richard, D. Evrard, P. Gros. *Electroanalysis* **2014**, *26*, 1390–1399.
98. S. Kumar, M. Umar, A.Saifi, S. Kumar, S. Augustine, S. Srivastava, B. D.Malhotra. *Anal. Chim. Acta* **2019**, *1056*, 135-145.
99. E. Bihar, S. Wustoni, A. M. Pappa, K. N. Salama, D. Baran, S. Inal. *npj Flex. Electron*. **2018**, *2*, 30.
100. R. K. Pal, S. Pradhan, L. Narayanan, V. K. Yadavalli. *Sens. Actuators B* **2018**, *259*, 498-504.
101. I. G. Trindade, F. Martins, P. Baptista. *Synth. Met*. **2015**, *210*, 179-185.
102. A. Achilli, A. Bonfiglio, D. Pani. *IEEE Sens. J.* **2018**, *18*, 4097–4107.
103. Y. Zhang, Y. Cui. *IEEE Trans. Electron Devices* **2019**, *66*, 3129-3133.
104. D. Khodagholy, T. Doublet, P. Quilichini, M. Gurfinkel, P. Leleux, A. Ghestem, E. Ismailova, T. Hervé, S. Sanaur, C. Bernard, G. G. Malliaras. *Nat. Commun*. **2013**, *4*, 1575
105. A. Campana, T. Cramer, D. T. Simon, M. Berggren, F. Biscarini. *Adv. Mater*. **2014**, *26*, 3874–3878.

106. L. H. Jimison, S. A. Tria, D. Khodagholy, M. Gurfinkel, E. Lanzarini, A. Hama, G. G. Malliaras, R. M. Owens. *Adv. Mater*. **2012**, *24*, 5919–5923.

107. V. F. Curto, M. P. Ferro, F. Mariani, E. Scavetta, R. M. Owens. *Lab Chip* **2018**, *18*, 933-943.

108. C. Liao, M. Zhang, L. Niu, Z. Zheng, F. Yan. *J. Mater. Chem. B* **2013**, *1*, 3820–3829.

109. M. Ghittorelli, L. Lingstedt, P. Romele, N. I. Crăciun, Z. M. Kovács-Vajna, P. W. M. Blom, F. Torricelli. *Nat. Commun.* **2018**, *9*, 1441.

110. P. Gkoupidenis, D. A. Koutsouras, G. G. Malliaras. *Nat. Commun*. **2017**, *8*, 15448.

111. J. Y. Gerasimov, R. Gabrielsson, R. Forchheimer, E. Stavrinidou, D. T. Simon, M. Berggren, S. Fabiano. *Adv. Sci.* **2019**, *6*, 1801339.

112. H. S. White, G. P. Kittlesen, M. S. Wrighton. *J. Am. Chem. Soc*. **1984**, *106*, 5375–5377.

113. E. W. Paul, A. J. Ricco, M. S. Wrighton. *J. Phys. Chem.* **1985**, *89*, 1441-1447.

114. S. M. Sze. "Physics of Semiconductor Devices". Wiley, **1981**, 2nd edition.

115. J. T. Friedlein, R. R. McLeod, J. Rivnay. *Org. Electron*. **2018**, *63*, 398-414.

116. J. Rivnay, S. Inal, A. Salleo, R. M. Owens, M. Berggren, G. G. Malliaras. *Nat. Rev. Mater*. **2018**, *3*, 17086.

117. D. A. Bernards, G. G. Malliaras. *Adv. Funct. Mater*. **2007**, *17*, 3538–3544.

118. J. Rivnay, P. Leleux, M. Ferro, M. Sessolo, A. Williamson, D. A. Koutsouras, D. Khodagholy, M. Ramuz, X. Strakosas, R. M. Owens, C. Benar, J.-M. Badier, C. Bernard, G. G. Malliaras. *Sci. Adv*. **2015**, *1*, e1400251.

119. F. Cicoira, M. Sessolo, O. Yaghmazadeh, J. A. DeFranco, S. Y. Yang, G. G. Malliaras. *Adv. Mater*. **2010**, *22*, 1012–1016.

120. A. Giovannitti, C. B. Nielsen, D.-T. Sbircea, S. Inal, M. Donahue, M. R. Niazi, D. A. Hanifi, A. Amassian, G. G. Malliaras, J. Rivnay, I. McCulloch. *Nat. Commun*. **2016**, *7*, 13066.

121. V. Venkatraman, J. T. Friedlein, A. Giovannitti, I. P. Maria, I. McCulloch, R. R. McLeod, J. Rivnay. *Adv. Sci. (Weinh).* **2018**, *5*, 1800453.

122. F. Lin, M. C. Lonergan. *Appl. Phys. Lett.* **2006**, *88*, 133507.

123. G. Tarabella, C. Santato, S. Y. Yang, S. Iannotta, G. G. Malliaras, F. Cicoira. *Appl. Phys. Lett.* **2010**, *97*, 123304.

124. G. Tarabella, F. Mahvash Mohammadi, N. Coppedè, F. Barbero, S. Iannotta, C. Santato, F. Cicoira. *Chem. Sci*. **2013**, *4*, 1395-1409.

125. T. Matsue, M. Nishizawa, T. Sawaguchi, I. Uchida. *J. Chem. Soc., Chem. Commun.* **1991**, *15*, 1029-1031.

126. M. Nishizawa, T. Matsue, I. Uchida. *Anal. Chem*. **1992**, *64*, 2642-2644.

127. D. T. Hoa, T. N. S. Kumar, N. S. Punekar, R. S. Srinivas, R. Lal, A. Q. Contractor. *Anal. Chem*. **1992**, *64*, 2645-2646.

128. Z. T. Zhu, J. T. Mabeck, C. C. Zhu, N. C. Cady, C. A. Batt, G. G. Malliaras. *Chem. Commun.* **2004**, *13*, 1556-1557.

129. D. A. Bernards, D. J. Macaya, M. Nikolou, J. A. DeFranco, S. Takamatsu, G. G. Malliaras. *J. Mater. Chem*. **2008**, *18*, 116–120.

130. P. Lin, F. Yan, H. L. W. Chan. *ACS Appl. Mater. Interfaces* **2010**, *2*, 1637–1641.

131. O. Yaghmazadeh, F. Cicoira, D. A. Bernards, S. Y. Yang, Y. Bonnassieux, G. G. Malliaras. *J. Polym. Sci., Part B: Polym. Phys.* **2011**, *49*, 34-39.

132. L. Contat-Rodrigo, C. Pérez-Fuster, J. V. Lidón-Roger, A. Bonfiglio, E. García-Breijo. *Org. Electron*. **2017**, *45*, 89-96.

133. I. Gualandi, E. Scavetta, F. Mariani, D. Tonelli, M. Tessarolo, B. Fraboni. *El. Acta* **2018**, *268*, 476-483.

134. H. Tang, F. Yan, P. Lin, J. Xu, H. L. W. Chan. *Adv. Funct. Mater*. **2011**, *21*, 2264-2272.

135. J. Liao, S. Lin, Y. Yang, K. Liu, W. Du. *Sens. Actuators B* **2015**, *208*, 457-463.

136. N. Saraf, E. R. Woods, M. Peppler, S. Seal. *Biosens. Bioelectron*. **2018**, 117, 40-46.

137. H. Tang, P. Lin, H. L.W.Chan, F. Yan. *Biosens. Bioelectron.* **2011**, *26*, 4559-4563.

138. G. Tarabella, A. G. Balducci, N. Coppedè, S. Marasso, P. D' Angelo, S. Barbieri, M. Cocuzza, P. Colombo, F. Sonvico, R. Mosca, S. Iannotta. *Biochim. Biophys. Acta* **2013,** *1830*, 4374–4380.

139. A.-M. Pappa, V. F. Curto, M. Braendlein, X. Strakosas, M. J. Donahue, M. Fiocchi, G. G. Malliaras, R. M. Owens. *Adv. Healthc. Mater*. **2016**, *5*, 2295-2302.

140. M. Braendlein, A.-M. Pappa, M. Ferro, A. Lopresti, C. Acquaviva, E. Mamessier, G. G. Malliaras, R. M. Owens. *Adv. Mater.* **2017**, *29*, 1605744.

141. E. Macchia, P. Romele, K. Manoli, M. Ghittorelli, M. Magliulo, Z. M. Kovács-Vajna, F. Torricelli, L. Torsi. *Flex. Print. Electron*. **2018**, *3*, 034002.

142. D. Nilsson, T. Kugler, P.-O. Svensson, M. Breggren. *Sens. Actuators B* **2002**, *86*, 193-197.

143. N. D. Robinson, P.-O. Svensson, D. Nilsson, M. Berggren. *J. Electrochem. Soc*. **2006**, *153*, H39-H44.

144. I. Gualandi, M. Marzocchi, A. Achilli, D. Cavedale, A. Bonfiglio, B. Fraboni. *Sci. Rep*. **2016**, *6*, 33637.

145. L. Basiricò, P. Cosseddu, A. Scidà, B. Fraboni, G.G. Malliaras, A. Bonfiglio. *Org. Electron*. **2012**, *13*, 244-248.

146. M. Demelas, E. Scavetta, L. Basiricò, R. Rogani, A. Bonfiglio. *Appl. Phys. Lett*. **2013**, *102*, 193301.

147. I. Gualandi, M. Marzocchi, E. Scavetta, M. Calienni, A. Bonfiglio, B. Fraboni. *J. Mater. Chem. B* **2015**, *3*, 6753-6762.

148. R. A. Picca, K. Manoli, E. Macchia, L. Sarcina, C. Di Franco, N. Cioffi, D. Blasi, R. Österbacka, F. Torricelli, G. Scamarcio, L. Torsi. *Adv. Funct. Mater*. **2019**, 1904513, 10.1002/adfm.201904513.

II. *In operando* study of OECTs by means of Scanning Electrochemical Microscopy

As anticipated in Chapter I, Organic Electrochemical Transistors belong to a highly cross-disciplinary domain and a comprehensive understanding of electrochemical and physical phenomena originating their response is crucial for improved handling and design of these devices. However, the lack of suitable tools for direct investigation of microscale effects has hindered the possibility to bridge the gap between experiments and theoretical models. In this chapter, a scanning probe setup is described to explore the operation mechanisms of OECTs by probing the local electrochemical potential and the local impedance of the organic film composing the device channel. Moreover, an interpretative model is developed in order to highlight the meaning of electrochemical doping and to show how the experimental data can give direct access to fundamental device parameters, such as local charge carrier concentration and mobility. This approach is versatile and provides insight into the organic semiconductor/electrolyte interface and useful information for materials characterization, device scaling and sensing optimization.

1. Background

Since the first example of an OECT was proposed by Wrighton et al. in 1984,[1] organic electronics has radically impacted on the development of smart bio-interfaces. OECTs are a special class of electrolyte-gated transistors where ionic to electronic transduction can take place with intrinsic amplification and low operating voltages. For this reason, these devices have entered successfully the fields of biosensors and bioelectronics, unfolding

their innovative potential in biomolecules detection,[2-5] electrophysiology,[6-8] in-vitro and in-vivo cellular recordings.[9-11] Currently, intensive research effort is focused on novel OECT channel materials[12] and architectures[13] to gain faster response time, increased sensitivity and lower power consumption targeting new applications in wearable technology and health care.[14-18] Despite their well-established relevance in the development of novel bio-technologies, the device physics still lacks a comprehensive understanding. Operational models able to accurately define and interpret the device working principle are required, as they would reveal well-aimed strategies for metrics refinement and guide targeted optimization of novel materials. Therefore, an improved knowledge of OECTs operation would impact on applications requiring higher sensitivity and amplification of the output signal, fast response time as well as selectivity.

As anticipated in the introductory chapter (Chapter I), in a typical OECT configuration an organic film deposited between two metal electrodes, i.e., source (grounded) and drain collectors, and a gate electrode are in contact with the same electrolyte solution. The organic material constituting the transistor channel is usually PEDOT:PSS (poly(3,4-ethylenedioxythiophene):poly(styrene sulfonate)), i.e., a polyelectrolyte complex containing a degenerately p-doped semiconductor (PEDOT) and a polyelectrolyte counterion (PSS). The presence of multiple phases in thin films of PEDOT:PSS at the nanoscale has been revealed by scanning probe microscopy. Pancake-shaped PEDOT-rich islands are separated by lamellas of PSS-rich domains, thus forming a blend of electronic and ionic phases.[19] Mixed ionic and electronic transport is crucial in OECT operation and originates from the reversible doping/de-doping mechanism of the organic film. It is well known that doping and de-doping of conjugated polymers like PEDOT rely on reversible electrochemical redox processes (oxidation and reduction, respectively).[20] Electrochemical doping is the phenomenon that rules OECTs operation and is driven by the applied potential between the polymer in the channel and the gate material. Concurrently, cations from the electrolyte are needed to compensate the charge excess of PSS^- when PEDOT is de-doped and therefore the speed of electrochemical doping depends on the rate of the ionic flux across the electrolyte.[21] Impedance analyses have given direct evidence of ion penetration throughout the full volume of the semiconductor film, suggesting that volumetric capacitance (C_V) is the appropriate parameter to describe OECTs physics.[22] The overall effect is that the application of a gate voltage (V_g) changes charge carrier concentration in the polymer channel, where PEDOT undergoes reversible

electrochemical doping. As the channel conductivity is altered, a modulation of the electronic current flowing in the OECT channel (drain current, I_d) due to the applied drain voltage (V_d) is observed. Transconductance ($g_m = \frac{\partial I_d}{\partial V_g}$) is the parameter that describes how much an OECT can amplify an input voltage at the gate into the output current flowing in the channel. It is known that, in the linear regime ($V_d \sim 0$), carrier transport in electrolyte gated transistors is related to both mobility and concentration variations of the charge carriers:[23]

$$I_d = \alpha \mu p \quad (1)$$

with μ and p being mobility and concentration of the charge carriers, respectively. α is a coefficient that only depends on controlled experimental parameters ($\alpha = Wtq\frac{V_d}{L}$, with q being the electron charge), such as device geometry (channel width, *W*, length, *L*, and thickness, *t*), as well as V_d. However, due to the disordered, non-crystalline structure of organic semiconductors, a carrier-concentration-dependent mobility model has been recently introduced to describe the steady state behaviour of OECTs.[24]

The performance of OECT materials is commonly evaluated from macroscopic electrical measurements and continuum models taking into account averaged drift-diffusion and electrostatics. A recent review by Friedlein et al.[25] collects the most relevant contributions to quantitatively model the OECT transient response with different degrees of sophistication.[23,26-28] So far, only indirect experimental approaches have been developed, where electrical potential and electrochromic variations in the millimetre scale along the OECT channel length have been used to support semi-empirical models.[21,24] At the same time, experiments that correlate the averaged microscopic film morphology, as characterized by NEXAFS and X-ray scattering experiments, with macroscopic ionic and electronic transport properties emphasize the crucial role of film morphology.[29] To extend this knowledge, a novel approach is needed that could investigate crucial transport parameters such as carrier mobility and concentration at a local scale in a working electrochemical transistor.

Scanning probe techniques have been demonstrated to provide access to local properties of organic semiconducting thin films. Electrostatic force microscopy has been used to investigate potential profiles, charge transport, field-effect mobility and trapping of charge carriers along the polymeric channel of field effect transistors operating in air.[30] In the case

of electrolyte-gated transistors, strong screening effects and electrochemical reactions at the semiconductor/electrolyte interface under investigation prevent the measurements of the quantities determining local electrical transport by means of electrostatic force microscopy. The presence of the electrolyte solution causes further sub-nanometric swelling due to ion uptake. The effect was quantified and related to local structure by i*n-operando* electrochemical strain microscopy (ESM) as demonstrated for poly(3-hexylthiophene) (P3HT) films.[31]

An alternative microscopic technique addressing this challenge is scanning electrochemical microscopy (SECM), which makes use of an accurately positioned microelectrode for the locally resolved electrochemical evaluation of a sample surface.[32,33] Since the investigated surface is assessed with the microelectrode acting as a spectator from the solution side, the electrochemical properties of interest can be investigated for devices under operation and for electroactive films deposited on different materials, including insulating substrates. In the analysis of conducting polymers, SECM has been used to monitor the flux of ions leaving or entering the polymer film, either by direct conversion of electroactive ions at the SECM tip[34-39] or by potentiometric detection using an ion-selective electrode as probe.[40,41] Moreover, SECM has been also used for the characterization of local electrochemical conductivity by monitoring the electron transfer between the evaluated conductive polymer and a soluble redox mediator recycled at the microelectrode.[42-47] Quantitative analyses have been also performed for the determination of lateral charge propagation in thin polymer films[48,49] and charge transfer kinetics at the polymer/electrolyte interface.[50,51] In addition, the capabilities of SECM for precisely positioning of the microelectrode probe were exploited for evaluating the effect of light-induced switching of conductance at a nanojunction after in-situ growing of PEDOT strands bridging a Pt tip and a substrate modified with Au nanoparticles.[52]

In the work presented in this chapter, a SECM setup is exploited to carry out local measurements of the electrochemical potential and impedance along the PEDOT:PSS channel during OECT operation in aqueous environment. A model to interpret the obtained local electrochemical data in buffered electrolyte solution and in the presence of ascorbic acid as reducing analyte is proposed. The results demonstrate the direct relation between electrochemical potential of the polymer and its doping state. Therefore, it is proved how fundamental OECT parameters, such as charge carrier concentration and mobility, as well as contact resistance and the effective electrical field, can be directly determined from the

microscopic in-operando measurements. The results concerning the local electrochemical potential are here reproduced with permission from F. Mariani, F. Conzuelo, T. Cramer, I. Gualandi, L. Possanzini, M. Tessarolo, B. Fraboni, W. Schuhmann, E. Scavetta: Microscopic Determination of Carrier Density and Mobility in Working Organic Electrochemical Transistors. Small, 2019, 15, 1902534. Copyright Wiley-VCH Verlag GmbH & Co. KGaA.[53] Finally, in-operando measurements of the local AC impedance along the channel are presented as a further example of SECM application to working OECTs.

2. Electrochemistry at the all-PEDOT:PSS OECT

As anticipated in Chapter I (paragraph 5.2.2.1), an all-PEDOT:PSS OECT is composed by a conducting channel and a gate electrode that are made of the same material. Indeed, the traditional, either ideally non-polarizable (such as Ag/AgCl) or metallic gate electrode is here replaced by a PEDOT:PSS film having the same channel thickness. In analogy to the conventional transistor configuration, the two transistor elements are immersed in the same electrolytic solution, the source is grounded and a bias is applied to the drain (V_d) that generates the flow of an electronic current throughout the channel (I_d). While the overall working principle still relies on the reversible modulation of I_d upon the gate action across the electrolyte, application of positive and negative biases at the gate terminal does not result in the simple polarization of the gate electrode. Indeed, bulk doping-dedoping redox processes occur in both the channel and the gate of an all-PEDOT:PSS OECT (**Figure 1**).

If the all-PEDOT:PSS OECT is operated in depletion mode, application of a positive V_g causes PEDOT oxidation at the gate. The electrons extracted at the gate are injected in the channel leading to a consequent reduction of PEDOT:PSS. At the same time, an injection of cations from the electrolyte is needed to maintain electroneutrality (Figure 1A). Since the oxidized centers of the polymer are the charge carriers, reduction of $PEDOT^+$ corresponds to holes extraction from the OECT channel, thus determining a decreased conductivity, and a smaller I_d is recorded. On the contrary, a negative gate bias causes $PEDOT^+$ reduction at the gate electrode, while electrochemical oxidation takes place in the channel (holes injection) (Figure 1B) leading to an increase of I_d.

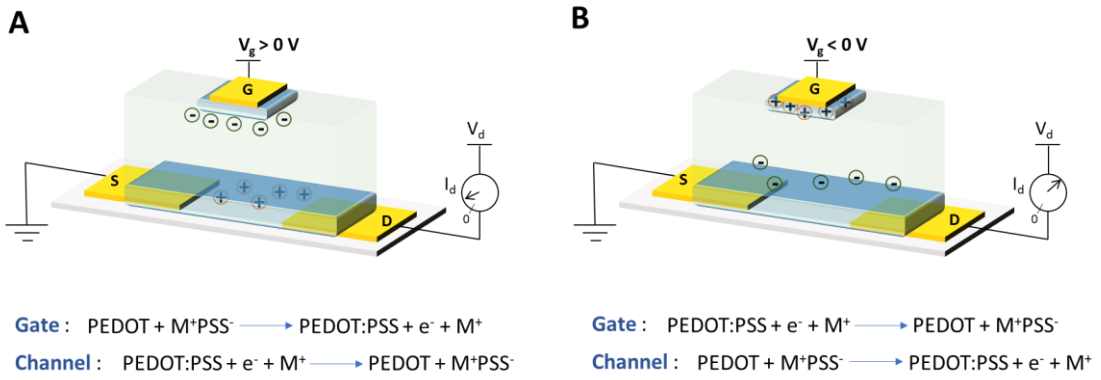

Figure 1. Operation of an all-PEDOT:PSS OECT. (**A**) Application of positive V_g leads to PEDOT oxidation at the gate electrode and holes extraction from the channel. (**B**) Application of negative V_g leads to $PEDOT^+$ reduction at the gate electrode and holes injection in the channel.

3. *In-operando* measurement of the local electrochemical potential

The local electrochemical potential (E_{SECM}) of the polymeric channel was measured during OECT operation using a SECM setup for controlled and precise positioning of a microelectrode probe (**Figure 2**A). A detailed description is given in the Materials and Methods section. Briefly, the transistor was biased with a bipotentiostat while E_{SECM} was measured as the voltage between a Pt microelectrode in contact with the channel surface and a quasi-reference electrode (Ag wire, QRE) immersed in the electrolyte (100 mM phosphate buffer solution, PBS, pH 7.0). The rationale behind this approach is illustrated in Figure 2 B-C (the representation of the PEDOT:PSS blend was oversimplified for graphical reasons). The Pt microelectrode forms an ohmic contact with the electronic PEDOT phase and thus reports the conducting polymer's electrochemical potential when measured with a high-impedance differential amplifier against the QRE. Application of a positive voltage to the gate electrode causes a drop in OECT channel conductance as electrons enter the electronic phase and deplete the OECT channel from hole carriers. Accordingly, the local E_{SECM} value becomes more negative, corresponding to a reduced state of the conjugated polymer in electrochemical terminology (Figure 2B). Conversely, application of a negative potential to the gate electrode causes the opposite reaction. The extraction of electrons from the electronic PEDOT phase leads to an increase in channel conductance and this phenomenon corresponds now to a more positive E_{SECM} and an oxidized state of the conjugated polymer (Figure 2C). Consequently, measuring the local value of E_{SECM} provides direct access to quantify the local changes in electrochemical

doping and carrier concentration as detailed below. Local gradients in E_{SECM} are further related to the local electric field that drives carrier transport enabling the measurement of local carrier mobility.

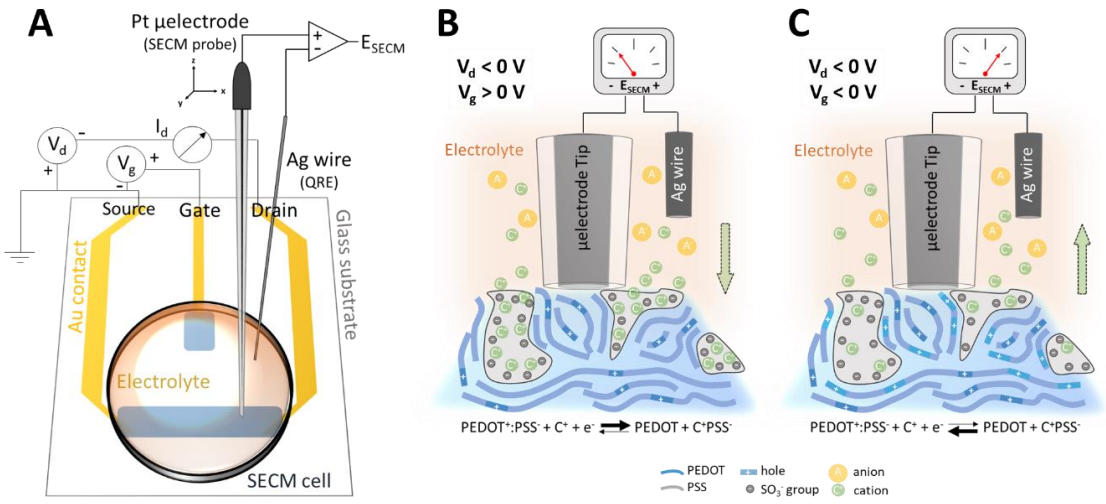

Figure 2. Reversible electrochemical doping revealed by SECM. (**A**) Experimental setup for microscopic in-operando analysis of OECTs, where the SECM cell containing the electrolyte solution was positioned on top of the device. Local electrochemical potential data were collected with a Pt microelectrode connected to a differential amplifier with respect to a quasi-reference electrode (QRE, Ag wire). (**B**, **C**) Schemes illustrating microscopic measurements of the electrochemical potential of the polymer channel during OECT operation. (**B**) Positive V_g leading to holes extraction and (**C**) negative V_g leading to holes injection that are revealed by different values of recorded electrochemical potential (E_{SECM}). Green arrows indicate the direction of cations flow.

In order to validate our approach, potentiometric SECM measurements were performed on a set of different OECTs that either vary due to channel or gate geometry (see the Experimental section), in buffer solution and in the presence of a redox active compound. **Figure 3**A reports a typical OECT output characteristic showing the expected I_d modulation upon gating. When acquired in the presence of ascorbic acid, AA (Figure 3A, dotted lines) a different output compared to the case in buffer solution (Figure 3A, solid lines) is obtained. In order to understand the microscale effects, the microelectrode probe was used to have direct access to the electrochemical phenomena taking place at the OECT channel. During OECT operation, a Pt microelectrode was accurately positioned in the desired location along the transistor channel by performing amperometric approach curves

as described in the Experimental section. Once the polymer surface was detected, the tip was retracted and then potentiometric approach curves were recorded from the bulk solution to the channel surface (Figure 3B). Small variations in the measured E_{SECM} in the bulk solution are ascribed to the gate leakage current across the electrolyte. Upon contact with the surface, E_{SECM} takes a constant value that reports the established ohmic contact between the microelectrode tip and the electronic PEDOT phase. The measured final E_{SECM} values are strongly dependent on the applied V_g, according to the doping state of the polymer in the OECT channel that is reversibly changed upon gating. Positive gate voltages (V_g = +600 mV) leading to holes extraction cause a shift towards more negative E_{SECM} values, while a shift towards more positive E_{SECM} values is observed during holes injection (V_g = -600 mV).

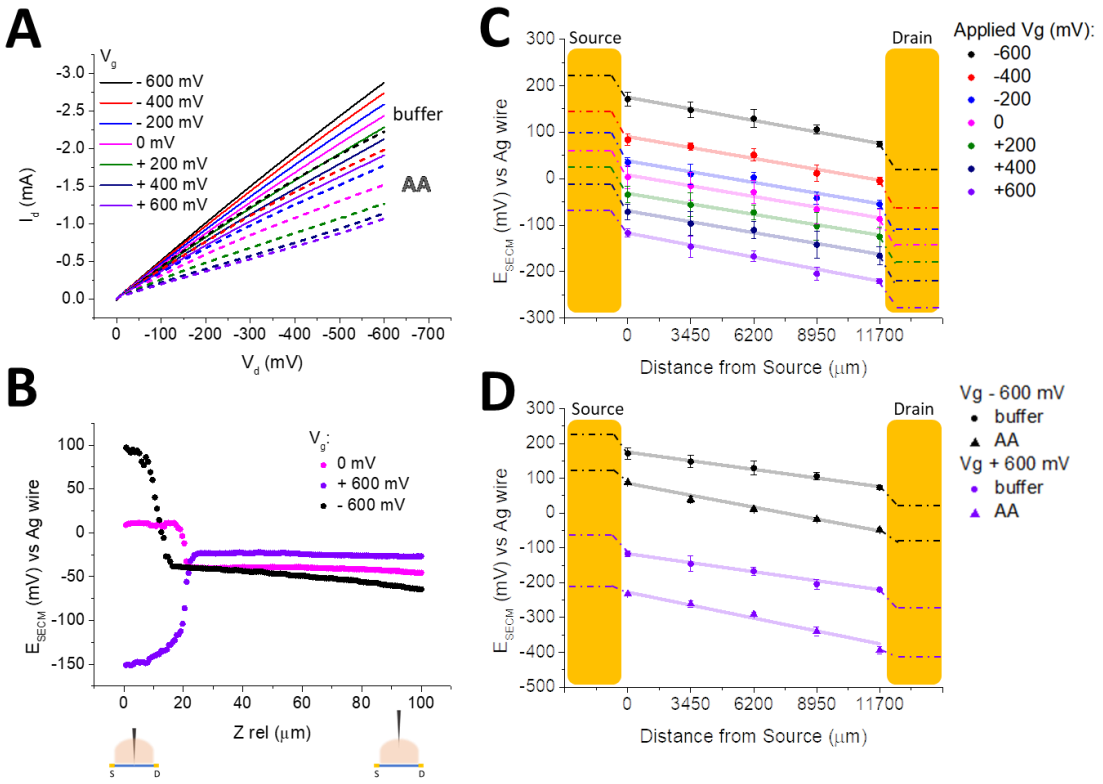

Figure 3. In-operando recordings of electrochemical potential. (**A**) Output curves recorded in 100 mM PBS (solid lines) and in the presence of 1 mM ascorbic acid, AA (dotted lines). V_d = -200 mV. (**B**) Approach curves recorded in 100 mM PBS while moving the SECM probe from the bulk solution to the polymer surface, in the middle of the OECT channel, at different applied V_g. V_d = -200 mV. (**C**, **D**) Electrochemical potential profiles along the OECT channel (**C**) in 100 mM PBS at different applied gate biases (V_d = -200 mV) and (**D**) in 100 mM PBS or in the presence of 1 mM AA at V_g = ± 600 mV. Dotted lines represent the potential drop occurring between gold source/drain contact and polymer film.

The local measurement of E_{SECM} was used to obtain potential profiles along the biased OECT channel (Figure 3, C and D). For this, the microelectrode tip was accurately positioned over the channel at five different locations between source (S) and drain (D). Electrochemical data were collected while keeping V_d constant (-200 mV) for various applied V_g, and in the absence or presence of AA in the electrolyte. A linear decrease of E_{SECM} from S to D confirmed the linear regime of operation. Moreover, when a reducing analyte (AA) is added (Figure 3D, triangles), its oxidation can take place at the gate or at the channel of an all-polymeric OECT depending on the applied V_g and, consequently, on the relative electrochemical potentials assumed by the organic gate and channel.[54] Compared to the buffer solution, in the presence of AA the recorded E_{SECM} drops to lower values as its oxidation always leads to a de-doping of the OECT channel.

Models explaining the OECT operation as sensors[55,56] are based on the hypothesis that the occurrence of redox reactions involving the analyte cause a variation of the effective gate voltage (V_g^{eff}), thus affecting the observed modulation of the channel current. In particular, V_g^{eff} changes can originate from gradients in the electrolyte potential and potential drops at the gate/electrolyte and channel/electrolyte interfaces. However, actual detection mechanisms are still unknown for a number of sensing devices. Thanks to the planar OECT geometry, we were able to test both gate and channel during the same experiment, as illustrated in **Figure 4**, providing a deeper insight into OECT operation.

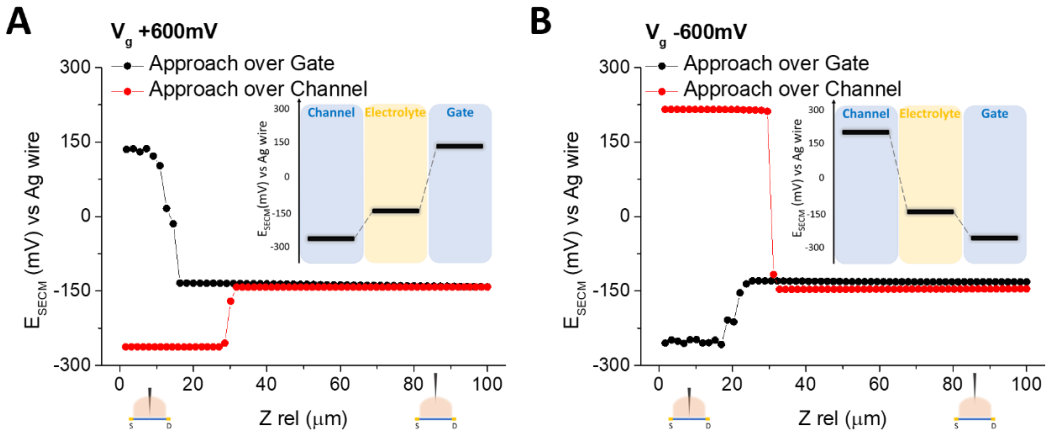

Figure 4. Potential distribution in the gate/electrolyte/channel interface. Approach curves recorded in 100 mM PBS while moving the SECM probe from the bulk solution to the polymer surface, in the middle of the OECT channel and gate, when a positive (**A**) or negative (**B**) V_g is applied. V_d = -200 mV. Insets show the potential diagrams drawn from the correspondent approach curves.

Approach curves were recorded to collect the local E_{SECM} from the bulk electrolyte until the microelectrode tip is coming in contact with the polymer surface in the middle of the gate or channel of a biased device. A positive V_g causes hole accumulation in the gate and depletion in the channel. Accordingly, a high E_{SECM} on the gate electrode and a low E_{SECM} on the channel is measured (Figure 4A). Conversely, the channel exhibits a higher E_{SECM} than the gate electrode when a negative V_g is applied, as holes are injected into the channel (Figure 4B). Consequently, these observations allow to draw experimental potential diagrams at the interface channel/electrolyte/gate during transistor operation, as shown in the insets of Figure 4. The direct measurement of the potential distribution between gate and channel is a capability unique to this technique and allows to predict where and to what extent an electrochemically active analyte will react during detection with an OECT sensor, offering experimental access to the mechanisms involved in analytes' detection.

3.1 Theoretical interpretation of measured data

In order to provide a quantitative interpretation of the SECM measurements, the schematic cross section of a PEDOT:PSS film contacted by an Au source electrode and in contact with the OECT electrolyte solution (100 mM PBS), as shown in **Figure 5**A, and the related energy level diagram in Figure 5B are considered.

As typical in OECTs, the Au source electrode is set to ground while a bias is applied to the gate electrode (not shown) that shifts the potential of the electrolyte solution. Consequently, the diagram of an OECT during operation does not report a thermodynamic equilibrium with a single, constant electrochemical potential throughout the connected phases. Instead, we distinguish three different electrochemical potentials. Note that the electrochemical potential is here used in equivalence to the Fermi level. Conversion between the two can be obtained by $E_F = E_{F,r} - qE(ref)$ where $E(ref)$ is an electrochemical potential measured with respect to a reference electrode, while $E_{F,r}$ is the Fermi level of the reference electrode ($E_{F,r}\,(vacuum\ scale) = -qV_{ref}\,(absolute\ scale)$, i.e., the reference electrode potential in absolute potential scale).[57,58]

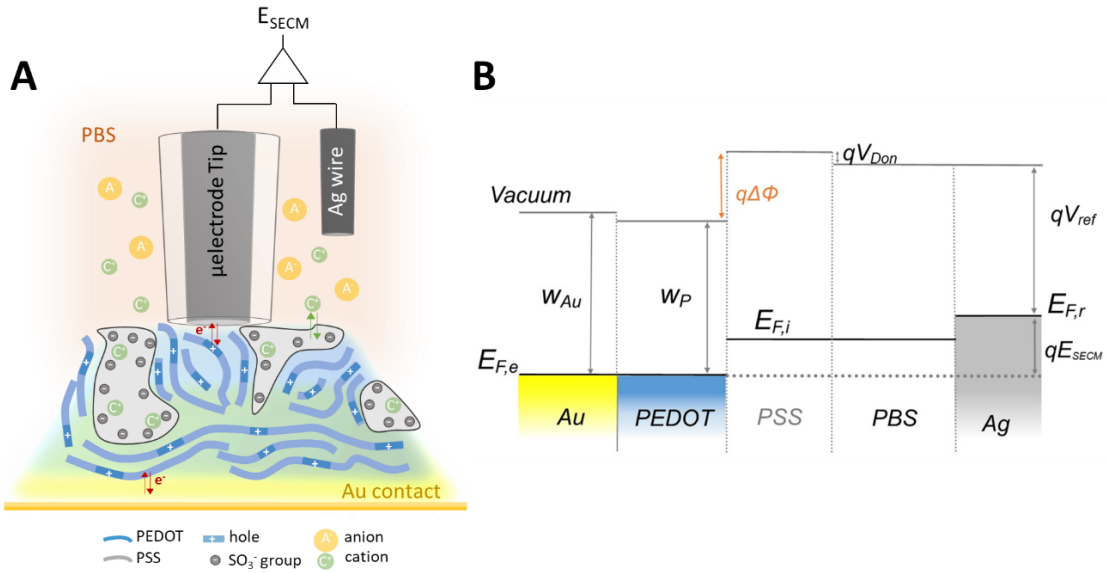

Figure 5. The PEDOT:PSS/electrolyte interface in a biased OECT. (**A**) Schematic cross section of a PEDOT:PSS film contacted by a source electrode (Au contact, grounded) and in contact with the electrolyte solution (100 mM PBS) during the SECM experiment. An electrical contact is established between the Pt microelectrode tip and the electronic PEDOT phase. (**B**) Energy diagram of Au/PEDOT/PSS/PBS/Ag QRE system interfaces in buffer solution. W_{Au} = gold work function; W_P = PEDOT work function; q = electron charge; $\Delta\Phi$ = difference in vacuum level between PEDOT and PSS phases; V_{Don} = Donnan potential; qV_{ref} = quasi-reference electrode energy level; E_{SECM} = potential difference measured between the quasi-reference electrode and the Pt tip in contact with the electronic PEDOT phase; $E_{F,e}$ and $E_{F,i}$ = Fermi levels of the electronic and ionic phases, respectively; $E_{F,r}$ = Fermi level of the quasi-reference electrode.

The first electrochemical potential represents the electronic phase $E_{F,e}$, which constitutes the gold source electrode and the conjugated polymer PEDOT. As there is typically a small offset between the Au and PEDOT workfunctions, a small shift in vacuum level appears when the materials come into contact. The next distinct electrochemical potential, $E_{F,i}$, regards the ionically conducting phase that is constituted by PSS-rich domains in the blend and the PBS electrolyte. The actual value of $E_{F,i}$ is determined by several processes, such as the capacitive couplings at the OECT channel and the gate electrode, Faradaic processes that lead to leakage current and the concentrations of electrochemically active species. In the diagram, $E_{F,i}$ is set at an arbitrary value that is representative for the experiments performed. At the interface between PSS and PBS, an offset in vacuum level appears due to the presence of immobile PSS anions. The limited ionic mobility corresponds to the presence of a semipermeable membrane, causing the existence of a Donnan potential, V_{Don}[59] at the PSS/PBS interface. The third electrochemical potential, $E_{F,r}$ regards the Ag

QRE. Although a constant dipole at the PBS/Ag interface is likely to exist, it is here neglected for simplicity, thus the vacuum level is aligned with the ionic phases. For this experiment, the difference between the vacuum and Fermi levels for the Ag QRE (qV_{ref}) is set to 4.9 eV (as calculated from[57]). In the SECM experiment, the Pt microelectrode establishes an ohmic contact with the PEDOT-phase and hence the differential amplifier reports the difference between Fermi levels of the electronic phase and the Ag QRE: $qE_{SECM} = E_{F,e} - E_{F,r}$.

The relationship between E_{SECM} and the carrier concentration p can be found considering the interface between the PEDOT and PSS microphases. The shift in vacuum level at this interface can be readily calculated from the energy diagram:

$$\Delta\Phi = V_{Don} + E_{SECM} + V_{ref} - W_P/q \quad (2)$$

The vacuum level shift is directly related to the charged double layer that originates at the interface of the two microphases, where anionic charges of PSS in the ionic phase counterbalance the local accumulation of positive hole charges on PEDOT chains in the electronic phase during electrochemical doping. This capacitive-like structure links the vacuum level shift with variations in the hole charge concentration Δp:

$$\Delta p = \frac{1}{q} C_V \Delta\Phi \quad (3)$$

where C_V is the volumetric capacitance.[22]

Note that the energy-level diagram in Figure 5B can be adapted for different operating conditions of the OECT, but Equation (2) and (3) remain always valid. For example, application of a negative bias to the gold electrode, as occurring at the drain electrode in OECT under operation, shifts the levels of the electronic phase upwards and, consequently, a smaller E_{SECM} value is measured (**Figure 6** A). In fact, a decrease in E_{SECM} is observed experimentally (Figure 3C) when the Pt microelectrode is positioned closer to the drain electrode. Similarly, the presence of a reducing agent (AA) leads to the formation of a positive electrostatic potential in the ionic phase that shifts the vacuum level downwards (Figure 6 B). The predicted decrease in E_{SECM} in the presence of AA is also observed experimentally (Figure 3D).

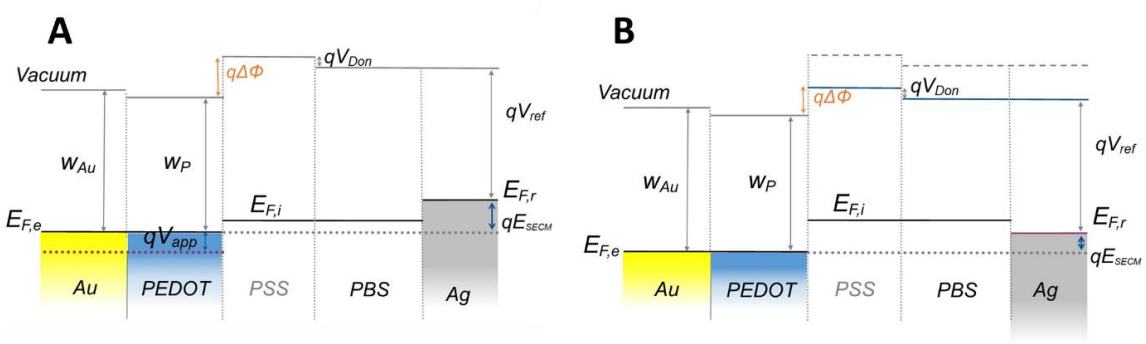

Figure 6. Energy diagram of the polymer/electrolyte interface: particular cases. (**A**) If a negative bias is applied at the Au/PEDOT:PSS electrode (e.g., -200 mV as happens at the drain contact), the Fermi level of the electronic phase shifts upwards (the red dotted line indicates the level of the grounded electrode), while the energy levels in the other phases remain unaltered. As a consequence, a smaller E_{SECM} is measured. (**B**) The addition of a reducing agent (e.g., ascorbic acid) reduces the chemical potential of the PBS phase. As its electrochemical potential is fixed due to the equilibrium with the gate electrode, a potential builds-up that shifts the vacuum level downwards. The consequence is a smaller measured E_{SECM} value.

Combination of Equation (2) and (3) finally provides a correlation between the electrochemical potential, E_{SECM}, and the carrier density, p:

$$p = p_{00} + \frac{1}{q} C_V E_{SECM} \quad (4)$$

where p_{00} stands for the intrinsic carrier density. A detailed description about the derivation of the interpretative model is given in the following.

The effective charge carrier density can be expressed as:

$$p = p_0 + \Delta p = p_{00} + \frac{1}{q} C_V E_{SECM} \quad (5)$$

where p_0 is the initial hole density in the organic semiconductor, q the electron charge, C_V the volumetric capacitance, E_{SECM} the electrochemical potential of the polymer film and p_{00}, i.e. intrinsic carrier density, can be defined as:

$$p_{00} = p_0 + \frac{1}{q} C_V (V_{Don} + V_{ref} - \frac{W_P}{q}) \quad (6)$$

where V_{Don}, V_{ref} and W_P stand for the Donnan potential, the quasi-reference electrode potential and PEDOT work function, respectively.

In the linear regime, where $V_d \sim 0$, the current density is constant and the electric field in the semiconductor can be approximated as $\xi = \frac{\Delta V_d}{L} = \frac{V_d}{L}$, if V_d is the potential applied at the drain electrode and L the channel length. Combining Equation (1) and (4), is possible to plot the product $I_d L/wtqV_d$, which is a mobility multiplied by carrier density, vs E_{SECM} according to the following equation:

$$\frac{I_d L}{wtqV_d} = \mu p_{00} + \frac{\mu C_V}{q} E_{SECM} \quad (7)$$

where I_d is the drain current, w the channel width, t the channel thickness and μ the charge carrier mobility.

Example: if we take an OECT with fixed and known w, t, and L, from the intercept and the slope it is possible to compute the mobility and the initial carrier concentration.

As demonstrated by Tybrandt et al.,[59] Equation (4) is only valid in the regime of high and intermediate hole concentrations (p > 20 mol m^{-3}), as it neglects variations in the chemical potential of the holes at low concentrations. However, for the presented measurements this condition is considered to be fulfilled. We also note that the fully depleted conjugated polymer would be too resistive to establish an electronic contact with the Pt microelectrode.

3.2 Experimental verification of electrochemical potential – carrier density relation

Equation (4) is valid independently of channel geometry, applied gate voltage or presence of electrochemically active compounds. In order to prove this universal validity, we tested four different devices (geometry parameters reported in the Experimental section) having different gate size (OECT 1 > 2 > 3 > 4), channel resistance and thickness, in buffer and in the presence of AA (1 mM). Transfer characteristics obtained in the linear regime for the four different OECTs are shown in **Figure 7** and it clearly stands out how the device geometry (Figure 7A) and the presence of a reducing agent (Figure 7B) have a profound impact on I_d amplitude and modulation upon gating. Nonetheless, if we plot the product of mobility and carrier density ($\mu_{eff} p = {}^{I_d}/_{\alpha}$) as a function of the measured E_{SECM} (recorded in the middle of the channel), all data converges on a straight line with slope $m = \mu_{eff} \frac{C_V}{q}$

and intercept $k = \mu_{eff}\, p_{00}$ (Figure 7, C and D), as predicted by Equation (4) multiplied by a constant effective mobility, μ_{eff}. Small deviations from linearity (OECT 1) are typically assumed to be caused by a carrier density dependent mobility (as described by Friedlein et al.[24]) or strong variations in the density of states. These data cover a variation of carrier density in the range of 2.2 to 3.9 $\times 10^{20}$ cm^{-3} in buffer solution, which is typical for OECT based sensors that employ maximum transconductance for signal amplification. In the presence of a reducing analyte, further modulation is achieved through chemical de-doping and charge carriers are depleted to a density of 1.2 $\times 10^{20}$ cm^{-3}.

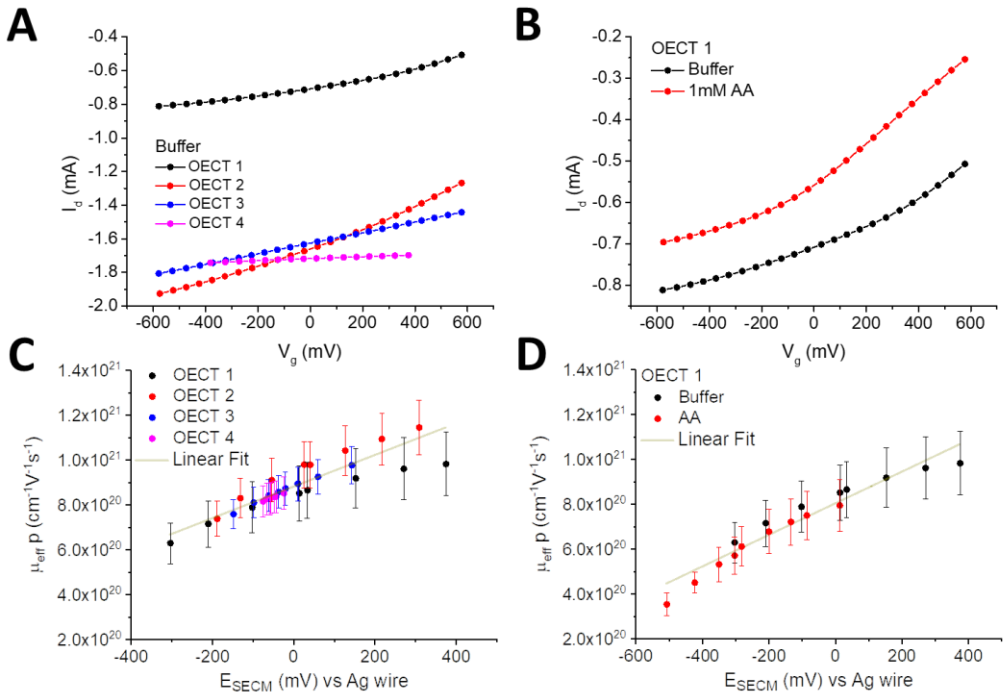

Figure 7. The relation $\mu_{eff}\, p$ vs E_{SECM}. Transfer characteristics of four devices having different geometries in buffer (**A**) and in the presence of 1 mM AA (**B**). V_d = -200 mV. Corresponding universal curve showing the linear relation between $\mu_{eff}\, p$ and E_{SECM} in buffer (**C**) and in the presence of 1 mM AA (**D**).

The linear fit and knowledge of the volumetric capacitance (C_V = (40 ± 3) F cm^{-3} obtained from IV characteristics) allow to determine the average carrier mobility (μ_{eff} = (2.8 ± 0.3) cm^2 V^{-1} s^{-1}) and the intrinsic carrier concentration (p_{00} = (3.1 ± 0.3) $\times 10^{20}$ cm^{-3}) from our microscopic measurements. The obtained values for μ_{eff} and p_{00} are compared in **Table 1** with values reported from macroscopic techniques.

μ_{eff} (cm^2 V^{-1} s^{-1})		p_{00} (cm^{-3})	
2.8 ± 0.3	This work	**(3.1 ± 0.3) × 10^{20}**	This work
9.7	[60]	3.0 × 10^{20}	[60]
4.0 ± 0.7	[61]	(1.50 ± 0.04) × 10^{21}	[61]
1.9 ± 1.3	[22]	10^{21}	[62]
1.7	[63]	6 × 10^{20}	[64]

Table 1. Reported values for μ_{eff} and p_{00}. Constant effective mobility and initial carrier density values calculated here and reported in other works using similar PEDOT:PSS formulations.

Overall, a good agreement is obtained in comparison with previous reports, whose variability could be related to either differences in the preparation of the PEDOT:PSS films or the effect of experimental conditions, such as ionic strength or temperature, on the measurement. By introducing the values of p_{00} and C_V in Equation (4), we obtain a quantitative expression that provides direct access to the local carrier density of an in-operando OECT by measuring the local electrochemical potential of PEDOT:

$$p = (3.1 \pm 0.3) \cdot 10^{20} + (2.5 \pm 0.2) \cdot 10^{20} \cdot E_{SECM} \qquad (8)$$

It is worth to emphasize that this expression has a general validity and is independent of the voltage applied to the drain or gate electrodes, as well as channel geometry or presence of electrochemically active compounds in the electrolyte. Implementation of the SECM method here reported to test smaller devices with higher spatial resolution can be achieved using sub-micrometre probes equipped with a suitable positioning system.

3.3. Improvement in the understanding of OECT operation

The direct experimental access to the local electrochemical potential in the OECT channel, as well as the absolute value of carrier concentration, provides additional options to investigate the OECT operation. In the following, a few examples are provided that underline the potential of SECM measurements applied to in-operando OECTs. An important issue regards the microscopic transport of carriers along the channel. With the understanding of E_{SECM}, we can establish an analytical model that describes the electrochemical potential along the channel as a function of drain voltage and gate potential.

V(x) is the local potential in the OECT channel with reference to the source electrode (grounded). In these experiments, $E_{SECM}(x)$ is measured with respect to Ag QRE. As a first approximation, the potential measured with SECM is:

$$E_{SECM}(x) = V(x) - V_d \frac{C_g}{(C_g + C_c)} - E_{offset} \quad (9)$$

where C_g and C_c are the gate and channel capacitance, respectively, and E_{offset} takes into account the use of an electrochemical reference. The integration with constant current density along the channel until distance *x* gives the following equation:

$$\frac{Ix}{wt} = \frac{\mu q p_0}{V_P}\left[\left(V_P - V_g\right)V(x) + \frac{1}{2}V(x)^2\right] \quad (10)$$

where V_P is the pinch-off voltage. Solving this equation for *V(x)* and considering that the current flowing through the OECT channel can be defined according to the Bernards model $I = G\left[1 - \frac{\left(V_g - \frac{1}{2}V_d\right)}{V_P}\right]V_d$,[23] where $G = \frac{\mu q p_0 wt}{L}$, the final expression for the local potential along the channel is:

$$V(x) = \sqrt{\left(V_P - V_g\right)^2 + \left[V_P - V_g + \frac{1}{2}V_d\right]V_d \frac{2x}{L}} - \left(V_P - V_g\right) \quad (11)$$

The Taylor approximation when $V_d \to 0$ (linear regime) gives Equation (12):

$$E_{SECM}(x) = \frac{V_d}{L}x + O(V_d^2) \quad (12)$$

where $O(V_d^2)$ represents all the terms higher than the second order that can be deemed insignificant.

The linear relation is used to fit the measured values in Figure 3 C and D. A discontinuity leading to a potential step ΔV_c at the contacts is observed and it is attributed to contact resistance. **Figure 8**A reports ΔV_c values calculated from the electrochemical potentials measured on source and drain contacts (E_s and E_d, respectively, whose values are showed in the inset) upon application of different gate voltages. The points scale linearly with the OECT channel current, highlighting an ohmic behaviour of the contact resistance, with R_c = (110 ± 20) Ω (average ± standard deviation of N = 3 devices with a channel width of 0.4 cm). A similar result has also been reported in[65] based on the transfer line method applied to OECTs. Because of the contact resistance, the local electric field in the OECT channel is reduced and can be calculated from the potential profile as $\xi(x) = {}^{dE_{SECM}}/_{dx}$.

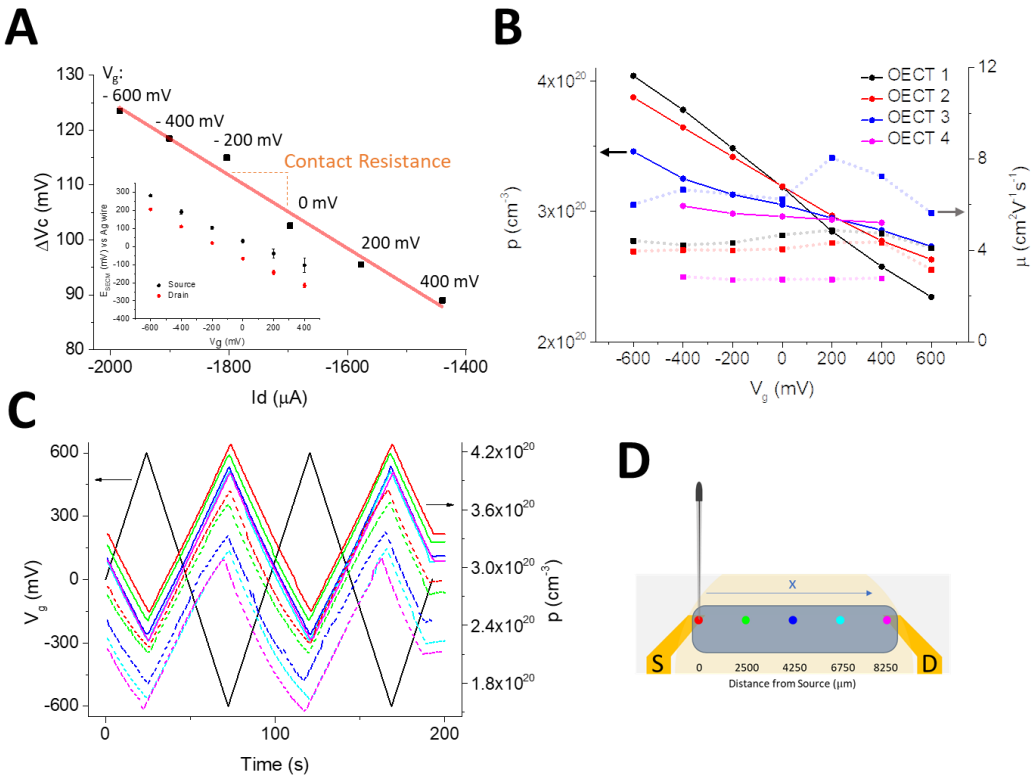

Figure 8. Insights about OECT operation processes. (**A**) Plot of contact potential drop (ΔV_c) as a function of drain current at different gate biases for OECT 2. R^2 = 0.981; V_d = -200 mV. ΔV_c values were calculated from E_{SECM} measured on Source and Drain contacts (inset). (**B**) Calculated charge carrier density (full colors, solid lines) and mobility (shaded colors, dotted lines) as functions of the applied gate voltage for OECTs 1 to 4. (**C**) Charge carrier density variation during dynamic change of V_g in buffer (solid lines) and in the presence of 1 mM AA (dotted lines) at five different positions along the OECT channel as depicted in the color map (**D**).

The combined knowledge of the local electric field, the local carrier concentration and the overall macroscopic current provides access to the local carrier mobility, according to $\mu(x) = {I_d}/{wtqp\xi(x)}$. Figure 8B shows the value of local carrier concentration and mobility obtained for different transistors as a function of the applied gate voltage. The mobilities exceed the effective channel mobility (μ_{eff}) that does not account for contact resistance effects by up to a factor of 3. It becomes also clear in the graph that the application of different V_g does not produce a consistent variation of μ, whose values remain almost constant for each device, despite current modulation. This evidence supports the assumption of a constant hole mobility in our interpretative model. The same figure contains the local carrier concentration in the middle of the OECT channel as a function

of V_g. Here, the four different devices distinguish from each other in the ratio of gate to channel areas ($\gamma = {A_g}/{A_{ch}}$). As expected from considerations of capacitive coupling, the highest γ value (OECT 1) causes the strongest variation of p.

Furthermore, the dynamic variation of p at the microscale is obtained during a transfer characteristic recording (Figure 8C). A triangular potential waveform was applied at the gate electrode (scan rate 25 mV s^{-1}) to dynamically switch on and off the transistor channel. At the same time, E_{SECM} data were collected at 5 different points along the channel (as indicated in the color map in Figure 8D). Reversible and stable variation of p over time at the microscale marks out the occurrence of doping/de-doping processes in the OECT channel upon gating. When AA is added to the electrolyte solution (dotted lines), the p curves shift downwards due to an increased extraction of holes taking place in the OECT channel. Small time-lag and hysteresis are ascribed to the slow response time of the millimetre-sized OECT.

4. *In-operando* measurement of the local impedance

SECM can be used in AC mode through the application of an alternating potential at the working electrode. This can be achieved by the internal oscillator of a lock-in amplifier (LIA) that sends a sinusoidal wavefunction to the potential input of the potentiostat. The generated current alternates at the same frequency and the current output of the potentiostat is fed back into the signal input of the LIA. The LIA output signal representing the alternating current signal consists of the current magnitude $|R|$, which is inversely proportional to the impedance $|Z|$, as well as the phase angle θ by which the sinusoidal current wave is shifted with respect to the perturbation voltage. In contrast to the "global" electrochemical impedance spectroscopy (EIS), the measurement is carried out with a SECM probe and, consequently, the delivered information is characteristic for a localized portion of the sample surface. Given the dependence of the AC-signal at the SECM tip on the tip-to-sample distance and depending on the experimental design, AC-SECM can be used to map the local electrochemical activity (e.g. formation of corrosion pits), image sample topography, probe the local surface conductivity (e.g. surface defects) and for SECM tip positioning.[66,67] Here, in analogy with the experiments carried out to record E_{SECM} but with a more qualitative approach, an AC-SECM setup was coupled with working

OECTs to measure the local impedance ($|Z_{SECM}|$) along the polymer channel. A scheme of the experimental setup is given in **Figure 9**A. For these experiments, the OECT was biased via a floating bipotentiostat in order to avoid alternative current paths through a common ground. The Pt microelectrode can be scanned in the x and y directions over the channel via the SECM positioning system and, in order to obtain the localized information (Figure 9B), the microelectrode tip must be kept in close proximity to the polymer surface and the tip area must be much smaller than the sample surface. A low ionic strength of the electrolyte solution was chosen (1mM PBS) in order to minimize the contribution of the solution resistance to the measured impedance.

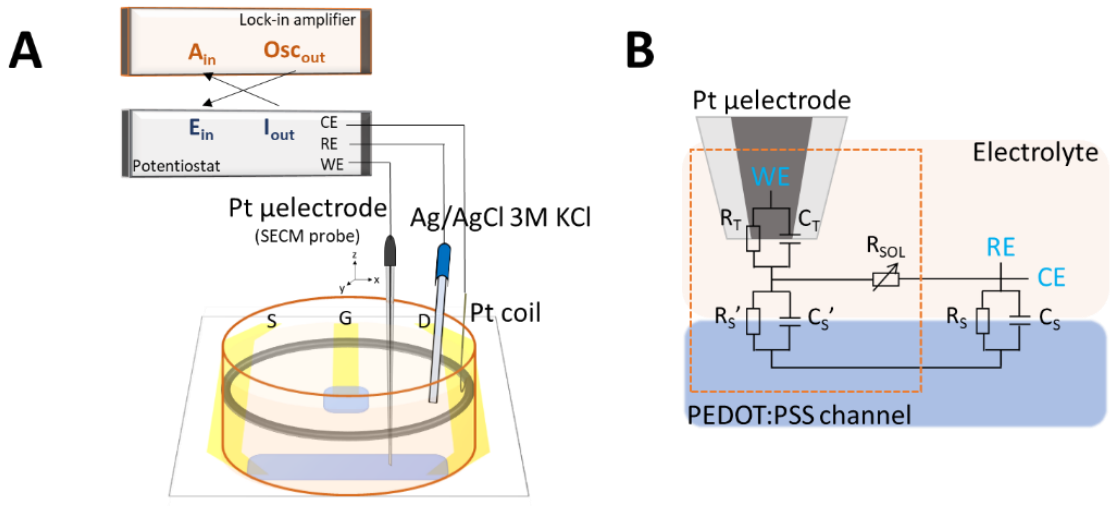

Figure 9. **AC-SECM experiments with OECTs.** (**A**) Experimental setup showing the three- electrode cell positioned on top of the OECT, which was biased via a floating bipotentiostat (not shown). The Pt microelectrode is scanned over the channel surface during application of an alternating potential and the generated current is used to extract impedance data. (**B**) Simplified equivalent circuit of the AC-SECM experiment scanning a large conductive sample. R_T and C_T are resistance and capacitance of the tip; R_{SOL} is the resistance of the electrolyte solution, R_S and C_S are the resistance and capacitance of the sample, with R_S' and C_S' being the same parameters at the specific area covered by the AC-SECM tip. The red dotted box is meant to highlight the localised acquisition.

4.1. Approach curves in AC-SECM mode

Once the polymer surface was detected by performing amperometric approach curves as described in the Experimental section, the Pt microelectrode was positioned at a distance of few micrometres above the OECT channel to record frequency spectra during transistor operation (not shown) to select the suitable frequency for the following AC-SECM

experiments. Indeed, depending on the experimental purpose, the oscillation frequency is a crucial parameter that should be chosen in order to ensure the best electrochemical resolution. Here, the selection criteria were the lowest noise level and the best discrimination between the on/off states of the OECT channel. The frequency of choice was therefore set at 5 kHz and all measurements were carried out applying 0 mV (i.e. open circuit potential of the SECM probe) with a perturbation amplitude of 50 mV.

In-operando approach curves were recorded from the bulk solution until the Pt tip was 7 µm above the channel surface (**Figure 10**).

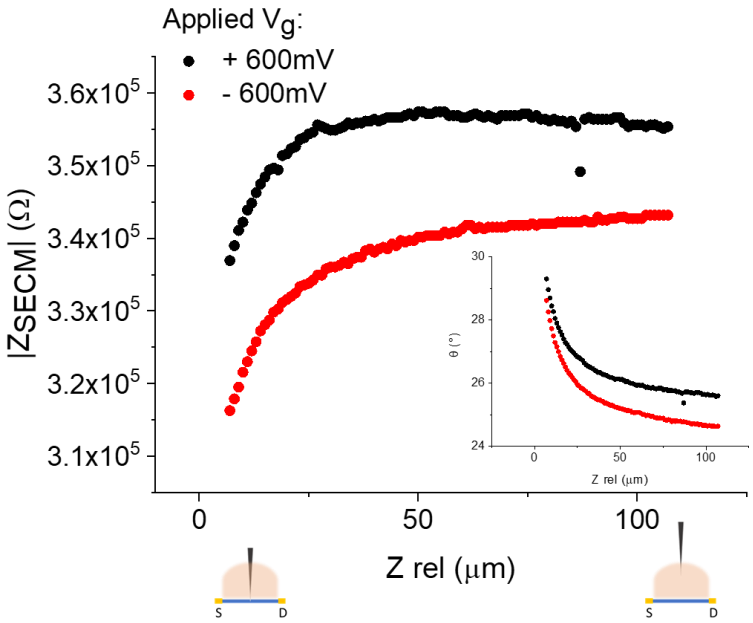

Figure 10. **In-operando AC approach curves in the middle of the channel.** Impedance and phase shift (inset) plotted as functions of the tip distance from the sample surface, at two different gate biases applied. Electrolyte was 1mM PBS, V_d = -200mV.

In analogy with the observations made for E_{SECM}, a different signal is recorded depending on the applied V_g, according to the doping state of the polymer in the OECT channel. While a positive gate voltage (V_g = +600 mV) leading to holes extraction causes a shift towards higher $|Z_{SECM}|$ values, a shift towards lower $|Z_{SECM}|$ values is observed during holes injection (V_g = -600 mV) as the channel shows higher conductivity. However, despite the applied V_g, a negative $|Z_{SECM}|$ feedback is dominating at the frequency of choice, meaning a positive feedback in terms of the recorded $|R|$. This, together with the fact that at lower frequency (1 kHz) the opposite trend is observed, is in accordance with the conducting character of the polymer substrate.[66] Moreover, the effect of the gate leakage current across

the electrolyte is more pronounced than in the E_{SECM} recordings, as here it possibly alters the current lines generated between the tip and the substrate thus affecting the recorded signal even if the tip is far away in the bulk solution.

4.2. AC imaging of the OECT channel

A major advantage of the AC-SECM method, with respect to the contact mode that is needed for E_{SECM} recordings, is the possibility to perform line scans during the acquisition that can be used to obtain 3D maps of the whole surface scanned by the SECM tip. For these measurements, tilt correction of the sample surface was made in order to hold the Pt tip at a constant distance of 5 µm above the plane offset. Concurrently, the tip was moved in x and y directions, from Drain to Source electrodes and over the whole channel width (as depicted in **Figure 11**A) to record $|Z_{SECM}|$ during transistor operation. The OECT geometry was the "OECT 2" type (see Table 2 in Materials and Methods section) in all experiments, but channels with different resistance were tested in buffer electrolyte (1 mM PBS) and in the presence of the reducing agent AA (1 mM).

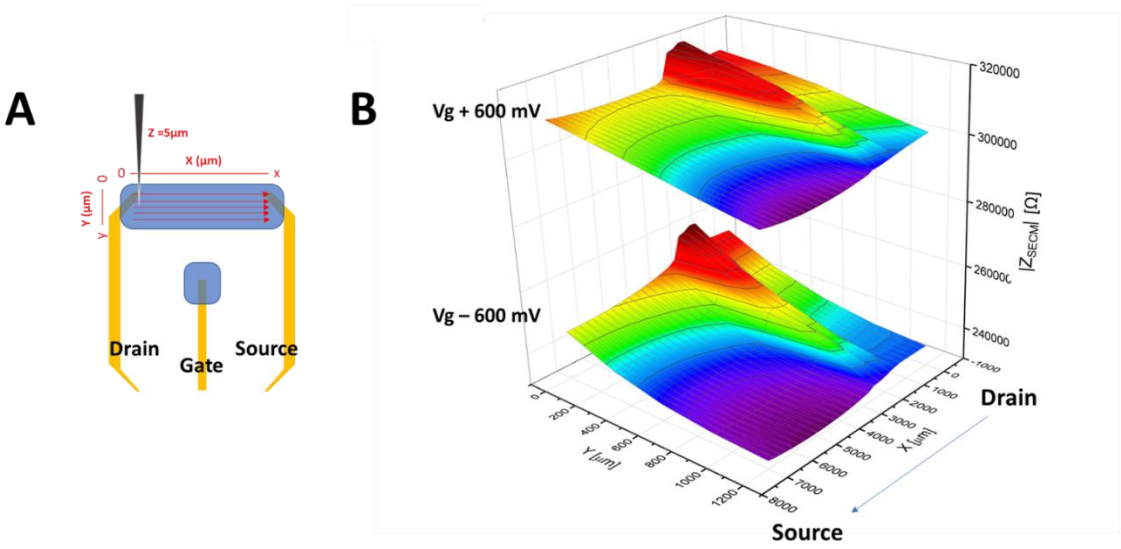

Figure 11. **3D maps of the local impedance**. (**A**) Sketch of the line scans experiments above the OECT channel. (**B**) 3D plots of $|Z_{SECM}|$ recorded from drain to source during transistor operation. V_d = -300 mV, $R_{channel}$ = 300 Ω.

Figure 11B shows the 3D plot of $|Z_{SECM}|$ recorded during line scans above an OECT channel upon application of positive and negative V_g values. What clearly stands out by comparing the 3D maps recorded at different V_g is that the overall $|Z_{SECM}|$ is higher upon

application of a positive gate bias, according to the lower channel conductivity due to charge carrier depletion. Interestingly, a well localized increase in $|Z_{SECM}|$ can be visualised between 1000 and 2000 μm on the x axis that is due to the presence of a scratch in the polymer film. Indeed, AC-SECM recordings are highly sensitive to substrate's inhomogeneities and this feature makes them particularly suited for surface topography studies.

Similar to what observed from the electrochemical potential profiles, $|Z_{SECM}|$ decreases in the scan direction and the less conducting portion of the channel is localized near the terminal that is negatively biased, i.e. the Drain (**Figure 12**).

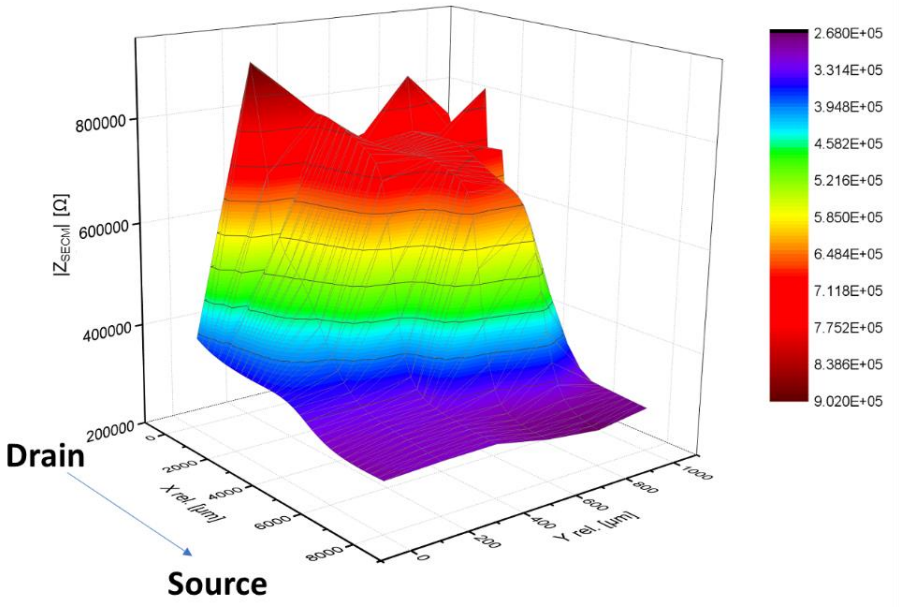

Figure 12. **$|Z_{SECM}|$ trend.** 3D plot of $|Z_{SECM}|$ recorded from drain to source during transistor operation. V_g = -600 mV, V_d = -300 mV, $R_{channel}$ = 150 Ω.

In order to investigate the effect of the reducing agent, one AA addition was made during line scans experiments. An example is reported in **Figure 13**. While buffer addition (control experiment) has the sole effect to locally perturb the current lines, a sharp increase of $|Z_{SECM}|$ is recorded right after AA addition that affects the measurement until the end of the scans. In this case, AA oxidation is favoured at the OECT channel due to the negative V_g applied. Therefore, the faradaic reaction directly dedopes the polymer channel, leading to a prominent decrease in conductivity.

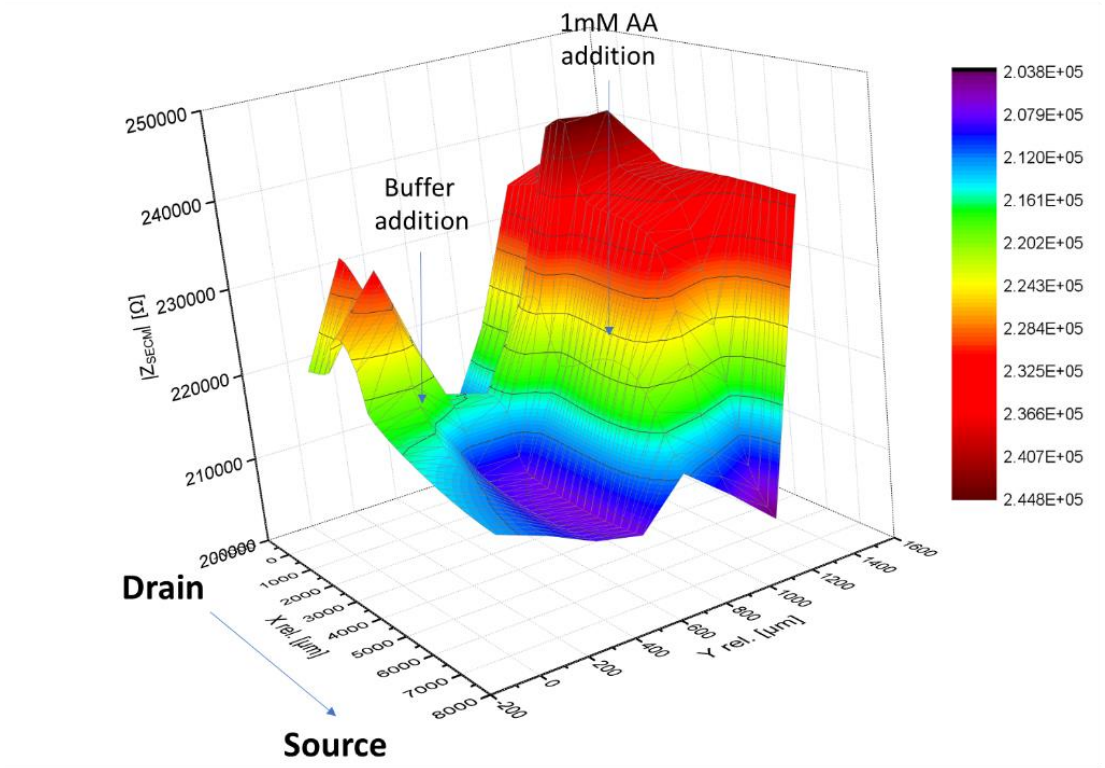

Figure 13. **Ascorbic acid effect.** 3D plot of $|Z_{SECM}|$ recorded from drain to source during transistor operation. Buffer and AA additions were made during the experiments and are indicated by the arrows. V_g = -600 mV, V_d = -300 mV, $R_{channel}$ = 300 Ω.

5. Materials and Methods

Chemicals and buffers. All reagents were of analytical grade and used without further purification. All chemicals were purchased from Sigma-Aldrich if not otherwise indicated. 0.1 M phosphate buffer solution (PBS) was made with 0.1 M KH_2PO_4 and corrected to the desired pH (7.0) with 1 M KOH. CLEVIOS PH 1000 suspension (PEDOT:PSS) was purchased from Heraeus. Ethylene glycol was obtained from Carlo Erba.

OECTs fabrication. Gate, drain, and source contacts made of Cr/Au (50 nm thickness) were deposited via thermal evaporation. PEDOT:PSS solution was prepared by adding 5% ethylene glycol, 0.25% dodecylbenzenesulfonic acid, and 1% 3-glycidyloxypropyltrimethoxysilane to the CLEVIOS PH 1000 suspension. The mixture was filtered through a 1.2 µm cellulose acetate filter and spin coated on the gate and between source and drain electrodes at 500 rpm for 3 s, and then annealed at 140 °C for 30 min. Geometric and electrical features of the tested devices are reported in **Table 2**.

	Gate Area (mm)	Channel Width (mm)	Channel Length (mm)	Channel Thickness (nm)	Channel Resistance (Ω)	γ ($Area_{Gate}/Area_{Channel}$)
OECT 1	56	3	14	700	340	1.3
OECT 2	42	4	15	950	116	0.7
OECT 3	20	4	16	1200	108	0.3
OECT 4	6	4	16	1200	113	0.1

Table 2. Device parameters for the different OECTs investigated. Gate and channel size, channel resistance and γ factor of the devices under test.

SECM probe fabrication. A Pt microelectrode was fabricated placing a 25 µm diameter Pt wire (Goodfellow) inside a borosilicate glass capillary (Hilgenberg) previously pulled using a heating coil. The Pt wire was sealed with the surrounding glass body by heating under vacuum and was further contacted with a copper wire using soldering tin. The tip of the microelectrode was polished using abrasive paper of decreasing particle size (3 µm and 1 µm, from 3M). Finally, and in order to achieve a desired relatively small RG value between 3 and 4 (RG = $r_{Glass}/r_{Electrode}$), the glass body was polished in a conical shape using abrasive paper (1 µm particle size). The SECM probe was characterized by cyclic voltammetry in an electrolyte containing 5 mM $[Ru(NH_3)_6]Cl_3$ and 100 mM KCl (see **Figure 14**).

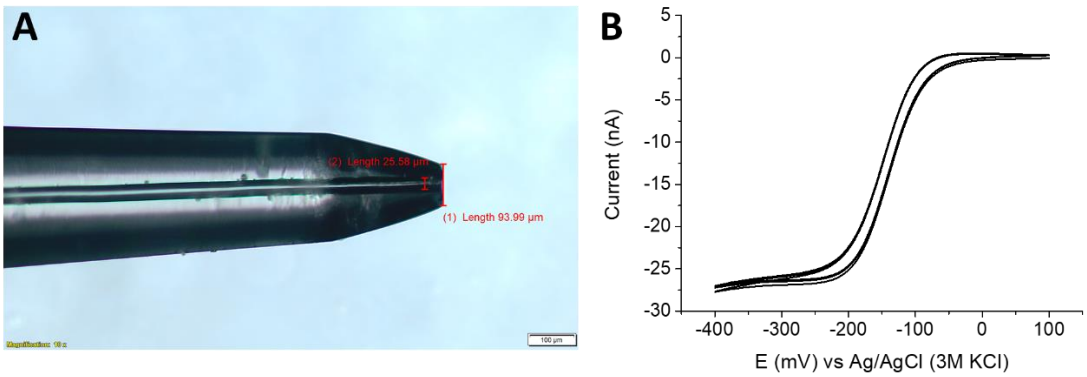

Figure 14. SECM Pt microelectrode. (**A**) Picture of the microelectrode tip. (**B**) Cyclic voltammogram of the microelectrode recorded in 5 mM $[Ru(NH_3)_6]Cl_3$ and 100 mM KCl. Scan rate 25 mV s^{-1}.

Microscopic measurement of E_{SECM}. A full scheme of the implemented setup is reported in **Figure 15**. The OECT was placed in a Teflon SECM cell sealed with an O-ring exposing an area of about 1.5 cm^2 and filled with 3 mL of 0.1 M PBS. The polymer was allowed to swell for 15 min before starting the experiment. The SECM setup consisted of three step-motor driven micrometer screws (Owis) and a piezoelectric stage (Nanocube, Physik Instrumente) for positioning of the SECM tip in x-, y- and z- directions, a bipotentiostat (PGU-BI 100, Jaissle) and a control software programmed using Visual Basic 6.0. The SECM tip used as probe (working electrode) was positioned in close proximity to the analysed sample by recording z-approach curves in air-equilibrated solutions. For this, the tip was polarized at −600 mV vs Ag/AgCl/3 M KCl (reference electrode) for the steady-state measurement of the oxygen reduction reaction (ORR). The counter electrode was a Pt mesh. The tip was then approached to the polymer surface while recording the tip current. In order to avoid any possible interference from the sample on the current recorded at the tip during the z-approach, the sample was kept unbiased, thus behaving as an electrochemically inactive surface leading to negative feedback approach curves. The tip was then left in contact with the polymer surface. After that, the OECT was connected to the bipotentiostat applying the desired source-drain (V_d) and source-gate (V_g) potentials and measuring the respective currents (I_d, I_g). The source collector was connected to the reference and counter electrode terminals of the bipotentiostat. Gate and drain were connected to the working electrode and the secondary electrode, respectively. The Pt microelectrode was connected through a high impedance module (IPS Elektroniklabor) to a wireless multimeter (CEM Instruments) and its electrochemical potential was measured with respect to a Ag wire quasi-reference electrode ($E_{Ag\ wire}$ = (250 ± 10) mV vs Ag/AgCl/3 M KCl in PBS 0.1M and (40 ± 10) mV vs Ag/AgCl/3 M KCl in 1 mM ascorbic acid). After each experiment, the Pt microelectrode was retracted, polished and the positioning procedure was repeated before probing a different location of the polymer surface.

All the measured values reported in this work are given as average ± standard deviation of $N \geq 3$ devices.

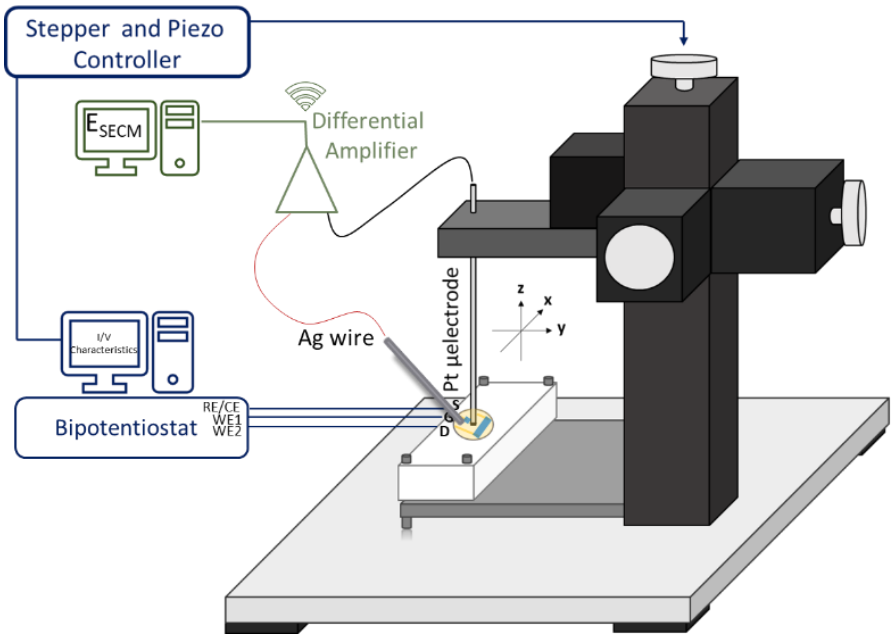

Figure 15. Scheme of the experimental setup used during in-operando recording of E_{SECM}

AC-SECM measurements. The already described SECM setup was equipped with a lock-in amplifier (LIA) as depicted in figure 8A in order to generate the alternating potential applied to the working electrode. The resulting current collected at the potentiostat was fed back into the signal input of the LIA. The LIA output signal representing the alternating current signal consists of the current magnitude $|R|$, from which $|Z_{SECM}|$ was extracted, and the phase angle θ. The OECT was biased via a floating bipotentiostat. A three-electrode setup was used for all in-operando recordings of $|Z_{SECM}|$, comprising a Pt microelectrode (WE, SECM probe), a Ag/AgCl 3M KCl electrode (RE) and a Pt coil (CE). The aforementioned Teflon SECM cell was used also for AC-SECM measurements and was filled with 3 mL of 1 mM PBS. The polymer channel was allowed to swell for 15 min before starting the experiment and tip positioning was achieved through amperometric approach curves, as described in the previous paragraph. For all measurements, the voltage applied to the WE was 0 V, with a perturbation amplitude of 50 mV and a frequency of 5 kHz.

6. Conclusion

OECTs are emerging devices that are attracting growing attention for a variety of bioelectronic applications. Understanding electrochemical and physical phenomena

underlying their operation is crucial for improved handling and design of these devices. To this regard, the concept of electrochemical doping well synthesizes the complexity arising at the interface between electrochemistry and semiconductor physics. Discrepancies in terminology, as well as the lack of suitable tools for direct *in-operando* experimental investigation of microscale effects to support theoretical models have profoundly hindered the achievement of a comprehensive knowledge of OECT's working principle.

In literature, morphological and spectroscopic studies have been carried out in order to shed light on OECTs operation mechanisms, however no attempt has been performed using an electrochemical probe. In this work, SECM was used to characterize OECTs *in-operando*, opening the way to multifaceted opportunities to explore unknown sensing mechanisms, visualize actual potential profiles across solid-liquid interfaces during operation, assess local barriers, directly and quantitatively have access to fundamental device parameters by locally probing a thermodynamic value, that is the electrochemical potential.

An interpretative model has been developed in order to introduce the measured electrochemical potential in the equations that describe the transistor operation, with the aim to bridge the device physics and electrochemistry. The local measurement of the electrochemical potential in the organic film composing the OECT channel is a straightforward approach that gives access to fundamental device parameters. A linear relationship is found between the experimental electrochemical potential and the concentration of charge carriers, allowing to directly calculate the local hole concentration during OECT operation. Due to the local acquisition at the microscale, mobility of holes, contact resistance and effective electric field in the transistor channel can be extracted, and hole density can be monitored over time during current modulation, allowing a direct assessment of the device electronics and metrics optimization to the desired performance. Also, the possibility to investigate the whole surface of a planar device during transistor operation is explored. OECTs have two important interfaces (i.e., gate/electrolyte and channel/electrolyte) and potential changes at any of them lead to the observed modulation of the current flowing through the channel. Optimization of both elements is crucial for the improvement of OECTs performance, for instance, in biomolecules detection.[68] Here potentiometric approach curves were used as a tool to record actual potential gradients occurring both in the OECT channel and gate electrode, as well as in the electrolyte. The technique can be applied for the study of already existing materials as well as the

development of novel materials for OECTs sensing, where mechanisms originating the detection are still unclear or unknown. A major limitation of this SECM method is that it cannot work on a depleted channel. In that case, the impedance between SECM tip and semiconducting material is so high that a meaningful potential cannot be measured. Another crucial point regards the size of the micrometric scanning probe collecting the electrochemical signal that consequently impacts on the size of the device under investigation and affects the resolution of the measurement. Nonetheless, the millimetre range here explored as a proof of principle can be decreased using nanometric probes that allow the local characterization of micrometric device components with high spatial resolution. Indeed, this approach is non-destructive and versatile, compatible with the implementation of other scanning probe microscopies, and tip/substrates materials. It should be noted that the possibility to perform *in-operando* measurements of electrochemical potential gradients across solid/liquid interfaces renders the SECM method unique among other scanning probe techniques, such as scanning Kelvin probe microscopy (SKPM), where charge screening in the electrolyte hinders its application despite the fine resolution achieved in voltage measurements.

Finally, the well-assessed AC mode of SECM was used to measure local changes in the impedance of the OECT channel during transistor operation. In contrast to the global sample impedance, the information delivered by this approach is spatially resolved and was here qualitatively exploited to investigate the conductivity of the channel surface upon gating. Indeed, the electrochemical contrast needed to discriminate local impedance variations during on/off switch of the channel can be achieved by selecting a suited frequency. Also, AC-SECM is a powerful imaging technique that was here interfaced with a working device to acquire 3D maps of the whole polymer surface. Thanks to the fact that the acquisition is made a few micrometres above the sample surface, it is possible to perform line scans experiments in the x and y directions. This way, defects formation and film delamination can be imaged directly in the liquid environment in which the device operates. Furthermore, the effect of a reducing analyte on the channel conductivity was investigated. The detected, sharp increase in the local impedance right after ascorbic acid addition gives a microscopically localized evidence of charge carrier depletion.

7. References

1. H. S. White, G. P. Kittlesen, M. S. Wrighton. *J. Am. Chem. Soc*. **1984**, *106*, 5375-5377.
2. C. Liao, M. Zhang, L. Niu, Z. Zheng, F. Yan. *J. Mater. Chem. B* **2013**, *1*, 3820-3829.
3. Gualandi, M. Marzocchi, E. Scavetta, M. Calienni, A. Bonfiglio, B. Fraboni. *J. Mater. Chem. B*. **2015**, 3, 6753-6762.
4. Gualandi, D. Tonelli, F. Mariani, E. Scavetta, M. Marzocchi, B. Fraboni. *Sci. Rep*. **2016**, *6*, 35419.
5. N. Saraf, E. R. Woods, M. Peppler, S. Seal. *Biosens. Bioelectron*. **2018**, *117*, 40-46.
6. A. Campana, T. Cramer, D. T. Simon, M. Berggren, F. Biscarini. *Adv. Mater.* **2014**, *26*, 3874-3878.
7. A. Williamson, M. Ferro, P. Leleux, E. Ismailova, A. Kaszas, T. Doublet, P. Quilichini, J. Rivnay, B. Rózsa, G. Katona, C. Bernard, G. G. Malliaras. *Adv. Mater.* **2015**, *27*, 4405-4410.
8. W. Lee, S. Kobayashi, M. Nagase, Y. Jimbo, I. Saito, Y. Inoue, T. Yambe, M. Sekino, G. G. Malliaras, T. Yokota. *Sci. Adv.* **2018**, *4*, eaau2426.
9. V. F. Curto, B. Marchiori, A. Hama, A. Pappa, M. P. Ferro, M. Braendlein, J. Rivnay, M. Fiocchi, G. G. Malliaras, M. Ramuz, R. M. Owens. *Microsystems Nanoeng*. **2017**, *3*, 17028.
10. V. F. Curto, M. P. Ferro, F. Mariani, E. Scavetta, R. M. Owens. *Lab Chip* **2018**, *18*, 933-943.
11. D. Khodagholy, T. Doublet, P. Quilichini, M. Gurfinkel, P. Leleux, A. Ghestem, E. Ismailova, T. Herve, S. Sanaur, C. Bernard, G. G. Malliaras. *Nat. Commun*. **2013**, *4*, 1575.
12. A. Giovannitti, C. B. Nielsen, D. T. Sbircea, S. Inal, M. Donahue, M. R. Niazi, D. A. Hanifi, A. Amassian, G. G. Malliaras, J. Rivnay, I. McCulloch. *Nat. Commun*. **2016**, *7*, 13066.
13. C. Pitsalidis, M. P. Ferro, D. Iandolo, L. Tzounis, S. Inal, R. M. Owens. *Sci. Adv*. **2018**, *4*, eaat4253.

14. N. Coppedè, G. Tarabella, M. Villani, D. Calestani, S. Iannotta, A. Zappettini. *J. Mater. Chem. B* **2014**, *2*, 5620-5626.

15. E. Battista, V. Lettera, M. Villani, D. Calestani, F. Gentile, P. Antonio, S. Iannotta, A. Zappettini. *Org. Electron*. **2017**, *40*, 51-57.

16. O. Parlak, S. T. Keene, A. Marais, V. F. Curto, A. Salleo. *Sci. Adv*. **2018**, *4*, eaar2904.

17. I. Gualandi, M. Tessarolo, F. Mariani, T. Cramer, D. Tonelli, E. Scavetta, B. Fraboni. *Sens. Actuators B* **2018**, *273*, 834-841.

18. F. Mariani, I. Gualandi, M. Tessarolo, B. Fraboni, E. Scavetta. *ACS Appl. Mater. Interfaces* **2018**, *10*, 22474-22484.

19. A. M. Nardes, M. Kemerink, R. A. J. Janssen, J. A. M. Bastiaansen, N. M. M. Kiggen, B. M. W. Langeveld, A. J. J. M. Van Breemen, M. M. De Kok. *Adv. Mater*. **2007**, *19*, 1196-1200.

20. J. Heinze, B. A. Frontana-Uribe, S. Ludwigs. *Chem. Rev*. **2010**, *110*, 4724-4771.

21. N. D. Robinson, P. Svensson, D. Nilsson, M. Berggren. *J. Electrochem. Soc*. **2006**, *153*, H39-H44.

22. J. Rivnay, P. Leleux, M. Ferro, M. Sessolo, A. Williamson, D. A. Koutsouras, D. Khodagholy, M. Ramuz, X. Strakosas, R. M. Owens, C. Benar, J. Badier, C. Bernard, G. G. Malliaras. *Sci. Adv*. **2015**, *1*, e1400251.

23. D. A. Bernards, G. G. Malliaras. *Adv. Funct. Mater*. **2007**, *17*, 3538- 3544.

24. J. T. Friedlein, S. E. Shaheen, G. G. Malliaras, R. R. Mcleod, Adv. Electron. Mater. **2015**, *1*, 1500189.

25. J. T. Friedlein, R. R. Mcleod, J. Rivnay. *Org. Electron*. **2018**, *63*, 398-414.

26. J. T. Friedlein, M. J. Donahue, S. E. Shaheen, G. G. Malliaras, R. R. Mcleod. *Adv. Mater.* **2016**, *28*, 8398-8404.

27. C. Faria, D. T. Duong, A. Salleo. *Org. Electron*. **2017**, *45*, 215-221.

28. M. Z. Szymanski, D. Tu, R. Forchheimer. *IEEE Trans. Electron Devices.* **2017**, *64*, 5114-5120.

29. J. Rivnay, S. Inal, B. A. Collins, M. Sessolo, E. Stavrinidou, X. Strakosas, C. Tassone, D. M. Delongchamp, G. G. Malliaras. *Nat. Commun*. **2016**, *7*, 11287.

30. B. Lukas, T. Richards, M. Chiesa, R. H. Friend, H. Sirringhaus. *Synth. Met*. **2004**, *146*, 297-309.

31. R. Giridharagopal, L. Q. Flagg, J. S. Harrison, M. E. Ziffer, J. Onorato, C. K. Luscombe, D. S. Ginger. *Nat. Mater*. **2017**, *16*, 737-742.

32. A. J. Bard, F. F. Fan, D. T. Pierce, P. R. Unwin, D. Wipf, F. Zhou. *Science* **1991**, *254*, 68-74.

33. D. Polcari, P. Dauphin-Ducharme, J. Mauzeroll. *Chem. Rev*. **2016**, *116*, 13234-13278.

34. J. Kwak, F. C. Anson. *Anal. Chem*. **1992**, *64*, 250-256.

35. C. Lee, F. C. Anson. *Anal. Chem*. **1992**, *64*, 528-533.

36. M. Arca, M. V Mirkin, A. J. Bard. *J. Phys. Chem*. **1995**, *99*, 5040-5050.

37. I. Kapui, E. Gyurcsa. *J. Phys. Chem. B* **1998**, *102*, 9934-9939.

38. V. Syritski, R. E. Gyurcsànyi, A. Opik, K. Tòth. *Synth. Met*. **2005**, *152*, 133-136.

39. N. Yang, C. G. Zoski. *Langmuir* **2006**, *22*, 10338-10347.

40. G. Denuault, M. H. T. Frank, L. M. Peter. *Faraday Discuss*. **1992**, *94*, 23-35.

41. M. H. T. Troise, G. Denuault. *J. Electroanal. Chem*. **1993**, *354*, 331-339.

42. F.-R. F. Fan, M. V Mirkin, A. J. Bard. *J. Phys. Chem*. **1994**, *98*, 1475-1481.

43. C. Borgwarth, C. Ricken, D. G. Ebling, J. Heinze. *Fresenius J. Anal. Chem.* **1996**, *356*, 288-294.

44. M. Quinto, S. A. Jenekhe, A. J. Bard. *Chem. Mater*. **2001**, *13*, 2824-2832.

45. J. Ghilane, P. Martin, M. Janin, H. Randriamahazaka, P. Hapiot, J. Lacroix. *Electrochem. Commun*. **2009**, *11*, 2304-2307.

46. J. Molina, J. Fernández, A. I. Río, R. Lapuente, J. Bonastre, F. Cases. *Polym. Degrad. Stab.* **2010**, *95*, 2574-2583.

47. J. Molina, M. F. Esteves, J. Fernández, J. Bonastre, F. Cases. *Eur. Polym. J.* **2011**, *47*, 2003-2015.

48. D. Mandler, P. R. Unwin. *J. Phys. Chem. B* **2003**, *107*, 407-410.

49. A. P. O' Mullane, J. V Macpherson, P. R. Unwin, J. Cervera-Montesinos, J. A. Manzanares, F. Frehill, J. G. Vos. *J. Phys. Chem. B* **2004**, *108*, 7219-7227.

50. M. Tsionsky, A. J. Bard, D. Dini, F. Decker. *Chem. Mater*. **1998**, *10*, 2120-2126.

51. A. Sumboja, U. M. Tefashe, G. Wittstock, P. S. Lee. *Adv. Mater. Interfaces* **2015**, *2*, 1400154.

52. Y. Ai, V. Q. Nguyen, J. Ghilane, P.-C. Lacaze, J.-C. Lacroix, Y. Ai, V. Q. Nguyen, J. Ghilane, P.-C. Lacaze, J.-C. Lacroix. *ACS Appl. Mater. Interfaces* **2017**, *9*, 27817-27824.

53. F. Mariani, F. Conzuelo, T. Cramer, I. Gualandi, L. Possanzini, M. Tessarolo, B. Fraboni, W. Schuhmann, E. Scavetta. *Small* **2019**, 10.1002/smll.201902534.

54. I. Gualandi, E. Scavetta, F. Mariani, D. Tonelli, M. Tessarolo, B. Fraboni. *El. Acta* **2018**, *268*, 476-483.

55. D. A. Bernards, D. J. Macaya, M. Nikolou, J. A. Defranco, S. Takamatsu, G. G. Malliaras. *J. Mater. Chem*. **2008**, *18*, 116-120.

56. F. Cicoira, M. Sessolo, O. Yaghmazadeh, J. A. Defranco, S. Y. Yang, G. G. Malliaras. *Adv. Mater*. **2010**, *22*, 1012-1016.

57. S. Trasatti. *Pure Appl. Chem*. **1986**, *58*, 955-966.

58. A. J. Nozik, R. Memming. *J. Phys. Chem*. **1996**, *100*, 13061-13078.

59. K. Tybrandt, I. V. Zozoulenko, M. Berggren. *Sci. Adv*. **2017**, *3*, eaao3659.

60. M. Yamashita, C. Otani, H. Okuzaki, M. Shimizu. In *XXXth URSI GASS*, Istanbul, **2011**.

61. N. Kim, B. H. Lee, D. Choi, G. Kim, H. Kim, J. R. Kim, J. Lee, Y. H. Kahng, K. Lee. *Phys. Rev. Lett*. **2012**, *109*, 106405.

62. D. A. Mengistie, C. H. Chen, K. M. Boopathi, F. W. Pranoto, L. J. Li, C. W. Chu. *ACS Appl. Mater. Interfaces* **2015**, *7*, 94-100.

63. Q. Wei, M. Mukaida, Y. Naitoh, T. Ishida. *Adv. Mater*. **2013**, *25*, 2831-2836.

64. Q. Wei, M. Mukaida, T. Ishida. *J. Phys. Chem. C* **2018**, *122*, 15922-15928.

65. V. Kaphle, S. Liu, A. Al-Shadeedi, C.-M. Keum, B. Lüssem. *Adv. Mater*. **2016**, *28*, 8766-8770.

66. K. Eckhard, T. Erichsen, M. Stratmann, W. Schuhmann. *Chem. Eur. J*. **2008**, *14*, 3968–3976.

67. K. Eckhard, W. Schuhmann. *Analyst*, **2008**, *133*, 1486-1497.

68. J. Liao, H. Si, X. Zhang, S. Lin. *Sensors* **2019**, *19*, 218.

III. Dopamine sensing with all-PEDOT:PSS OECTs

The detection of Dopamine (DA) is the unifying theme of the works presented in this Chapter. Due to the paramount role that plays in our nervous system, DA is one of the most studied analytes in electroanalysis and biomedicine. However, DA detection implies several analytical challenges, including a physiological concentration that typically lies in the low nanomolar range in the presence of similarly redox-active molecules, whose concentrations can be up to 1000-fold higher. Therefore, important issues in terms of sensitivity and selectivity should be addressed in the development of novel sensing technologies. As already discussed in the Introduction, OECTs have entered successfully the field of sensors and biosensors thanks to the inherent signal amplification and the simple device geometry. In particular, all-polymeric OECT sensors can be realized with simple and low-cost fabrication procedures and show enhanced versatility for unconventional applications. In view of achieving a superior sensing response needed for DA detection, two strategies were developed that are described in the following. On one hand, a novel analytical approach was developed to provide a simple, all-PEDOT:PSS OECT sensor with selectivity towards DA, showing performances that are comparable to those obtained with sophisticated electroanalytical techniques. On the other hand, an improved detection limit suited for physiological determinations was achieved through the realization of a PEDOT:PSS-based OECT nanosensor.

1. Background

Electrochemical methods have been applied for the detection of many analytes in a great variety of matrices, the most widespread being the common blood glucose detection systems used by diabetic patients. Electrochemical sensors have attracted much attention thanks to major advantages such as short analysis times, when compared to spectroscopic techniques, and simple experimental procedures which can be applied to a variety of physiological samples.[1,2] They mostly operate in amperometric mode and thus require the use of a reference electrode.

The selective detection of Dopamine (DA), one of the most important neurotransmitters in biological organisms,[3] is currently a subject of significant interest. The rapid, accurate and even spatially resolved determination of DA, for instance in close proximity to dopaminergic axons, is crucial in the diagnosis of neurological disorders, such as Parkinson's disease, autism, schizophrenia.[4] The main problem related to the electrochemical detection of Dopamine is that its oxidation potential is close to that of other endogenous substances such as uric acid (UA) and ascorbic acid (AA), which leads to poor selectivity and sensitivity in DA detection.[5] To overcome these problems, different kinds of electrochemical sensors using amperometric transduction have been proposed in the literature.[6-8] The use of a conductive polymer as electrode coating allowed to selectively detect AA, UA and DA, and interesting results in terms of sensitivity and peak resolution have been obtained using a sensitive technique such as differential pulse voltammetry (DPV).[9] Nevertheless, Dopamine concentration can be very low in biological samples (for blood < 1 nmol L^{-1}) and such sensors do not exhibit an adequate sensitivity for real-life applications. A very interesting device that has recently attracted large attention for its high sensitivity in bio analytes detection is the organic electrochemical transistor (OECT). OECTs can work as chemical sensors, as long as the analytes affect the electrochemical processes that control the doping of conductive polymers and thus change the current that flows in the channel. The transistor configuration guarantees signal amplification since small potential changes due to the analyte presence are followed by a large variation of the channel current, thus assuring high sensitivity and a very low limit of detection (LOD) of the analytical determination.

H. Tang et al. first studied DA detection by means of an OECT-based sensor, investigating the effect of different gate electrodes (Pt, Au, graphite) and comparing their responses to

DA in terms of sensitivity and limit of detection. The OECT operation depends on both gate electrode and applied voltage and the device with a Pt gate electrode shows the highest sensitivity and a detection limit lower than 5 nM.[10] However, this first OECT sensor does not address the problem of the interfering species in DA detection. C. Liao et al. exploited a Pt gate electrode coated by Nafion or chitosan to overcome the issue of AA and UA interference; moreover, the sensor response was also enhanced with graphene flakes.[11] The devices with a metal gate modified with Nafion–graphene showed a detection limit down to 5 nM and an excellent selectivity in DA determination.

The metal gate electrode of an OECT can be replaced by PEDOT:PSS, significantly further reducing the fabrication cost and enabling the whole device preparation with a single-run, low cost deposition technique. As discussed in Chapters I and II, it has been demonstrated that an all PEDOT:PSS OECT can be used as a sensor for AA, exploiting the capability of PEDOT:PSS itself to directly electrocatalyze AA oxidation, thus obtaining an enzyme-free, all-PEDOT:PSS chemical sensor.[12] The device operation mode is based on the extraction of charge carriers from the transistor channel, following AA oxidation at the gate electrode, which leads to a decrease of the drain current. The variation in hole concentration can be monitored by the measurement of the electrochemical potential with respect to a reference electrode, indicating that the OECT is ruled by the same electrochemical processes that rule the operation of chemically modified electrodes. It is evident that a drawback of such a device is its poor selectivity: any analyte able to undergo oxidation at the PEDOT:PSS gate electrode can contribute to the experimental response and thus the sensor selectivity is a key issue to address. In the first section of this Chapter, the first example of selective DA detection using an all-PEDOT:PSS OECT is described. The use of transconductance measurements to discriminate among different analytes represents a novel potentiodynamic approach by which the device is capable to handle interference with AA and UA without the need of introducing any additional modifying agent, membrane or metal electrodes. Through the identification of the suited operating gate bias and scan rate, the all-PEDOT:PSS OECT satisfies both the requirements of selectivity and of detection of low amounts of bioanalytes, thus opening new ways in the development of flexible, all-plastic devices for real-life applications. The results presented here are part of a published work.[13]

On the other hand, the perspective of downscaling the device architecture in the nanorange is considered an essential technological evolution in the field of integrated circuits and

holds great potential for recording biological signals. Examples of submicrometric organic channels have been reported in the literature by which the transistor density within a bioelectronic interface can be very high, thus increasing the number of recording sites. Donahue et al. well contextualise this topic in the state of the art and report the fabrication and characterization of OECTs with vertically stacked contacts, alternative to the conventionally planar structure, with minimum channel length of 450 nm.[14] More recently, a channel length of 50 nm has been reached in an ion-gel-gated OECT based on different electrochemically doped polymers.[15] A captivating example that well describes the importance of transistor density in neural interfaces has been given by Nagarajan and Stevens, where they identify the synapse as the "smallest computer element that transmits and transforms information" in our brain, whose density in the grey matter reaches 10^9 synapses μL^{-1}.[16] Apart from compactness, but still inspired by neural cells and brain activity, the most appealing feature of downscaled OECTs is probably the capability to achieve fast operation speed. In this regard, a thorough study has been very recently carried out on OECTs with submicrometric channel sizes fabricated on electrode gaps by electromigration induced break junction technique. Here, the authors report superior amplifying properties of fast varying signals and time responses in the millisecond scale.[17] However, it should be noted that all devices reported so far are based on chip-like geometries.

Even in the field of electroanalysis, the use of nanometre-sized devices holds key advantages including high sensitivity and spatial resolution in localized electrochemical measurements for molecules detection.[18] In particular, superior spatial resolution can be obtained by the use of sub-micrometric, needle-type structures, such as carbon nanopipettes (CNPEs) and nanoelectrodes (CNEs), whose high aspect ratio provides a mean of interfacing a nanoscopic structure with a macroscopic handle without a need for any assembly and allowing precise positioning of the sensing device at the single-cell level.[19] Thanks to the sharp geometry that facilitates penetration and implantation for localized measurements in distinct regions of small organisms, a CNPE sensor has been used to detect endogenous dopamine release in the dopaminergic centers of *Drosophila larvae*.[20]

Recent advancements towards the reproducible fabrication of CNEs have been achieved, thus significantly improving their manipulation and reliable applicability for analytical purposes.[21] For instance, a syringaldazine-based CNE has been reported as voltammetric

nanosensor for pH imaging at high scan rate (0.66 V s^{-1}) and with high spatial resolution.[22] Coupling such nanometric objects and transistor-like configuration represents a clear breakthrough for single-cells analysis and has led to highly sensitive and fast responses thanks to the transistor amplification. In this view, FETs and nanopore platforms have been merged to develop a nanopipette-based PPy ionic-FET, where the distribution of ions in the overlapping electric double layer inside the nanopore is altered upon modulation of the potential applied to the PPy gate, thus allowing efficient control of the molecular transport at the single-molecule level. The device is used to detect single-molecule translocation events of DNA and, with insulin-modified PPy, IgG antibodies.[23] Moreover, the use of a Au gate equipped nanopore−FET has been demonstrated to allow the synchronized detection of single molecule events in both nanopore and gate channels.[24] With a different approach, nanometric field-effect-transistor (FET) sensors were obtained on the tip of spear-shaped dual carbon nanoelectrodes by electrodeposition of a PPy channel. By this nano biosensor, real time monitoring of extracellular acidity in the microenvironment of cancer cells was carried out and, after binding hexokinase to the PPy channel, extracellular ATP concentrations down to 10 nM were detected.[25] Following this approach, a nanosized OECT was realised combining single-barrel and double-barrel CNEs, both coated with PEDOT:PSS that comprises the gate and the channel of the transistor. In the second part of this Chapter, fabrication, characterization and use of such a device as a nanosensor for DA detection will be discussed.

2. Selective detection of dopamine with an all PEDOT:PSS Organic Electrochemical Transistor

Figure 1A and B show the experimental setup used for the electrochemical measurements in the 3-electrode amperometric cell and in the OECT configuration, respectively. Given that the all PEDOT:PSS OECT response is ruled by the analyte oxidation at the gate electrode,[12] the AA, DA, and UA responses were studied at a PEDOT:PSS electrode, made exactly as an OECT gate electrode, in a classical three electrode cell by cyclic voltammetry (CV) and differential pulse voltammetry (DPV) at different scan rates. First of all, the CV electrochemical behavior of the three individual redox compounds was assessed. In a CV experiment, the working electrode potential is ramped linearly versus time and the ramps in potential may be repeated as many times as desired (Figure 1 A).

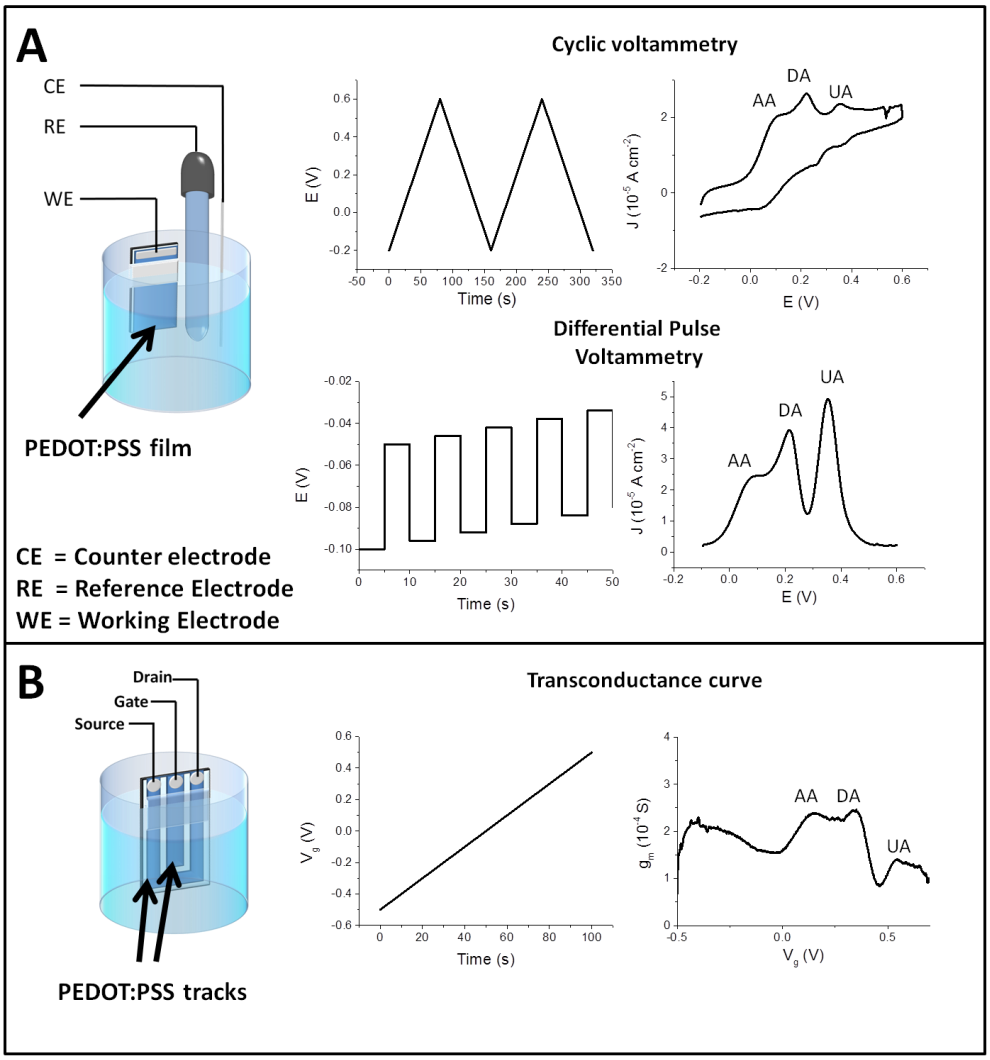

Figure 1. Experimental setup, potentials waves and responses that are used for electrochemical experiments in the 3-electrode amperometric cell (**A**) and OECT configuration (**B**).

The current is measured at the working electrode and it is plotted versus the applied voltage (i.e., the working electrode's potential) to give the CV trace. **Figure 2** reports the CVs recorded for the three different analytes at different concentrations. The CV of each biomolecule exhibits a peak associated to the analyte electro-oxidation that occurs at a characteristic potential measured with respect to a saturated calomel electrode (SCE). The peak potential value depends both on the thermodynamics and on the kinetics of the redox reaction. The peak current is linearly related to the analyte concentration (Figure 2) and the slope is the sensitivity of the CV detection. **Table 1** reports the anodic peak potential and the sensitivity of calibration line

obtained by CV experiments at 0.020 V s^{-1} for each analyte. The sensor exhibits the best sensitivity for DA detection, while AA shows the lowest redox signal.

	Three electrode cell				OECT	
	CV		DPV			
	E_{pa}[a] (V vs SCE)	Sensitivity[b] (LOD)[c]	Sensitivity[b] (LOD)[c]	Sensitivity[e]	Sensitivity[d] (LOD)[c]	Sensitivity[e]
AA	0.29	0.063 ± 0.005 ($1\ 10^{-4}$)	0.00967 ± 0.0003 ($2\ 10^{-5}$)	0.193 ± 0.003	0.102 ± 0.004 ($7\ 10^{-5}$)	0.85 ± 0.03
DA	0.35	0.109 ± 0.009 ($3\ 10^{-4}$)	0.448 ± 0.006 ($2\ 10^{-6}$)	9.0 ± 0.1	1.09 ± 0.04 ($6\ 10^{-6}$)	9.1 ± 0.3
UA	0.41	0.090 ± 0.002 ($2\ 10^{-4}$)	0.065 ± 0.001 ($6\ 10^{-6}$)	1.30 ± 0.02	0.40 ± 0.01 ($2\ 10^{-5}$)	3.33 ± 0.08

[a] anodic peak potentials evaluated by CV for 1 mM solutions
[b] expressed in A M^{-1} cm^{-2}
[c] expressed in M
[d] expressed in S M^{-1}
[e] normalized sensitivity expressed in S M^{-1} cm^{-2}. The DPV and OECT sensitivities are normalized to pulse amplitude and gate area, respectively.

Table 1. Performance of CV, DPV and OECT in the detection of AA, DA and UA.

Since the electrochemical processes under investigation occur at different potentials, it is possible to selectively determine the redox signal associated to each analyte when DA, AA and UA are simultaneously present in the solution and, consequently, to exploit it in order to determine its concentration. Figure 2 D shows the CVs recorded at different scan rates in a solution containing AA (1.0 mM), DA (1.0 mM) and UA (1.0 mM). The graph points out that the scan rate affects the kinetics of charge transfer and, consequently, this parameter can be useful to control the intensities and the potentials of the redox waves. For each tested scan rate, the UA peak is well separated from the AA and DA signals. The redox waves of DA and AA are not well-defined at the highest scan rates (0.010 - 0.050 V s^{-1}), the best resolution being obtained at 0.001 V s^{-1}. Such phenomena can be explained considering the slow kinetics of AA electro-oxidation: when the scan rate is lowered, the reaction has more time to occur and, consequently, a lower over-potential is required for the AA electro-oxidation, thus leading to a separation from the DA peak, which occurs at a slightly more positive potential.

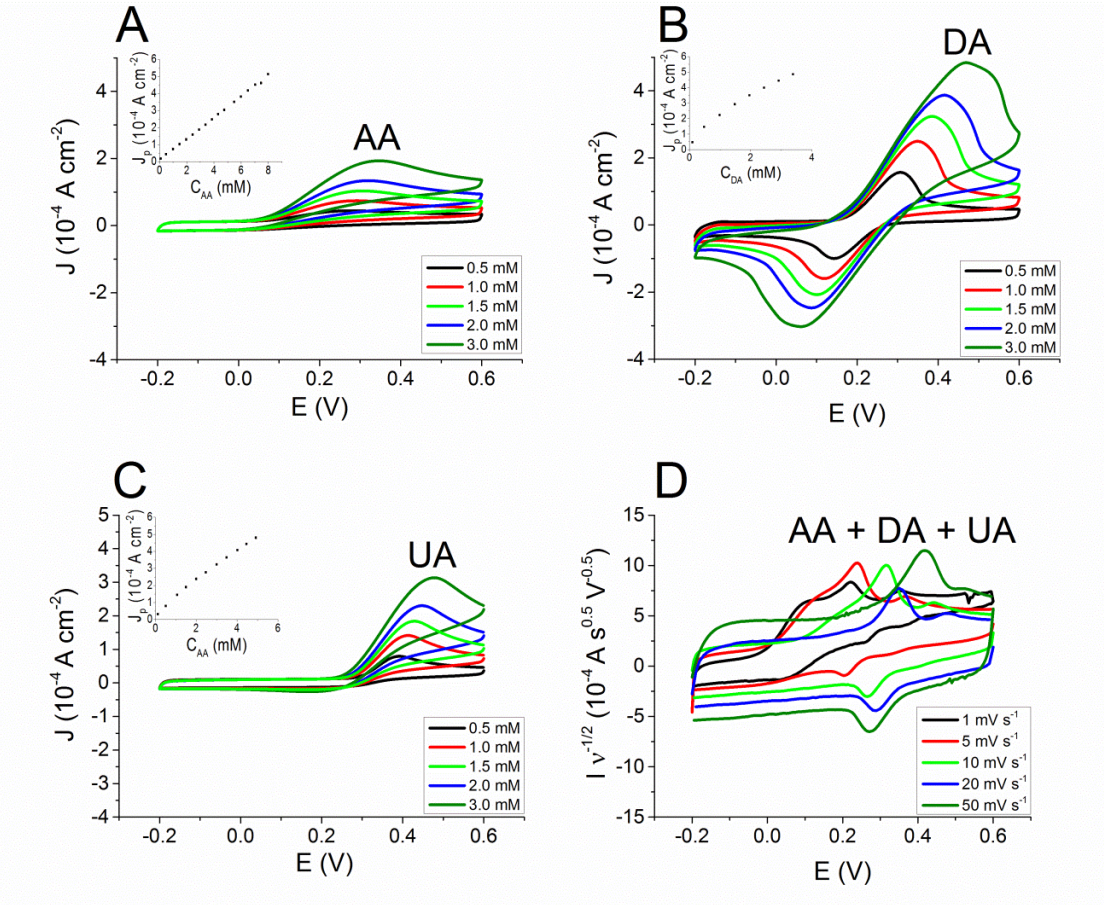

Figure 2. CV curves at 0.020 V s^{-1} recorded in a solution containing AA (**A**), DA (**B**) and UA (**C**) at different concentrations (insets: calibration plots). (**D**) CV curves recorded at different scan rates in a solution containing AA (1 mM), DA (1mM) and UA (1mM).

The electrochemical responses of the three bio-compounds were also studied by using DPV, a sophisticated electrochemical technique. During DPV, the working electrode is polarized with a series of regular voltage pulses superimposed on stair-steps (Fig. 1 A). The current is measured immediately before each potential change and the difference between the currents measured after and before the pulse is used as signal. Such a procedure allows to minimize the capacitive current contribution due to the charging of PEDOT:PSS through the hole injection/extraction and the ions exchange with the solution. As a consequence, the measurement of the faradic current associated to the analyte reaction is more accurate than in a CV experiment and a higher sensitivity can be obtained. **Figure 3** reports the DPVs recorded for solutions containing solely AA, DA or UA at different concentrations. The setup parameters were chosen on the basis of the CV results that enabled the best

separation between the peaks, i.e. a very low scan rate. Also, in DPV each analyte exhibits a redox wave at a characteristic potential and the peak current linearly depends on the analyte concentration. Table 1 reports the parameters of the calibration plots obtained by DPV (Figure 3) and the DPV sensitivities normalized to the pulse amplitude of the potential wave in order to compare the DPV performance with the one of OECT sensors. The sensitivities must be expressed per voltage unit, because the pulse amplitude plays a key role in determining the intensity of faradic currents. It is worth noting that DPV exhibits, for each compound, a LOD value that is about one order of magnitude lower than that obtained by CV.

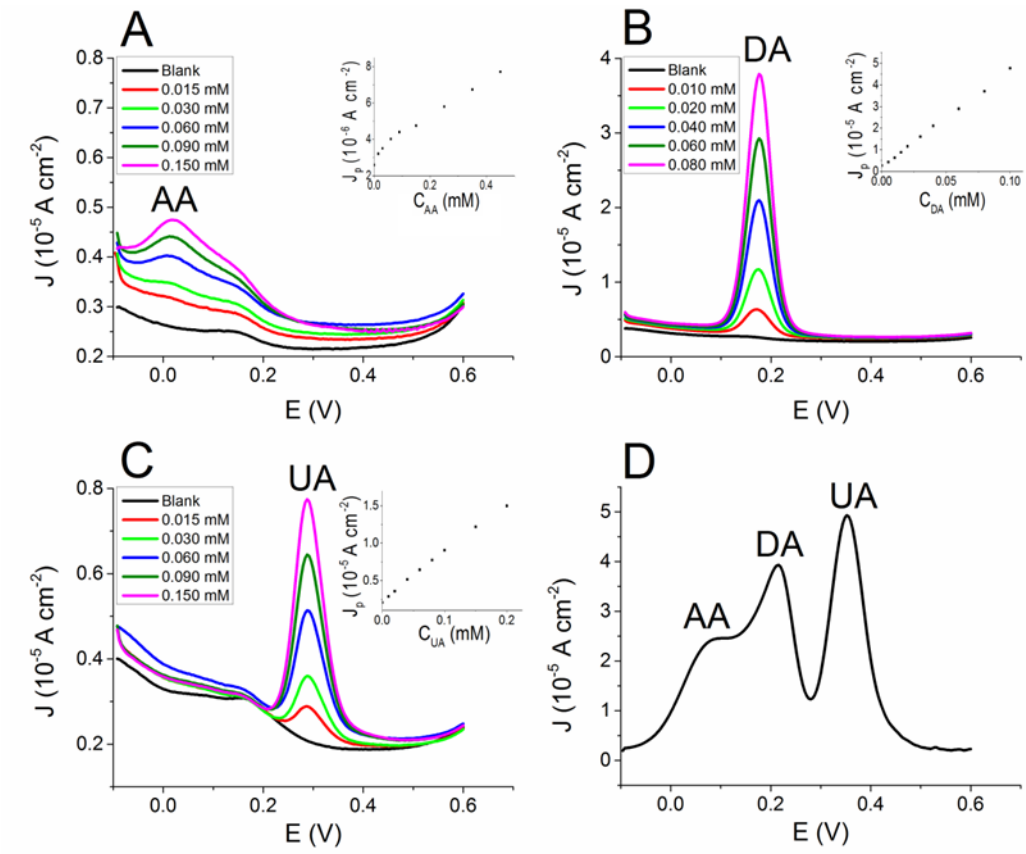

Figure 3. DPV curves recorded in a solution containing AA (**A**), DA (**B**) and UA (**C**) at different concentrations (Insets: calibration plots). (**D**) DPV recorded in a solution containing AA (1 mM), DA (0.07 mM) and UA (0.4 mM)

Figure 3 D shows a typical DPV signal recorded for a solution containing 1 mM AA, 0.07 mM DA and 0.4 mM UA. The redox peak of each bio-analyte is clearly visible in the response and the resolution between the peaks is much better than the one obtained by CV. These results clearly show that the amperometric detection of AA, DA and UA can be carried out by using a PEDOT:PSS coated electrode by either CV or DPV. It is worth underlining that the performance of an amperometric sensor can be improved by using a potential wave that allows the minimization of the background capacitive current. Consequently, DPV ensures a lower LOD than CV and it is one of the most sensitive electroanalytical techniques. However, the use of a sophisticated potential wave, with a careful setting of the different parameters, requires an elaborated read out electronics and may not be the best technique to choose for practical real-life applications.

Although step potential techniques are widely employed for the selective amperometric detection through the use of sensors based on chemically modified electrodes, this approach has never been applied to OECTs. Here, for the first time, this opportunity is explored by recording the transfer curves of an OECT in solutions containing different analytes at the same time. A transfer curve is a I_d-V_g curve that is acquired by linearly varying the potential applied to the gate electrode and recording the current that flows at the drain collector. Therefore, the gate electrode carries out a potential scan that is very similar to that applied to the working electrode in a CV. In the OECT operation mode, the redox process induced by the gate potential variation affects the electrical conductivity of the channel. The evaluation of the different contributions to the electrical signal due to various analytes is finally made possible by a V_g scan, with the key advantage that the transistor configuration of the OECT provides an intrinsic signal amplification (**Figure 4**). The transfer curve obtained for the blank solution is practically a straight line. This evidence can be explained by considering that, in this condition, the only process occurring at the gate electrode is PEDOT:PSS oxidation. Since PEDOT:PSS typically exhibits a capacitive behavior with a rectangular-shaped CV, also the current that flows at the gate electrode is constant and independent from V_g. Considering that I_g represents also the number of charge carriers extracted from the channel, a V_g variation exerts a constant action on the channel conductivity

independently of the applied V_g. Therefore, in a solution not containing any analyte the plot I_d-V_g is a straight line.

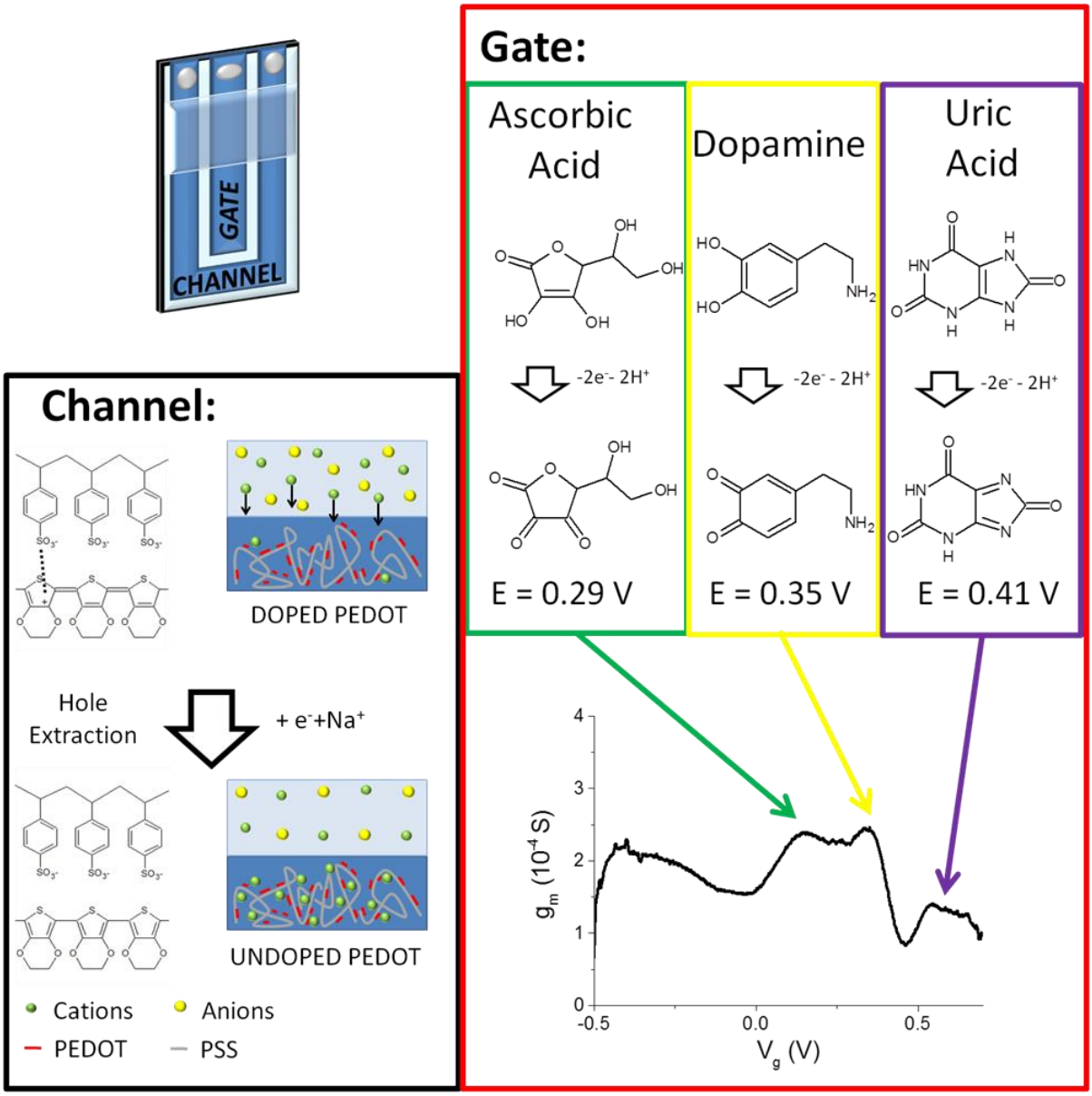

Figure 4. Working principle of the selective all-PEDOT:PSS OECT. The oxidation reactions of AA, DA and UA take place at different electrochemical potentials and, consequently, also at different gate potentials in an OECT. When a faradic process occurs at the gate electrode, more cations are injected in the PEDOT:PSS of the channel leading to an extraction of holes from the conductive polymer. Consequently, the gate effect is enhanced by a rise of the transconductance value. The OECT sensor identifies the contributions of different analytes as peaks in the transconductance plot.

When DA is added to the solution (**Figure 5** A), the I_d-V_g curve acquires a sigmoidal-like shape. This behavior can be explained by considering that a new electrochemical process, i.e. dopamine oxidation, takes place at the gate electrode. This process occurs exclusively at an electrochemical potential that is characteristic of dopamine and it affects the gate current, and consequently I_d, only at a specific V_g. Since DA oxidation leads to a I_g increase, likewise the gate action increases and more charge carriers are extracted from the channel with respect to the blank solution, leading to a higher I_d decrease. Since the redox current is directly proportional to DA concentration, the I_d decrement increases by increasing DA concentration.

Actually, these measurements demonstrate that the presence of a redox compound in the electrolyte solution increases the gate action on I_d. In order to highlight this phenomenon, the transconductance g_m was also studied. As explained in Chapter I, transconductance is the electrical characteristic relating the current through the output of a device to the voltage across the input of a device. In order to calculate the transconductance as a function of V_g, the transfer curve was derived according to its definition.

Since in an OECT the gate action is mediated by the electrolyte solution, the presence of an electro-active compound can induce a significant variation in its trans-conductance when an appropriate V_g is applied. In particular, the occurrence of a faradic process associated to the analyte oxidation leads to an increase in current modulation, and hence of the trans-conductance value. Figure 5 B reports the transconductance curves obtained from the transfer curves recorded in a solution containing DA at different concentrations. In the transconductance plot, the DA signal displays a peak-like shape and the intensity of this peak is linearly related to DA concentrations in the 0.005 – 0.100 mM range.

The same result can be obtained in solutions containing AA or UA (see Figure 5 D). For each analyte, calibration plots were obtained and the characteristic parameters are reported in Table 1. It is worth noting that for all the tested analytes, the OECT LOD values are lower than those observed by CV, the electrochemical technique that uses the same shape of the potential wave. Moreover, looking at the sensitivity values normalized with respect to the gate area so that a comparison with DPV

results is possible, the sensitivities are comparable or even higher DPV measurements, highlighting the great advantage due to the signal amplification deriving from the transistor architecture.

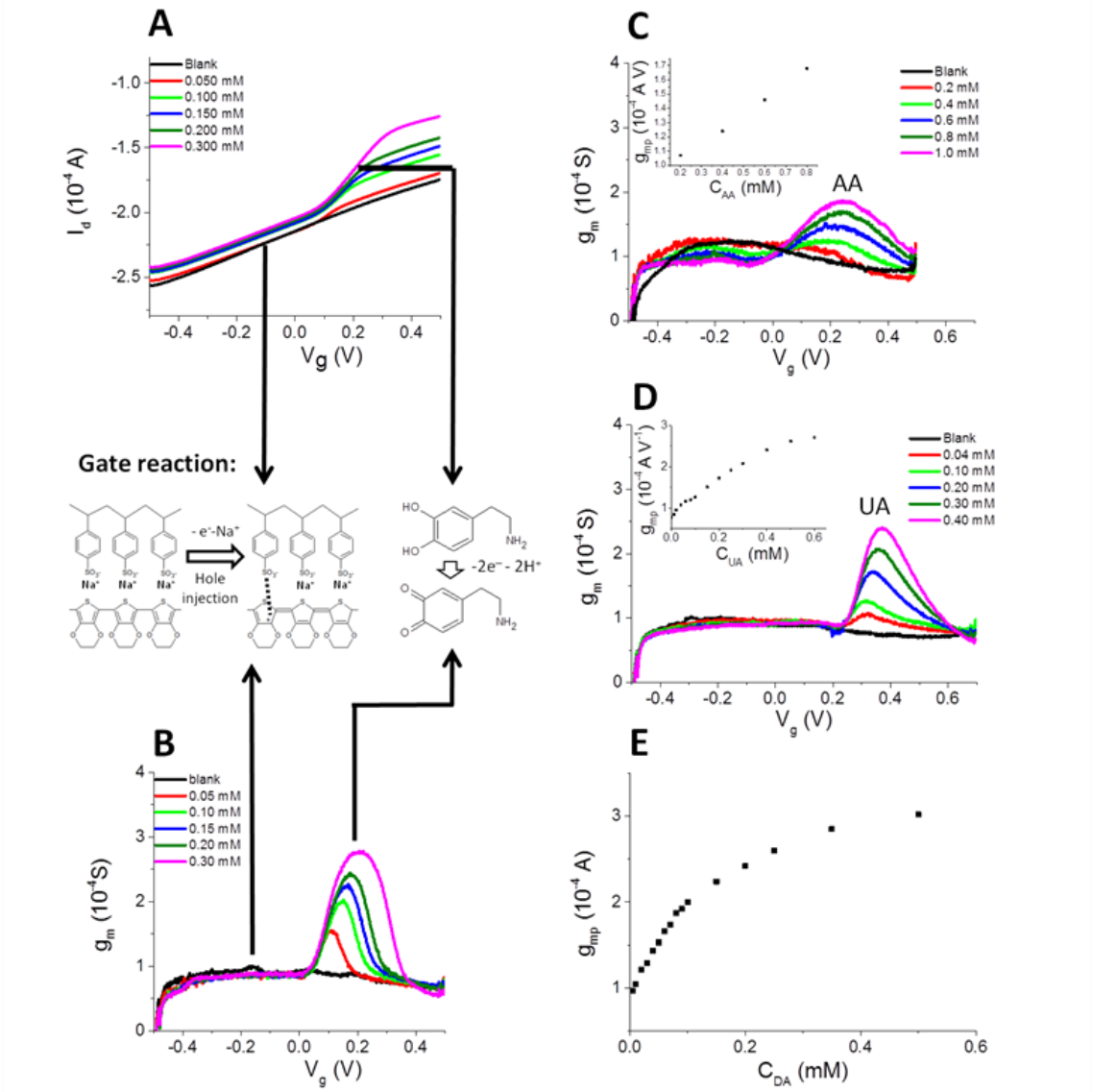

Figure 5. (**A**) Transfer curves recorded in a solution containing DA at different concentrations. (**B**) Transconductance curves obtained from transfer curves reported in (A). Trans-conductance curves recorded in a solution containing AA (**C**) and UA (**D**) at different concentrations. In the insets the calibration plots are reported. (**E**) Calibration plot obtained for dopamine. The chemical scheme shows the reactions which take place in different areas of the graphs. Only PEDOT:PSS oxidation occurs in the blank and at low gate voltage (V_g). In the presence of DA, also the DA oxidation occurs at $V_g \sim 0.2$ V.

The device exhibits a limit of detection for DA equal to 6 μM, which is still higher than those achievable with OECT having a Pt gate electrode,[10,11] but comparable to that obtained by more sophisticated techniques such as for example fast scan cyclic voltammetry at a patterned 10 μm gold microelectrode using an additional PEDOT:PSS OECT to amplify the FSCV signal.[26] The strength of this study lies in the demonstration that an all-plastic OECT enables the discrimination among DA and interfering species. Obviously, future work will be devoted to the LOD improvement, for example by changing the gate electrode geometry.

Transconductance curves were recorded for a solution containing DA, AA and UA simultaneously in order to demonstrate the applicability of this approach to the selective detection of the three analytes at the same time (Figures 4 and 6 A). **Figure 6** A shows that the resolution between the three waves associated to the redox compounds depends on the scan rate as previously observed for CV, being the best for the lowest scan rate. The different redox waves can be assigned to the different redox species considering the peak potentials determined by CV. The peaks at 0.16, 0.34 and 0.54 V are thus ascribed to AA, DA and UA, respectively. These results have been experimentally confirmed by sequentially adding different amounts of each analyte to a solution containing all the compounds, in order to identify which peak increases.

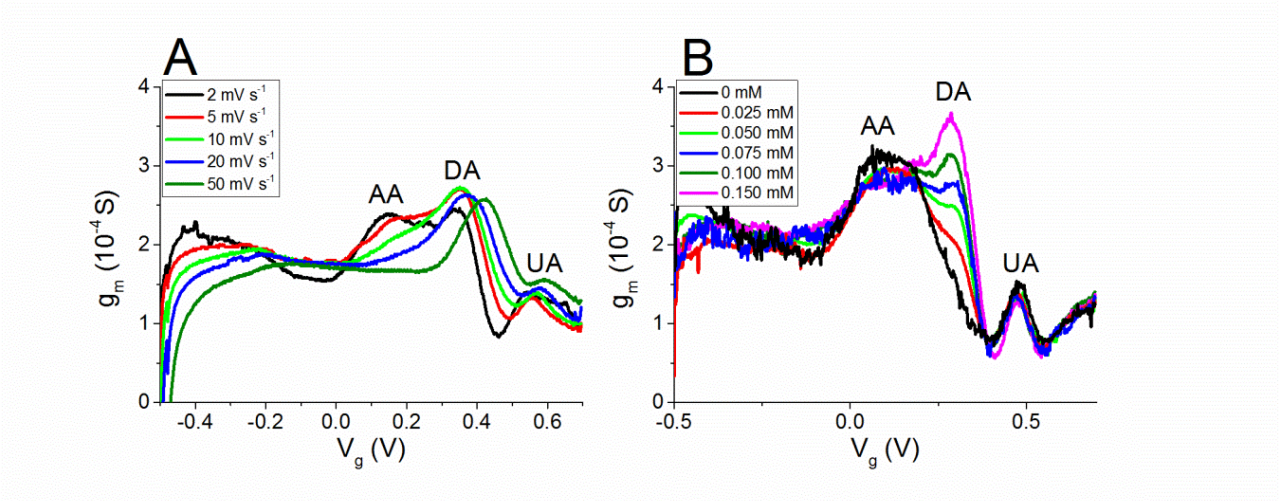

Figure 6. Transconductance curves recorded (**A**) in a solution containing AA (1 mM), DA (0.1 mM) and UA (0.5 mM) at different scan rates and (**B**) in a solution containing dopamine at different concentrations plus 0.1 mM UA and 0.5 mM AA (fixed concentrations) at 0.002 V s^{-1}.

The scan rate variation affects the OECT response in a way that is similar to that observed in CV experiments with a 3-electrode cell setup. By increasing the scan rate, the AA peak moves towards higher V_g and it merges with DA peak. Such phenomenon can be ascribed to the slow kinetics of AA electro-oxidation at the gate electrode, as previously stated. Nevertheless, the shift of AA peak does not affect the intensity of the DA peak up to the highest tested scan rate. This observation agrees with the literature data on amperometric detection,[26] which reports that it is possible to avoid the AA interference in DA determination by working at high scan rate.

The final part of this work is devoted to demonstrate that the described step potential technique can be successfully employed in the selective DA detection in the presence of AA and UA as interferents. Figure 6 B shows the transconductance curves recorded at a scan rate of 0.002 V s^{-1} in a solution containing 0.5 mM AA and 0.1 mM UA while increasing DA concentration. The figure clearly shows that DA peak is well separated from AA and UA signals and that the peak current linearly depends on the dopamine concentration, with a slope equal to 1.32 ± 0.07 S M^{-1}. Such value is the same as that obtained when a solution containing only DA was studied in the same condition of scan rate. This is a further confirmation that all-PEDOT:PSS OECT devices can be effectively used as selective sensors for DA detection when a step potential technique is employed.

3. Development of an all-PEDOT:PSS OECT nanometric sensor for Dopamine detection

Schematics of the needle-type OECT are presented in **Figure 7**. The OECT channel is a thin film of PEDOT:PSS bridging spearhead source and drain carbon nanoelectrodes. A gate voltage (V_g) is applied to the spearhead gate electrode, which is coated by the same semiconducting polymer, to modulate the current I_d flowing through the OECT channel due to the applied V_d (Figure 7A). Fabrication steps for the realization of the OECT components are illustrated in Figure 1B. Single and double barrel carbon nanoelectrodes (sbCNE and dbCNE) are obtained after pyrolytic decomposition of a butane and propane gas mixture to yield a conductive, graphitic carbon filler deposited inside pulled quartz capillaries. As for the dbCNE, a nanometre-sized quartz wall separates the two

nanoelectrodes that are individually adressable and therefore can be referred to as source and drain terminals. Afterwards, PEDOT:PSS is electrodeposited on the tip of the spearhead CNEs. A nanodisk-shaped PEDOT:PSS gate electrode is generated from the sbCNE. In the dbCNE tip, the semiconducting polymer film connecting source and drain forms the OECT channel. In the following, fabrication and characterization procedures optimized for the two needle-type OECT components, i.e. gate anche channel, are discussed in detail.

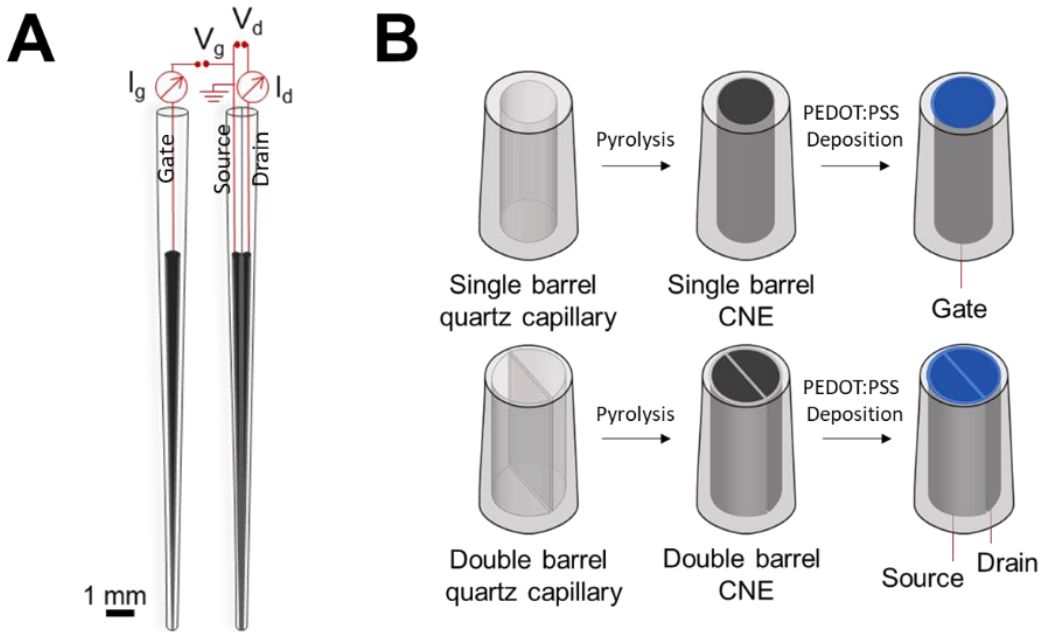

Figure 7. Device schematics. (**A**) Configuration of the needle-type CNEs. (**B**) Fabrication steps of PEDOT:PSS spearhead gate and channel.

3.1 Needle-type gate electrode

After pyrolytic carbon decomposition (see Materials and Methods for fabrication details), the electrochemically active surface of the CNE was characterized by evaluation of the steady-state limiting current (i_{ss}) ascribed to the reduction of the redox probe $[Ru(NH_3)_6]^{3+}$ (**Figure 8**A). However, due to the shape uncertainty at the nanometre scale, estimations made from classical expressions correlating i_{ss} and electrode geometry, as well as assumptions on the basis of well-defined sigmoidal voltammograms are scarcely predictive.[21] For this reason, the actual geometry of nanoscale sbCNEs was always assessed by SEM (Figure 8B). SEM pictures reveal a hollow quasi-disk structure of the

tip, with geometrical radius of 139 ± 3 nm. sbCNEs were coated by a thin film of semiconducting polymer to yield polymeric gate electrodes for the OECT.

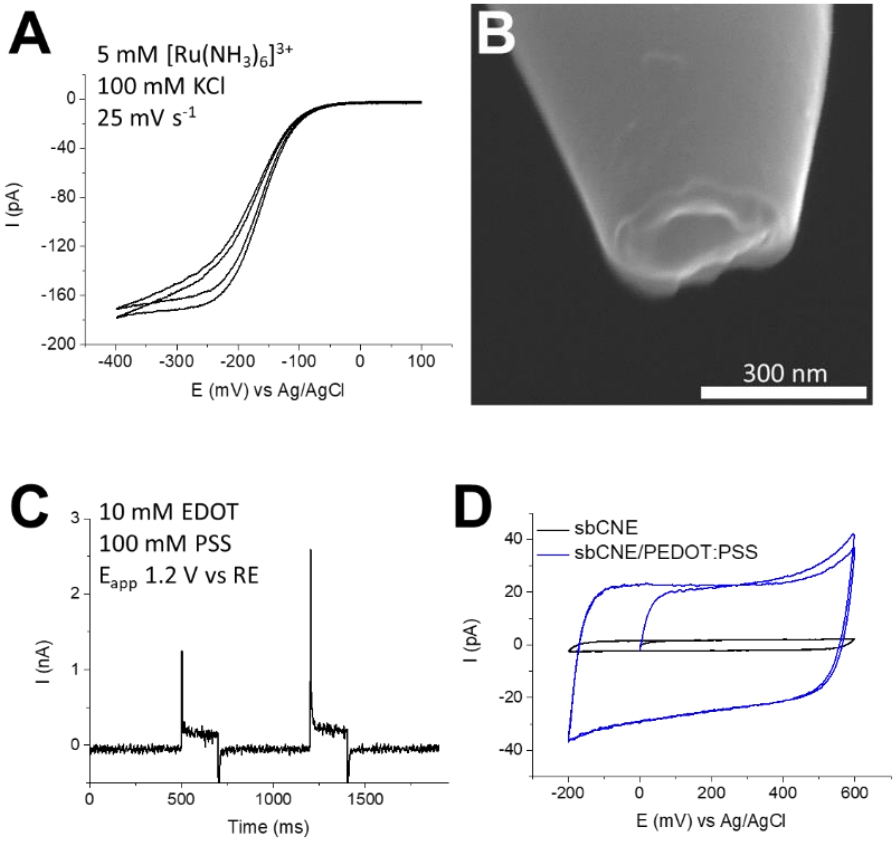

Figure 8. PEDOT:PSS spearhead gate electrode. (**A**) Electrochemical characterization of sbCNE. (**B**) Side and view of the sbCNE. (**C**) PEDOT:PSS pulse electrodeposition at sbCNE. (**D**) CV characterization of sbCNE/PEDOT:PSS electrode in phosphate buffer. Scan rate 50 mV s^{-1}.

To this end, cyclic voltammetry (CV) and pulse profile were compared for PEDOT:PSS electrodeposition. Examples of the electrode's shape obtained by the two methods can be visualized in **Figure 9**. Together with the potential waveform, monomer concentration (10 or 5 mM) and other parameters specific to the technique of choice (scan rate and number of cycles for CV; number and duration of pulses for pulse deposition) were varied, while keeping fixed PSS concentration (0.1 mM), pulse potential (E_{app} = 1.2 V vs Ag/AgCl) and CV potential window (0 < E_{app} < 1.2 V vs Ag/AgCl). Pulse potential, as well as anodic potential limit, were chosen to trigger the monomer oxidation and promote the polymerization without causing PEDOT overoxidation. It is evident that CV is not the

suited deposition technique to obtain thin films. Indeed, bunchy structures of increasing size are realized upon potential cycling (Figure 9A, B, C).

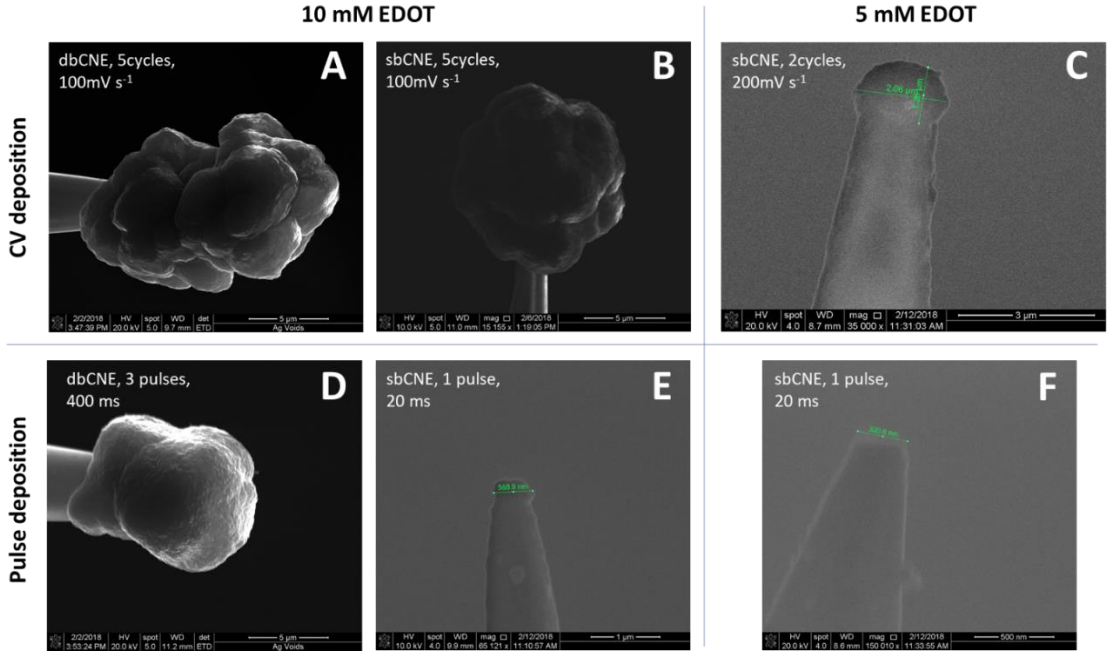

Figure 9. SEM images of CNEs after PEDOT:PSS electrodeposition. The depositions were carried out in aqueous solutions containing the monomer (5 or 10 mM) and PSS (0.1 mM) upon application of either potential cycles in the interval $0 < E_{app} < 1.2$ V vs RE (**A**, **B**, **C**) or potential pulses with $E_{app} = 1.2$ V vs RE (**D, E, F**).

The voltammogram recorded during the deposition of the CNE showed in Fig. 9C is reported in **Figure 10**. It is well-known that EDOT oxidation occurs at higher poitentials with respect to PEDOT and the polymer growth is facilitated cycle by cycle. The shape of the electrode obtained after 2 cycles could suggest that the formation of one PEDOT-bubble roughly follows one potential cycle and faster scan rates might produce more flat deposits. The structures obtained after pulse depostion (Fig. 9D, E, F) also present some globular features, however the time scale (tens/hundreds of milliseconds) is far smaller than CV. This hinders the formation of large aggregates and, upon selection of the suitable parameters (pulse duration and frequency) it is possible to obtain film-like and controlled depositions. Overall, it was noted that use of the lower monomer concentration (5 mM) during both CV and pulse deposition, as well as frequent pulses with the shorter duration (20 ms) lead to less stable PEDOT:PSS deposits on the CNEs that often detach during utilization.

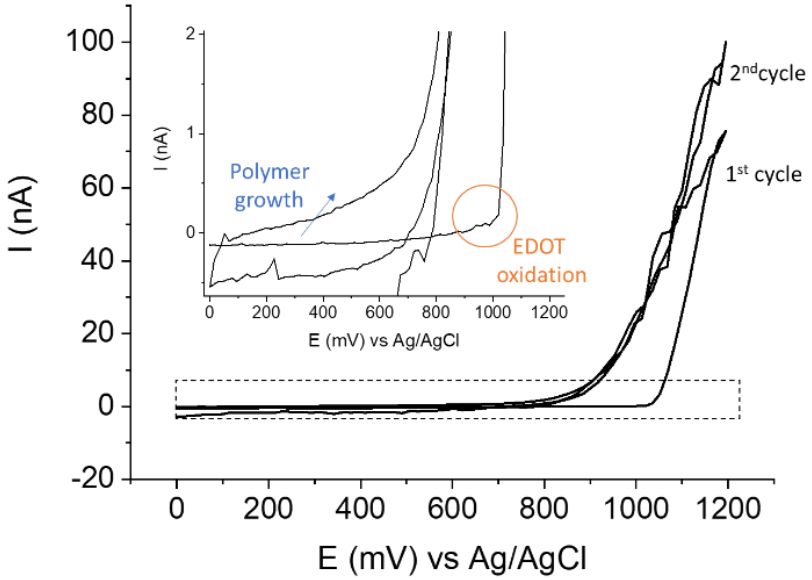

Figure 10. PEDOT:PSS deposition at CNE by CV to obtain the electrode shown in Figure 9C. Inset: zoom of the voltammogram region highlighted by the dotted rectangle that shows monomer oxidation and polymer growth upon cycling.

For these reasons, pulse profile was the technique of choice that allows adequate control of the polymeric film deposited. Two potential pulses of 200 ms (E_{app} = 1.2 V vs Ag/AgCl 3M KCl) were applied to the sbCNE in the polymerization solution containing the monomer EDOT (10 mM) and the counterion PSS (0.1 mM) (Figure 8C). As reported in Figure 8D, a significant increase of the capacitive current recorded during CV characterization before and after deposition confirmed the growth of the polymer film on the sbCNE. A rough ten-fold increment of the electrode charge is found with respect to the bare sbCNE.

3.2 Needle-type channel

The optimized procedure for dbCNEs fabrication includes the use of focused ion beam (FIB) milling to yield electrodes with controlled geometry and size (**Figure 11**). Indeed, dbCNEs obtained after pyrolysis as such present more defects and poor size reproducibility with respect to sbCNEs. By introduction of the additional FIB milling step, it is possible to cut off the dbCNE tips with carbon overgrowth, cracks and recessed carbon edges (Figure 11A, B and C, respectively), leading to regular and well-defined shapes.

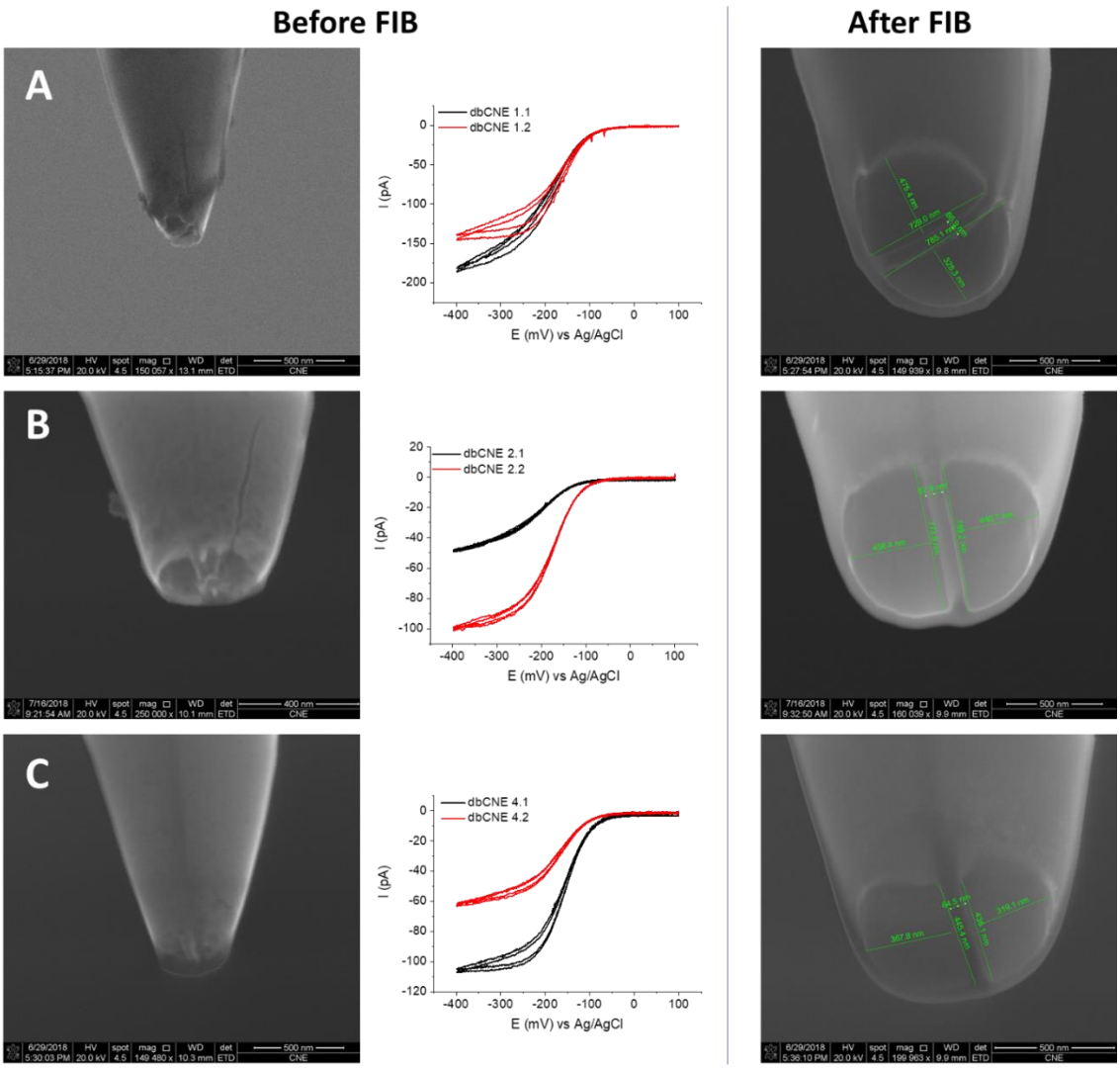

Figure 11. dbCNEs before and after focused ion beam milling. Left panel: SEM pictures and correspondent characterization voltammograms, recorded at 25 mV s^{-1} a solution containing 5 mM $[Ru(NH_3)_6]^{3+}$ and 100 mM KCl, of the dbCNEs after pyrolysis. Right panel: SEM pictures of the dbCNEs after the FIB milling step.

The resulting two barrels, with a radius of 430 ± 70 nm, are individually addressable and separated by a thin quartz wall of 48 ± 8 nm. They can be virtually seen as source and drain electrodes. Based on the considerations made for the sbCNEs, a pulse profile (**Figure 12**B) was chosen to deposit a film of PEDOT:PSS that bridges the two barrels to form the semiconducting channel. In this case, at least three pulses are statistically needed to obtain a stable polymeric film, with a thickness ranging from 240 to 300 nm, that provides the desired electrical connection between source and drain. Figure 12A and C show SEM pictures of a dbCNE before and after PEDOT:PSS electrodeposition, respectively, where

the deposited layer covers completely the quartz wall and establishes a nanojunction between the barrels. The presence of the polymeric channel is further assessed by SEM-EDS mapping (Figure 12D), where Sulfur atoms distrubution, coming from tiophene rings of PEDOT and sulfonate groups of PSS, is also localized on the quartz wall of the dbCNE after electrodeposition.

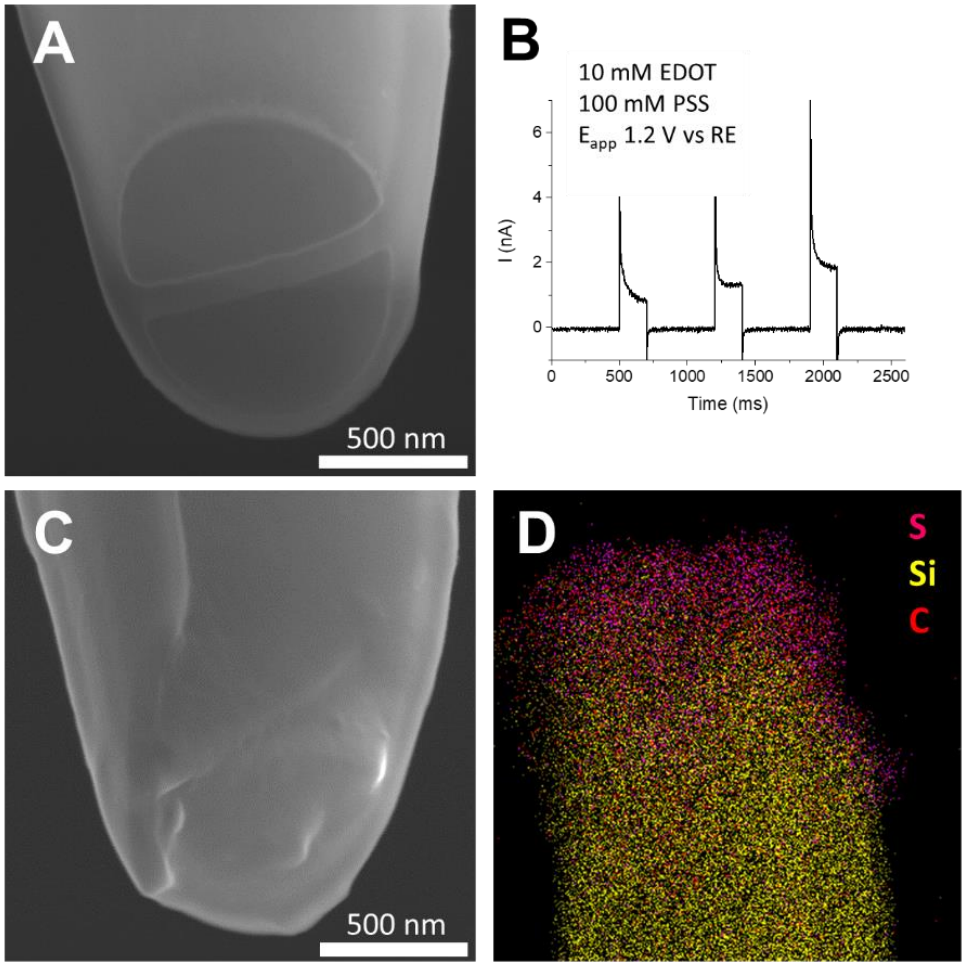

Figure 12. PEDOT:PSS spearhead channel. (**A**) SEM picture of the dbCNE. (**B**) I vs time curve recorded during PEDOT:PSS pulse electrodeposition on dbCNE. (**C**) SEM picture and (**D**) EDS map of the PEDOT:PSS channel bridging the two barrels.

3.3 Fabrication of the needle-type OECT

Following this fabrication procedure, all-PEDOT:PSS spearhead gate electrode and channel with a diameter of about 300 and 900 nm, respectively, are obtained. Coupling the two electronic components leads to the fully functioning, needle-type OECT configuration

illustrated in Figure 7A. The transistor was characterized by recording I-V curves in buffer solution (**Figure 13**). Output characteristics in Figure 13A show that I_d vs V_d curves recorded with different voltages applied to the gate electrode. I_g is an ionic current that travels across the electrolyte and affects the electronic current that flows through the channel, depending on the applied V_g. Due to a positive gate bias, cations are injected into the polymeric channel and compensate the negatively charged sulfonate groups of PSS. Consequently, holes extranction takes place and channel conductivity decreases, causing the observed I_d modulation. Despite the sub-micrometric size, the so-called "short-channel effects"[15] resulting, for example, in a lack of current saturation or non-linear output characteristics, are not observed. OECT operation is well described by the transfer characteristics in Figure 13B, where the output I_d was measured while linearly scanning the gate voltage, at fixed V_d values. The OECT amplification is expressed by the transconductance g_m, which is the effective parameter to quantitatively describe the modulation of the channel current upon gating (Figure 13C). It has to be noted that g_m values are significantly lower than those reported for other nanometric OECTs, typically lying in the mS range.[14,15] However, given the round-shaped channel geometry and the fact that the polymer films were obtained by electrodeposition, in contrast to typically planar, rectangular channels deposited from commercial PEDOT:PSS inks, comparison with the state of the art might be not meaningful.

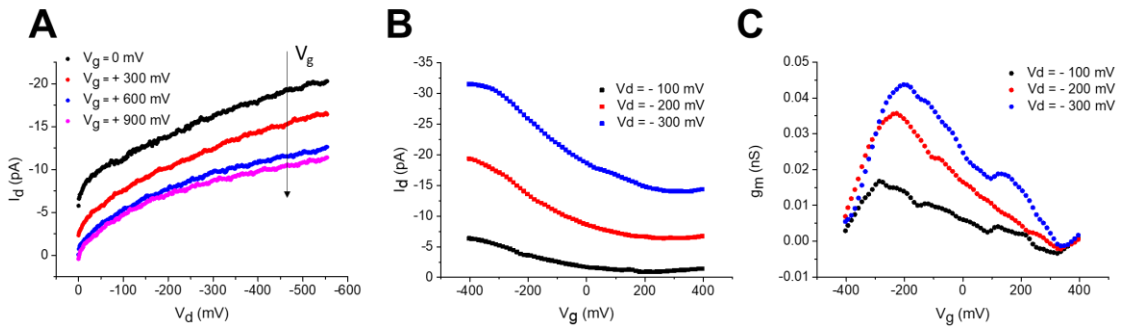

Figure 13. OECT characterization in buffer solution. (**A**) Output characteristics recorded at 20 mV s^{-1}. (**B**) Transfer curves recorded at 100 mV s^{-1} and (**C**) correspondent transconductance vs V_g plot. All measurements were acquired in 100 mM PBS.

3.4 Dopamine sensing with the needle-type OECT

Figure 14A shows the voltammogram obtained at a spearhead PEDOT:PSS gate electrode in buffer and after addition of DA. A couple of well defined and reversible peaks, with Ep_A = + 194 mV and Ep_C = + 123 mV vs RE, appears due to the reversible redox reaction of DA at the PEDOT:PSS electrode. As long as a chemical species is able to take part in the doping/de-doping mechanism that rules the transistor operation, it can be detected by the OECT. In the case of a redox active molecule like DA, the occurrence of its oxidation can be favoured either at the polymeric gate or channel, depending on their relative electrochemical potentials. As an OECT works in depletion mode, this always leads to a decrease of the channel conductivity.[27] This phenomenon can be exploited for sensing with OECTs and can be observed by either using a potentiodynamic gate bias or applying fixed V_d and V_g. Transfer characteristics were recorded in the presence of increasing DA concentrations in the nM range, upon application of a linear ramp to the gate electrode (Figure 14B). If V_g is sufficiently negative, DA oxidation is favoured at the OECT channel, which is the OECT component with the highest electrochemical potential. Here, PEDOT undergoes reduction resulting in a decrease of I_d and transfer curves shift upwards by increasing DA concentration. The presence of an oxidisable species like DA in solution can be in fact imagined as an "extra gate" switching off the OECT channel. Consequently, the higher the concentration of DA, the more difficult to trigger a current flow through the channel. The gate bias that is needed to turn the transistor on is known as threshold voltage, V_T, and it can be extracted from the linear region of the transfer curves as the x-axis intercept.[28,29] As reported in Figure 14C, V_T scales linearly with the logarithm of DA concentration (R^2 0.996). Sensing performances of three needle-type OECTs were tested upon application of fixed V_g and V_d (-900 and -300 mV, respectively) by adding increasing amounts of DA to the buffer solution under controlled conditions, while I_d was measured over time (Figure 14D). As expected, each addition was followed by an I_d decrement due to the depletion of holes from the channel boosted by DA oxidation. The modulated current exhibits logarithmic dependence on the analyte's concentration that was varied by 6 orders of magnitude, from the pM to the μM range (Figure 14E). Considering a signal to noise ratio equal to 3, the calculated detection limit (LoD) for DA was 240 pM.

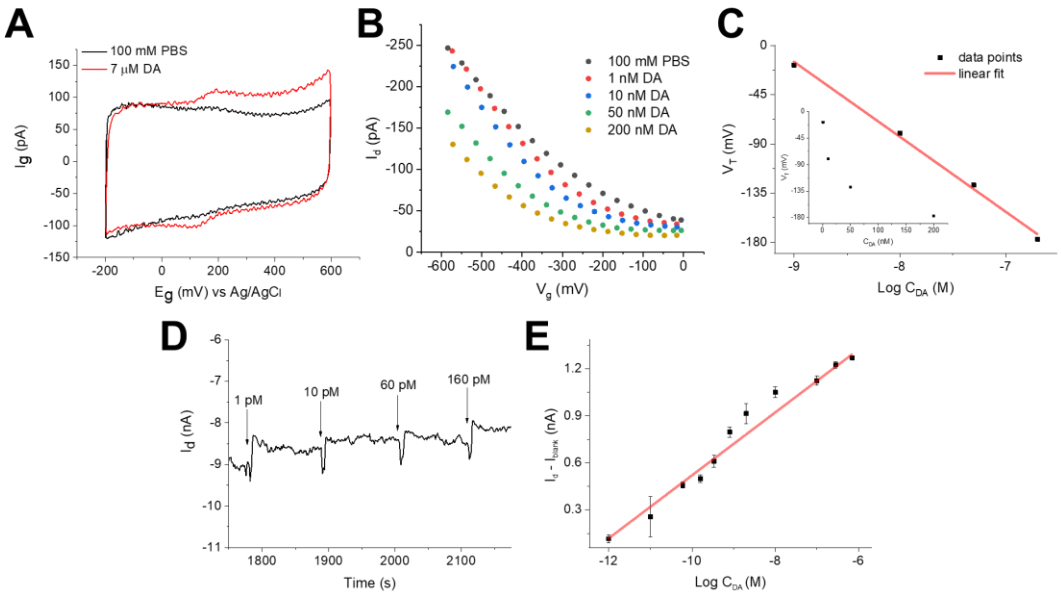

Figure 14. Dopamine detection with the needle-type OECT. (**A**) Electrochemical response of the PEDOT:PSS gate electrode to Dopamine (DA). Scan rate 100 mV s^{-1}. (**B**) Transfer curves recorded in presence of increasing amounts of DA. V_d = - 200 mV, scan rate 10 mV s^{-1}. (**C**) Threshold voltage response to DA concentration (inset) and logarithm of DA concentration in the nanomolar range. (**D**) I_d vs time curve to increasing additions of DA. V_g = - 900 mV; V_d = -300 mV. (**E**) Calibration curve obtained from (D). R^2 = 0.988.

4. Materials and Methods

OECT fabrication with chip-like geometry. The OECT was prepared by spin coating CLEVIOS PH 1000 suspension (PEDOT:PSS) on a glass slide at 500 rpm per 3 s. Figure 1 A reports a schematic representation of the device; the external PEDOT:PSS stripe was used as the source-drain channel while the inner one worked as the gate electrode.

Electrochemical Measurements with planar OECTs. The electrochemical characterizations were carried out by CV and DPV in a three-electrode cell using a 0.1 M phosphate buffer solution (PBS), pH 5.5, as electrolyte. The electrochemical potentials were measured with respect to an aqueous saturated calomel electrode (SCE), a Pt wire was used as the counter electrode and a PEDOT:PSS thin film deposited on a glass slide was used as the working electrode. The electrochemical responses were acquired employing a CH Instrument 660C that was controlled by personal computer CHI Software. For DPV, the instrumental variables were studied

and the optimum conditions resulted: pulse amplitude: 0.050 V; increment: 0.004 V; sample width: 4 s; pulse width: 5 s; pulse period: 10 s; sensitivity: 1×10^{-4}A**.**

Two Sourcemeters 2400 SMU (KEITHLEY) controlled by a personal computer via a homemade LAB-VIEW software were simultaneously employed in order to carry out the electrical measurements (Figure 1 C) by applying source-drain (V_d) and source-gate (V_g) potentials and measuring the respective currents (I_d, I_g). A defined area both for the gate (0.3 x 0.3 cm^2) and the channel (0.3 x 3.0 cm^2) was left unprotected and exposed to the electrolyte solution. The OECT was dipped in PBS under magnetic stirring and the transfer curves were acquired in absence and in presence of the analytes at different concentrations. The trans-conductance curves were obtained by deriving the transfer curves with origin software. The OECT performance has been evaluated by considering the sensitivity and the limit of detection.

Nanoelectrodes fabrication and characterization. For the fabrication of nanopipettes, single- and double-barrel quartz theta capillaries (o.d. 1.2 mm, i.d. 0.9 mm, Sutter Instruments) were pulled with a P-2000 laser puller (Sutter Instruments) using the following parameters:

Type	Heat	Filament	Velocity	Delay	Pull
Single Barrel	800	4	45	130	90
Double Barrel	800	4	45	130	100

Table 2. Pulling parameters optimized for double- and single-barrel nanopipettes fabrication.

Afterwards, a custom-made pyrolysis setup[21] was employed to fill the nanopipettes with carbon, thus yielding single- and double-barrel Carbon Nano Electrodes (sbCNEs and dbCNEs). During pyrolysis (**Figure 15**B), the Ar counter-flow (Air Liquide, 99.999%) was set at a rate of 50 mL min^{-1} with the Ar pressure fixed at 0.5 bar. Pyrolysis gas was introduced as a mixture of propane (Air Liquide, technical grade) with a pressure of 3 bar and n-butane (Air Liquide, 99.5%) with a pressure of 1.1 bar. Coil movement and heating current were simultaneously controlled by a homemade programmed software. Optimized temperature profiles used during pyrolysis are showed in fig. 15C for sbCNEs and

dbCNEs. After pyrolysis, the electrode was allowed to cool down under Ar stream for at least additional 35 s to prevent burning away of carbon under atmospheric conditions.

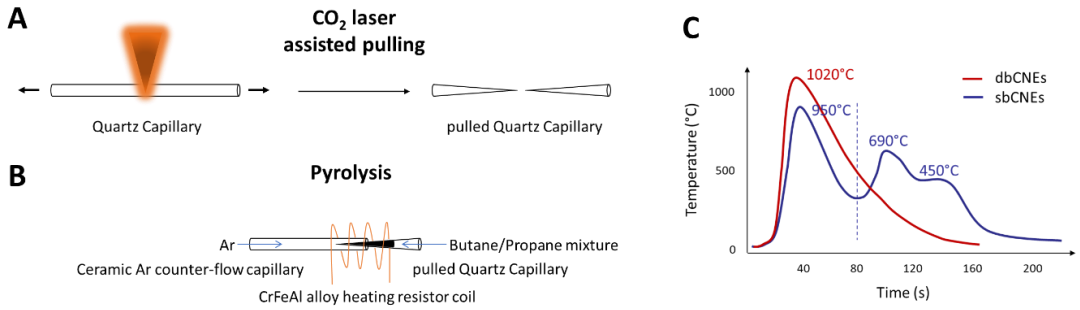

Figure 15. **Fabrication of single- and double-barrel CNEs.** Schemes of (**A**) the laser pulling and (**B**) the pyrolysis steps. (**C**) Optimized temperature profiles used during pyrolysis.

Following this, an additional step was necessary to obtain dbCNEs with controlled geometry and size consisting in focused ion beam (FIB) milling. The resulting sbCNEs and dbCNEs were electrochemically characterised by cyclic voltammetry ($0.1 < E < -0.4$ V; 0.025 V s^{-1}) with a redox probe and the apparent sizes in nm were approximated from the recorded steady state current in pA. One copper wire was inserted into each barrel to make a connection with the pyrolyzed carbon. Electrochemical characterisation was performed inside a Faraday cage using a VA-10 voltammetric amplifier (npi) in a two-electrode setup. An Ag/AgCl/3 M KCl electrode served as reference and counter electrode. The redox mediator solution was prepared using $[Ru(NH_3)_6]^{3+/2+}$ (Sigma Aldrich) with a concentration of 5 mM in 0.1 M KCl (J.T. Baker) aqueous solution. After this, the actual size and geometry of the electrodes were assessed by Scanning Electron Microscopy.

OECT fabrication with needle-like geometry. Electrodeposition of the polyelectrolyte complex PEDOT:PSS was carried out to coat the carbon nano tips with the electroactive polymeric film. Electrochemical deposition was performed inside a Faraday cage using a Jaissle bipotentiostat in a three-electrode setup. An Ag/AgCl/3 M KCl electrode served as reference electrode and a Pt wire acted as the counter electrode. The polymerisation solution was prepared using 10 mM EDOT monomer and 0.1 mM PSS as counter ion in distilled water and, before starting the deposition, the solution was kept under magnetic stirring and deareated under Ar flow for 20'. When a sbCNE was employed as working electrode, one copper wire was inserted into the barrel to make a connection with the

pyrolyzed carbon; otherwise, when a dbCNE was employed as working electrode, two copper wires shorted together were inserted into the barrels to make a connection with the pyrolyzed carbon and thus apply the potential to both barrels. 2 and 3 potential pulses at 1.2 V were applied for 200 ms with 500 ms intervals at 0 V for sbCNEs and dbCNEs, respectively. To assess the presence of the polymer film after deposition, the electrodes were imaged and characterised by SEM-EDX. Enhanced capacitive current in buffer solution and electrocatalytic properties towards redox active analytes (either AA or DA) due to the presence of the polymer layer were verified by CV for the nano gate electrodes. For the nanosized channels, the connection between Source and Drain was verified by recording the current flowing through the connecting channel upon application of a constant drain bias.

Characterization of needle-type OECTs. The OECT components were assembled as in Fig. 7A. I-V characteristics were recorded in 0.1 M phosphate buffer solution using a bipotentiostat to apply gate and drain potentials and record the generated currents. In a Faraday cage, the needle-type gate electrode was connected to the WE1 of the bipotentiostat, the drain was connected to WE2 and RE/CE were shorted to the Source electrode (grounded).

Dopamine sensing with needle-type OECTs. The same experimental setup described for the OECT characterization was employed to assess the OECT response to Dopamine (DA) in an electrochemical cell containing 5 mL buffer solution (0.1M PBS). A fixed potential was applied to the drain (-200 or -300 mV), while either a potentiodynamic wave ($0 < V_g < -600$ V) or a fixed potential (-900 mV) were applied to the gate electrode for the threshold voltage and the I_d/t measurements, respectively. To avoid contaminations, all solutions (buffer and analyte-containing buffer) were prepared with doubly distilled water and acid-cleaned glassware was used. A soft nitrogen flux was used to gently mix the solution after each DA addition.

5. Conclusion

Organic Electrochemical Transistors (OECTs) have been proposed as chemical sensors thanks to their remarkable features such as signal amplification, very low operating

potentials and adsorbed power. In this Chapter, Dopamine (DA) detection is performed using all-PEDOT:PSS devices, where the absence of metal contacts significantly reduces cost ad time of fabrication and leads to superior versatility of the device configuration.

Nevertheless, the lack of selectivity hinders a widespread use in real-life applications, due to the fact that all the oxidizable molecules can be detected at the all-polymeric OECT. Potentiodynamic techniques are commonly employed to separate the redox waves associated to different analytes for common 3-electrode electrochemical sensors based on an amperometric transduction, but this approach had not yet been explored for OECT sensing. Here, a new approach to selectively identify and determine the contributions of different analytes to the OECT electrical output signal through a linear scan of the gate potential is described. By CV and DPV characterizations in a 3-electrode cell set-up, a deeper insight into the electrochemical processes that occur at the polymer gate electrode was achieved, showing that: i) the oxidation of different analytes occurs at different potentials and ii) the scan rate affects the separation between the redox waves by influencing the kinetics of charge transfer reactions. It was demonstrated how OECTs can profit from PEDOT:PSS electrochemical features by selectively detecting the electro-oxidation of three different analytes (ascorbic acid, uric acid and dopamine) present in the same solution, as they occur at different gate potentials. The signal related to each one of the three different analytes can be individually detected and resolved by recording the trans-conductance, obtaining a linear response for all the analytes. The all-PEDOT:PSS OECT sensor can thus separate the redox waves associated to each compound and the scan rate is the key parameter to obtain both selectivity and a good resolution. The results reported here also demonstrate that all-PEDOT:PSS OECTs sensitivities and limits of detection are comparable or even higher than the ones achievable by DPV. In particular, the limits of detection are comparable to those obtained by DPV, a technique that employs a sophisticate potential wave and read-out system in order to maximize the performance of electrochemical sensors and that can hardly be considered a viable readout method in practical applications. The validity of the proposed approach has been assessed by using all-PEDOT:PSS OECTs as sensors for dopamine in presence of ascorbic acid and uric acid. The resulting interference of both compounds was very low, even if the concentrations of the interfering agents were noticeably higher than the dopamine's one. A limit of detection of 6 μM was reached, which is still higher than the value desirable for DA detection in biological samples, but the results described here open new perspectives on a simple tool

that greatly improves the performance of all-PEDOT:PSS OECTs, by demonstrating the proof-of-principle of their selectivity and, thus, the possibility to employ them as bioanalytical sensors in real-life applications.

From a different perspective, the concept of the all-PEDOT:PSS OECT sensor was coupled to a significant downscaling of the device geometry. Not only sub-micrometric sizes were explored, but also the conventional chip-like architecture was revolutionized to fabricate a needle-type OECT with cell-compatible dimensions, capable of spatially-resolved DA sensing. The geometry was optimized starting from single- and double-barrel quartz capillaries, which were laser pulled and filled with pyrolyzed carbon to yield single and double barrel nanoelectrodes. Therefore, PEDOT:PSS was electrodeposited at the nanometric tips to obtain polymeric spearhead gate electrodes and channels with sub-micrometric size. The fully assembled, needle-type OECT was then characterized by recording I-V curves. Despite the clear advantages resulting from such a novel OECT geometry, including the perspective of locally resolved, single-cell analyses, deeper studies are needed to correlate the transistor behavior and figure of merits with the state-of-the-art devices. However, sensing performances of the needle-type OECT were tested for DA detection in buffer solution. In this configuration, the all-PEDOT:PSS OECT sensor responds to DA in a wide concentration range covering 6 orders of magnitude (from 10^{-12} to 10^{-6} M), reaching a detection limit of 240 pM that is suited for *in vivo* applications. The selectivity issue has not been addressed yet, but a proof-of-principle that the needle-type OECT can be used for spatially resolved sensing purposes *in vivo* is given.

6. References

1. J.-M. Zen, A. S. Kumar, D.-T. Tsai. *Electroanal*. **2003**, *15*, 1073–1087.
2. S. A. Wring, J. P. Hart. *Analyst* **1992**, *117*, 1215–1229.
3. N. F. Atta, A. Galal, F. M. Abu-Attia, S. M. Azab. *J. Electrochem. Soc.* **2010**, *157*, F116-F123.
4. A. Spooren, P. Rondou, K. Debowska, B. Lintermans, L. Vermeulen, B. Samyn, K. Skieterska, G. Debyser, B. Devreese, P. Vanhoenacker, U. Wojda, G. Haegeman, K. Van Craenenbroeck. *Cell. Signal.* **2010**, *22*, 600–609.

5. F. Shang, L. Zhou, K. A. Mahmoud, S. Hrapovic, Y. Liu, H. A. Moynihan, J. D. Glennon, J. H. Luong. *Anal. Chem.* **2009**, *81*, 4089–4098.
6. C. L. Sun, H.-H. Lee, J.-M. Yang, C.-C. Wu. *Biosens. Bioelectron.* **2011**, *26*, 3450-3455.
7. H. Teymourian, A. Salimi, S. Khezrian. *Biosens. Bioelectron.* **2013**, *49*,1-8.
8. Q. Lian, Z. He, Q. He, A. Luo, K. Yan, D. Zhang, X. Lu, X. Zhou. *Anal. Chim. Acta* **2014**, *823*, 32-39.
9. C. Zanardi, F. Terzi, R. Seeber. *Anal. Bioanal. Chem.* **2013**, *405*, 509–31.
10. H. Tang, P. Lin, H. L. W. Chan, F. Yan. *Biosens. Bioelectron*. **2011**, *26*, 4559- 4563.
11. C. Liao, M. Zhang, L. Niu, Z. Zheng, F. Yan. *J. Mater. Chem. B* **2014**, *2*, 191- 200.
12. I. Gualandi, M. Marzocchi, E. Scavetta, M. Calienni, A. Bonfiglio, B. Fraboni. *J. Mater. Chem. B* **2015**, *3*, 6753–6762.
13. I. Gualandi, D. Tonelli, F. Mariani, E. Scavetta, M. Marzocchi, B. Fraboni. *Sci. Rep.* **2016**, *6*, 35419.
14. M. J. Donahue, A. Williamson, X. Strakosas, J. T. Friedlein, R. R. McLeod, H. Gleskova, G. G. Malliaras. *Adv. Mater*. **2018**, *30*, 1705031.
15. Q. Thiburce, A. Giovannitti, I. McCulloch, A. J. Campbell. *Nano Lett*. **2019**, *19*, 1712-1718.
16. N. Nagarajan, C. F. Stevens. *Curr. Biol*. **2008**, *18*, R756-R758.
17. P. D'Angelo, S. L. Marasso, A. Verna, A. Ballesio, M. Parmeggiani, A. Sanginario, G. Tarabella, D. Demarchi, C. F. Pirri, M. Cocuzza, S. Iannotta. *Small* **2019**, *15*, 1902332.
18. J. Clausmeyer, W. Schuhmann. *Trends Anal. Chem*. **2016**, *79*, 46–59.
19. S. E. Anderson, H. H. Bau. *Nanotechnology* **2015**, *26*, 185101.
20. H. R. Rees, S. E. Anderson, E. Privman, H. H. Bau, B. J. Venton. *Anal. Chem*. **2015**, *87*, 3849–3855.
21. P. Wilde, T. Quast, H. B. Aiyappa, Y.-T. Chen, A. Botz, T. Tarnev, M. Marquitan, S. Feldhege, A. Lindner, C. Andronescu, W. Schuhmann. *Chem. Electro. Chem.* **2018**, *5*, 1–7.
22. M. Michalak, M. Kurel, J. Jedraszko, D. Toczydlowska, G. Wittstock, M. Opallo, W. Nogala. *Anal. Chem*. **2015**, *87*, 11641−11645.
23. R. Ren, Y. Zhang, B. P. Nadappuram, B. Akpinar, D. Klenerman, A. P. Ivanov, J. B. Edel, Y. Korchev. *Nat. Commun.* **2017**, *8*, 586.
24. L. Xue, P. Cadinu, B. P. Nadappuram, M. Kang, Y. Ma, Y. Korchev, A. P. Ivanov, J. B. Edel. *ACS Appl. Mater. Interfaces* **2018**, *10*, 38621−38629.
25. Y. Zhang, J. Clausmeyer, B. Babakinejad, A. Lopez Cordoba, T. Ali, A. Shevchuk, Y.

Takahashi, P. Novak, C. Edward, M. Lab, S. Gopal, C. Chiappini, U. Anand, L. Magnani, R. C. Coombes, J. Gorelik, T. Matsue, W. Schuhmann, D. Klenerman, E. V. Sviderskaya, Y. Korchev. *ACS Nano* **2016**, *10*, 3214-3221.

26. K. Tybrandt, S. B. Kollipara, M. Berggren. *Sens. Actuator B* **2014**, *195*, 651–656.
27. I. Gualandi, E. Scavetta, F. Mariani, D. Tonelli, M. Tessarolo, B. Fraboni. *El. Acta* **2018**, *268*, 476-483.
28. L. Torsi, M. Magliulo, K. Manoli, G. Palazzo. *Chem. Soc. Rev*. **2013**, *42*, 8612-8628.
29. Y. Swami, S. Rai. *Circuits Syst*. **2016**, *7*, 4248-4279.

IV. PEDOT:dye-based, flexible Organic Electrochemical Transistor for highly sensitive pH monitoring

Organic electrochemical transistors (OECTs) are bioelectronic devices able to bridge electronic and biological domains with especially high amplification and configurational versatility, thus standing out as promising platforms for healthcare applications and portable sensing technologies. In view of achieving selective sensing responses, a viable strategy is the design of functional materials. In this Chapter, the synthesis of two pH-sensitive composites of PEDOT doped with pH dyes (BTB and MO, i.e. Bromothymol Blue and Methyl Orange, respectively) was optimized, showing their ability to successfully convert the pH into an electrical signal. The PEDOT:BTB composite, exhibiting the best performance, was used as the gate electrode to develop an OECT sensor for pH monitoring that can reliably operate in a twofold transduction mode with super-Nernstian sensitivity. In analogy with the potentiodynamic approach discussed in Chapter III, when the OECT transconductance is employed as analytical signal, a sensitivity of 93 ± 8 mV pH unit^{-1} is achieved by successive sampling in aqueous electrolytes. When the detection is carried out by dynamically changing the pH of the same medium, the offset gate voltage of the OECT shifts by (1.1 ± 0.3) x 10^2 mV pH unit^{-1}. As a further step, the optimised configuration was realised on a PET substrate and the performance of the resulting flexible OECT was assessed in artificial sweat within a medically relevant pH range.

1. Background

pH is an essential parameter in almost any research or industrial scenario. Indeed, its monitoring and adjustment underlie thermodynamic and kinetic control of a wide variety of processes and as many domains, encompassing biology[1-3] and healthcare,[4] nutrition,[5] catalysis and biocatalysis,[6,7] as well as pharmaceutical chemistry,[8] food manufacturing and processing,[9,10] agronomy[11] and environmental science.[12] Despite the vital role played by pH, the glass electrode has remained the unchanged gold standard of pH sensing for more than a century,[13] thus confining technological monopoly and major advancements to potentiometric techniques.

Conventional ion-selective sensors for potentiometric determinations consist of a membrane-based ion-selective electrode and a reference electrode, both of which require an internal solution to ensure a stable and sensitive response and however need frequent recalibration. Today, the accurate determination of pH and its variation in emerging research fields, such as bioelectronics, poses several challenges to commercially available glass electrodes and microelectrodes. Indeed, highly innovative applications of pH sensing may implicate technological barriers like miniaturisation and targeted geometry, as well as require ultra-sensitivity, for instance to monitor local and narrow pH variations in a tumour microenvironment[3,14] or inflammatory phenomena directly in a cell culture. Furthermore, flexibility and adaptability of the sensing device to unconventional configurations are also desired, for example for portable and wearable applications. In particular, real-time, non-invasive pH monitoring of biofluids such as human sweat for accessing information from our body is currently attracting a great deal of interest[15,16] as its relationship with key physiological conditions, such as dehydration or alkalosis, has been reported.[17,18]

Several wearable sensing platforms have been presented to date and those comprising pH sensors are mostly based on colorimetric determination by means of pH indicators,[19,20] as well as potentiometric transduction through electropolymerised polyaniline (PANi).[21] However, a major limitation of optical systems relies in the fact that a complex readout apparatus is often required, thus hindering their miniaturisation and manageability for non-expert users. On the other hand, the sensitivity of potentiometric systems is mostly limited to the ideal Nernstian sensitivity of 59 mV pH unit^{-1} and they need a reference electrode. Nakata et al. recently proposed an Al_2O_3 ion selective membrane for their flexible and referenceless Ion Sensitive Field Effect Transistor (ISFET) sensor for sweat pH, however

the Nernstian limit was not overcome.[22] To this regard, an Organic Charge-Modulated Field-Effect Transistor (OCMFET) was developed by Spanu et al. showing tunable super-Nernstian sensitivity by increasing the sensing area, made of a plasma-activated layer of Parylene C.[23] Despite the intriguing performance, the linear response of the OCMFET pH sensor is limited to the 6-8 pH range and relatively high applied voltages are required to operate the device.

In this scenario, OECTs show favourable features to address the aforementioned limitations and, due to their biocompatible constituents,[24,25] these devices have already entered successfully the biomedical arena with a wide spectra of both in vitro and in vivo bio-applications, ranging from metabolite sensing,[26-28] ion sensing[29] and neurophysiology.[30] As already discussed, when an OECT is used as a sensor, V_g can be exploited to drive the electrochemical potentials of the OECT elements and allow the detection of redox-active compounds. Therefore, the electrochemical reaction involving the analyte alters the doping-dedoping processes that modulates the current flowing through the channel, thus providing the intrinsic transistor amplification.[31] Consequently, these devices can achieve very high sensitivities even for trace amounts of analytes. Additionally, OECTs exhibit intriguing features for portable applications, due to the simple readout electronics required, the low supply voltage and subsequently low power consumption (usually applied voltages < 1 V and power supply < 100 μW). Also, OECT configuration does not require freestanding reference electrodes used in conventional electrochemical setups and offers design freedom in terms of device geometries and substrate. In addition to their ease of integration, OECTs can be miniaturized and fabricated with low-cost materials and large-scale production technologies. In particular, when realized using all-polymeric constituents, no metal electrodes hinder the device adaptability to textiles or flexible platforms.[26,27]

To date, few examples of pH responsive OECTs have been reported in literature. Among them, Choi et al.[32] synthesised a Carbon Nanotubes-Nafion composite that works as the pH sensing element in an OECT, where, however, the need of an external Ag/AgCl gate electrode stand out as the main physical barrier. More recently, Malliaras and co-workers[33] fabricated a OECT modified Wheatstone bridge on a flexible polyethylene naphtalate substrate for pH sensing. Two active gate materials were tested by the authors, i.e. Iridium Oxide (IrOx) and PANi, the first exhibiting super-Nernstian sensitivity. Although the

choice of this circuit obviates the need of a reference electrode, a time-stable reference solution is still essential to allow the differential measurement of the sample pH.

The work presented in this Chapter focuses on the design of new PEDOT based materials that can be exploited as the active elements in chemical sensing, with the final aim of developing wearable or/and portable devices, which could be embedded in real-life objects such as patches or textiles.[34] In this study, a flexible OECT pH sensor was realized having simple and robust geometry, super-Nernstian sensitivity and operational versatility, targeting bioelectronic and wearable applications. To transduce the pH signal, PEDOT:dye composites were synthesised using Bromothymol Blue (BTB) and Methyl Orange (MO) pH dyes as PEDOT counterions. Electrosynthesis of PEDOT doped with BTB was first reported by Balamurugan et al. and the electrochemical sensor modified with the resulting material, namely PEDOT:BTB, showed Nernstian sensitivity to pH (60mV pH $unit^{-1}$ reported).[35] Following this approach, the phenomenon that originates pH sensitivity in such materials is ascribed to the change of the dyes' electronic charge with pH. Since these small molecules act as dopants of the conducting polymer, this will consequently influence PEDOT features. PEDOT:BTB was first synthesised on different substrates with optimised procedures focused on material characterisation in comparison with standard PEDOT films and PEDOT:MO composite. The pH-sensing mechanism was thoroughly studied by different analytical techniques to assess the origin of the pH sensitivity. After that, the material ensuring the best performance, i.e. PEDOT:BTB, was chosen to functionalise the gate electrode of an OECT, that was able to operate in a twofold transduction mode and showed super-Nernstian sensitivity thanks to the amplification given by the transistor configuration. We assessed the device robustness and reversible response, finally exploring the possibility to fabricate the OECT pH sensor on a flexible substrate that is able to work in complex media, such as artificial sweat. The results reported in this Chapter are reproduced with permission from F. Mariani, I. Gualandi, M. Tessarolo, B. Fraboni, E. Scavetta: PEDOT: Dye-Based, Flexible Organic Electrochemical Transistor for Highly Sensitive pH Monitoring. ACS Appl. Mater. Interfaces, 2018, 10, 22474-22484. Copyright 2018 American Chemical Society.[36]

2. Optimisation of the pH sensitive material

2.1 Dyes optical characterisation and PEDOT:dye films electrosynthesis

Acid-base equilibria involving BTB and MO and correspondent UV-Vis spectra of the dyes dissolved in different pH buffers are shown in **Figure 1**A and B. Experimental pKa value equal to 7.1 ± 0.1 was found for BTB, whose acidic (yellow) and basic (blue) forms present maximum absorbance peaks at 435 and 616nm, respectively. Differently, a pKa of 3.34 ± 0.03 was calculated for MO, which undergoes deprotonation turning from red to yellow and giving rise to a shift in the maximum absorbance peak from 510 to 465nm.

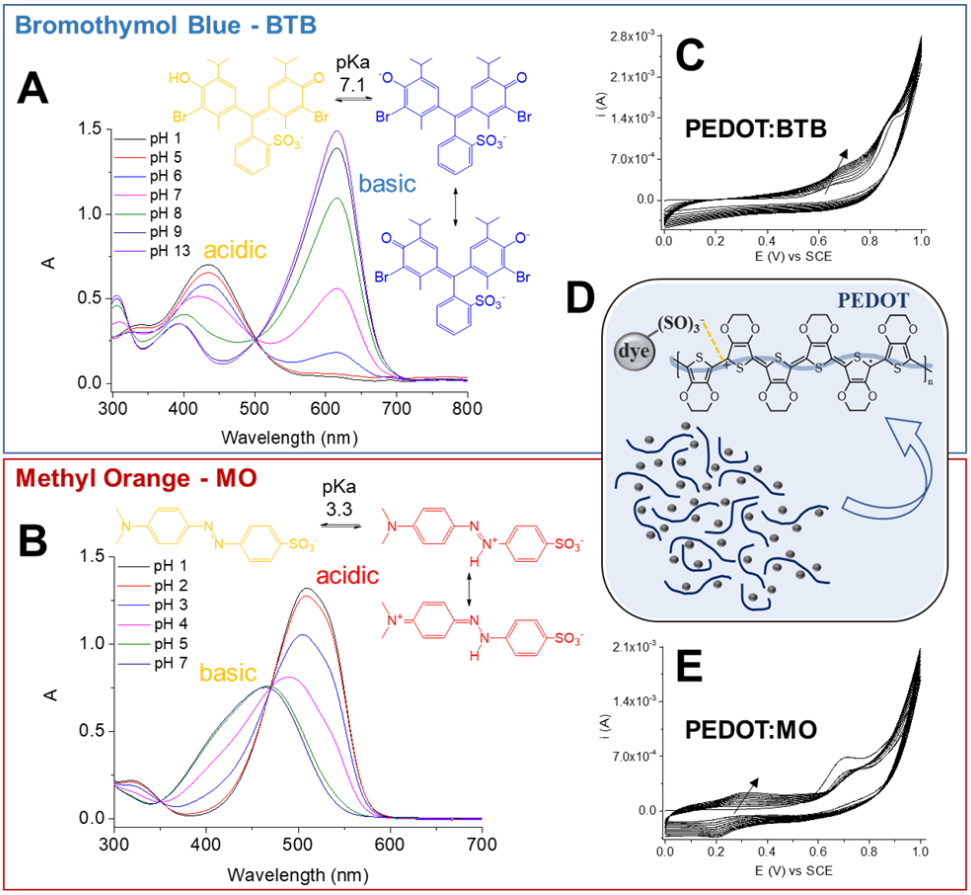

Figure 1. **Dyes optical characterisation and PEDOT:dye films electrosynthesis**. Absorption spectra of (**A**) 0.02 mM BTB and (**B**) 0.02 mM MO dissolved in different pH buffers and correspondent acid-base equilibrium. (**C**) and (**E**) Electrodeposition curves of PEDOT:BTB and PEDOT:MO, respectively, at a GCE. (**D**) Proposed interaction between the doping dye and the polymer.

Once assessed their optical properties, the two dyes were exploited to synthesise PEDOT:dye-based materials on Glassy Carbon Electrodes (GCEs) by potentiodynamically scanning the potential from 0 to 1V in aqueous solutions containing the precursors.

Deposition curves for PEDOT:BTB and PEDOT:MO are reported in Figures 1C and E, respectively. In the range 0 - 0.8 V, the recorded current is mainly due to the redox process involving the conductive polymer. Therefore, its increase after consecutive cycles is ascribed to the polymer growth at the electrode surface, demonstrating that both dyes can act as counterions for PEDOT. Indeed, in the experimental condition of choice, the film forming process is driven by the oxidative polymerisation of EDOT, which is in turn allowed and assisted by the electrostatic interaction established between the available negatively charged sulfonate group of the dyes and the growing polycationic chains of PEDOT, as depicted in Figure 1D.

2.2 Effect of the Dye Counterions

Proof of dyes intercalation within the polymer matrix was given by FTIR-ATR spectroscopy (**Figure 2**). Looking at the fingerprint region (zoom from 2000 to 500 cm^{-1}) of BTB, the bands at 1190 and 1051 cm^{-1} are attributed to the stretching of the sulfonate group[37] and corresponding signals at 1183 and 1047 cm^{-1} are found in PEDOT-BTB. As regards MO, characteristic bands at 1598 and 1519 ascribed to the benzene ring and the signal at 1360 cm^{-1} (azo bond)[38] are located at 1600, 1520 and 1363 cm^{-1}, respectively, in the spectrum of PEDOT-MO.

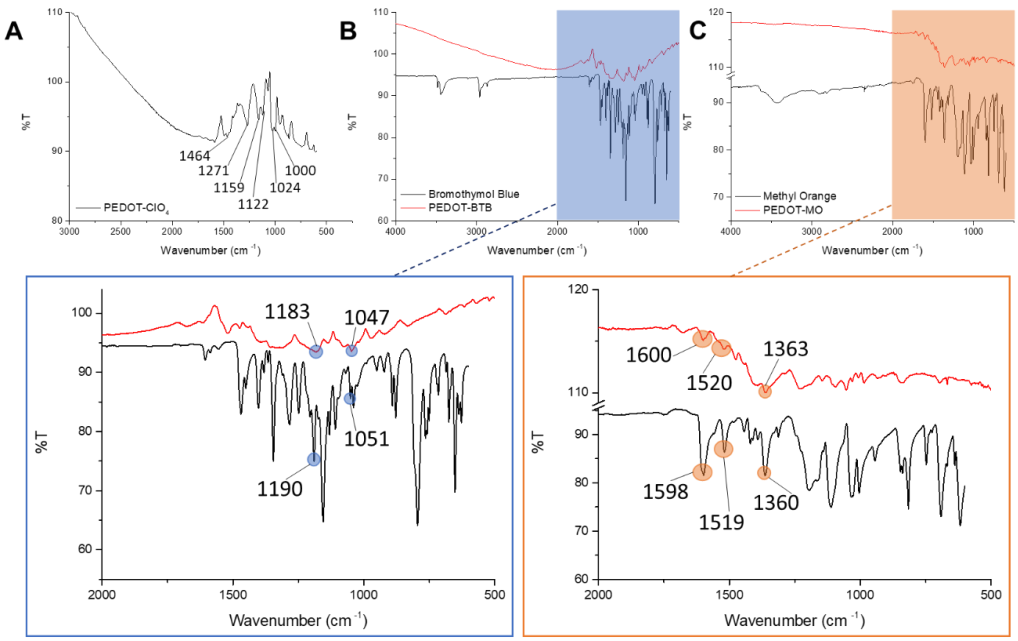

Figure 2. **FTIR-ATR Spectra** of (**A**) PEDOT:ClO4, (**B**) BTB powder (black line) and PEDOT:BTB (red line), (**C**) MO powder (black line) and PEDOT:MO (red line). All polymeric films are deposited on graphite sheets. Fingerprint regions in (B) and (C) are highlighted by the rectangular shadows and zoomed.

Considering that none of these diagnostic bands is present in the spectrum of the reference PEDOT-ClO_4, it can be concluded that the new spectroscopic features found for the composite films are originated by the functionalities belonging to the embedded dye.

Furthermore, UV-Vis spectroelectrochemistry was carried out in pH buffers below and above the dyes' pKa values, while changing the redox state of PEDOT:BTB and PEDOT:MO films electrodeposited on ITO glass (**Figure 3**). In this case, optoelectronic features of the newly synthesised materials clearly result from the convolution of the two interacting components, i.e. the conducting polymer and the dye. Consequently, the absorbance spectra are pH-dependent, as they change with the dye turning acidic or basic.

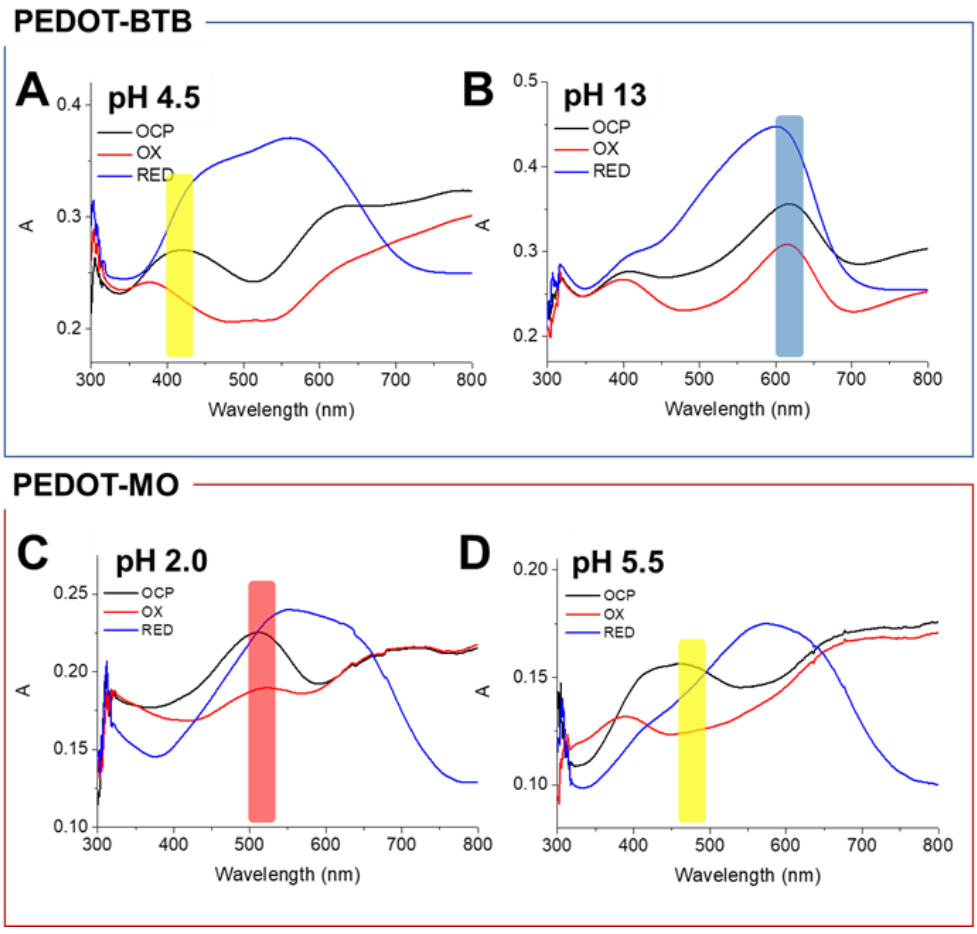

Figure 3. Absorption spectra of PEDOT:BTB (**A**, **B**) and PEDOT:MO (**C**, **D**) films on ITO at their Open Circuit Potential, after Oxidation and Reduction in pH buffers below and above each dye pKa. Rectangular shadows represent the region of main absorption of the dye alone in each pH buffer.

Such pH-dependency was further investigated in comparison with reference PEDOT:PSS and PEDOT:ClO_4 films electrochemically deposited on GCEs. Cyclic voltammograms of the four polymer coated electrodes were acquired by scanning the applied potential from -1.5 to +0.6 V in two aqueous pH buffers, i.e. below and above the dyes' pKa values, and are reported in **Figure 4**A.

Looking at the curves, it clearly stands out that a capacitive shape is dominating in the case of PEDOT:PSS and PEDOT:ClO_4 films, while evident faradaic features, highlighted by the presence of one or more well defined peaks, compete with the capacitive behaviour in PEDOT:BTB and PEDOT:MO coated electrodes. Secondly, the newly-synthesised PEDOT:dye materials exhibit considerable pH-induced changes in their electrochemical response.

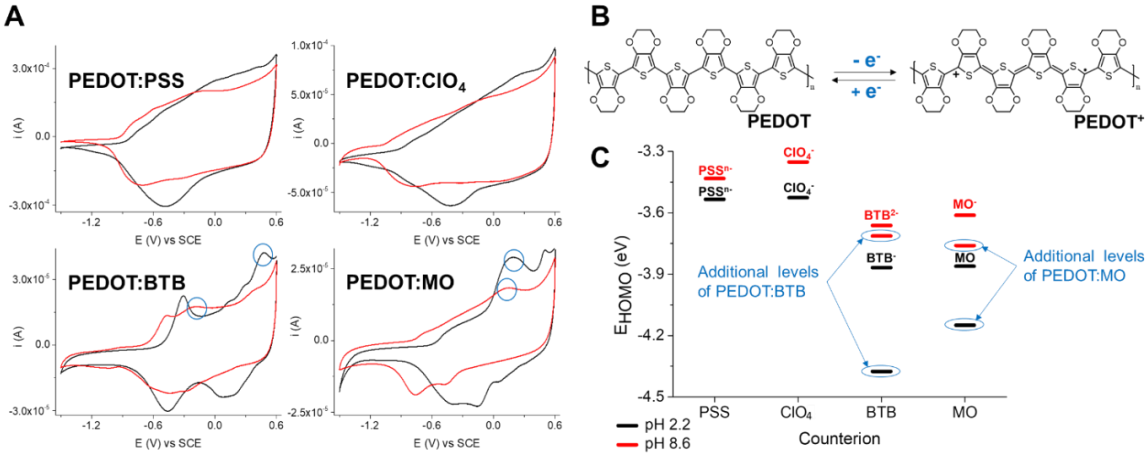

Figure 4. Electrochemical analysis and HOMO levels determination. (**A**) Cyclic voltammograms obtained at 50mV s^{-1} in buffers at pH 2.2 (black) and 8.6 (red) for the four films deposited on GCEs. (**B**) Redox equilibrium involved in polaron formation. (**C**) Energy diagram of the HOMO levels calculated from the CV of each film at the two pH values.

Since BTB electropolymerisation in the anodic region has been reported in literature[35,39] a detailed study of BTB behaviour was carried out to shed light on possible redox processes. No faradaic processes are observed at the bare Pt electrode cycled in the BTB containing solution (**Figure 5**A), indicating that the dye does not undergo redox reactions upon scanning the applied potential in the range of interest. Differently, a reversible intercalation of the dye occurs when cycling the polymeric film in the presence and then in the absence of BTB. This phenomenon is observable in Figure 5B and C, where a growing peak appears when the PEDOT:PSS film is exposed to the BTB-containing buffer (black curve) and subsequently disappears (red curve) when cycling the same film in the BTB-free buffer.

Therefore, data suggests that BTB can act as mobile counterion for PEDOT:PSS, probably promoted by a purely electrostatic incorporation within the residual polycationic segments unbalanced by PSS^-. Contrarily, this phenomenon becomes irreversible when an electrodeposition is carried out including BTB in the polymerisation solution as the only doping agent available for the growing $PEDOT^+$ chains. In conclusion, no redox processes are known to involve MO and BTB in the applied potential range.

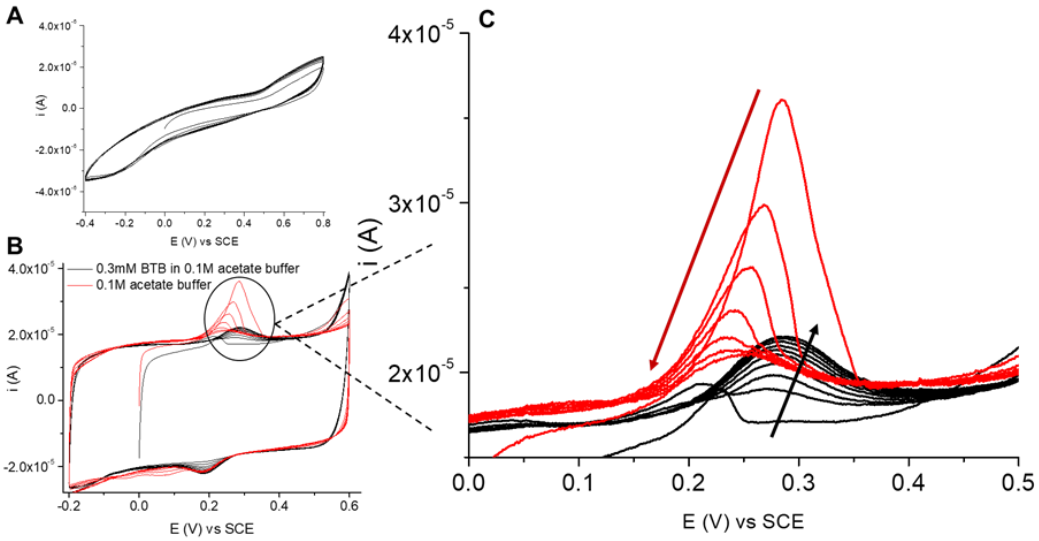

Figure 5. (**A**) CV of 0.3 mM BTB in 0.1M acetate buffer recorded at a Pt electrode. SR 10mV s^{-1}. (**B**) CV of 0.3 mM BTB in 0.1M acetate buffer recorded at a PEDOT:PSS coated glass slide (black line). The same electrode was then cycled in the absence of BTB (red line). SR 10mV s^{-1}. (**C**) Zoom of the region circled in (B).

In situ rearrangements of PEDOT electronic bands can also give rise to faradaic features. Indeed, it is well-known that PEDOT has three fundamental redox states,[40] i.e. neutral, polaronic and bipolaronic forms, the last two originating from electrons extraction/holes injection into the Highest Occupied Molecular Orbital (HOMO) of PEDOT. Polaron and bipolaron formation induces a local relaxation of the polymer lattice and creating new electronic states within the Energy Gap, due to local upward or downward shifts of the HOMO and LUMO (Lowest Unoccupied Molecular Orbital) levels, respectively.[41,42] The energy of frontier orbital levels can be estimated from electrochemical analysis (Cyclic Voltammetry (CV)). HOMO levels of PEDOT:BTB and PEDOT:MO were here determined from the voltammograms in figure 4A and compared with reference PEDOT:PSS and PEDOT:ClO_4 films. Following CVs recording in aqueous environment,

the HOMO energy level, E_{HOMO}, was calculated from the onset oxidation potential, E_{OX}^{onset}, ascribed to the formation of $PEDOT^+$ (Fig. 4B) for each film vs SCE[43-46] and the resulting energetic diagram is reported in figure 4C. As expected, HOMO levels of PEDOT:PSS and PEDOT:ClO_4 do not change significantly upon pH buffer variation. Differently, PEDOT:BTB and PEDOT:MO display additional HOMO-1 levels, i.e. -4.4 eV and -4.1 eV at pH 2.2 for PEDOT:BTB and PEDOT:MO, respectively, -3.7 eV and -3.8 eV at pH 8.6 for PEDOT:BTB and PEDOT:MO, respectively. Indeed, the dyes are deprotonated at a different extent upon pH variation and consequently interact in a pH-susceptible fashion with PEDOT. Looking at the data, at pH 8.6 (red lines) both dyes are deprotonated at their maximum extent, that is BTB^{2-} and MO^-, consequently making electron extraction easier. On the other hand, when the pH is below both pKa values (i.e. 2.2, black lines), BTB^- is monoanionic while MO has zero net charge, thus providing an energetic barrier to further oxidise PEDOT. However, since the couple of HOMO-1 levels shows a variation of 0.7 eV in PEDOT:BTB and 0.3 eV in PEDOT:MO depending on the electrolyte pH, it can be hypothesised that BTB shows the strongest interaction with PEDOT.

Summarising, if PEDOT is doped with BTB or MO, i.e. counterions involved in weak acid-base equilibria, electrochemical and spectroscopic characterisations highlight the presence of a new HOMO-1 level. Unlike the capacitive band that is usually observable in PEDOT:PSS or PEDOT:ClO_4, the energy of the HOMO-1 level is strongly affected by the pH of the electrolyte solution and this feature consequently gives rise to a higher pH sensitivity when the conductive polymer is exploited as sensing material.

2.3 Electrochemical performance of the pH-sensitive materials

In order to study the materials response to pH, a narrower potential window was chosen so as to focus on the pH-dependent faradaic peaks encircled in Fig. 4 and ascribed to the HOMO-1 levels of PEDOT:BTB and PEDOT:MO. **Figure 6** shows the voltammograms recorded at 10 mV s^{-1} for the PEDOT:dye films in aqueous pH buffers at the same ionic strength. In both cases, a couple of reversible peaks arises, with Peak Potentials (E_p) shifting towards less anodic values by increasing the pH of the electrolyte solution, accordingly to what already mentioned by Balamurugan et al. for PEDOT:BTB.[35] Moreover, it is evident that well-defined peaks are obtained in a wide pH range in the case

of PEDOT:BTB, while PEDOT:MO displays broadened waves that are only detectable in the pH range 1-3.

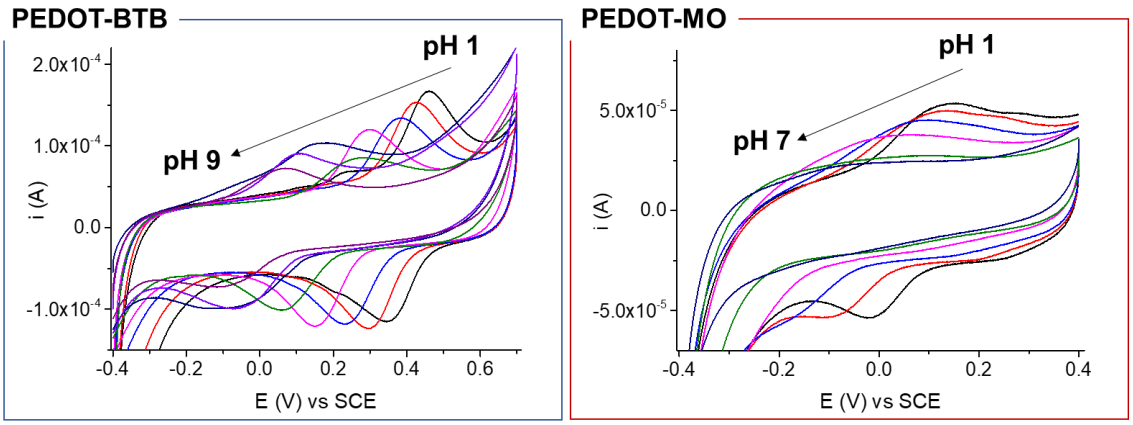

Figure 6. **pH response of the newly-synthesised materials**. CV of PEDOT:BTB and PEDOT:MO films on GCEs recorded at 10 mV s^{-1} in different pH buffers.

The electrochemical features of the pH-sensitive films were compared by taking the forward or the backward segment of the last cycle. For each segment, E_p was plotted vs the pH of the electrolyte solution, thus obtaining a calibration curve. Both PEDOT:dye materials exhibited a linear response to pH changes. In particular, PEDOT:BTB shows a forward sensitivity equal to 48 ± 2 mV pH $unit^{-1}$ (mean value ± standard deviation) in the pH range 1-7, and a backward sensitivity of 62 ± 2 mV pH $unit^{-1}$ in the pH range 1-9, thus underlying a monoelectronic process. Differently, the forward sensitivity of PEDOT:MO was equal to 31 ± 2 mV pH $unit^{-1}$ from pH 1 to 4.5, suggesting that 2 electrons are exchanged. For PEDOT:MO it was not possible to calculate the backward sensitivity. Further spectroelectrochemical measurements were useful to confirm that the different sensitivities originate from a different number of exchanged electrons (**Figure 7**). When biased at +0.8 V, neutral PEDOT is oxidised forming radicalcations, whose excited states display a characteristic absorption band in the NIR region.[40] Figure 7 shows the spectra recorded for oxidised PEDOT:BTB and PEDOT:MO films on ITO in two pH buffers below and above the dyes' pKa. For PEDOT:MO having the dye turning from acidic to basic form, no shift in the absorption band's maximum position is observable (λ = 1.8 eV). Differently, a 0.2 eV shift, from λ = 1.7eV at pH 8 up to 1.9 eV at pH 2, is observable for PEDOT:BTB. Therefore, only BTB actively interacts with the radicalcationic form of PEDOT, while MO seems not to take part into the redox equilibrium involving neutral PEDOT and $PEDOT^+$. Consequently, it could be argued that the acid-base equilibrium of

BTB and the redox reaction responsible for polarons formation in PEDOT mutually take place and affect each other in the final material, where an overall $1e^-$ to $1H^+$ mechanism occurs and explain the Nernstian behaviour pointed out by CV. On the other hand, the $2e^-$ Nernstian response found for PEDOT:MO is thought to come from a preferential interaction of MO with the diradicalcationic form of the polymer. If so, MO might stabilise the formation of bipolarons, thus explaining the $2e^-/1H^+$ behaviour found electrochemically.

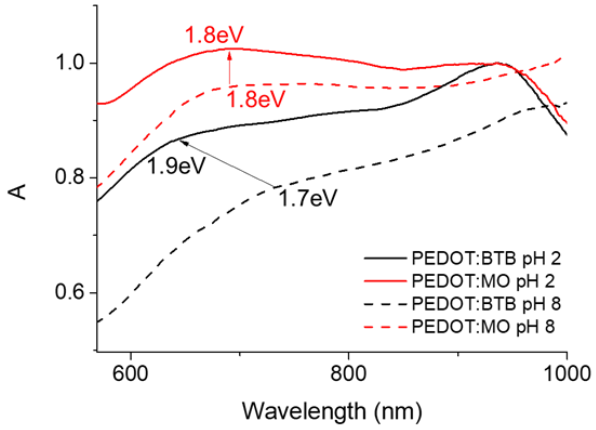

Figure 7. Vis-NIR spectra of PEDOT:BTB (black lines) and PEDOT:MO (red lines) films deposited on ITO glass after oxidation at +0.8 V vs SCE for 60 s. The spectra were recorded in electrolyte solutions at pH values below (solid lines) or above (dotted lines) the dyes' pKa.

3. OECT pH sensing

Since both PEDOT:dye materials can convert a chemical signal such as pH into an electrical one, they were integrated as sensitive elements in an OECT in order to implement a device with higher performances. A planar configuration was adopted in which the gate electrode is located inside an U-patterned channel, as described in previous publications regarding all-PEDOT:PSS OECT sensors.[26,27,31] However, electrochemical transducers are usually integrated in an OECT by means of gate functionalisation and, for this reason, a gold gate electrode was here employed to allow the straightforward electrodeposition of our pH-sensitive polymers. Additionally, gold source and drain electrodes served to improve current stability through the spin-coated PEDOT:PSS channel (see **Figure 8**A).

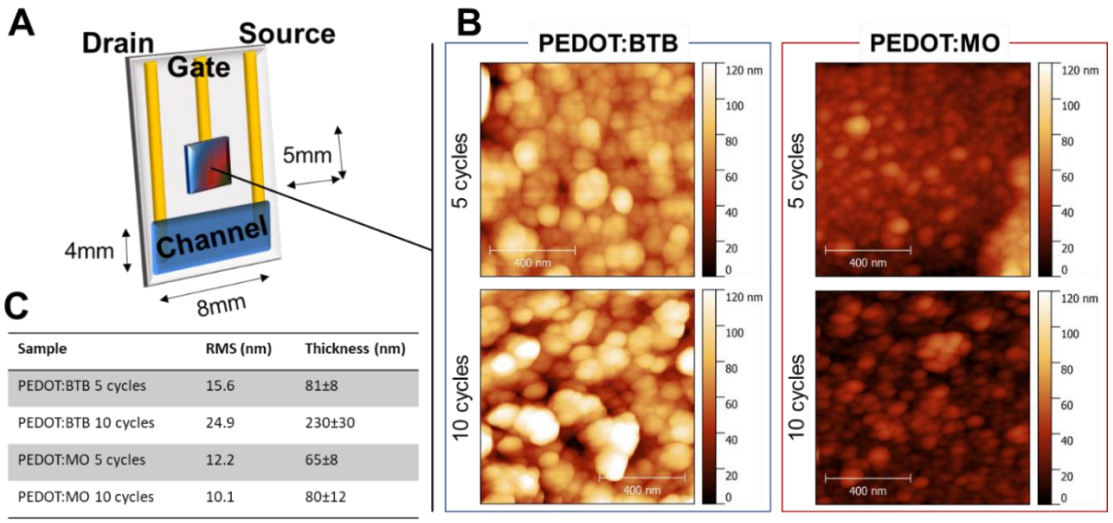

C

Sample	RMS (nm)	Thickness (nm)
PEDOT:BTB 5 cycles	15.6	81±8
PEDOT:BTB 10 cycles	24.9	230±30
PEDOT:MO 5 cycles	12.2	65±8
PEDOT:MO 10 cycles	10.1	80±12

Figure 8. OECT Geometry and Gate Morphology. (**A**) Cartoon of the resulting device after Gate functionalisation with the pH sensitive materials. Drain, Source and Gate gold contacts were opportunely insulated with PDMS to define the active areas. (**B**) 1x1 μm^2 topography maps obtained by AFM imaging for Gate electrodes modified with 5 or 10 deposition cycles PEDOT:BTB (left) and PEDOT:MO (right) films. (**C**) Corresponding Root Mean Square roughness and Thickness values.

3.1 Gate Functionalisation and Morphology

The gate electrode of the OECT was coated by PEDOT:BTB or PEDOT:MO films by potentiodynamic electrodeposition, by scanning the applied potential from 0 to 1V for 5 or 10 deposition cycles. Geometry and size of the resulting device are reported in Figure 8A. AFM imaging was used to investigate morphology and surface roughness of the functionalised gate electrodes. Figure 8B and C show topography maps of the samples and corresponding Root Mean Square (RMS) roughness and thickness values, respectively. The two composite films show similar morphological features with the presence of discrete particles and comparable roughness values, while film thickness clearly increases with the number of deposition cycles. Such structure with well-defined globular grains is generally observed for electrodeposited PEDOT, while films prepared from commercial suspensions exhibit a flatter surface.[24] In particular, PEDOT:BTB exhibits larger and more uniformly distributed domains with respect to PEDOT:MO.

Due to the broader operation pH range and the higher sensitivity shown by CV analyses, PEDOT:BTB was the material of choice for the Gate electrode of the OECT pH sensor that we have assessed. We have investigated two operation modes, i.e. potentiodynamic and potentiostatic, demonstrating that our OECT sensor can operate with a twofold transduction process, showing super-Nernstian sensitivity to pH and robustness.

3.2 Potentiodynamic operation of the OECT sensor

The potentiodynamic approach to operate an all-PEDOT:PSS OECT has been discussed for Dopamine detection in Chapter III.[27] For this work, it is schematically illustrated in **Figure 9**A. I_g-V_g curves and Transfer characteristics (Figure 9B) were recorded while keeping the device dipped in different pH buffers. Looking at the I_g-V_g curves, a couple of well-defined and reversible peaks can be observed and follows the same trend found for E_p and pH value by CV (see Figure 6); indeed, here the peak potential V_g moves towards less anodic values by increasing the pH of the electrolyte solutions tested successively, i.e. from pH 1 to 9. At the same time, the current flowing through the negatively biased channel is modulated by the gate action, which is in turn sensitive to the pH of the contact solution. Moreover, the magnitude of modulation increases changing the electrolyte from acidic to basic and the transfer curves shift upward, showing inflection points that gradually move to less anodic V_g values.

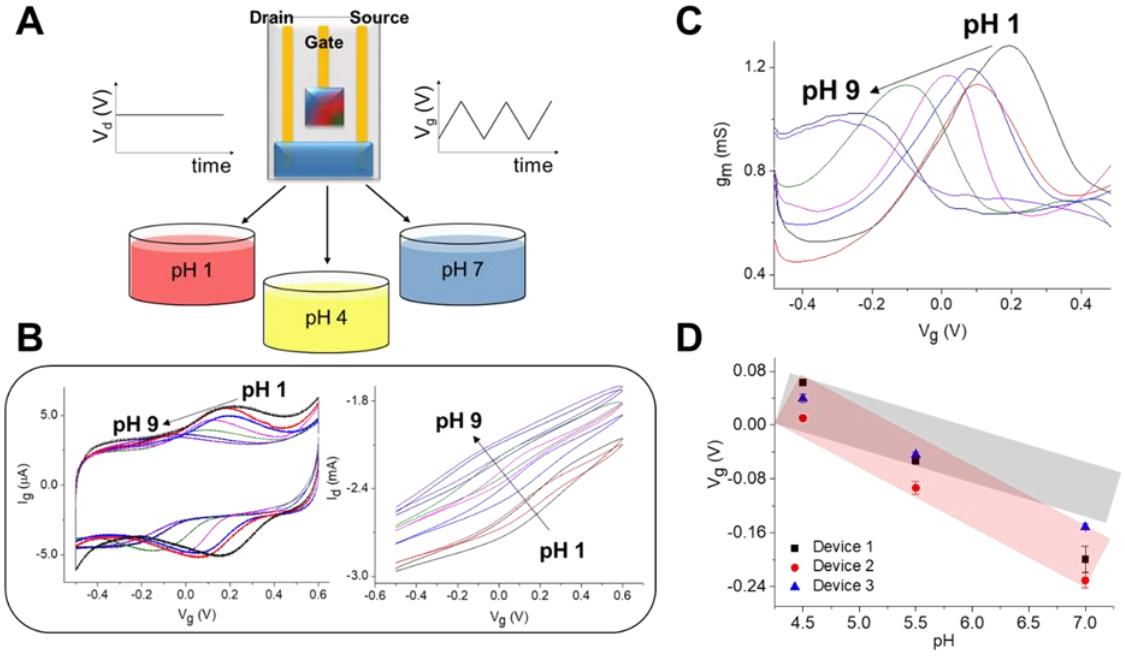

Figure 9. **Potentiodynamic OECT pH sensor**. (**A**) Scheme of the potentiodynamic approach. (**B**) I_g-V_g and Transfer curves in different pH buffers. V_g scanned from -0.5 to +0.6 V at 10 mV s^{-1}; V_d = -0.3 V. (**C**) Transconductance calculated from the backward scan of the transfer curves in (B) versus V_g. (**D**) Transconductance peak potential versus pH for 3 devices tested 3 times. Error bars indicate the standard deviation. The dark shadow represents the Nernstian slope -59 mV pH $unit^{-1}$ for comparison.

Figure 9C reports the plot of the OECT transconductance versus V_g. To extract g_m, we chose the backward scan of each V_g cycle because it shows a better peak to peak resolution and repeatability than the forward one (see **Figure 10**).

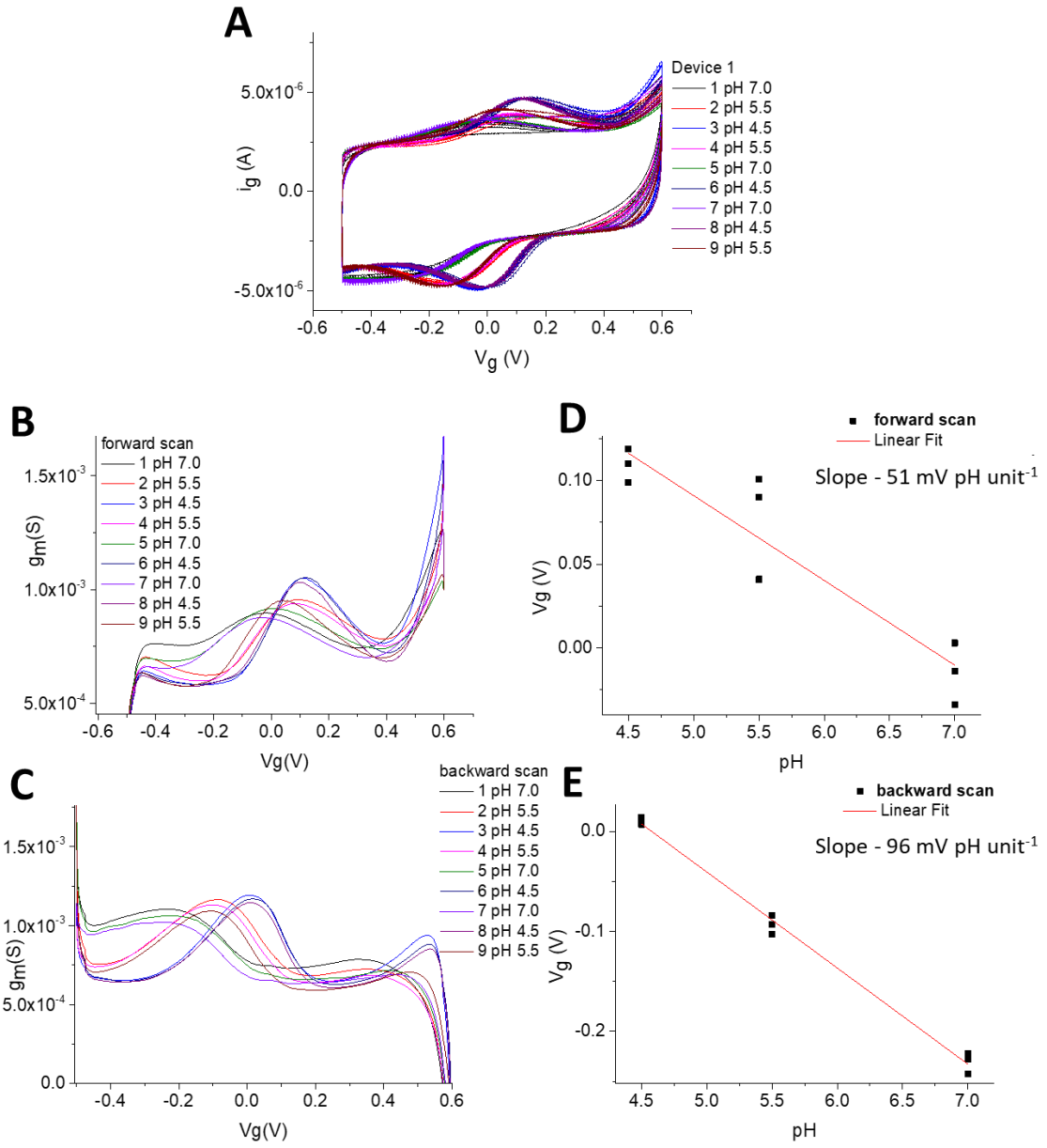

Figure 10. **Repeatability of the OECT pH sensor using the potentiodynamic approach**. Independent potentiodynamic measurements were carried out with the same device tested randomly in buffers at pH 7.0, 5.5 and 4.5, three times per each. SR 10 mV s^{-1}; V_d = -0.3 V. (**A**) I_g vs V_g curves recorded during the experiments. (**B**, **C**) Transconductance plots obtained using the forward and the backward scan of the transfer characteristics and (**D**, **E**) correspondent calibration curves.

Transconductance is commonly accepted as OECTs' figure of merit and represents the device amplification. Here, also g_m displays a trend where the maximum shifts towards more cathodic V_g values while increasing the electrolyte pH. The g_m maximum peak potential was chosen as analytical signal, showing a linear response to pH in the range 1 – 9. A sensitivity equal to 93 ± 8 mV pH unit^{-1} was calculated for 3 different OECT pH sensors, each of them randomly tested three times in buffers at pH 4.5, 5.5 and 7.0 (Figure 9D). The super-Nernstian sensitivity exhibited by these sensors can be graphically visualized by comparing the red shadow with the dark one, which represents the theoretical Nernstian slope of 59 mV pH unit^{-1}. In this case, the film thickness does not affect the sensor performance, as highlighted in **Figure 11**, in which we report the response of a device having a gate electrode coated by a thinner PEDOT:BTB layer (5 deposition cycles).

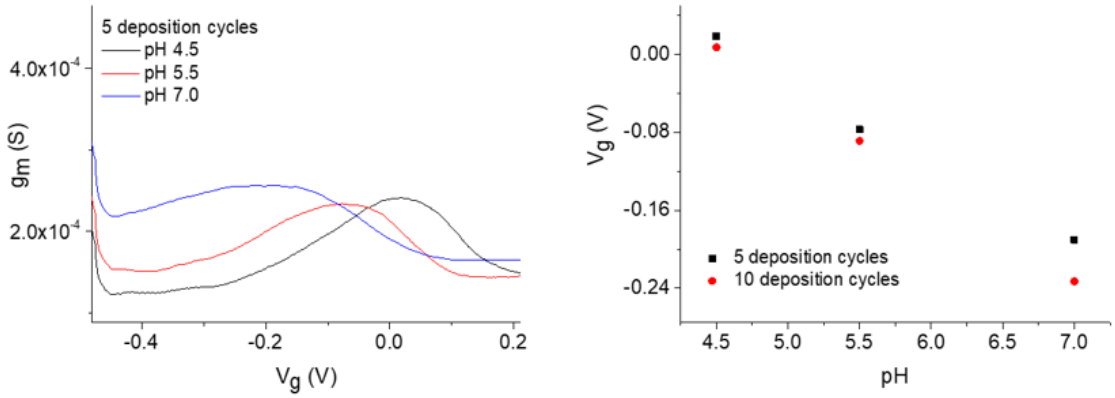

Figure 11. **Influence of the number of deposition cycles of PEDOT:BTB on device performances using the potentiodynamic approach**. Left: g_m vs V_g curves at different pH obtained with a OECT prepared by 5 deposition cycles of PEDOT:BTB on the gate electrode, instead of 10. Right: comparison between V_g vs pH responses of the sensors prepared using 5 or 10 deposition cycles.

3.3 Potentiostatic operation of the OECT sensor

Aiming to the detection of pH variations in real time, the OECT pH sensor was tested in potentiostatic mode while dynamically changing the pH of the electrolyte solution through 1M KOH additions (see scheme in **Figure 12**A).

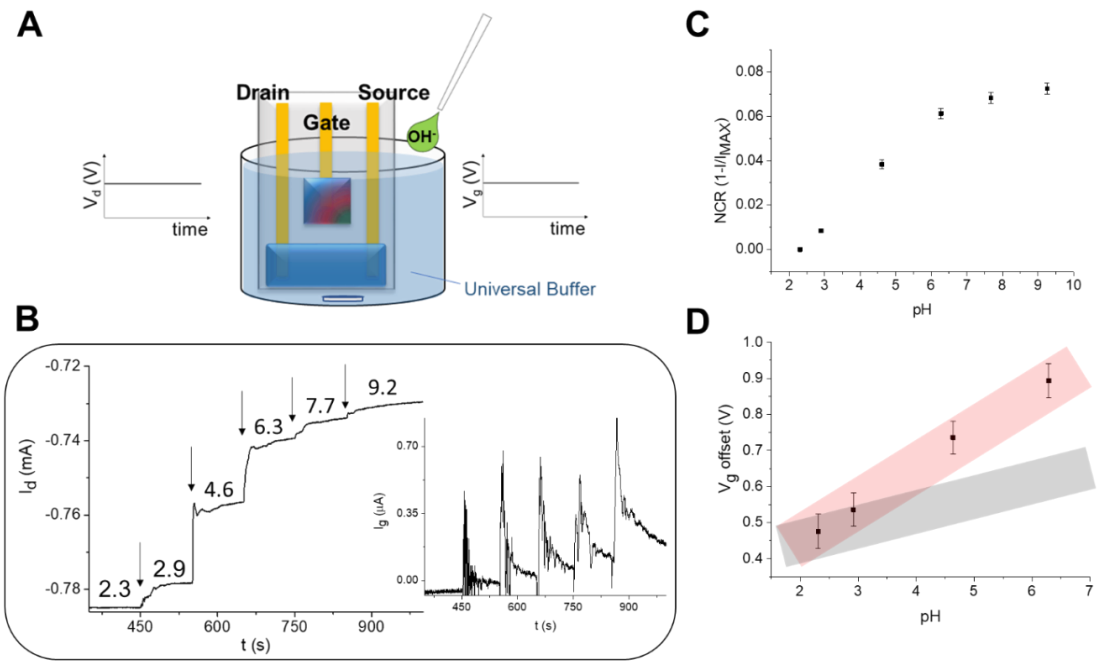

Figure 12. **Potentiostatic OECT pH sensor**. (**A**) Scheme of the potentiostatic approach. (**B**) I_d-t and I_g-t (inset) curves recorded for equimolar additions of KOH to universal buffer under stirring. V_d = -0.2 V, V_g = -0.1 V. (**C**) Normalised Current Response vs pH. (**D**) Offset gate potential of the transistor vs pH in the linearity range. The dark shadow represents the Nernstian slope -59 mV pH unit^{-1} for comparison.

In this approach, the transistor still operates in depletion mode and V_g is set at -0.1 V, i.e. the potential value that allows the most effective separation among the transfer characteristics recorded in different pH buffers. Drain and gate current vs time responses are reported in figure 12B and inset. Once a steady–state current is reached at both gate and drain, base additions in the buffer under stirring cause I_g to increase and, consequently, the expected modulation of the current flowing through the channel occurs. It is worth to note that I_g variations (figure 12B inset), which are 3 orders of magnitude smaller than that of I_d due to the OECT amplification, do not produce a usable signal as no steady-state current is recovered after pH changes. The normalized current response (NCR) of the same device employed in 4 independent measurements is plotted as a function of pH in figure 12C. A linear correlation is observed in the pH range 2-7, with a slope equal to (14.8 ± 0.5) × 10^{-3} pH unit^{-1}. This normalization facilitates comparison between different devices. However, in order to express the sensor performances in terms of potential, the offset gate potential, V_g^{offset}, was chosen as analytical signal. This parameter was first introduced by Bernards et al.[47] for OECT-based enzymatic sensors and has been discussed in Chapter I. It enters the expression of the effective gate potential, V_g^{eff}, whose variation has been studied in OECT sensors and biosensors for glucose,[48] dopamine[49] and ions.[29] Briefly,

while V_g^{eff} represents the gate voltage that is effectively acting on the transistor channel when charge-transfer reactions due to the presence of redox-active species alter the chemical potential equilibrium between the gate electrode and the electrolyte, the voltage shift is called V_g^{offset} and is linked to the electrochemical potential of the solution, which is in turn described by the Nernst equation.[47] For this reason, V_g^{offset} is linearly dependent on the logarithm of analyte concentration and can be used directly as analytical signal. V_g^{offset} vs pH was found to exhibit the same trend of NCR and figure 12D reports the response curve obtained from 3 OECT pH sensors in their linearity range (pH 2 to 7). The mean sensitivity was (1.1 ± 0.3) x 10^2 mV pH $unit^{-1}$, being super Nernstian and still comparable to that exhibited by the device operating in the potentiodynamic mode. Repeatability studies were carried out for four independent measurements using the same device and are reported in **Figure 13**.

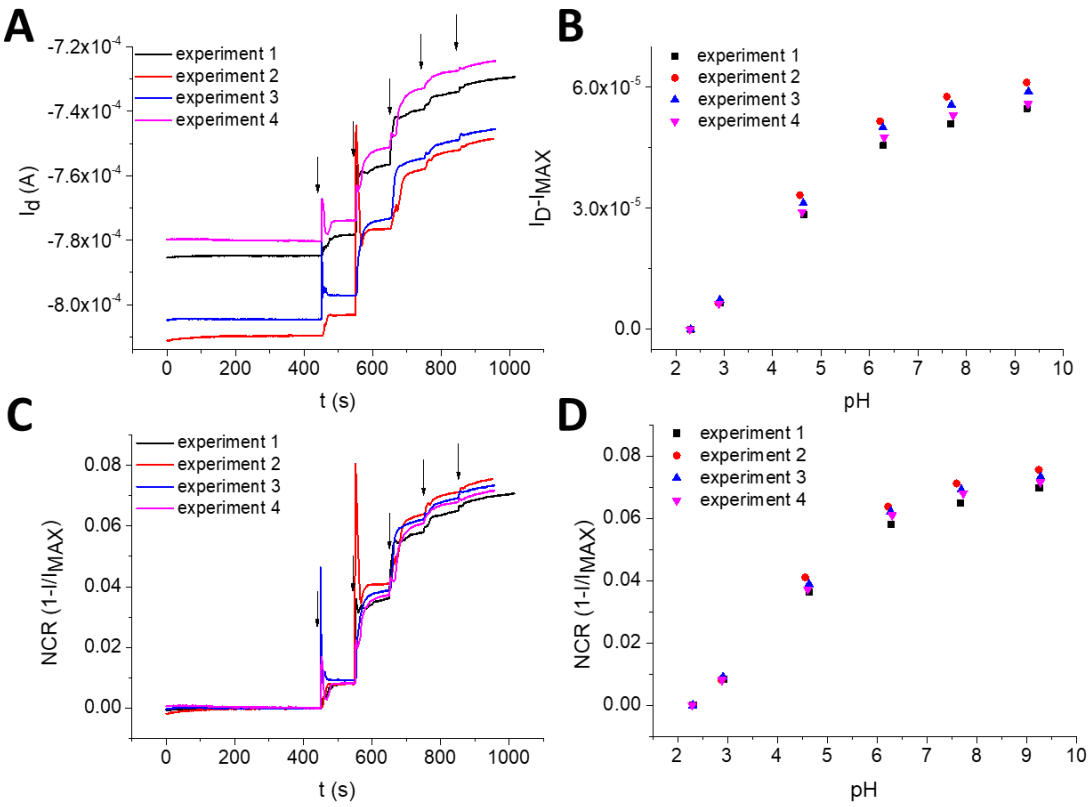

Figure 13. Repeatability of the OECT pH sensor using the potentiostatic approach. (**A**) Four independent measurements were carried out with the same device immersed in universal buffer under stirring during equimolar KOH additions. V_g = -0.1 V; V_d = -0.3 V. Corresponding plots reporting (**B**) current variations vs pH and NCR response (**C**) vs time and (**D**) vs pH.

In this approach, the thickness of the gate material affects the sensing performance. **Figure 14** shows a comparison among devices modified with 3, 5 and 10 deposition cycles. All results correspond to OECTs prepared with 5 deposition cycles of PEDOT:BTB, i.e. the condition showing the best performances.

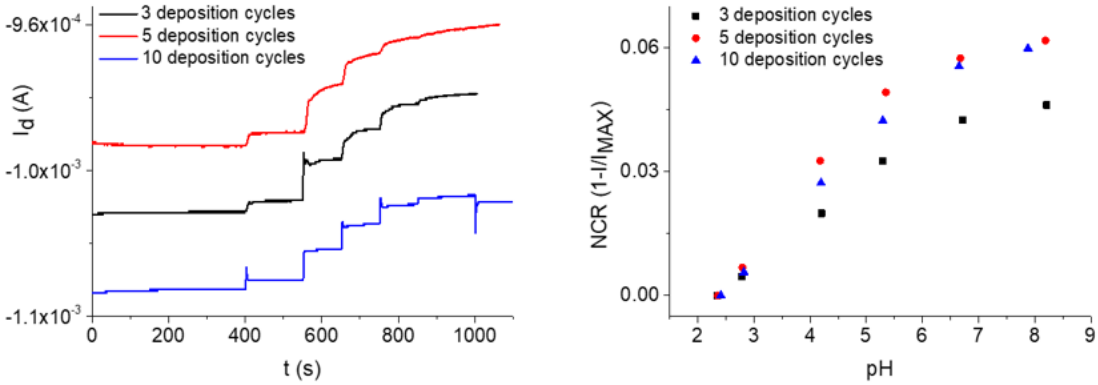

Figure 14. Influence of the number of deposition cycles of PEDOT:BTB on device performances using the potentiostatic approach. (Left) I_d vs t and (right) NCR vs pH plots obtained for 3 different devices tested in universal buffer under stirring during equimolar KOH additions. The OECTs were prepared using 3, 5 or 10 cycles during PEDOT:BTB deposition on the gate electrodes.

Finally, the response of our OECT pH sensor to acidic and basic pH oscillations was assessed by successive 1M HCl or 1M KOH additions to the universal buffer and a reversible signal was recorded (**Figure 15**), thus demonstrating the robustness of the proposed device. However, it is worth to underline that the device exhibits a slightly different sensitivity to acidic variations with respect to basic ones. The reason is likely to be related to the fact that the transistor is working in depletion, thus each I_d increment following acid addition might be somehow physically penalised. Nonetheless, the OECT response could be corrected accordingly.

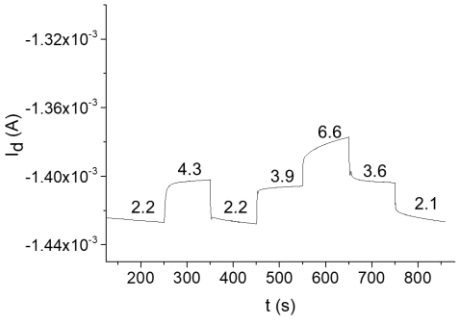

Figure 15. Reversible response of the OECT pH sensor fabricated on glass and tested potentiostatically in universal buffer under stirring, during 1M HCl or 1M KOH additions. V_g = -0.1 V; V_d = -0.2 V.

3.4 Discussion on the OECT pH sensor response

PEDOT:BTB is known in the literature as an electrochemical transducer that exhibits Nernstian sensitivity to pH[35] and, in this paper, we have demonstrated that the material response originates from the formation of pH dependent electronic states in the semiconducting polymer interacting with the dye counterion. Here, for the first time PEDOT:BTB was exploited as sensing element in an OECT by modification of the gate electrode. It is shown that a major consequence of providing the OECT with a PEDOT:BTB gate electrode is the achievement of a pH dependent output signal by means of a referenceless device. The electrochemical processes that rule the OECT working as pH sensor are proposed in **Figure 16**A, where M^+ represents the cation coming from the electrolyte solution upon gating. Here it is shown how the acid-base equilibrium of BTB directly affects the doping level of PEDOT at the gate electrode and consequently takes part in the overall doping/dedoping process occurring at the PEDOT:PSS channel when cations are extracted/injected due to the gate action across the electrolyte. In particular, the protonation/deprotonation of the counterion BTB impacts on the electrochemical potential and thus on the capacitance of PEDOT at the gate, eventually imparting the observed pH-dependency to the modulation of I_d. The ionic circuit of the OECT pH sensor is reported in Figure 16B, being R_s the resistance of the electrolyte solution, C_{ch} and C_g the capacitances of PEDOT:BTB (gate material) and PEDOT:PSS (channel material), respectively.

The resulting OECT pH sensor yields a super-Nernstian sensitivity, i.e. 93 ± 8 mV pH unit^{-1} in potentiodynamic mode and (1.1 ± 0.3) x 10^2 mV pH unit^{-1} in potentiostatic mode, which is an essential feature for a bioelectronic device to detect small pH variations in physiological conditions. It is worth to underline that the Nernstian limit of 59 mV pH unit^{-1} was overcome thanks to the transistor configuration. Indeed, it can be demonstrated that while the functional gate action imparts pH dependency to the output channel current, the inherent amplification provided by the OECT configuration allows to exceed the performance of the electrochemical transducer PEDOT:BTB. In particular, figure 16C shows the applied gate voltage, V_g, and the corresponding electrochemical potential of the gate, E_g, measured in 0.1M PBS (pH 7.0) while a fixed V_d of -0.2 V was applied. E_g and V_g can be linearly correlated (red line) and the slope V_g/E_g gives an estimation of the OECT amplification, being equal to 1.6. The blue line, with a slope equal to 1.0, simulates the case in which to amplification is observed. It is worthy to note that the OECT sensitivity

values (93 and 110 mV pH unit^{-1}) are very close to the product between the V_g vs E_g slope and the voltammetric sensitivity (62 mV pH unit^{-1} × 1.6 = 99 mV pH unit^{-1}). These results highlight that the transistor architecture plays a key role in the achievement of the observed amplified signal.

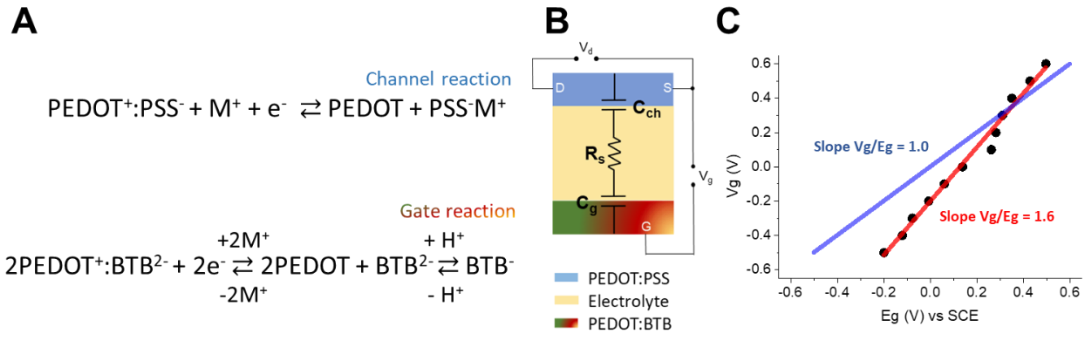

Figure 16. Insight into the OECT pH sensor response. (**A**) Electrochemical processes that rule the OECT working as pH sensor. (**B**) Equivalent circuit of the OECT. (**C**) V_g vs E_g data recorded in 0.1M PBS (pH 7.0). V_d = -0.2 V. The red line shows that the data are linearly correlated with a slope > 1; the blue line simulates the case in which no amplification is observed.

3.5 Flexible OECT sensor for pH monitoring in Artificial Sweat

Aiming at portable as well as wearable applications, flexibility should be targeted as an essential device feature. For this reason, the OECT pH sensor was realized on a thin, transparent film of Polyethylene terephthalate (PET) as shown in **Figure 17**A, and to simulate a real life condition where continuous, real-time monitoring of the human sweat pH is desired, we tested the flexible sensor in potentiostatic mode, dipped in Artificial Sweat, in a medically relevant pH range (Figure 17B). Figure 17C reports the proof of principle that the flexible pH sensor can reliably operate in a complex sample solution and readily detects small pH oscillations. In these conditions, the flexible device shows a fairly lower sensitivity with respect to that fabricated on glass (32 ± 2 mV pH unit^{-1} for 1M KOH additions between pH 5.7 and 7.0). It must be said that a higher resistance was measured for the channels spin-coated on plastic with respect to those fabricated on glass (440 ± 60 Ω vs 150 ± 50 Ω, respectively), thus limiting the performance of the flexible OECT pH sensor. However, this device can reliably estimate a pH value with a standard deviation equal to 0.06 pH units.

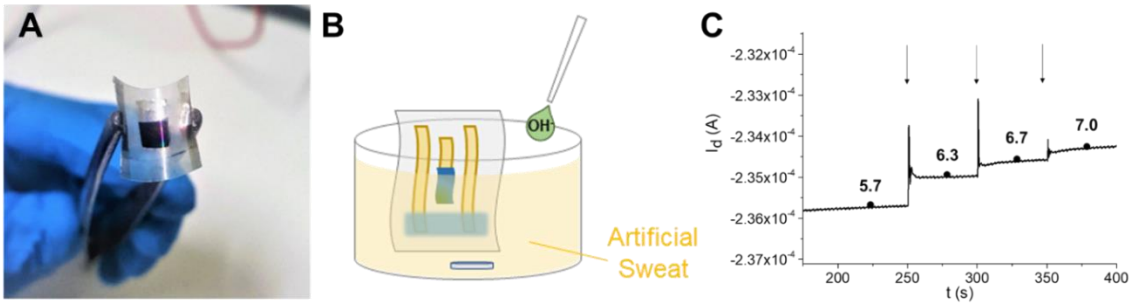

Figure 17. Flexible OECT pH sensor in Artificial Sweat. (**A**) Picture of the flexible sensor fabricated on a PET film. (**B**) Scheme of the flexible device operating in potentiostatic mode in artificial sweat. (**C**) I_d vs time curve recorded in artificial sweat with base equimolar additions. V_g = -0.1 V; V_d = -0.2 V.

4. Materials and Methods

Chemicals and Buffers. Sodium polystyrene sulfonate (NaPSS), 3,4-ethylenedioxythiophene (EDOT), lithium perchlorate, ethanol, potassium nitrate, potassium hydroxide, sodium chloride, sodium dihydrogen phosphate, 37% v/v hydrochloric acid, acetic acid, sodium acetate, 85% phosphoric acid, boric acid, bromothymol blue (BTB), methyl orange (MO), (3-glycidyloxypropyl)trimethoxysilane and sodium dodecylbenzenesulfonate were purchased from Sigma Aldrich. CLEVIOS™ PH 1000 suspension (PEDOT:PSS) was purchased by Heraeus. Monobasic and dibasic potassium phosphate were bought from Fluka. Ethylene glycol was obtained from Carlo Erba. All chemicals were of reagent grade or higher. A Combined Glass Ag/AgCl electrode (Amel) was employed for pH measurements. The ionic strength of all solutions was buffered with 0.1 M KNO_3. Acidic buffers at pH 1-3 were prepared with 0.1, 0.01 and 0.001 M HCl; pH 4.5 buffer solution contained 0.1 M CH_3COOH and 0.1 M CH_3COONa; the phosphate buffer solutions (PBS) employed as pH 5.5 and 7 buffers were made up by 0.1 M KH_2PO_4 and corrected to the desired pH with 1 M KOH; 0.004 M KH_2PO_4 and 0.02 M K_2HPO_4 aqueous solution was used as pH 8 buffer; the pH 9 buffer was 0.02 M K_2HPO_4; 0.1 M KOH was the pH 13 buffer solution. The Universal Buffer Solution was made up with 0.01 M H_3PO_4, 0.01 M H_3BO_3 and 0.01 M CH_3COOH. Artificial Sweat formulation (ISO pH 5.5) contained 0.05% w/v L-Istidine (Sigma Aldrich), 0.5% w/v NaCl and 0.22% w/v NaH_2PO_4.

Apparatus. All potential controlled measurements were carried out in a single compartment, three-electrode cell via a potentiostat (CH Instrument 660 C). Electrode potentials were measured with respect to an aqueous saturated calomel electrode (SCE), a Pt wire was used as the counter electrode and different substrates were employed as working electrodes. UV-Vis measurements of the dyes (0.02 mM in pH buffers) were performed using a Hewlett-Packard 8453 diode array spectrophotometer. Spectroelectrochemical analyses of the PEDOT:dyes and PEDOT:PSS modified ITO glass were obtained with the same apparatus equipped with an in situ electrochemical cell interfaced with a potentiostat (CH Instruments). IR-ATR spectra of the dyes and the PEDOT:dyes and PEDOT:ClO_4 modified graphite sheets were obtained with a Perkin-Elmer FT-IR spectrometer spectrum two. Morphology characterization and thickness evaluation of the PEDOT:dye modified gate electrodes were carried out in in air and at room temperature in tapping mode with an Atomic Force Microscopy (AFM) Park System NX10.

Electrochemical deposition of PEDOT:dye. The Polymerisation Solution (PS) employed for PEDOT:dyes electrodeposition was made of 10 mM EDOT, 1 mM dye (BTB or MO) and 1 mM PBS (pH 7.0) in 0.1M KNO_3 aqueous solution as the solvent. The PS was kept under stirring for 15' and then purged with N_2 for 5'. Afterwards, the electrodeposition of PEDOT:dye was carried out by Cyclic Voltammetry in a three-electrode cell (apparatus described above) containing the PS. The Working Electrode (WE) was immersed in the PS and a potential wave ranging from 0 to 1V vs SCE was applied with a scan rate of 0.1 V s^{-1} for 5 or 10 cycles. After electrodeposition, the blue iridescent film of PEDOT:dye covering the WE surface was rinsed with distilled water.

OECT pH sensor preparation. Gate, drain and source contacts made of Cr/Au (50 nm) were deposited via thermal evaporation. PEDOT:PSS solution was prepared by adding 5% ethylene glycol, 0.25% dodecylbenzene sulfonic acid and 1% 3-glycidyloxypropyltrimethoxysilane to the CLEVIOS™ PH 1000 suspension. The mixture was filtered through a 1.2 μm cellulose acetate filter and spin coated between gold source and drain electrodes at 500 rpm for 3 s, following annealing at 140 °C for 30 min. The final thickness of the PEDOT:PSS channel was 800 nm. Afterwards, the gate electrode of the transistor was modified with PEDOT:dye. Therefore, a 25 mm^2 gate area was defined with

Teflon tape in order to be exposed to the PS and the gate terminal was connected to the WE of the Potentiostat. Electrochemical deposition of PEDOT:dye was carried out following the procedure described above.

OECT measurements. A bipotentiostat (CH Instrument 900 B Scanning Electrochemical Microscope) was used to perform the electrical measurements by applying source-drain (V_d) and source-gate (V_g) potentials and by measuring the respective currents (I_d, I_g). The source collector was connected to the reference and counter electrode terminals of the bipotentiostat. Gate and drain were connected to the working electrode and the secondary electrode, respectively. A defined area for both the gate and the channel was left unprotected and exposed to the electrolyte solution. During potentiodynamic measurements, a triangular potential waveform was applied to the PEDOT:BTB gate electrode in the range $-0.5 < V_g < +0.6$ V (4 cycles, scan rate 20 mV s^{-1}), while V_d was fixed at -0.3 V. In the potentiostatic mode, V_g and V_d were kept at -0.1 V and -0.2 V, respectively.

5. Conclusion

In this work, the synthesis of two pH-sensitive composites of a semiconducting polymer doped with pH dyes, namely PEDOT:BTB and PEDOT:MO was optimised and their ability to successfully convert a chemical signal such as pH into an electrical one was demonstrated. The transduction mechanism of the proposed materials has been thoroughly studied by electrochemical and spectroscopic analyses and the change of the dyes' electronic charge with pH has been showed to affect the doping level of the semiconducting polymer. The electrochemical response of both materials to pH variations was assessed and resulted 62 ± 2 mV pH $unit^{-1}$ for PEDOT:BTB and 31 ± 2 mV pH $unit^{-1}$ for PEDOT:MO due to a different number of exchanged electrons, as proven by spectroelectrochemical characterisation. PEDOT:BTB exhibited the highest sensitivity in the broadest pH range (from 1 to 9) and was therefore chosen to functionalise the gate electrode of an OECT to obtain a pH sensor. The resulting device has a planar architecture and can reliably operate in a twofold transduction mode with super-Nernstian sensitivity, thanks to the inherent amplification provided by the transistor configuration coupled with

the functional gate element. pH detection was carried out by successive sampling in aqueous electrolytes (93 ± 8 mV pH unit^{-1}), as well as by dynamically changing the pH of the same medium ((1.1 ± 0.3) x 10^2 mV pH unit^{-1}). Finally, the device was successfully realised on a flexible PET substrate in order to prove its applicability as wearable platform. In this condition, we were able to estimate the pH of an artificial sweat sample with a standard deviation equal to 0.06 pH units within a medically relevant range.

6. References

1. J. R. Casey, S. Grinstein, J. Orlowski. *Nat. Rev. Mol. Cell Biol.* **2010**, *11*, 50–61.
2. T. Krulwich, G. Sachs, E. Padan. *Nat. Rev. Microbiol.* **2011**, *9*, 330–343.
3. Y. K. Reshetnyak. *Clin. Cancer Res*. **2015**, *21*, 4502–4505.
4. A. Koh, D. Kang, Y. Xue, S. Lee, R. M. Pielak, J. Kim, T. Hwang, S. Min, A. Banks, P. Bastien, M.C. Manco, L. Wang, K. R. Ammann, K.-I. Jang, P. Won, S. Han, R. Ghaffari, U. Paik, M. J. Slepian, G. Balooch, Y. Huang, J. A. Rogers. *Sci. Transl. Med.* **2016**, *8*, 366ra165.
5. G. K. Schwalfenberg. *J. Environ. Public Health* **2012**, *2012*, 727630.
6. J. Huang, F. Cheng, B. P. Binks, H. Yang. *J. Am. Chem. Soc*. **2015**, *137*, 15015–15025.
7. P. Gruber, M. P. C. Marques, P. Sulzer, R. Wohlgemuth, T. Mayr, F. Baganz, N. Szita. *Biotechnol. J.* **2017**, *12*, 1600475.
8. V. Balamuralidhara, T. M. Pramodkumar, N. Srujana, M. P. Venkatesh, N. V. Gupta, K. L. Krishna, H. V. Gangadharappa. *Am. J. Drug Discov. Dev.* **2011**, *1*, 24–48.
9. W. Huang, S. Deb, Y. Seo, S. Rao, M. Chiao, J. C. Chiao. *IEEE Sens. J.* **2012**, *12*, 487–495.
10. P. Upreti, L. E. Metzger, P. Bühlmann. *Talanta* **2004**, *63*, 139–148.
11. O. Husson. *Plant Soil* **2013**, *362*, 389–417.
12. G. Boczkaj, A. Fernandes. *Chem. Eng. J.* **2017**, *320*, 608–633.
13. F. Haber, Z. Klemensiewicz. *Z. Phys. Chem*. **1909**, *67*, 385–431.
14. Y. Zhang, J. Clausmeyer, B. Babakinejad, A. Lopez Cordoba, T. Ali, A. Shevchuk, Y. Takahashi, P. Novak, C. Edward, M. Lab, S. Gopal, C. Chiappini, U. Anand, L. Magnani, R. C. Coombes, J. Gorelik, T. Matsue, W. Schuhmann, D. Klenerman, E. V. Sviderskaya, Y. Korchev. *ACS Nano* **2016**, *10*, 3214-3221.

15. S. Jadoon, S. Karim, M. R. Akram, A. K. Khan, M. A. Zia, A. R. Siddiqi, G. Murtaza. *Int. J. Anal. Chem*. **2015**, *2015*, 164974.
16. J. Heikenfeld. *Electroanalysis* **2016**, *28*, 1242–1249.
17. M. J. Patterson, S. D. R. Galloway, M. A. Nimmo. *Acta Physiol. Scand.* **2002**, *174*, 41–46.
18. R. M. Morgan, M. J. Patterson, M. A. Nimmo. *Acta Physiol. Scand*. **2004**, *182*, 37–43.
19. V. F. Curto, C. Fay, S. Coyle, R. Byrne, C. O. Toole, C. Barry, S. Hughes, N. Moyna, D. Diamond, F. Benito-Lopez. *Sens. Actuators B* **2012**, *171–172*, 1327–1334.
20. V. Oncescu, D. O'Dell, D. Erickson. *Lab Chip* **2013**, *13*, 3232–3238.
21. T. Guinovart, G. Valdøs-Ramírez, J. R. Windmiller, F. J. Andrade. *Electroanalysis* **2014**, *26*, 1345-1353.
22. S. Nakata, T. Arie, S. Akita, K. Takei. *ACS Sensors* **2017**, *2*, 443–448.
23. A. Spanu, F. Viola, S. Lai, P. Cosseddu, P. C. Ricci, A. A. Bon. *Org. Electron*. **2017**, *48*, 188–193.
24. M. Marzocchi, I. Gualandi, M. Calienni, I. Zironi, E. Scavetta, G. Castellani, B. Fraboni. *ACS Appl. Mater. Interfaces* **2015**, *7*, 17993–18003.
25. F. Amorini, I. Zironi, M. Marzocchi, I. Gualandi, M. Calienni, T. Cramer, B. Fraboni, G. Castellani. *ACS Appl. Mater. Interfaces* **2017**, *9*, 6679–6689.
26. I. Gualandi, M. Marzocchi, E. Scavetta, M. Calienni, A. Bonfiglio, B. Fraboni. *J. Mater. Chem. B* **2015**, *3*, 6753–6762.
27. I. Gualandi, D. Tonelli, F. Mariani, E. Scavetta, M. Marzocchi, B. Fraboni. *Sci. Rep*. **2016**, *6*, 35419.
28. A. M. Pappa, V. F. Curto, M. Braendlein, X. Strakosas, M. J. Donahue, M. Fiocchi, G. G. Malliaras, R. M. Owens. *Adv. Healthc. Mater*. **2016**, *5*, 2295–2302.
29. P. Lin, F. Yan, H. L. Chan. *ACS Appl. Mater. Interfaces* **2010**, *2*, 1637–1641.
30. D. Khodagholy, J. Rivnay, M. Sessolo, M. Gurfinkel, P. Leleux, L. H. Jimison, E. Stavrinidou, T. Herve, S. Sanaur, R. M. Owens, G. G. Malliaras. *Nat. Commun*. **2013**, *4*, 2133.
31. I. Gualandi, E. Scavetta, F. Mariani, D. Tonelli, M. Tessarolo, B. Fraboni. *El. Acta* **2018**, *268*, 476–483.
32. W. Choi, T. An, G. Lim. *Nanoscale Res. Lett*. **2011**, *6*, 339.
33. G. Scheiblin, R. Coppard, R. M. Owens, P. Mailley, G. G. Malliaras. *Adv. Mater. Technol.* **2016**, *2*, 1600141.
34. Gualandi, M. Marzocchi, A. Achilli, D. Cavedale, A. Bonfiglio, B. Fraboni. *Sci. Rep*. **2016**, *6*, 33637.

35. A. Balamurugan, Z.-W. Chen, S.-M. Chen. *J. Electrochem. Soc*. **2008**, *155*, E151-E156.
36. F. Mariani, I. Gualandi, M. Tessarolo, B. Fraboni, E. Scavetta. *ACS Appl. Mater. Interfaces* **2018**, *10*, 22474−2248.
37. R. M. Silverstein, F. X. Webster, D. J. Kiemle. "Spectrometric Identification of Organic Compounds". John Wiley & Sons, **2006**.
38. Y. Lau, Y. Wong, T. Teng, N. Morad, M. Rafatullah, S.-A. Ong. *RSC Adv*. **2015**, *5*, 34206–34215.
39. P. Pradhan, R. J. Mascarenhas, T. Thomas, I. N. N. Namboothiri, O. J. D. Souza. *J. Electroanal. Chem.* **2014**, *732*, 30–37.
40. N. Massonnet, A. Carella, O. Jaudouin, P. Rannou, G. Laval, C. Celle, J.-P. Simonato. *J. Mater. Chem. C* **2014**, *2*, 1278–1283.
41. A. Elschner, S. Kirchmeyer, W. Lovenich, U. Merker, K. Reuter. "PEDOT: Principles and Applications of an Intrinsically Conductive Polymer". CRC Press, **2010**.
42. J. L. Brédas, G. B. Street. *Acc. Chem. Res*. **1985**, *18*, 309–315.
43. D. M. De Leeuw, M. M. J. Simenon, A. R. Brown, R. E. F. Einerhand. *Synth. Met*. **1997**, *87*, 53–59.
44. Y. Li, Y. Cao, J. Gao, D. Wang, G. Yu, A. J. Heeger. *Synth. Met.* **1999**, *99*, 243–248.
45. W.-L. Yu, Y. Cao, J. Pei, W. Huang, A. J. Heeger. *Appl. Phys. Lett*. **1999**, *75*, 3270.
46. C. M. Cardona, W. Li, A. E. Kaifer, D. Stockdale, G. C. Bazan. *Adv. Mater.* **2011**, *23*, 2367–2371.
47. D. A. Bernards, D. J. Macaya, M. Nikolou, J. A. DeFranco, S. Takamatsu, G. G. Malliaras. *J. Mater. Chem*. **2008**, *18*, 116–120.
48. H. Tang, F. Yan, P. Lin, J. Xu, H. L. W. Chan. *Adv. Funct. Mater*. **2011**, *21*, 2264-2272.
49. H. Tang, P. Lin, H. L.W. Chan, F. Yan. *Biosens. Bioelectron.* **2011**, *26*, 4559-4563.

V. Development of two-terminal chemical sensors inspired to the Organic Electrochemical Transistor

The development of portable and wearable sensors is of high importance in several fields, such as point-of-care medical units, monitoring systems for athletic training performance and environmental monitoring, and can significantly profit from ubiquitous smart technologies and wireless communication networks nowadays. A crucial bottleneck to design robust wireless sensor networks is the development of new transducer materials capable to effectively convert the biological or environmental event (for example, concentration changes of chemical markers, or the presence of hazards in the surrounding) into the electronic domain. Such objects have to match several criteria, including low power consumption, robustness and user-friendly operability, and address a number of technical requirements. Among them, biocompatible physicochemical properties should be combined with a specific functionality and an amplifying transduction mechanism to account for small signal variations that occur in a noisy biological background or complex environmental matrices.

As already discussed in this thesis, amplified transduction of ionic or electrochemical signals is nowadays achieved in sensors that have three electrical connections to operate in a transistor configuration[1-3] such as OECT sensors: Source and Drain electrodes drive an electronic current through a semiconducting channel that is coupled to the gate electrode through an ionically conductive analyte solution. Variations in analyte concentration cause

a potential offset ΔV at the gate, thus leading to an amplified variation in electronic current response. Moreover, the opportunity to realize all-plastic devices makes OECT sensors even more appealing for wearable technologies. In the previous Chapters, PEDOT:PSS-based OECT sensors operated in the so-called "amperometric mode" have been studied in comparison with standard electroanalytical techniques. The use of a potentiodynamic approach, as well as the design of novel functional materials, have been proposed as strategies that allow selective analyte's detection and, finally, device downscaling has been carried out to improve sensitivity. The work presented in this Chapter is dedicated to the use of OECT sensors in a potentiometric-like fashion, where the application of a potential at the gate electrode is not necessary. Indeed, as suggested at the end of Chapter 1, exploitation of spontaneous redox processes during the analytical detection, i.e. that occur at zero gate bias, allows to quickly reach a stable response while maintaining the conditions for maximum amplification. Such a behavior is the rationale behind the work described in this Chapter and can be realized by the targeted design of functional materials that combine the features of the organic semiconductor and a specific transducing capability. It should be noted that this strategy not only improves the sensing performance, but also impacts dramatically on the required electronics, power consumption and geometry of the resulting device, which show appealing features as platforms for portable and wearable applications. All the aspects concerning the development of novel transducing materials to realize two-terminal sensors for Chloride and pH detection will be discussed in the following.

1. Background

Over the past decade, medical applications of IoT have received the greatest attention. Real-time collection and sharing of information regarding our body status are significant not only for hospitalized situations, but also during routine daily activities. For instance, continuous monitoring of vital parameters is crucial to take precautionary measures during sport activity or in the wearer's workplace, especially in the presence of diagnosed, chronical diseases. In this view, wearable sensors can be a mean to realize the so-called personalized-medicine and revolutionize our way to manage healthcare and practice medicine. Despite the recognized relevance of wearable sensors, they have been experiencing unbalanced growth in research and development.[4] Existing wearable sensors are indeed based on the transduction of physical parameters, with most solutions targeting

blood pressure,[5,6] ECG[7-9] or body motion.[10-12] In contrast, the transduction of chemical information, which can provide much further insight into the overall health status than physical parameters alone, is at a far earlier stage of development.[13] The inherently higher degree of complexity involved in the construction and operation of wearable chemical sensors compared to the physical counterparts has been addressed as the "chemical sensor paradox".[14] The main constraints that hinder a straightforward realization of reliable wearable chemical sensor are related to the low analyte concentrations, small sampling volumes and fluid stagnation, mechanical resiliency, signal stability, biofouling and biocompatibility issues, together with the need to operate in physiological conditions, adapt to the human body without causing discomfort and work with low power consumption, thus requiring simple electronic components. In general, the central idea shared by wearable technologies is the *wear-and-forget* functionality, which automatically excludes all approaches with an intrusive nature that rely, for instance, on blood samples.[13]

Sweat, saliva, interstitial fluids, tears and breath are biological fluids that contain abundant information about health status, are readily accessible and can be sampled for non-invasive monitoring. In particular, human sweat contains a rich library of solutes and metabolites and can be collected after excretion form pores in the epidermis. Sweat tests are carried out to detect metabolites of illicit drugs[15,16] and chloride content in sweat is used in the diagnosis of cystic fibrosis, a progressive genetic disease, in newborns. The sweat test is routinely performed in laboratory facilities and involves transdermal administration of pilocarpine by iontophoresis to stimulate sweat gland secretion, followed by collection and quantitation of sweat onto gauze or filter paper; finally, chloride content is quantitatively determined by validated analytical methods.[17,18] Required amount of sweat and sensitivity of the analytical technique are major limitations of the described procedure. In this regard, a paper-based test strip device with rapid and selective response that needs only 2 μL of sweat sample has been very recently proposed.[19] In addition to well-assessed medical tests, sweat analysis can provide abundant information about the human body status and has been focus of intensive research effort for the development of wearable devices, including tattoo-based systems,[20,21] textile sensors,[22-25] smart wristbands and headbands,[26] wearable systems comprising disposable sensing components,[27] devices equipped with drug delivery systems[28] and microfluidic platforms.[29,30] It has been reported that determination of sweat sodium and chloride is important to assess proper hydration levels and electrolyte balance in athletes,[31,32] while quantification of sweat glucose has utility in screening tests for

diabetes[33] and its consumption can be tracked during sport activity to monitor fatigue levels. Lactate concentration is an indication of body exertion and exercise intensity, while cortisol is a subject-specific, stress-related biomarker.[34,35] Finally, variations in sweat pH have been related to metabolic alkalosis.[36] While skin contamination, low-sampling rates, body motion artifacts, analyte dilution and dependency on sweat rate remain major constraints affecting sensors' reliability,[35] renewed interest in the collection of raw data, establishment of correlations between sweat and blood compositions and definition of microfluidic models to shed light on biomarkers partitioning and transport from blood into sweat is emerging.[37-41]

Other than the aforementioned biological fluids for continuous on-body measurements, wound exudate is another biofluid that is currently attracting interest in the field of wearable sensing technologies. The wound healing process to repair injured skin and tissues is a complex cascade of physiological events, vulnerable to diseases, such as diabetes or autoimmune diseases, body status, including age or nutritional defects, and external factors or agents like bacteria that can cause infections and/or turn a lesion into a chronic wound, which does not heal in an orderly or timely manner. Chronic wounds exceed a 3-month healing process and are recognized as a major source of mortality in bed-ridden and diabetic patients.[42] Current treatment of chronic wound relies on wound dressings tailored to the state of the wound and specific healing case. Wound dressings are chosen depending on the infection status, moisture level and exudate volume and can be classified as passive, interactive, advance and bioactive, the latter comprising bio-films or even drug delivery systems that play an active role in the healing process.[43] However, as underlined by Qin et al.,[44] while wound dressings should be frequently changed for hygienic reasons and therapy efficacy, this is sometimes done unnecessarily, with persistent risk of causing a second injury or interrupt the wound healing process. The paradox consists in the fact that the wound status cannot be evaluated without removing the bandage. Considering this, the realization of smart wound dressings with integrated sensors that are able to non-invasively monitor the wound site would impact dramatically on the current treatment approaches, with potential to improve significantly the wound management and decrease the healing time. In this view, critical biomarkers to be monitored are glucose, lactate, pH, oxygen, interleukin-6, together with temperature, blood pressure and bacterial colonization at the wound site.[43] In particular, pH values ranging from 4 to 7 are desired during the healing process as, in such conditions, control of collagen

formation, increased fibroblasts activity and hampered bacteria proliferation are ensured. Conversely, more alkaline pH values (7 – 9) are typical of chronic wounds and may suggest abnormal healing processes. In general, the pH value on the wound site has been found to vary according to the wound healing stages and, for this reason, pH monitoring can be useful to assess the wound state and the efficacy of the therapeutic strategy.[44-46] A smart bandage able to sense bleeding, pH and external pressure levels has been recently reported that comprises a disposable, ink-jet printed component and is equipped with a wireless communication system, thus providing the user with hand-held capability to monitor the wound healing process.[47] Other examples of smart dressings for wound pH monitoring have been proposed as proof of principle studies based on either potentiometric[48] and colorimetric transduction.[49,50]

The wearable sensing technologies discussed above are all devoted to self-monitoring by an *inward-looking* approach. A distinct class of wearable devices comprises *outward-looking* sensors, which can offer valuable information from the surrounding environment for improved safety and health, particularly for emergency responders or inspectors.[51] Miniaturized dosimeters and belt-worn analytical tools available to the market mainly target real-time monitoring of air pollution, indoor air quality, aerosol exposure and detection of biothreat agents. Despite portability and robustness, such devices rely on sophisticated light-scattering or Raman detectors that profoundly impact on the final cost of the product.[52,53] On the other hand, a variety of low-cost, wearable chemo-sensors for external monitoring of gaseous threats is at a primal stage of development. For instance, J. Wang's group has reported the realization of a wireless chemical sensor platform in the form of a smart ring for the electrochemical detection of nitroaromatic and peroxide explosives, together with organophosphate nerve agents[54] and a tattoo-based potentiometric sensor for G-type nerve agents.[55] Focusing on textile gas sensors that can be conveniently integrated into everyday clothes or work overalls, they have been fabricated on both natural and synthetic fibres, the majority exploiting chemoresistive materials for the detection of volatile organic compounds[56-58] and ammonia.[59-62] Despite the fact that the use of a chemoresistive transduction is particularly suited to a thread-like architecture for sensing, it typically implies the continuous application of high operation voltages (5 V and more) that are not desirable for safety reasons and impact on the required electronics.

In the following paragraphs, a potentiometric-based strategy will be discussed to fabricate chemical sensors in a 2-terminal configuration that can be easily realized on threads and other wearable supports, with the key advantage of operating at low applied bias (< 0.5 V). A novel composite material based on Ag/AgCl nanoparticles and PEDOT:PSS has been designed for chloride detection in human sweat.[63] Moreover, the PEDOT:BTB OECT sensor discussed in Chapter IV is here proved to be able to operate in the 2-terminal architecture and single threads functionalisation is carried out to perform pH detection in biofluids. Finally, a newly- synthesised pH transducer based on IrO_2 particles and PEDOT:PSS is characterized in liquid samples in the 2-terminal architecture and is then implemented as a gas sensor for ammonia detection.

2. Nanoparticles gated Chloride sensor

A semiconducting polymer-nanoparticle composite (SP/NP) is designed to combine in a single material the transduction features of the gate electrode and the amplification properties of the OECT, allowing for new transistor-like configurations to be simply obtained with a two- terminal device. In order to explain the working principles of SP/NP and the transduction mechanism, the composite based on PEDOT:PSS and Ag/AgCl NPs is thoroughly investigated. Finally, a chloride sensor is realized and implemented as a smart electronic textile device and as an environmental sensor. This approach is general and can be exploited to design new simple sensors for other target compounds. The results reported here are reproduced from I. Gualandi, M. Tessarolo, F. Mariani, T. Cramer, D. Tonelli, E. Scavetta, B. Fraboni: Nanoparticle gated semiconducting polymer for a new generation of electrochemical sensors. Sensors & Actuators B, 2018, 273, 834-841. Copyright 2018, with permission from Elsevier.

2.1 Expected response of an OECT as Chloride sensor

Figures **1**A, 1B and 1C show a typical OECT-based electrochemical sensor and its current response to increasing levels of chloride anions in the aqueous electrolyte. Here, a selective sensitivity for Cl^- ions is obtained by employing an Ag wire with AgCl coating as the gate electrode. In this way, a spontaneous Faradaic redox equilibrium, $Cl^- + Ag \leftrightarrows AgCl + e^-$, is established at the gate electrode's surface that produces an electrochemical potential E, measured with respect to a reference electrode, and described by the Nernst equation[64]:

$$E = E° + \frac{kT}{e} ln[Cl^-] \quad (1)$$

where E° is the standard potential of the Ag/AgCl redox couple, $[Cl^-]$ denotes the Cl^- ions concentration, k is the Boltzmann constant, T the absolute temperature and e the elementary charge. A variation in Cl^- concentration results in an offset in the electrochemical potential E of the analyte solution with respect to the metallic gate electrode. Considering the transistor geometry that is here used, the variation in the electrochemical potential E corresponds to an offset of the effective gate potential (ΔV_g).[65] In the capacitively coupled semiconducting channel, it causes a variation in carrier density and in the consequently measured source-drain current response. In PEDOT:PSS, hole charges constitute the mobile carriers, therefore a positive potential offset leads to their replacement by immobile cations migrating from the solution into the semiconductor composite. The quantitative device response (ΔI_d) is thus related to the potential offset (ΔV_g) and follows directly from the transistor geometry:

$$\Delta I_d = - g_m \times \Delta V_g \quad (2)$$

with g_m is the transconductance of the OECT defined as $g_m = \mu C_V t V_d W/L$ in the linear regime (where t is the PEDOT:PSS layer thickness, C_V the volumetric capacitance of PEDOT:PSS, μ the mobility of the charge carriers W and L are the width and the length of the channel, respectively, and V_d the drain potential). Here g_m amounts to 9 10^{-4} A V^{-1}, and this value is in agreement with the ones reported in literature.[66] Moreover, the transconductance exhibits the maximum value around 0 V, suggesting that this is the best condition for an OECT used as two-terminal device as stated by Rivnay et al..[67]

Combining Equations 1 and 2, the quantitative expression is obtained:

$$\Delta I_d = -g_m \times \frac{kT}{e} ln \frac{[Cl^-]_2}{[Cl^-]_1} \quad (3)$$

where $[Cl^-]_1$ and $[Cl^-]_2$ are the chloride concentrations that cause the variation of conductivity ($[Cl^-]_1$ the starting and $[Cl^-]_2$ the final value, respectively). The typical plot of current variation ΔI_d vs analyte concentration (Figure 1 C) shows the expected logarithmic dependency of Equation 3 with a slope, expressed as normalized current ($1-I/I_{max}$), of 0.05 ± 0.01 $decade^{-1}$ demonstrating the excellent Faradaic efficiency and large transconductance. It is worth to note that in the OECT device, efficient and amplified detection occurs at 0V bias applied to the gate. This results from two main reasons: 1) the

PEDOT:PSS based channel is equivalent to a doped semiconductor that works in depletion mode, 2) the Ag/AgCl redox reaction with Cl^- ions is spontaneous and reversible. Therefore, maximum transconductance occurs without the need to apply a bias to the gate.[66,68]

2.2 Response of the SP/NP based Chloride sensor

Figures 1D and 1E show the basic idea about how to design a simpler device based on innovative SP/NP materials, so as to maintain the amplification effect without the requirement of a gate electrode. To this end, the SP/NP material has to integrate the semiconducting channel with an additional electrochemical functionality provided by NPs. In particular, a Faradaic reaction is needed to set the potential of the solution/PEDOT:PSS interface and to provide a potential offset ΔV that varies specifically as a function of the analyte concentration. We obtain the functional SP/NP material by growing into the semiconducting polymer Ag/AgCl NPs and demonstrate its selectivity towards the chloride anion (Cl^-). The presence of NPs does not affect the features of PEDOT:PSS as organic semiconductor, even though the occurrence of redox processes involving NPs strongly reduces the range of potentials that can be applied.

Figure 1F reports the typical current response to variations in chloride concentration of a two terminal SP/NP based sensor that employs Ag/AgCl NPs. The fabrication of the composite semiconducting channel follows a simple two step procedure described in the Materials and Methods section. The functionality of the two-terminal device was evaluated by adding the same amounts of Cl^- into the analyzed solution as in the OECT experiment (Figure 1 C). Similarly to what happens for an OECT, increases of Cl^- concentration lead to a decrease of drain current that is linearly related to the logarithm of the analyte's concentration. It is possible to quantitatively compare the two and three terminal devices by their sensitivity, expressed as normalized current variation ($\Delta(1-I/I_{max})/\Delta(\log[Cl^-])$). For the SP/NP material, 0.06 ± 0.02 decade^{-1} (average and standard deviation for 3 different devices) is obtained, compared with 0.05 ± 0.01 decade^{-1} for the traditional OECT (with 0 V applied to the Ag/AgCl gate electrode). This result shows that the device based on the new PEDOT:PSS Ag/AgCl NPs composite maintains the intrinsic amplification which is observable for an OECT. The sensor works between 10^{-4} and 1 M, and the limit of detection is equal to $0.5\ 10^{-4}$ M. Moreover, it is worthy of note that this device exhibits a response time (evaluated as the time that is required to gain 90 % of the final signal) equal to 15 ±

3 s for a Cl^- addition of 100 mM. This value is significantly lower than the one observed with a traditional OECT at the same concentration (118 ± 8 s). Indeed, the intimate contact between the semiconducting polymer and the NPs minimizes the electrical resistances between the sensitive material (Ag/AgCl) and PEDOT:PSS, with a consequent enhancement of the performance in terms of response time. In addition, the recovery time of the signal was evaluated after a 25 mM Ag^+ addition to a sample containing 50 mM Cl^-. This procedure leads to the precipitation of AgCl salt and to a decrease of the Cl^- concentration to reach the value of 25 mM. The current fastly takes on the value previously observed for 25 mM and the recovery time is 30 ± 4 s. It is worth to underline that this is the first example of a SP/NP material that can operate as an OECT-like device only by means of only two electrodes, thus requiring just one external bias to be applied.

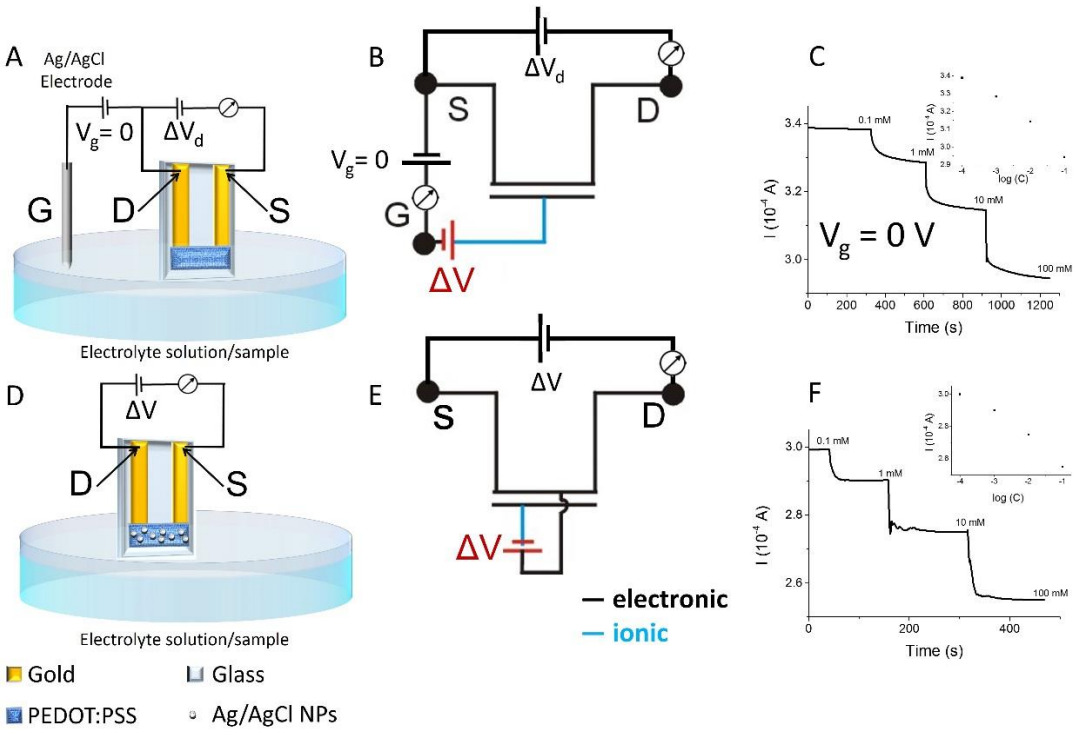

Figure 1. OECT Chloride sensor (**A,B,C**): (A) schematic layout of an OECT composed by a PEDOT:PSS channel and an Ag/AgCl gate electrode; (B) schematic circuit; (C) Source-Drain current vs time plot recorded while increasing the concentration of Cl^- in the 0.1 M KNO_3 solution (V_g = 0 V; V_d = + 0.05 V). **SP/NP-based Chloride sensor** (**D, E, F**): (D) schematic layout of the here proposed SP/NP-based two terminal sensor, composed by a PEDOT:PSS strip modified with Ag/AgCl NPs; (E) schematic circuit; (F) Source-Drain current vs time plot recorded while increasing the concentration of Cl^- in the electrolyte (V_d = + 0.05 V).

2.3 SP/NP materials: physical and chemical properties

In order to understand the structural and electronic properties of the SP/NP material, Atomic Force Microscopy (AFM) and Scanning Electron Microscopy (SEM) analyses coupled with Energy Dispersive X-ray microanalysis (EDX) were carried out (**Figure 2**). The surface morphology as obtained by AFM and SEM (Figures 2 A, B and D) shows that PEDOT:PSS is uniformly covered by NPs having a diameter of 300 ± 80 nm, with a density of 7.5 particles μm^{-2}. The NPs do not establish a continuum layer that can effectively transport the charge, thus the electrical features of the composite material have to be mainly ascribed to the PEDOT:PSS conductive properties. In fact, the electrical resistance of the channel does not significantly change after the electrodeposition of Ag/AgCl nanoparticles (200 ± 10 Ω vs a starting value of 100 ± 8 Ω). EDX analysis (Figure 2 C) performed on the NPs indicates the presence of a higher concentration of Ag than Cl (0.22 (atomic %) ± 0.02 of Ag vs. 0.18% (atomic %) ± 0.01 of Cl). Moreover, since the Ag/Cl ratio is always higher than 1, i.e. the theoretical value of AgCl, the hypothesis that the NPs are made by both Ag and AgCl is confirmed.

AFM in Scanning Kelvin-Probe Mode (SKPM) was employed to gain information about the electronic structure of the material. SKPM allows to measure the local surface potential. As the doped semiconducting polymer as well as the NPs behave as conductors, we related variations in the surface potential to local differences in Work Function (WF). As reference material, a pure gold film was used, whose WF is set to 5.1 eV. The resulting WF maps of a nanoparticle deposited onto the PEDOT:PSS film is shown in Figure 2 E. The surrounding PEDOT:PSS film is at an average WF of 5.05 eV that well compares with the values in literature (for PEDOT:PSS PH1000, 5.0 eV).[69] On the NPs two main phases can be observed: one at the boundaries and one in the middle of the particles. The red color of the boundaries indicates a work function of 5.5 eV, which is higher than the value found for PEDOT:PSS and thus we relate it to the presence of AgCl.[70] The blue and white colors in the middle of the particle show that the WF decreases below the level of PEDOT:PSS. This can be attributed to the presence of metallic Ag in the core of the particles, which is responsible of the electrostatic interaction with the AFM tip. The measured value of 4.7 – 4.8 eV compares well with values found in literature for elementary Ag (4.3 – 4.7 eV).[71] As a consequence, it can be said that the NPs are composed by a core of Ag and an external shell of porous AgCl. The well-defined contrast in surface potential is clearly related to the differences in WF. Consequently, the different constituents of the composite material,

the semiconducting polymer and the NPs, are in direct electrical contact and a single Fermi-level is defined throughout the material.

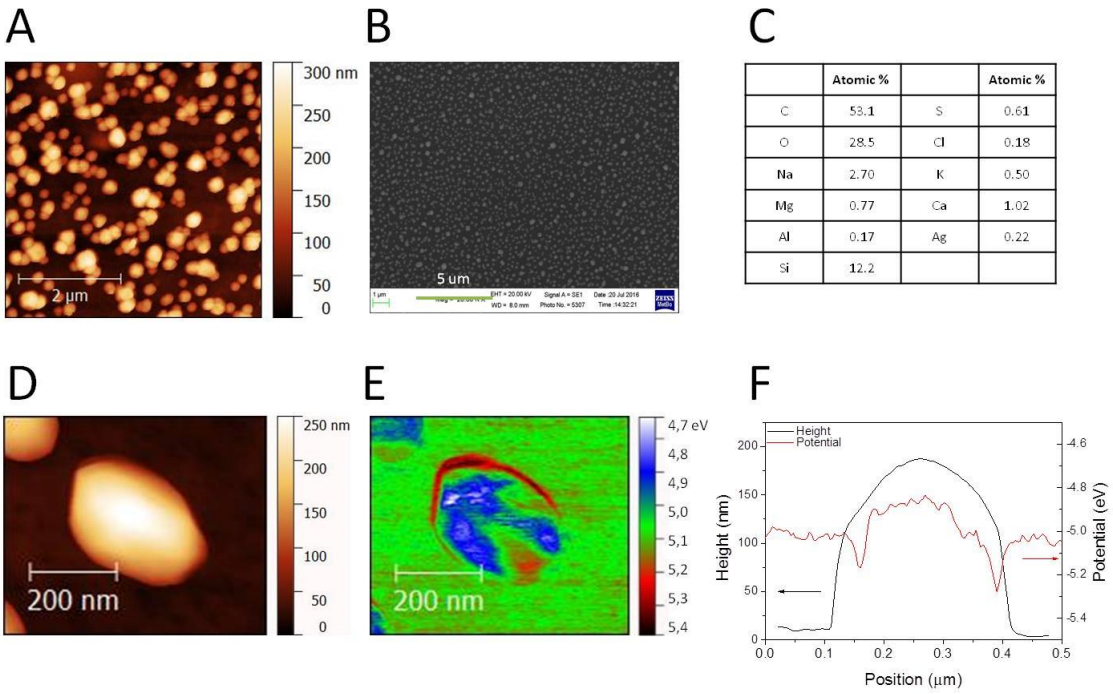

	Atomic %		Atomic %
C	53.1	S	0.61
O	28.5	Cl	0.18
Na	2.70	K	0.50
Mg	0.77	Ca	1.02
Al	0.17	Ag	0.22
Si	12.2		

Figure 2. AFM (**A** and **D**), SEM (**B**) and KPFM (**E**) images of PEDOT:PSS modified with Ag/AgCl NPs. C) Atomic % estimated with EDS analysis. **F**) Profile of NPs obtained with AFM and KPFM.

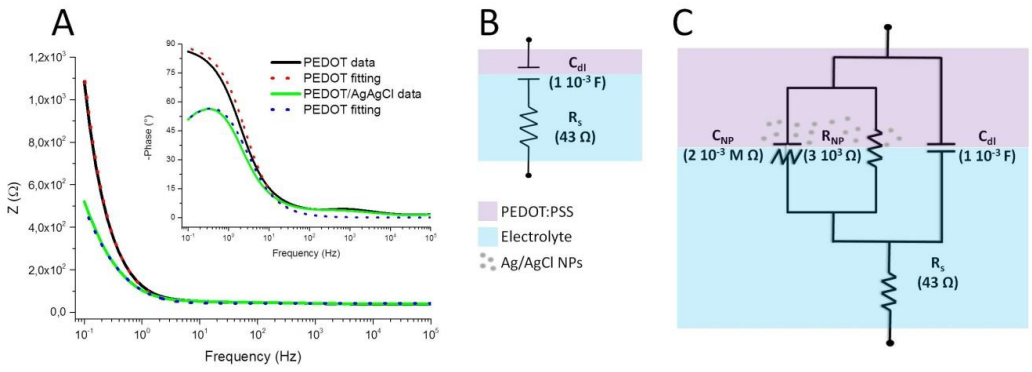

Figure 3. (**A**) Bode plots (main figure) and Phase trends (inset) obtained by Electrochemical Impedance Spectroscopy (EIS) for bare PEDOT:PSS and PEDOT:PSS/Ag/AgCl NPs composite. The fitted data are reported as dotted lines and were obtained using the equivalent circuits shown in (**B**) and (**C**) for the bare PEDOT:PSS and the PEDOT:PSS Ag/AgCl NPs composite, respectively.

Next, a deeper insight into the electric coupling between the SP/NP and the aqueous electrolyte is provided by Electrochemical Impedance Spectroscopy (EIS) (**Figure 3**). Figure 3 A shows the Impedance spectra and fitted data collected for the same PEDOT:PSS film, before and after modification with Ag/AgCl NPs. Comparing the Bode plots and the correspondent Phase trends, a variation in the impedance at the electrode/solution interface stands out as a major effect at low frequencies. Indeed, while the pristine polymeric film shows the highest impedance, this feature is halved after Ag/AgCl NPs electrosynthesis. The recorded data were fitted with an equivalent circuit, in order to extract the relevant output values for each element. Figure 3 B and C show the equivalent circuits used for bare PEDOT:PSS and SP/NP material, respectively. A PEDOT:PSS film is simply represented as R_s and C_{dl} in series, accounting for the electrolyte resistance and the double layer capacitance arising at the electrode/solution interface. The output values obtained for these elements were fixed to fit the same film after the modification with NPs. In order to properly design an equivalent circuit for the SP/NP material, the contribution of NPs has been described as an additional circuit in parallel to that of PEDOT:PSS, composed by a resistance (R_{NP}) and a constant phase element (CPE_{NP}) in parallel (constant parameter α_{CPE} = 0.48). A CPE behavior may arise from a variety of surface properties such as porosity, surface roughness or 3-dimensional distribution[72] and, therefore, it can be reliably adapted to our composite system. The impedance analyses confirm that the PEDOT:PSS/electrolyte interface has changed after the modification with Ag/AgCl NPs. The overall impedance at low frequencies and the equivalent circuit required to fit the composite material demonstrate the occurrence of a new charge transfer process mediated by the NPs.

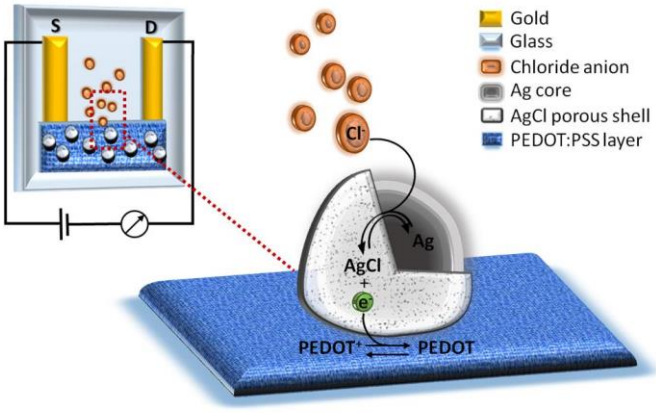

Figure 4. Operation mechanism of the Cl^- sensor composed by a PEDOT:PSS stripe modified with Ag/AgCl NPs.

2.4 Transduction mechanism

Figure 4 shows a rendering of the charge transfer process (resulting in the output electrical signal) generated within the new SP/NP material due to the interaction of chloride ions with AgCl NPs in the PEDOT:PSS film. When the Cl^- concentration increases, the redox equilibrium involving Ag and AgCl leads to the release of electrons that are collected by PEDOT:PSS due to the electrical contact existing between the two materials (i.e., the semiconducting polymer and the NPs). The consequent electron-hole recombination in the semiconducting polymer causes a decrease in charge carriers concentration, thus lowering the source-drain current.

For low applied V_d, the PEDOT:PSS conductivity (σ) is linearly related to the charge carrier density (n) by the formula[73]:

$$\sigma = n\, e\, \mu \quad (4)$$

where μ is the mobility of the charge carriers. The amount of charge carriers injected in the polymer (Δn) due to a potential difference (ΔV) can be expressed taking into account the volumetric capacitance (C_V) of the material as reported by Malliaras et al.[74]

$$\Delta n = \frac{C_V}{e}\, \Delta V \quad (5)$$

In the SP/NP material, the potential difference ΔV is generated by the redox reaction involving Ag and AgCl governed by the Nernst equation (Equation 1). Combining Equations 1 and 5, the logarithmic relationship between the variation of electrical conductivity and the Cl^- concentration is obtained:

$$\Delta\sigma = -C_V\, \mu \left(\frac{kT}{e} \ln \frac{[Cl^-]_2}{[Cl^-]_1}\right) \quad (6)$$

By considering the geometric factors and the applied potential to the resistor, it is possible to obtain an analytical expression of the current variation:

$$\Delta I = -\frac{W\, t\, C_V\, \mu\, V_d}{L} \left(\frac{kT}{e} \ln \frac{[Cl^-]_2}{[Cl^-]_1}\right) \quad (7)$$

Equation 7 results equal to Equation 3, thus demonstrating that the SP/NP response is equal to the one observed for an OECT endowed with an Ag/AgCl gate electrode. For a PEDOT:PSS channel a proportional constant c can be defined that links current and E

variations that resembles the formula for the OECT transconductance (Equation 2) and can be used to evaluate the amplification. *c* can be calculated by differentiating current *vs* E curves.

2.5 Real-life applications

In order to validate the reliability of the real-time, low-cost sensing devices for practical applications, their performance were assessed in real-life scenarios (**Figure 5**): i) detection of water salinity and Cl^- content; ii) smart textile biomedical applications. For both applications, a dedicated portable electronic reader was realized that is wirelessly connected to a custom smartphone application, allowing a real-time, in-situ reading with a user friendly interface. Thanks to the low power consumption of the reader and the zero gate voltage applied for sensor operation, a 3 V coin cell battery was enough to provide the operation power for more than 100 readings.

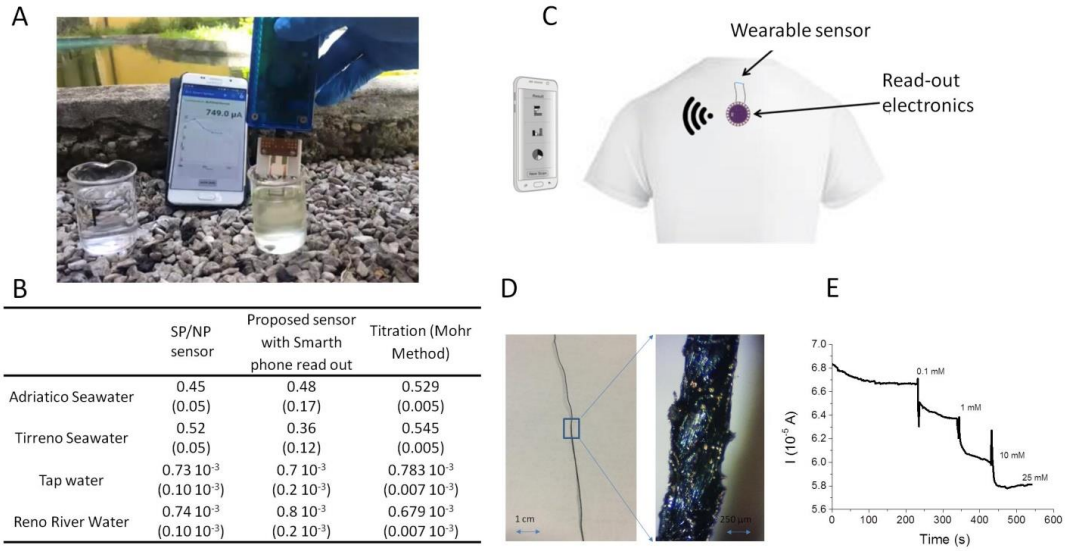

	SP/NP sensor	Proposed sensor with Smarth phone read out	Titration (Mohr Method)
Adriatico Seawater	0.45 (0.05)	0.48 (0.17)	0.529 (0.005)
Tirreno Seawater	0.52 (0.05)	0.36 (0.12)	0.545 (0.005)
Tap water	$0.73\ 10^{-3}$ ($0.10\ 10^{-3}$)	$0.7\ 10^{-3}$ ($0.2\ 10^{-3}$)	$0.783\ 10^{-3}$ ($0.007\ 10^{-3}$)
Reno River Water	$0.74\ 10^{-3}$ ($0.10\ 10^{-3}$)	$0.8\ 10^{-3}$ ($0.2\ 10^{-3}$)	$0.679\ 10^{-3}$ ($0.007\ 10^{-3}$)

Figure 5. Water analysis (A, B): (A) a typical real-time analysis carried out with one of the 2-terminal SP/NP-based sensor, coupled to a portable electronic readout device, wirelessly connected to a custom smartphone application; (B) Chloride concentrations measured in 4 different water samples (expressed as M) (standard deviation from 3 measurements) determined with the proposed sensor and with the Mohr method. **Textile biomedical sensor (C, D and E):** (C) Cartoon of a wearable Cl^- sensor fabricated directly onto a T-shirt; (D) Optical microscopy images of a cotton thread modified with the PEDOT:PSS/Ag/AgCl NPs composite material; (E) Source-drain current vs time plot obtained for the textile SP/NP-based sensor while the Cl^- concentration was increased in the 0.1 M KNO_3 solution by progressive additions of 1 M KCl solution.

2.5.1 Water analysis

The sensors were calibrated according to recent literature.[75] As reported by Seeber et al. for traditional electrochemical sensors, the calibration curve should be drawn considering random concentrations of analytes in order to evaluate fouling and hysteresis effects on the analytical performance. Therefore, the sensors were also randomly calibrated using solutions with different Cl^- concentrations (10^{-4} M, 10^{-3} M, 10^{-2} M, 10^{-1} M) and each solution was tested 3 times. For each repeated measurement carried out at 10^{-3}, 10^{-2}, 10^{-1} M, the standard deviation of the source-drain current value was lower than 0.3 %, however the percentage error increases to 5% when the data are expressed in terms of concentration. Such results highlight that a high repeatability is achieved with the here proposed sensors, whose robustness should be related to the Ag/AgCl redox couple that is widely used in electrochemistry to fabricate electrodes with a stable and well-known potential.

Therefore, four water samples (river, sea and tap water) were analyzed both with the here proposed SP/NP sensor and using a traditional procedure (Mohr titration)[76] (Figures 5A and 5B). The obtained results are in very good agreement (t test with probability equal to 5 %) with the ones obtained by Mohr method, thus confirming the reliability of the proposed sensor. The precision of the dedicated portable electronics is higher than the one obtained with the portable kits available on the market,[77,78] suggesting that the present sensor could be a valuable tool for easy and portable determination of ions content in water. Such a device may be employed for agricultural applications, to monitor the Cl^- content in swimming pools and SPAs, as well as to analyze river or sea waters for environmental and marine biological studies.

2.5.2 Textile biomedical sensor

The salt content in sweat is linked to the hydration status of the body, which is of crucial importance in diagnostics (for example dysentery) and healthcare (i.e. sport activity monitoring) (Figure 5 C). Therefore, the 2-terminal SP/NP based sensors were applied to investigate the Cl^- content in artificial sweat obtaining results comparable to the ones obtained in a standard electrolyte. Then, a wearable sensor was fabricated by directly depositing Ag/AgCl NPs on a cotton thread previously modified with PEDOT:PSS, so as to demonstrate that the two terminals device can be easily applied to a new and unconventional configuration that does not require a gate electrode and an electrolyte between the gate and the channel (Figure 5 D). As already observed for the sensor in the

water analyses application (Figures 5 A and 5 B), the single-fiber textile sensor exhibited a logarithmic response with increasing Cl^- concentration. The reliability of the sensor has been assessed in this case by comparing its response to increasing Cl^- concentration (Figure 5 E) with the one observed in a 0.1 M KNO_3 solution (see Figure 1). The sensitivity, expressed as normalized current, was equal to 0.051 ± 0.009 $decade^{-1}$. This value is comparable to the one observed for the devices fabricated onto planar substrates, providing the proof of principle for a thread sensor that can be easily sewed on clothes for monitoring Cl^- content in sweat.

Finally, the selectivity of the sensor was investigated (**Figure 6**). Each chemical species that affects the Ag^+ concentration can interfere with the determination. Since I^- and Br^- form salts with Ag^+ that are more insoluble than AgCl they can be detected by the sensor when their concentrations are close to the Cl^- one. Nevertheless, in sweat Br^- and I^- exhibit concentrations that are several orders of magnitude lower than Cl^-. In addition, the sensor response to compounds that are usually present in sweat at their typical concentration in human perspiration thoroughly studied.[79] In all examined cases, no interference was observed on the Cl^- determination, clearly demonstrating the reliability of the present device.

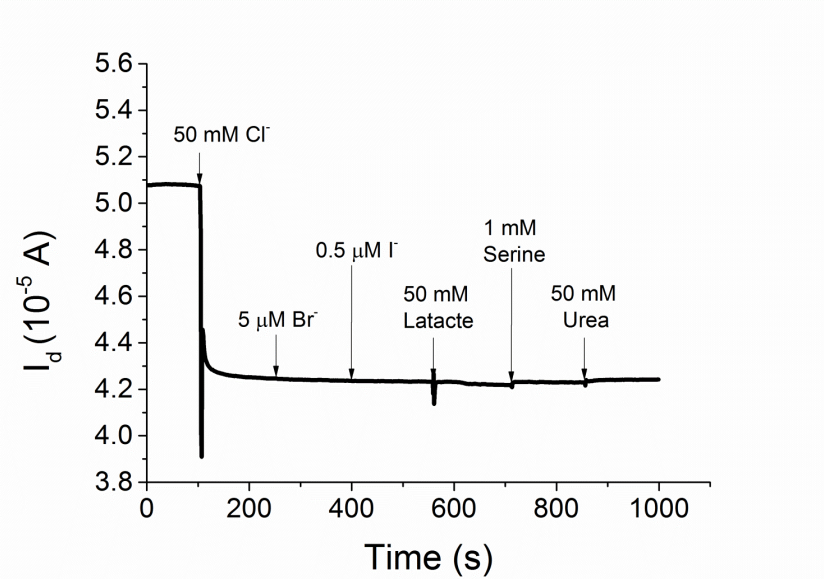

Figure 6. Interference study with different species evaluated in artificial sweat.

3. Two-terminal pH sensors operating in aqueous environment

Inspired by the transduction mechanism discussed in the previous section, two pH-sensitive materials were applied for the realization of two-terminal sensors for determinations in aqueous media targeting wearable applications. In the first case, the already discussed PEDOT:BTB transducer (Chapter IV) was electrodeposited on top of a PEDOT:PSS film to impart pH-sensitivity at zero gate bias in the output current of the two-terminal device. Following characterization on a rigid substrate, textile pH sensors were realized starting from natural and synthetic threads, whose performance is currently under evaluation in artificial sweat. The second part of this section is instead dedicated to the development of another pH-sensitive material, consisting of a composite of chemically synthesised IrO_2 and PEDOT:PSS, where the involved Ir species is a well-known pH transducer in electroanalysis. With a sensing mechanism analogous to the one demonstrated for Ag/AgCl NPs/PEDOT:PSS, the resulting composite was exploited for the realization of a two-terminal pH sensor, finally implemented in a fully-assembled, wearable patch.

3.1 PEDOT:BTB

PEDOT:BTB is a composite material, whose pH transduction ability and application as gate modifier to develop an OECT sensor for pH detection have been thoroughly discussed in Chapter IV. Briefly, the sensing mechanism comes from the pH-susceptible nature of the counterion BTB, a common pH dye, that is capable of providing $PEDOT^+$ with extra-stabilization depending on the electrolyte pH, thus leading to an overall pH-dependent conductivity of the organic material.

It is essential to underline that the electrochemical response of PEDOT:BTB relies on spontaneous redox events that follows acid-base equilibria. This can be demonstrated by the simple study of the pH response of a PEDOT:BTB film electrodeposited on a glassy carbon electrode (GCE), as illustrated in **Figure 7**. For this experiment, a conventional electrochemical setup (Fig. 7 A) was employed where the PEDOT:BTB/GCE was the Working Electrode (WE) and a saturated calomel electrode (SCE) and a Pt electrode acted as reference (RE) and counter electrode (CE), respectively. The measured signal was either (Fig. 7 B) the current recorded upon application of a fixed potential, equal to the WE Open Circuit Potential (OCP) in Universal Buffer (U. B.) at pH 2.2, or the OCP itself (Fig. 7 C) during 1 M KOH additions in the electrolyte solution (U. B.). In the chronoamperometry

experiment, it is clear that the application of a fixed potential to the WE (here E_{app} = 0.246 V vs SCE) hampers the spontaneous redox reactions that originate the pH-dependent response. Indeed, minimal current variations following base additions cannot be correlated to pH changes. Contrarily, when the Electrochemical Potential of the WE (OCP) is recorded vs time in the absence of current flow, its value changes spontaneously upon base additions, until a steady-state is achieved where the system establishes a condition of thermodynamic equilibrium. A decrease of the OCP values occurs as the pH moves towards more alkaline values, in analogy with the CV characterization showed in Fig. 6 - IV. Here, steady-state OCP values can be linearly correlated to pH variations (inset) in the already defined interval (2 – 7) with a slope equal to 45 ± 1 mV pH unit^{-1} in accordance with the Nernstian response expected for a monoelectronic process.

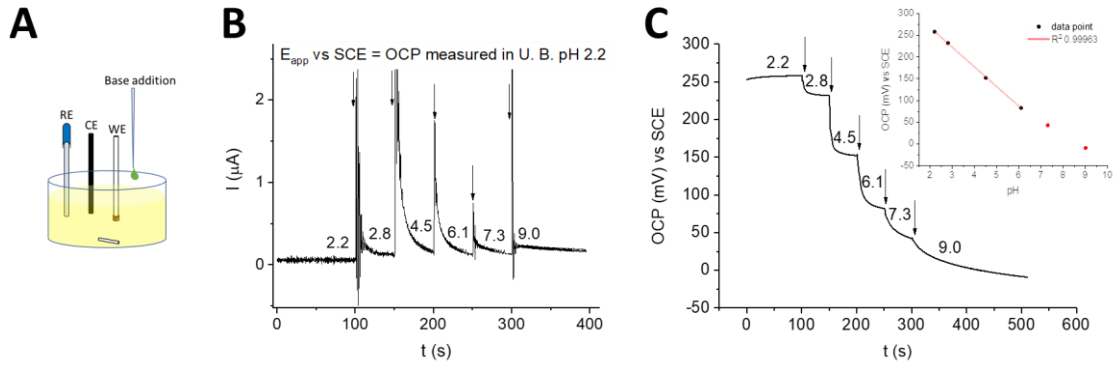

Figure 7. **Potentiometric behaviour of the PEDOT:BTB composite**. (**A**) Experimental setup used to record (**B**) chronoamperometric and (**C**) potentiometric response of PEDOT:BTB/GCE during 1 M KOH additions to a Universal Buffer solution. The inset in (C) reports the calibration plot obtained from the OCP measurement. Addition times are indicated by arrows and numbers correspond to the pH of the solution, previously assessed in a blank experiment.

Following these observations, PEDOT:BTB was electrodeposited on the gate electrode of an OECT to realize a pH sensor with the same configuration presented in Chapter IV to verify the possibility of operating in potentiostatic mode at zero gate bias (**Figure 8**). For this, a fixed potential of -200 mV was applied at the drain terminal, while no potential was applied at the functionalized gate, in a way that its Electrochemical Potential, E_g, was free to vary according to the solution pH. Therefore, I_d was recorded during base additions in U. B. (Figure 8B). It is clear that modulation of the output current is achieved through the electrolyte even if no gate bias is applied: the gate action only results from spontaneous

variations of E_g due to pH changes. The sensitivity calculated from the normalized current response (NCR) results (18 ± 2) × 10^{-3} pH $unit^{-1}$ that is sensibly higher than the one found for the OECT operated in potentiostatic mode ((14.8 ± 0.5) × 10^{-3} pH $unit^{-1}$) upon application of V_g = -0.1 V in the same pH range. This may suggest that if the OECT is used in a potentiometric-like mode, i.e. E_g is free to vary, the spontaneous gate action exerted through the solution is stronger and, consequently, a higher I_d modulation is achieved. However, such results are not very meaningful as, in this configuration, a steady-state signal is hardly achieved. Indeed, current drift can be clearly observed from Fig. 8B that negatively impacts on the quality of the correlation (Fig. 8C).

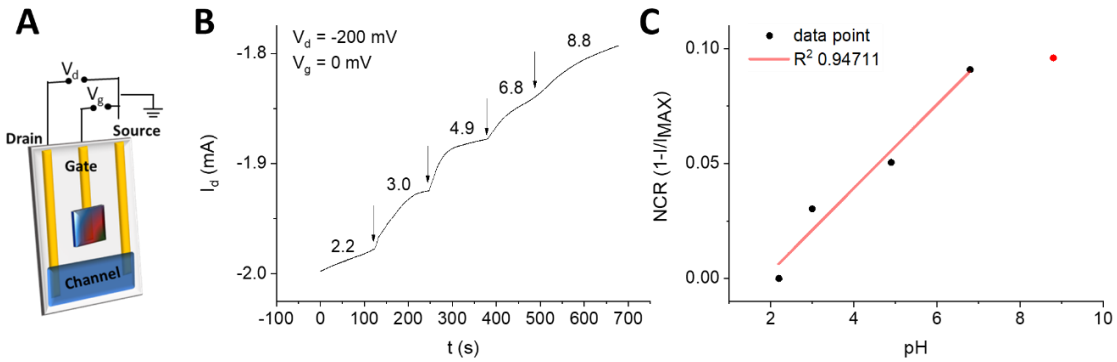

Figure 8. **Potentiostatic operation of the OECT pH sensor at zero gate bias**. (**A**) OECT configuration with the PEDOT:BTB gate electrode. (**B**) Drain current response to pH variations in Universal Buffer following base additions. No bias was applied to the gate electrode. (**C**) Normalized current response vs pH.

Once assessed that the OECT pH sensor does not require the application of a potential to the gate to perform the analysis, a simpler configuration was chosen. Here, the terminal dedicated to the control of the gate electrode was eliminated, thus yielding a two-terminal device that allows the application of only one potential (V_{app}), which serves to generate the current I flowing through the organic semiconductor channel. To provide it with pH sensibility, PEDOT:BTB was electrodeposited on top of the PEDOT:PSS layer (see Materials and Methods). A scheme of the resulting device is given in **Figure 9**A. The two-terminal pH sensor was tested in U.B., as described above, applying a fixed V_{app}, whose value was optimised in order to obtain the highest current variations and the best signal reversibility following pH changes (V_{app} = ± 50, ± 100, -200 mV were tested). Figure 9B reports the response of a two-terminal sensor in the optimized conditions (V_{app} = -200 mV).

In analogy of what observed for the tree-terminal counterpart, the current *I* is modulated according to pH variations, but shows higher stability and better defined steps if compared to Fig. 8B. As suggested for Ag/AgCl NPs/PEDOT:PSS, the electrical contact between the pH transducer and PEDOT:PSS leads to a situation where PEDOT:BTB imparts its electrochemical potential to the latter, thus directly dedoping the PEDOT:PSS layer, with improved efficacy with respect to the case in which the gate was physically separated and I_g had to travel across the electrolyte (Figure 8). In spite of that, significantly lower sensitivity to pH was calculated in the two-terminal configuration. Figure 9C shows repeatability of the sensor over 3 independent measurements, from which the average NCR sensitivity resulted equal to $(8.3 \pm 0.2) \times 10^{-3}$ pH unit^{-1} (N = 3, R^2 = 0.991). The lower sensitivity can be explained considering that in this case the transducer is electrodeposited in the form of a semiconducting layer on top of the PEDOT:PSS film, causing a significant increase of the total channel thickness.

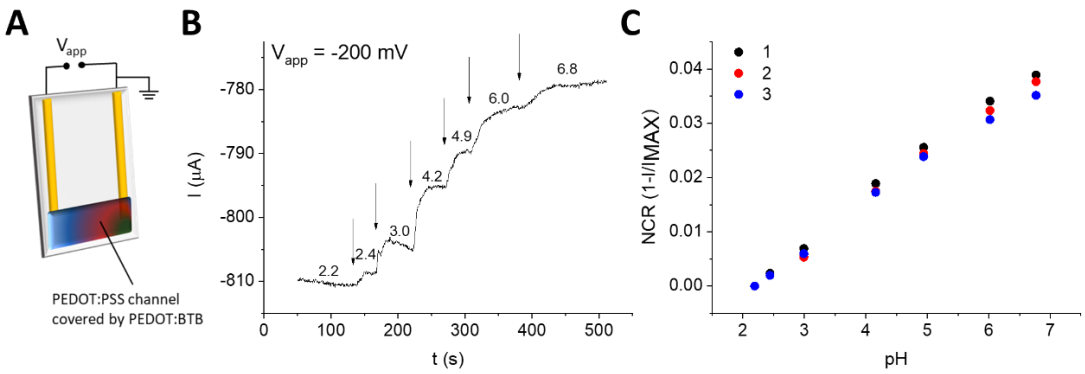

Figure 9. **Response of the two-terminal pH sensor modified with PEDOT:BTB.** (**A**) Scheme of the two-terminal sensor. (**B**) Current response to pH variations in Universal Buffer following base additions. (**C**) Normalized current response vs pH recorded for the same device in three independent measurements.

Thanks to the sensor capability to work in the two-terminal geometry, the functional channel optimized on a rigid substrate (glass) was realized on synthetic and natural threads. **Figure 10**A reports a picture of the thread pH sensor, that was realized starting from either silk, polyester or cotton threads that were rolled in a conducting ink of PEDOT:PSS, whose composition was optimized in order to achieve good plasticity and conductivity. Details about the preparation of the conducting threads and electrical contacts are given in Materials and Methods. Afterwards, the coated threads were functionalized with PEDOT:BTB, that was electrodeposited following the procedure described for the rigid substrates. Figure 10B shows an example of PEDOT:BTB electrochemical deposition on

a PEDOT:PSS/silk thread, where the well-defined redox system can be observed, together with the current increase upon cycling that originates from the progressive growth of the polymer at the conducting thread's surface. Due to the fact that the transducer is formed and deposited electrochemically, it has been essential to fabricate conducting threads with $R < 250\ \Omega\ cm^{-1}$ and minimize contact resistances (averaged resistance values for the three fibers are reported in Table 1, Materials and Methods).

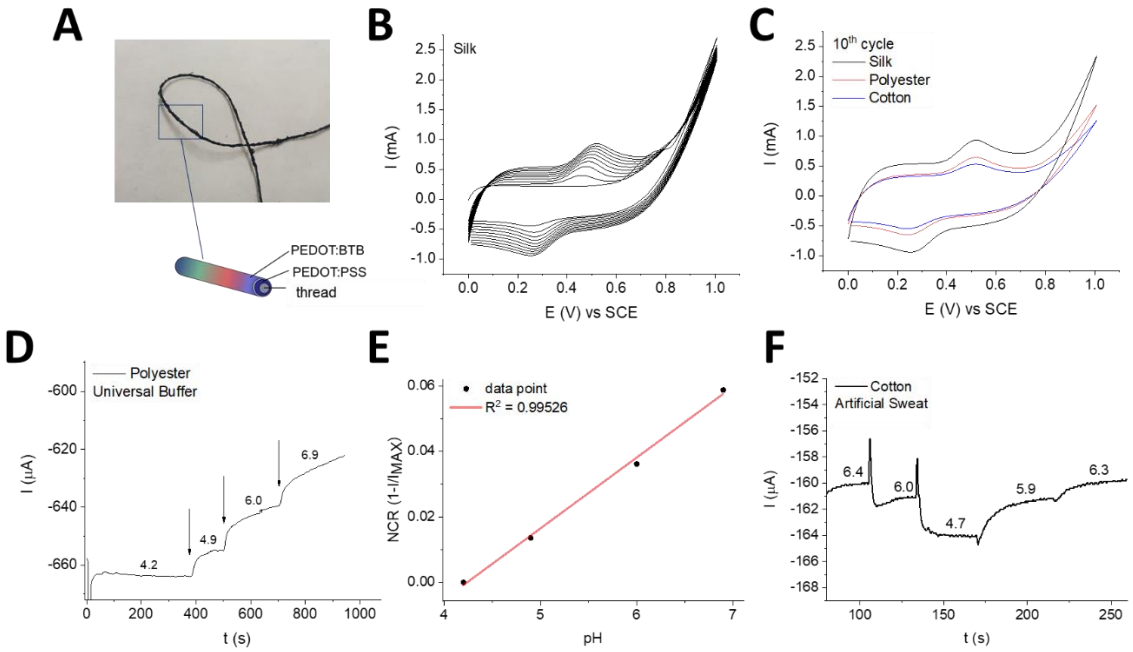

Figure 10. **Thread pH sensors functionalised with PEDOT:BTB.** (**A**) Picture and scheme of the thread sensor. (**B**) PEDOT:BTB electrodeposition on a conducting silk thread. (**C**) Last deposition cycles recorded using silk, polyester and cotton threads. (**D**) Polyester pH sensor tested in U.B. upon base additions. V_{app} = -200 mV and (**E**) correspondent Normalised Current Response vs pH plot. (**F**) Cotton pH sensor tested in Artificial Sweat upon base additions. V_{app} = -200 mV.

It is worthy of note that the fabrication procedure suffers from a certain variability and the different knotwork and physical properties (surface properties, impregnation ect.) of the textile supports play a key role in determining the final characteristics and further characterization studies are ongoing. Among the conducting threads realized using the same procedure, conducting silk threads showed the lowest resistance and the highest current intensity was recorded during electrodeposition (Fig. 10C). Overall, resistance values after PEDOT:BTB deposition increased of about 40 Ω over 2 cm long silk threads,

while a decrease of about 30 and 100 Ω was measured over 2 cm long polyester and cotton threads, respectively. However, successful functionalization of all textile supports was achieved. The thread pH sensors were therefore tested in U. B. and Artificial Sweat. Figure 10 D reports the pH response of a polyester thread sensor upon base additions in U.B. within a medically relevant pH range and correspondent calibration curve is given in Figure 10 E. The calculated NCR sensitivity was $(21.6 \pm 0.9) \times 10^{-3}$ pH unit^{-1}, which results sensibly higher that the value found for the 3-terminal glass sensor operated at zero gate bias. Finally, Figure 10 F reports the response of a cotton thread sensor tested in the same pH range in Artificial Sweat highlighting the reversibility of the response, which is a very important feature for a sensor.

3.2 IrO_2 Ps/PEDOT:PSS

Iridium oxide is a long-time consolidated pH transducer in potentiometry, with well-assed Nernstian behaviour over a wide operative pH range and long-term stability.[80-82] Recently, IrO_2 films have been used to modify a silver/stainless steel mesh to obtain a potentiometric textile pH electrode showing Nernstian sensitivity.[83] Nernstian limit has been overcome by using IrO_2 as gate electrode material in a Wheatstone bridge OECT sensor realized on a flexible polyethylene naphtalate substrate and tested in real sweat samples[84] and by the implementation of iridium oxide films grown on Si-based thin-film platinum microelectrodes and modified with urease for biomedical analysis of urine samples.[85] Iridium oxide has been employed as pH transducer also in the form of nanoparticles. For instance, a flexible potentiometric pH sensor has been obtained by ink-jet printing of iridium oxide NPs,[86] while super-Nernstian response has been reported for potentiometric sensors realised by IrOx NPs electrodeposition on stainless steel[87] and Au.[88]

In this section, the development of a two-terminal pH sensor made of a composite material that comprises IrOx particles (Ps) and PEDOT:PSS is presented, with potential in textile applications such as the assembly of wearable pH-sensing bandages.

3.2.1 Synthesis and characterization of IrO_2 particles

IrO_2 particles were chemically synthesised adapting a procedure reported in literature. $IrCl_4$ was here chosen as the starting material, a commercially available Ir(IV) salt that is cheaper

than K_2IrCl_6 used in the reference paper.[89] A 2 mM $IrCl_4$ aqueous solution was treated with 10% NaOH to promote the occurrence of the basic hydrolysis (Reaction 1):

$$IrCl_4 + 6OH^- + nH_2O \rightarrow Ir(OH)_6^{2-} + IrO_x \cdot nH_2O + 4Cl^- \qquad (1)$$

Afterwards, acidic condensation was favoured upon addition of 3M HNO_3 (Reaction 2):

$$Ir(OH)_6^{2-} + IrO_x \cdot nH_2O \underset{OH^-}{\overset{H^+}{\rightleftharpoons}} IrO_x \cdot nH_2O \qquad (2)$$

Detailed synthesis procedure is reported in Material and Methods. A deep-blue acidic suspension of IrO_2 particles was obtained at the end of the synthesis that was stable for up to 2 months if opportunely kept at 4° C and protected from light sources.

The IrO_2 Ps suspension was characterized by UV-Vis spectroscopy and Dynamic Light Scattering (DLS). Absorbance spectra of the Ps suspension recorded upon pH variations are reported in **Figure 11**A.

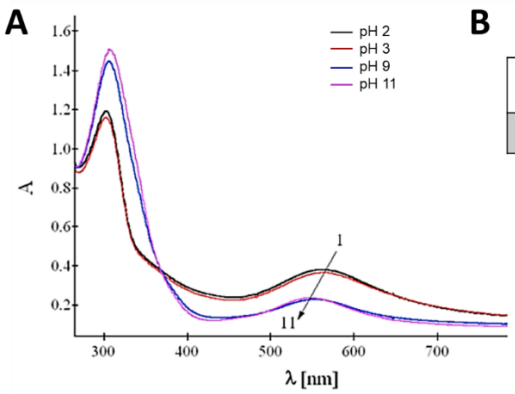

Diameter (µm)	PDI	Z potential (mV)
1.1 ± 0.5	0.3 ± 0.2	-6.2 ± 0.1

Figure 11. **UV-Vis and DLS analysis of the Ps suspension.** (**A**) Absorbance spectra recorded from Ps suspensions at different pH. (**B**) Summary of the DLS analysis with average particles' diameter and Z potential, polydispersity index of the suspension.

The isosbestic point highlights the coexistence of two absorbing species: in accordance with literature, the peaks at 304 and 574 nm can be ascribed to $[Ir(OH)_6]^{2-}$ and $IrOx \cdot nH_2O$, respectively, which are in equilibrium depending on the solution pH (Reaction 2). Diameter, Polydispersity Index (PDI) and Z potential of the IrOx Ps were determined by DLS and the results are summarized in Fig. 11B. Despite the good PDI indicating a

homogeneous distribution of the sample size, the average diameter is in the micrometre range, in contrast with the results reported in.[89] Considering the relatively low Z potential, which is associated with particles stability in the suspension, the unexpected size is likely to be due to the aggregation of sub-micrometric entities.

3.2.2 IrO_2 Ps/PEDOT:PSS composite material

After 24 h stabilization at 4°C, the acidic suspension was allowed to reach room temperature and was employed as prepared as electrodeposition solution to carry out the functionalization of a two-terminal device, as indicated schematically in **Figure 12** A. The PEDOT:PSS film was used as the working electrode (WE) in a standard electrochemical cell and its potential was swept between 0 and 1V vs SCE for 100 deposition cycles at 100 mV s^{-1}. The potential range was optimized in order to avoid PEDOT overoxidation. Current increase upon potential cycling indicates progressive growth of the material deposited at the WE (Figure 12 B). Redox systems ascribed to different Iridium species appear during deposition and are evidenced in Figure 12 C, reporting the 1st cycle voltammogram. The reversible systems A/A', B/B' and the less defined C/C' were attributed to the redox couples Ir(III)/Ir(IV), Ir(IV)/Ir(V) and Ir(V)/Ir(IV), respectively.

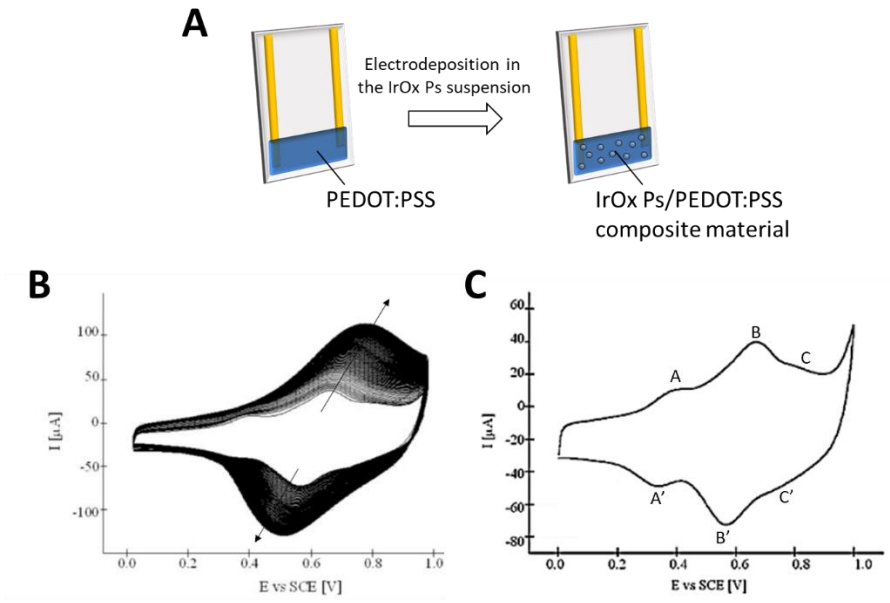

Figure 12. **Electrochemical synthesis of the IrOx Ps/PEDOT:PSS composite material.** (**A**) Schematic of the functionalization of a PEDOT:PSS two-terminal device with IrOx Ps. (**B**) Voltammograms recorded during 100 cycles deposition at 100 mV s^{-1}. The Ps suspension was used as the electrodeposition solution. (**C**) First cycle recorded during deposition highlighting the redox systems ascribed to Ir species.

Following electrochemical deposition, the composite material was characterized by SEM-EDS and Cyclic Voltammetry (CV). As stands out from **Figure 13** A, discrete particles are revealed by SEM imaging with inhomogeneous distribution on the PEDOT:PSS film. However, EDS analyses (data not shown) detect Ir over the whole polymer sample, thus not suggesting a surface-level deposition, but rather the Ps inclusion within the PEDOT:PSS film.

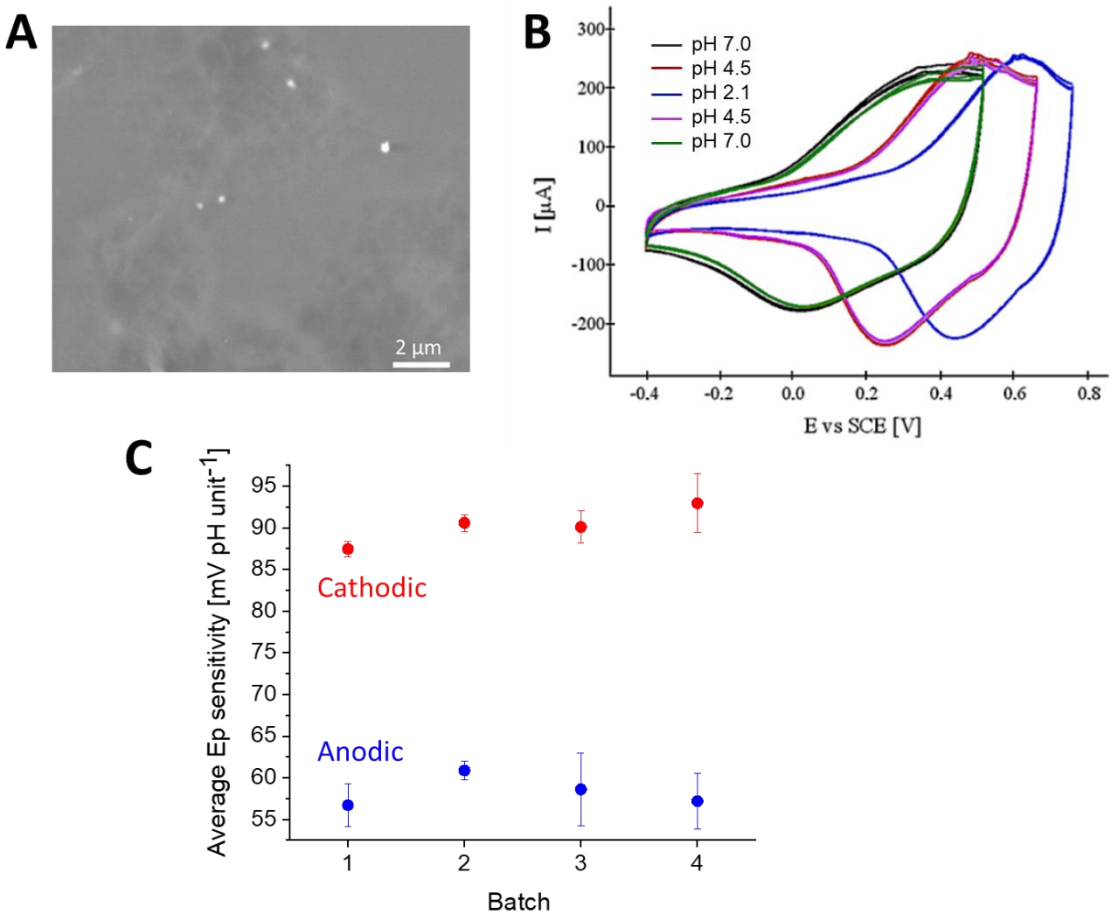

Figure 13. **Characterization of the IrOx Ps/PEDOT:PSS composite material.** (**A**) SEM picture of a sample after Ps electrodeposition. (**B**) Voltammograms recorded from a IrOx Ps/PEDOT:PSS film randomly immersed in three pH buffers. Scan rate 20 mV s^{-1}. (**C**) Plot showing the average variation of anodic and cathodic peak potentials upon pH changes vs the Ps synthesis batch. Each data point is the average calculated for N = 3 devices and bars indicate standard deviations.

Electrochemical activity of the composite films was highlighted by CV measurements in three pH buffers with the same ionic strength and are reported in Fig. 13 B. Upon random tests at different pH (in the order: 7.0, 4.5, 2.1, 4.5 and 7.0) the reversibility of the

electrochemical system is assessed and, in analogy to the observations made for PEDOT:BTB films (Chapter IV), a well-defined couple of redox peaks shifts its peak potentials (Ep) towards more cathodic values as the solution pH becomes more alkaline. Anodic and cathodic Ep of three different devices were plotted vs pH, showing linear correlation and different slopes associated to forward and backward scans, as already seen for PEDOT:BTB. In particular, cathodic Ep shifts almost double pass the anodic ones upon pH variations. With the aim to highlight the consistent reproducibility of the entire procedure, including Ps synthesis and electrodeposition, average Ep sensitivities were plotted as function of the Ps synthesis batch (Figure 13 C). The overall sensitivity values for Ep_A and Ep_C calculated among the different synthesis batches were (58 ± 2) and (90 ± 2) mV pH $unit^{-1}$, respectively.

3.2.3 Performance of the IrO_2 Ps/PEDOT:PSS two-terminal pH sensor

Following material characterization and once assessed the pH-dependent electrochemical activity of IrO_2 Ps/PEDOT:PSS composite material, the two-terminal device as described above was tested as pH sensor in U. B. (**Figure 14**). A fixed potential of -200 mV was applied to one terminal and the generated current was recorded over time during base additions. The solution pH was varied in the interval 2.2 – 9.7 and the sensor repeatability was tested by recording 3 independent I-t curves (Fig. 14 B). According with what observed from CV characterizations, the more alkaline the pH, the lower the electrochemical potential of the redox system: indeed, upon pH increase, the channel conductivity is lowered and a smaller current is recorded.

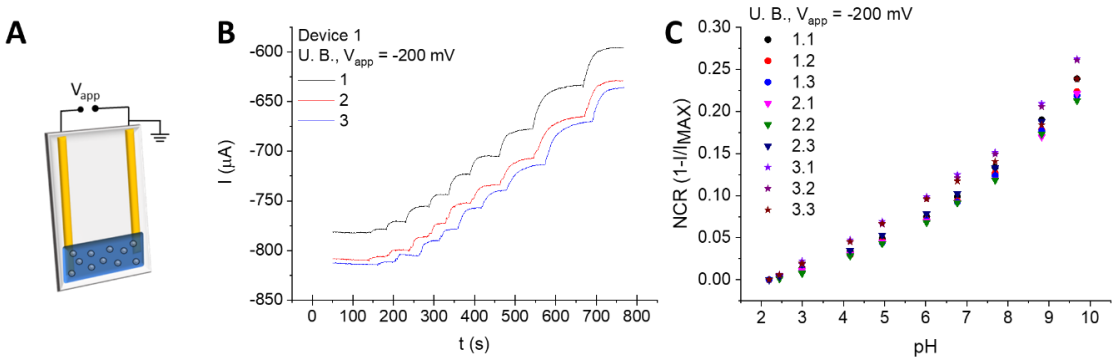

Figure 14. **Performance of IrOx Ps/PEDOT:PSS two-terminal pH sensors.** (**A**) Scheme of the resulting 2T sensor. (**B**) Current responses vs time upon base additions in Universal Buffer recorded with Device 1. (**C**) Normalized current response vs pH plots recorded with Devices 1 (dots), 2 (down triangles) and 3 (stars), tested 3 times each in U.B.

The mechanism resembles that of PEDOT:BTB/PEDOT:PSS 2T sensors. To assess the reproducibility among different devices, three identical sensors (1, 2 and 3) were prepared and tested three times each. The NCR vs pH responses are reported in Figure 14 C. Calculated NCR sensitivity resulted equal to $(23.6 \pm 0.4) \times 10^{-3}$ pH unit^{-1}, thus being the highest found among the 3T and 2T pH sensors presented in this Thesis.

In addition to the good pH sensing capability, the IrOx Ps/PEDOT:PSS composite has the major advantage to be easily obtainable in the form of an ink, thus opening the way to realize simple patterns on non-conducting substrates with a single printing step. To this aim, the formulation of a conducting ink was optimized, including IrOx Ps suspension (20% v/v) and Clevios PH1000 (69% v/v), and the 2T sensor geometry was reproduced by screen-printing through a suitable mask on a medical bandage (**Figure 15** A).

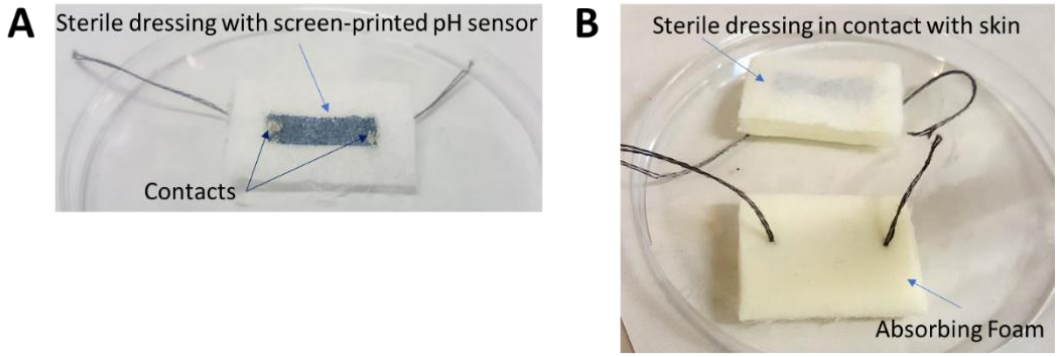

Figure 15. **Fabrication of the sensing bandage.** (**A**) 2T pH sensor screen-printed onto a medical dressing. (**B**) Fully assembled smart bandage including a protective sterile dressing and the absorbing foam, where the biofluid of interest is collected. The actual size of the fully assembled bandage is 6 cm^2.

Textile supports were kindly provided by Plastod SpA, specialized in advanced wound care and wound dressings. The printed sensor was provided with electrical connections using commercially available conducting threads that were sewed at the two extremities of the sensor, where some Ag paint served to improve the electrical contacts between the threads and the sensing material. Then, insulation of both the threads and the sewing points was obtained by application of a silicone-based sealant. The as-obtained bandage sensor was assembled in between of another sterile dressing and an absorbing foam in a sandwich-like fashion, as illustrated in Fig. 15 B. In such a way, the skin does not come in contact with the sensing part but, at the same time, collection and analysis of the biofluid of interest (either wound exudate of sweat) is facilitated. Indeed, as soon as the first drop reaches the

absorbing foam, the biofluid flow is driven through the sensing bandage due to the absorbing gradient that is established throughout the assembled materials, thus avoiding sample dilution or stagnation at the sensing part.

3.2.4 Study of the sensing mechanism

The transduction mechanism that rules the pH-sensitive response of the composite material can be interpreted in analogy to the working principle of Ag/AgCl NPs/PEDOT:PSS. However, with the aim to demonstrate that this is again the case in which the metallic particles act exactly as a gate electrode integrated within the semiconducting channel, *ad-hoc* experiments were carried out with three-terminal devices having a special geometry.

For this, a set of OECTs with an architecture that is very close to that proposed by Wrighton's group in the first papers describing OECTs[90-92] was fabricated (**Figure 16**A).

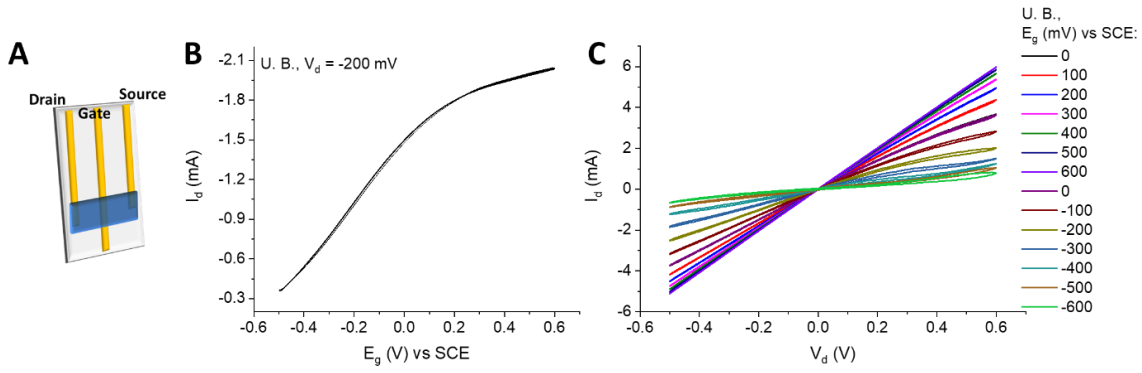

Figure 16. **OECTs inspired to the "Wrighton's geometry".** (**A**) Scheme of the device geometry. (**B**) Transfer and (**C**) Output characteristics recorded in U. B. at pH 2.2. Scan Rate 20 mV s^{-1}.

As in the commonly used geometry, the outer gold tracks are the source and drain terminals, and are connected by a PEDOT:PSS channel. The most important feature that distinguishes the "Wrighton's geometry" from the others is associated to the gate electrode. Indeed, the gate terminal (inner gold track) is longer than source and drain ones, as it was designed to allow the electrodeposition of the transducer at the gate without immersing the channel in the electrolyte solution. Such a configuration implies that the gate electrode is in electrical contact with the conductive polymer present in the channel. Therefore, if the device is operated in an electrolytic solution and connected to a potentiostat, the electrochemical potential of the channel material can be directly controlled from the gate terminal. In practice, I-V characteristics can be acquired by using a source-meter unit that

applies V_d and records the generated current I_d, while the gate bias is controlled through a potentiostat and applied vs a reference electrode, thus being addressable as the gate electrochemical potential (E_g). The transfer curve of the transistor is reported in Figure 16 B. As explained above, the gate electrode is in direct electrical contact with the PEDOT:PSS channel and, consequently, the two elements reach an equilibrium state where they have the same electrochemical potential. In other words, their Fermi Levels are aligned, as occurs at a semiconductor/metal interface. Therefore, positive E_g values cause a positive polarization of the PEDOT:PSS channel, thus leading to cations repulsion and holes injection. Electrochemically speaking, the channel material undergoes oxidation according with the reaction:

$$PEDOT + M{:}PSS \rightarrow PEDOT{:}PSS + M^+ + e^- \qquad (3)$$

where M^+ represent cationic species in the electrolyte solution. The overall result is the increased conductivity of the channel and higher I_d values are recorded. Conversely, application of negative E_g lead to channel dedoping and the consequent I_d modulation is observed. Output characteristics are showed in Figure 16 C that demonstrate that the device works as a transistor.

Following transistor characterization, the gate electrode of the OECT was modified with the pH transducer IrOx Ps by electrochemical deposition (**Figure 17** A).

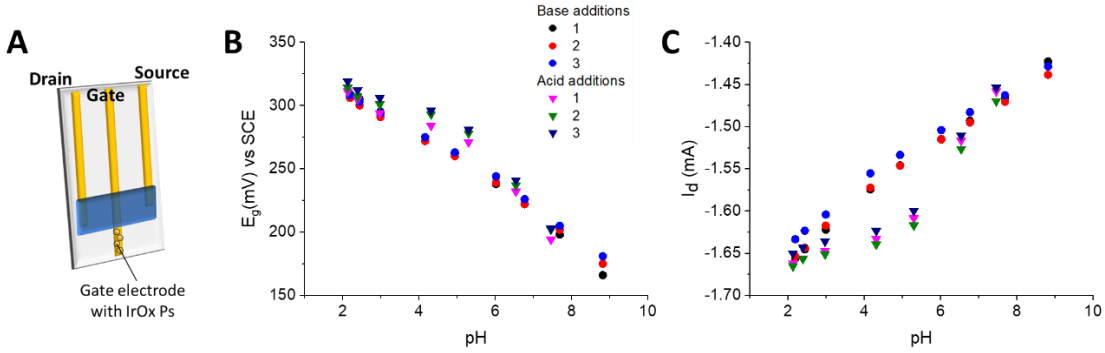

Figure 17. **Device response to pH variations.** (**A**) Scheme of the device after IrOx Ps electrodeposition of the gate electrode. (**B**) Electrochemical potential and (**C**) current variations vs pH recorded during the same experiments, where base or acid additions were made in U.B. Each experiment was repeated 3 times. V_d = -200 mV.

This situation is virtually equal to the one realized in the two-terminal pH sensor, where electrical contact between the Ps and the semiconducting polymer is obtained following electrodeposition in the polymer channel. Afterwards, both E_g and I_d were measured at the same time, through the potentiostat and the source-meter unit, respectively, during acid and base additions in U. B. (Figure 17 B, C). A fixed potential was applied to the drain electrode (-200 mV) and each measurement was repeated 3 times.

Therefore, the measured values for E_g and I_d that are reported in Fig. 17 B, C were averaged and plotted together to obtain the graph showed in **Figure 18** A. This graph already suggests that a correlation between the two parameters exists, resulting from the fact the electrochemical potential of the gate controls the transistor behaviour.

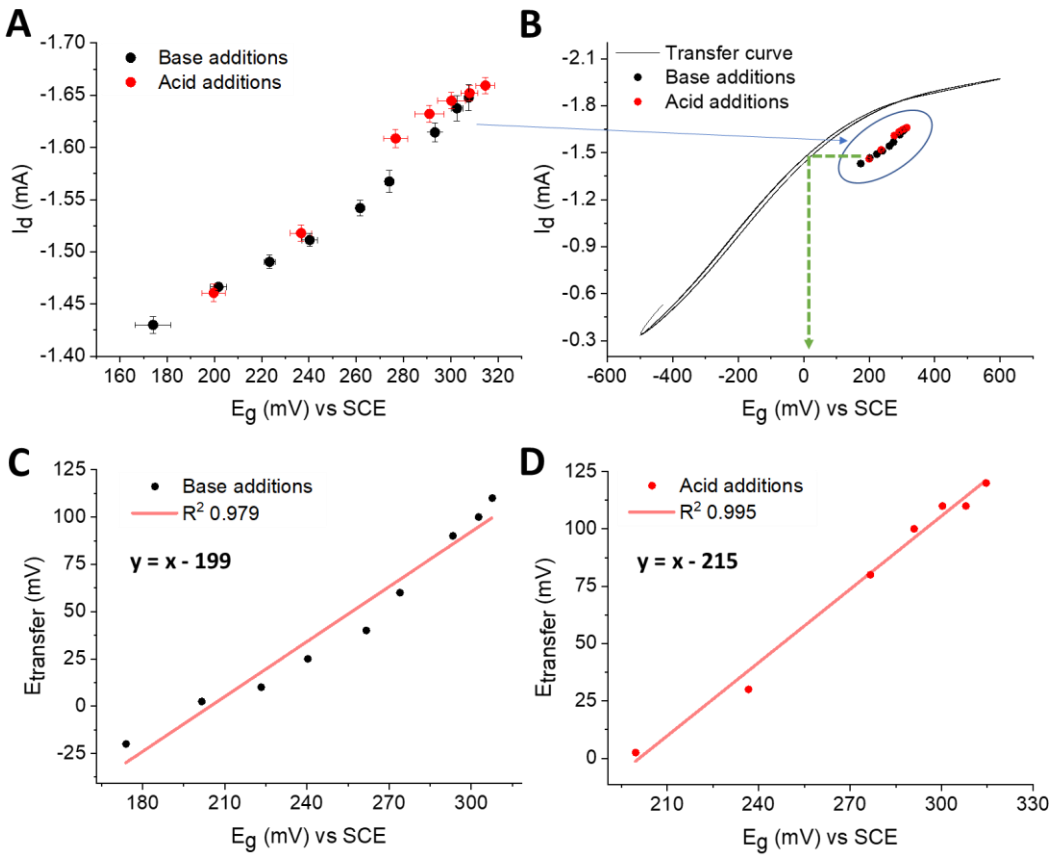

Figure 18. **The transistor response is controlled by the electrochemical potential of IrOx Ps.** (**A**) I_d vs E_g plot obtained from the measurements presented in Fig. 17 B, C. (**B**) Extraction of $E_{transfer}$ values from the transfer curve. $E_{transfer}$ vs E_g plots corresponding to the OECT responses during (**C**) base and (**D**) acid additions in U.B.

For each data point, an $E_{transfer}$ value was extracted from the transfer curve, as illustrated in Fig. 18 B. Finally, $E_{transfer}$ values were plotted as function of the measured E_g during base/acid additions (Figure 18 C, D, respectively). In both cases, a linear correlation was found with slopes equal to 0.97 ± 0.08 and 1.07 ± 0.05 for base and acid addition experiments, respectively, thus demonstrating that the transistor response is ruled by a variation of the electrochemical potential of the Ps deposited on the gate electrode.

4. Two-terminal pH sensor operating in gaseous environment

As discussed in Section 1, another class of wearable devices that is attracting a great deal of interest is that of *outward looking* sensors. The work presented in the following is focused on the development of a two-terminal device that is capable to detect a volatile, hazardous molecule like ammonia, whose vapours exposure can cause severe respiratory issues and is recognized as bio-threat for operators working in many industrial context.[93] In order to provide a 2T device with ability to perform NH_3 sensing, the acid-base nature of the analyte was exploited. Indeed, the presence of NH_3 can be detected by means of a pH sensitive transducer and, for this, IrO_2 Ps/PEDOT:PSS was chosen since it showed the best performance in aqueous environment. However, aiming at the design of a gas sensor, it has been necessary to build up a suited interface to assist the interaction of the solid-state sensor and the gas phase.

4.1 Design of the Two-terminal gas sensor

The starting platform of choice for the fabrication of the 2T gas sensor for NH_3 detection was the IrO_2 Ps/PEDOT:PSS based pH sensor presented in Section 3. The device as such is able to work in aqueous environment, where the pH modulates of the output signal due to doping/dedoping processes involving PEDOT as long as cations exchange with the electrolyte solution occurs. Differently, NH_3 sensing has to be performed in gaseous matrices and, therefore, it was necessary to provide the device with a semi-solid, electrolytic interface that could mimic the aqueous environment. For this, the formulation of an Agarose-based hydrogel was optimized to guarantee adhesion and good mechanical match with the polymer channel, robustness and capability of reversible adsorption of the gaseous analyte. In particular, 0.7% wt. Agarose was solubilized in 0.1 M KNO_3

containing 100 mM NH_3. For Agarose, the minimum concentration was chosen that allowed reticulation of the gel, while the addition of ammonia served to neutralize the pristine acidic character of the gel. The hydrogel layer was deposited on the device by dip-coating and allowed to reticulate by cooling down to room temperature. Following this, an additional step of immersion in glycerol was necessary to partially substitute and better stabilize water molecules inside the hydrogel film by H-bonds formation. The modification of the 2T pH sensor with the hydrogel interface is schematically reported in **Figure 19**. The resulting device showed impressive stability, maintaining unaltered aspect and humidity for up to 3 weeks, even if stored in dry conditions.

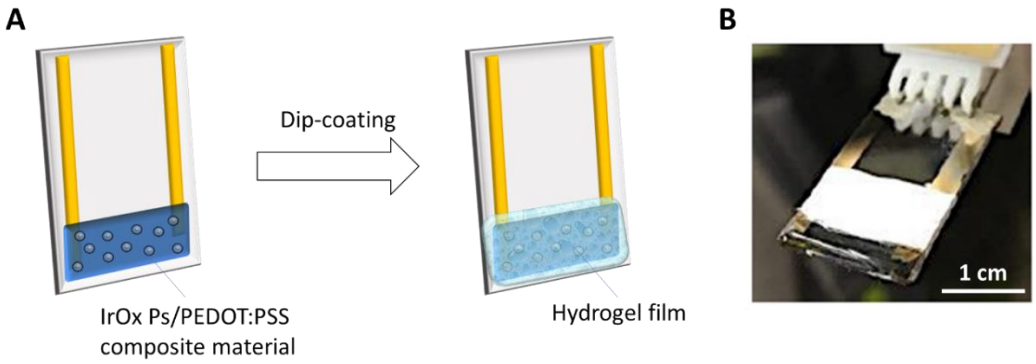

Figure 19. (**A**) Schematic of the 2T gas sensor assembly. (**B**) Picture of the resulting device. Teflon tape was used to protect the gold tracks during dip-coating.

4.2 Study of the sensor response

In order to expose the 2T sensor to a gaseous atmosphere with controlled NH_3 vapours content and therefore be able to study the sensor's response to different concentrations of $NH_{3,\,gas}$, a bench-size stripping system was built inside a lab fume hood. Briefly, a pump for atmospheric sampling was used to drive the gas flow, alternatively coming from two Drechsels containing water and NH_3 aqueous solutions of known concentration, throughout a detection chamber hosting the sensor and accurately sealed to avoid gas leakage. The system was calibrated by means of a validated analytical method (titration) to establish the exact correlation between $[NH_3]_{liq}$ and $[NH_3]_{gas}$. The experimental conditions were therefore set, with a constant gas flow fixed at 2 L min^{-1}. As the carrier gas, laboratory air was chosen so as to resemble real-life conditions and a valve served to

alternate the humid air flow to NH_3-containing air, which was delivered to the detection chamber for a fixed time of 100 s. A constant V_{app} of -200 mV was applied to one terminal of the sensor using a source-meter unit and the generated current was recorded as a function of time. In the described experimental conditions, the output signal of the 2T sensor was found to reversibly vary in the presence of increasing amounts of NH_3 in the gas flow (**Figure 20** A). Despite the fast response time (< 60 s in this stripping plant), the recovery of the initial baseline was waited after each 100 s long exposition to the analyte, resulting in a very high recovery time. The I variations with respect to the baseline was here used as analytical signal, showing linear dependence with the logarithm of $[NH_3]_{gas}$ with R^2 equal to 0.99965 (Figure 20 B). Therefore, the sensor can be used for the analytical quantification of NH_3 content in gas phase.

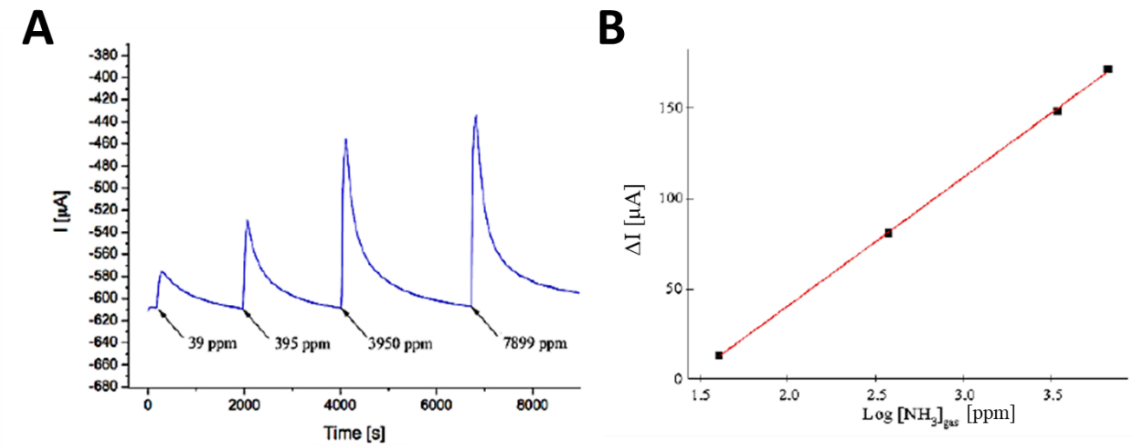

Figure 20. **Gas sensor response.** (**A**) Current vs time trace recorded by alternating air and NH_3-containing air in the detection chamber. Time of exposition to the analyte vapours was 100 s, V_{app} -200 mV. (**B**) Corresponding calibration curve.

On the basis of the considerations made in the previous section for the 2T pH sensor and its response observed during gas detection, the response mechanism can be hypothesised as follows. As soon as the analyte vapours reach the sensor, NH_3 is adsorbed as diffuses throughout the gel phase. Concurrently, pH of the aqueous environment provided by the hydrogel changes, becoming more alkaline in dependence of NH_3 concentration. As the pH of the environment surrounding the pH transducer IrO_2 Ps/PEDOT:PSS varies, the electrochemical potential of the particles decreases spontaneously, thus promoting holes

extraction from the semiconducting polymer and leading to a decrease of the current flowing through the channel. After 100 s, when the gas flow is changed to deliver the humid air flow to the chamber, NH_3 is progressively desorbed from the hydrogel, which in turn establishes its pristine pH condition, and the measured *I* slowly recoveries the starting value.

4.3 Sensor performance in real-life conditions

Once assessed the possibility to perform quantitative analyses for ammonia detection in gas phase, the performance of the 2T sensor was evaluated in experimental conditions that were considered closer to a real application. For this reason, the sensing capability was verified in a case where the baseline is not recovered (**Figure 21** A). In this case, the humid air flow was delivered for 600 s between successive NH_3-containing streams. The result was compared with the response reported in Fig. 20. Not only the current variations are still consistent within the same concentration range, but also sensitivity values are comparable, as showed in Figure 21 C. Moreover, the response time is unaffected by the baseline recovery, while detection limits slightly change. In these conditions, repeatability and reproducibility of the optimized sensor were assessed.

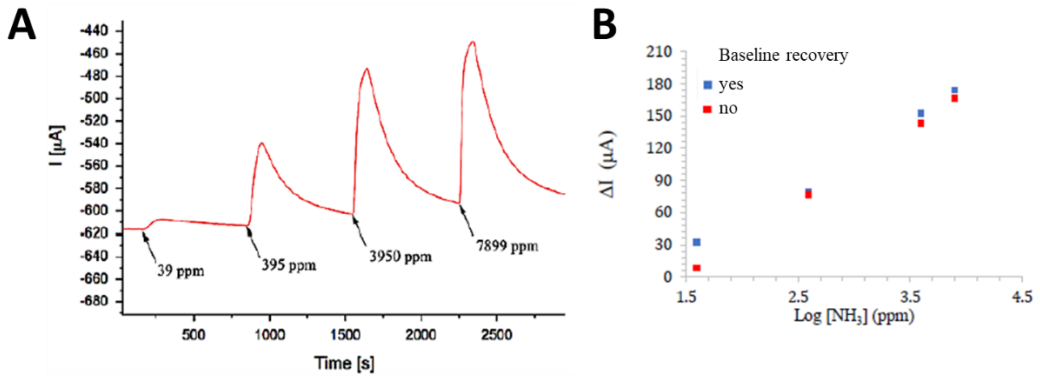

C

Baseline recovery	Sensitivity [µA decade^{-1}]	LOD [ppm]	Response time [s]
yes	64 ± 6	11	55
no	68 ± 1	15	55

Figure 21. **Gas sensor performance in real-life condition.** (**A**) Current vs time trace recorded by alternating air and NH_3-containing air in the detection chamber and without waiting the baseline recovery. Time of exposition to the analyte vapours was 100 s, recovery time was 600 s, V_{app} -200 mV. (**B**) Comparison between the two experimental conditions in terms of current variations and (**C**) summary of the sensor figure of merits in the two cases.

Additionally, the sensor response was assessed during exposition to random NH3 concentrations in the gas phase. The result is reported in **Figure 22** A and compared with the one obtained upon delivery of increasing concentrations (Fig. 22 B). In this case, a lower sensitivity was calculated (51 ± 5 μA decade^{-1}).

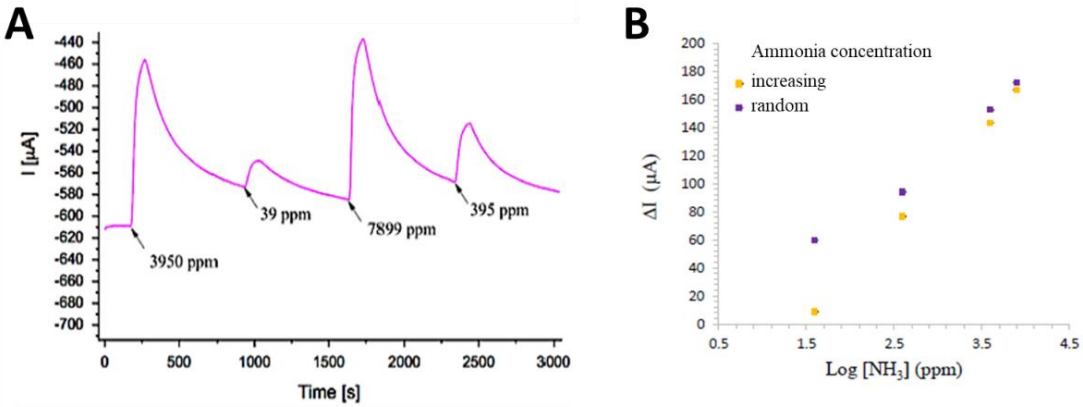

Figure 22. **Response to random concentrations.** (**A**) Current vs time trace recorded upon sensor exposition to random ammonia concentrations. Time of exposition to the analyte vapours was 100 s, recovery time was 600 s, V_{app} -200 mV. (**B**) Comparison between the two experimental conditions (increasing and random analyte's concentration) in terms of current variations.

5. Materials and Methods

Chemicals and Buffers. CLEVIOS^{TM} PH 1000 suspension (PEDOT:PSS) was purchased by Heraeus. (3-glycidyloxypropyl)trimethoxysilane (GOPS), sodium dodecylbenzenesulfonate, potassium nitrate, silver nitrate, potassium hydroxide, agarose, glycerol, poly(ethylene glycol) (PEG) and boric acid were purchased by Sigma Aldrich. Monobasic potassium phosphate and potassium chloride were bought from Fluka. Ethylene glycol (EG) was obtained from Carlo Erba. $IrCl_4$ was purchased by Alfa Aesar. Silicone elastomer and curing agent for preparation of PDMS were obtained from Sylgard. Silicone sealant was purchased by Pattex. For all chemicals and buffers used for pH sensing in aqueous environment, refer to Materials and Methods - Chapter IV.

Sensors fabrication in planar geometry (two-terminal). The device is composed by two parallel Cr/Au electrodes (distance of about 1 cm) that work as source and drain and a PEDOT:PSS stripe between them. The conductive materials are deposited on a glass slide

with the following procedure. The Cr/Au (50 nm) stripes were deposited via thermal evaporation by using a mask. Then, the PEDOT:PSS is deposited to partly overlap the two gold electrodes gold to obtain an electrical contact between gate and source electrode. CLEVIOS^{TM}PH 1000 suspension was mixed with ethylene glycol (secondary dopant), dodecylbenzene sulfonic acid (surfactant), and 3-glycidyloxypropyltrimethoxysilane (cross linker) in the following volumetric ratio 78.95:20:0.05:1. The solution was sonicated for 10 min before spinning. The substrates were cleaned in sequential sonicating baths of deionized water, acetone and isopropanol for 15 min. Then, the substrates were masked and the PEDOT:PSS solution was spun cast at 500 rpm, obtaining a film with a thickness of 800 nm.

- Ag/AgCl NPs were prepared by electrodeposition using a three electrodes cell setup (working electrode: device; reference electrode: saturated calomel electrode (SCE); counter electrode: Pt wire) connected to a potentiostat (CH instruments Scanning Electrochemical Microscope). Ag NPs were deposited by applying -0.2 V for 30 s while PEDOT:PSS was dipped in 0.1 M $AgNO_3$ solution. Then, the device was washed with distilled water and, after that, the Ag/AgCl composite was formed by applying +0.6 V for 30 s in 1 M KCl solution. Prior to use, PEDOT:PSS modified with Ag/AgCl NPs was soaked in 1 M KCl for two hours in order to hydrate the conductive polymer film.

- PEDOT:BTB was electrosynthesised by cyclic voltammetry, following the same procedure described for the functionalization of the gate electrodes in the OECT pH sensors (Chapter IV). Briefly, the Polymerisation Solution (PS) was made of 10 mM EDOT, 1 mM BTB and 1 mM PBS (pH 7.0) in 0.1M KNO_3 aqueous solution as the solvent. The PS was stirred for 15' and then electrodeposition was carried out in a three-electrode cell, where the two terminals of the device were shorted together and connected to the WE (a Pt wire and a SCE were CE and RE, respectively). A potential wave ranging from 0 to 1V vs SCE was applied to the WE with a scan rate of 0.1 V s^{-1} for 5 cycles. After electrodeposition, the blue iridescent film of PEDOT:dye covering the polymer channel was rinsed with distilled water.

- IrOx particles were chemically synthesised starting from a 2 mM $IrCl_4$ aqueous solution. 10% wt. NaOH was added dropwise to brown solution under stirring, until

the solution pH turned basic giving a light yellow color. The solution was then heated at 90° C for 1h under stirring, until a homogeneous light blue color appeared. Therefore, it was fast cooled down in an ice bath and 3M HNO_3 was added dropwise until the solution pH turned acid. Finally, the solution is kept under stirring for 80 minutes at room temperature. At the end of this procedure, the dark-blue suspension containing IrOx particles was left at 4°C, protected from light sources, for 24 h. Prior to use, the suspension was allowed to reach room temperature. It was stored at 4° C for a maximum period of 2 months. Once synthesised, the suspension as such was employed as electrolyte solution to carry out the Ps electrodeposition. A standard electrochemical cell was used where the polymer film of a two-terminal device was the WE, a Pt wire and a SCE were CE and RE, respectively. Here, the potential was scanned between $0 < E < 1$ V vs SCE for 100 cycles at 100 mV s^{-1}. The sensor was then thoroughly rinsed with distilled water and stored at ambient conditions.

- As for use as gas sensor, the as described IrOx Ps/PEDOT:PSS film was coated with an agarose hydrogel. A 0.7 % wt. agarose solution in 0.1 M KNO_3 containing 100 mM NH_3 was prepared and heated at 90° C, until a viscous and clear mixture was obtained. It was then allowed to cool down at 40 - 50° C. Teflon tape was applied to the 2T sensor to protect the gold tracks and the gel was deposited by dip-coating inside the warn agarose mixture. Once reached room temperature, the hydrogel forms spontaneously onto the device. After that, the device was immersed in glycerol for 20 minutes and then left at room temperature for 1 h.

Textile sensors fabrication.

- For thread Chloride sensors, a solution of PEDOT:PSS Clevios PH1000 with 1% GOPS and 20% of EG was prepared and sonicated for 10 minutes. In order to obtain the suitable viscosity for the deposition, the solution was warmed up in an oven at 70°C to lose about 40% of the initial weight. Then, a cotton fiber was rolled in the dense solution and annealed at 70°C for 30 minutes. The procedure was repeated twice in order to obtain a homogenous conductive fiber with a resistivity of 70 Ohm/cm. The Ag/AgCl NPs were deposited on a 2 cm long cotton wire modified with PEDOT:PSS. Ag NPs were deposited by applying -0.2 V for 120 s while the PEDOT:PSS was dipped in a 0.1 M $AgNO_3$ solution. The device was subsequently washed with distilled water

and, later, the Ag/AgCl composite particles were formed by applying +0.6 V for 120 s in 1M KCl solution.

- For thread pH sensors, a solution of PEDOT:PSS Clevios PH1000 with 1% v/v GOPS, 15% v/v EG and 10% w/w PEG was prepared and sonicated for 10 minutes. Then, the same procedure described above was followed for the preparation of cotton, polyester and silk conductive threads (2 cm length). Electrical contacts were made using Ag paste to cover a knot made between the PEDOT-coated threads and a commercial conducting thread. Insulation of the contacts was made with PDMS. For this, silicone elastomer and curing agent were mixed in a ratio 10:1 and stirred for 10 minutes. Then, the knots with Ag were coated with few drops of the mixture, which was allowed to polymerize for 20 minutes at 100° C. The resulting threads showed average resistance values as reported in **Table 1** (N = 3). Afterwards, PEDOT:BTB was electrodeposited on the threads with same procedure described for the rigid substrates for 10 cycles. After that, the thread sensors were thoroughly rinsed with distilled water.

Thread	Resistance [Ω cm^{-1}]
Silk	100 ± 10
Polyester	250 ± 50
Cotton	400 ± 100

Table 1. Resistance of the conducting threads.

- Smart bandages for pH sensing were fabricated through the procedure described in the following. A conducting ink was made with 69% v/v PH1000, 20% v/v IrOx Ps suspension, 10% v/v and 1% v/v GOPS. In order to obtain the suitable viscosity for the deposition, the ink was warmed up in an oven at 70°C to lose about 40% of the initial weight. Then, a mask was employed to screen-print the desired sensor pattern (2 x 0.5 cm^2 stripe) onto a sterile dressing (Royale 100, Plastod SpA), which was then allowed to dry for 10’ at 40° C. Afterwards, commercial conducting threads were sewed at the edges of the printed sensor and the knots were coated with Ag paste and insulated with silicone sealant. Therefore, the printed bandage was assembled in a sandwich-like

fashion in between another sterile dressing (Royale 100, Plastod SpA) and an absorbing foam (3.5 mm, Plastod SpA).

Cl^- measurements. A bipotentiostat (CH Instrument 900 B Scanning Electrochemical Microscope) was mainly used to perform the electrical measurements. The source collector was connected to the reference and counter electrode terminals of the bipotentiostat. Two different measurements were carried out to study the sensor performances. In all configurations, a potential equal to 10 mV was applied to the PEDOT:PSS stripe while the current was measured. In the first configuration, the sensor was dipped in 0.1 M KNO_3 solution containing 10^{-4} M KCl under stirring and, after current stabilization, different amounts of 1 M KCl were gradually added to the electrolyte. This kind of measurement was performed with both planar and textile devices. In the second experiment, the sensor was randomly dipped in a 0.1 M KNO_3 solution containing Cl^- at different concentrations (1×10^{-4}, 1×10^{-3}, 1×10^{-2}, 1×10^{-1} M). All solutions were tested at least three times for the evaluation of the response repeatability. The measurements were also performed by used a read-out electronics wirelessly connected to a custom smartphone application kindly provided by Elements s.r.l..

pH measurements. In analogy to what described above, a bipotentiostat (CH Instrument 900 B Scanning Electrochemical Microscope) was mainly used to perform the electrical measurements with the 2T PEDOT:BTB/PEDOT:PSS sensors, where the source collector was connected to the reference and counter electrode terminals of the bipotentiostat. In all configurations, a potential equal to -200 mV was applied to the second terminal of the 2T device and the generated current was measured. All tests were performed in 0.1 M KNO_3 Universal Buffer or Artificial Sweat, where the solution pH was changed upon dropwise addition of 1 M KOH or 1 M HNO_3 under gentle stirring. The exact solution pH value after each addition was determined in blank experiments with a glass electrode connected to a pH-meter.

Quantification and sensing of gaseous NH_3. A bench-size stripping system was built inside a lab fume hood, in order to obtain ammonia rich vapours of controlled concentration from ammonia aqueous solutions (**Figure 23**). A pump for atmospheric sampling was used to apply a vacuum to the sample line and drive the gas flow, alternatively coming from a Drechsel containing water or NH_3 aqueous solutions of known concentration, throughout

a detection chamber hosting the sensor and accurately sealed to avoid gas leakage. Active carbon filters were positioned in the head part of the system to avoid contamination of organic species traces in the air of the lab.

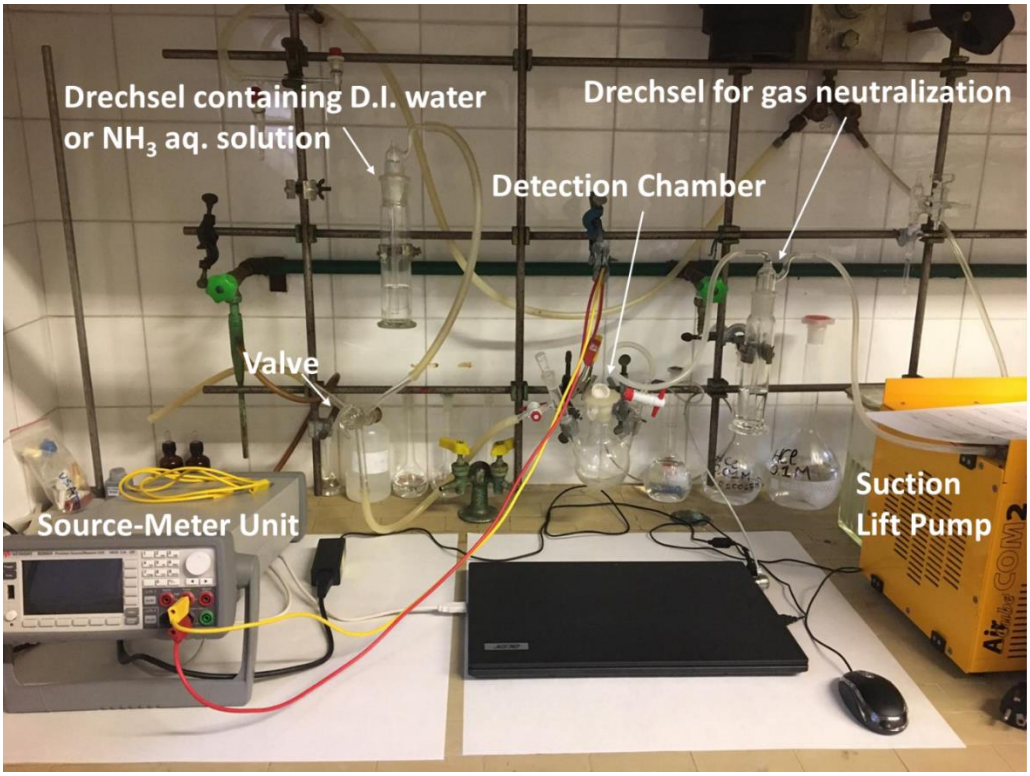

Figure 23. Picture of the bench-size system employed for NH_3 stripping.

The system was calibrated by means of a validated analytical method (titration) to establish the exact correlation between $[NH_3]_{liq}$ and $[NH_3]_{gas}$. For this, a modified version of the Kjeldahl method was chosen[94] that consisted in two steps: (i) complexation of $NH_{3,\,gas}$ with boric acid (0.1 M solution) to form $(NH_4)B(OH)_4$ and (ii) potentiometric titration with standardized 0.01 M HCl. Consequently, the equation correlating $[NH_3]_{liq}$ and $[NH_3]_{gas}$ in the as described stripping system was obtained (**Figure 24**). Ammonia determination with the 2T gas sensor based on IrOx Ps was then carried out by placing the device inside the detection chamber. Only the sensing part of the device was exposed to the gas flow, while the gold tracks were kept outside the chamber and connected to a Source-measure Unit (Keysight B2902A). One terminal was grounded, a fixed potential of -200 mV was applied to the other and the generated current was measured vs time. Humid air flow was used as the carrier gas with a fixed flow rate of 2 L min^{-1}. The carrier gas and NH_3-containing air ($[NH_3]_{gas}$ known from the system calibration) were alternatively delivered to the detection

chamber by rotating a valve. NH_3-containing air was always dispensed for 100 s. For the experiments where the baseline recovery was not considered, a fixed recovery time was set at 600 s, in which carrier gas only was delivered to the chamber.

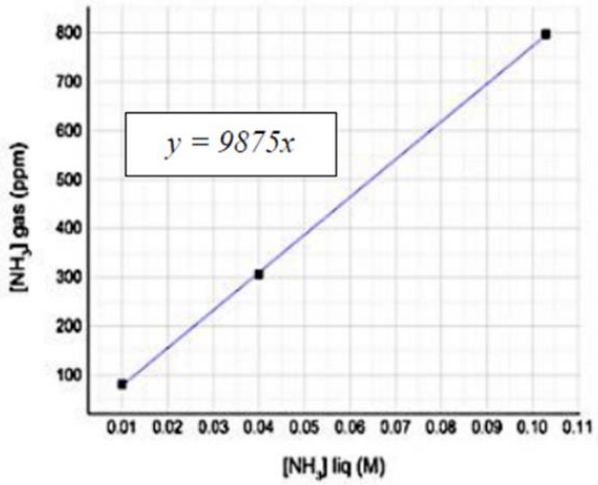

Figure 24. Calibration of the system developed for ammonia stripping from aqueous solution of known concentration.

AFM and KPFM characterization. Measurements combining AFM with KPFM were performed with a Park NX10 system operated in noncontact mode using Point Porbe Plus (PPP)- Non Contact/Soft Tapping Mode (NCST) Au probes (nanosensors). In the KPFM mode, an AC signal of 1 V was applied to the tip at 17 kHz. Measurements were carried out under controlled ambient conditions. The same tip was used for all measurements. Tip wear effects could be excluded here due to strict noncontact operation minimizing mechanical shear forces between sample and tip. In order to evaluate the absolute scale of work function, a surface potential of pure Au was measured and used as reference value.

EIS. Electrochemical Impedance Spectroscopy measurements were performed with an Autolab potentiostat (PGSTAT 204 equipped with FRA32M module) in a three-electrode cell using 0.1 M KCl as electrolyte solution. The same PEDOT:PSS channel was used pristine and after Ag/AgCl NPs electrosynthesis as working electrode, while a Pt wire and a SCE acted as counter and reference electrode, respectively. The spectra were recorded at the samples' OCPs (open circuit potentials) by applying a sinusoidal waveform with 10

mV amplitude and frequency ranging from 0.1 to 100,000 Hz. Fitting and simulation procedures were carried out with NOVA software.

UV-Vis and DLS characterizations. UV-Vis measurements were performed using a Hewlett-Packard 8453 diode array spectrophotometer. The IrOx Ps suspension was diluted in distilled water (dilution factor 2.5) and four samples at different pH were prepared upon addition of 1% NaOH. The samples were tested in a quartz cuvette in the wavelength range 200 – 800 nm. For the DLS analyses, IrOx Ps suspension was tested as such and diluted with distilled water (1:1) using a Zetasizer Nano, Malvern Panalytical.

6. Conclusion

In conclusion, an innovative, material-based strategy to integrate the amplified electrochemical response and sensitivity of a three-terminal OECT into a simpler two terminal device was presented in this Chapter, with potential to pave the way for a new generation of electrochemically gated smart sensors.

In Section 2, the use of functionalized metallic nanoparticles that add a reversible charge transfer process between the semiconducting polymer and the analyte was introduced. In order to demonstrate this strategy, the novel SP/NP composite material was thoroughly investigated and showed that the spontaneous interaction between the NPs and Cl^- ions present in the sample solution is directly coupled to the charge transfer process into the semiconductor, inducing a fast modulation of the channel conductivity. As a result, the current flowing in the channel is directly related to the logarithm of Cl^- concentration. The proposed sensor maintains the high sensitivity associated to the transistor design and can be easily adapted to unconventional configurations (e.g., threads), thanks to the simpler architecture. The reliability of the sensor was clearly demonstrated by analyzing real-life samples and achieving output values comparable to the ones obtained with traditional calibration methods. The potentiality of the new material has been further established by directly embedding the sensor into a cotton thread, thus implementing a wearable sensor application that is not feasible with traditional technologies. Moreover, the 2-terminal device configuration offers great advantages over a three-terminal device, including simpler read-out electronics as well as an easier integration in portable and wearable devices. Remarkably, since the solution under investigation just stands for the sample (it

is not a circuit element of transistor), its electrical features do not affect the sensor operation and its applicability. Therefore, the here-proposed approach offers a new technological platform for the development of portable and wearable sensors through the smart design of the sensing material.

In Section 3, the possibility to exploit the abovementioned strategy was explored to develop two-terminal pH sensors based on the already presented PEDOT:BTB (Chapter IV) and a newly designed composite material including IrO_2 particles and PEDOT:PSS. The spontaneous variation in the electrochemical potential of the composite materials upon pH variations was verified in both cases, suggesting a potentiometric-driven response of the sensor that is the key feature to realize the two-terminal configuration. The pH sensors performances, characterized on a glass substrate during pH determination in Universal Buffer (N = 3), are summarized in **Table 2**:

Sample	NCR Sensitivity (pH unit $^{-1}$)	pH range
IrOx Ps/PEDOT:PSS	23.6 ± 0.4 x 10^{-3}	2 - 10
PEDOT:BTB/PEDOT:PSS	8.3 ± 0.2 x 10^{-3}	2 - 7

Table 2. **2T pH sensors performance.** Sensitivity and operation range of the two-terminal sensors realized on glass and tested in Universal Buffer. In both cases, V_{app} = -200 mV.

In spite of the lower sensitivity showed by the all-polymeric composite, a wearable thread-sensor was realized based on PEDOT:BTB using synthetic and natural fibers. The sensor realized on a polyester thread overperformed the glass-supported counterpart with a sensitivity of (21.6 ± 0.9) × 10^{-3} pH unit^{-1} calculated under the same experimental conditions. Moreover, a proof-of-principle measurement with a cotton thread-sensor operating in Artificial Sweat within a medically relevant pH range was carried out. Reproducibility, washability and interference studies are ongoing, with the final aim to design a multiplexed platform for biofluid sampling and analysis. As for the IrOx Ps/PEDOT:PSS transducer, its major advantage of being obtainable in the form of a conducting ink, as an alternative to the electrodeposition method, allowed the design of screen-printed, prototype smart bandages. Such wearable patches were realized using

medical dressings assembled with an absorbing foam that provides effective collection of the biological fluid of interest, such as sweat or wound exudate, for real-time pH monitoring. The smart patches are presently provided with an adhesive layer and assessment of the sensing ability is on the way by means of a HPLC pump to simulate the flow of μL-sized volumes of buffered and unbuffered samples, in order to mimic human perspiration. Future work will comprise studies on possible particles' release for safety reasons.

Finally, being the most performant between the two pH transducers, the composite material containing IrOx Ps was employed in a two-terminal sensor implemented to perform analytical determinations of ammonia in gas phase (Section 4). Optimum hydrogel formulation was found that guarantees a semi-solid, electrolytic interface able to reversibly adsorb the gaseous analyte and change its pH nearby the sensing material, so that to induce variations in the output sensor signal. The gas sensor performance was tested in different experimental conditions, demonstrating that the device can reliably carry out quantitative detection of NH_3 in air at room temperature and upon application of a small potential (-0.2 V) with good reproducibility. Interference study are presently ongoing over other hazardous volatile chemicals. Indeed, since the detection is based on pH variations, local changes in CO_2 levels are, for instance, expected to interfere. However, the presence of volatile compounds inducing acidic pH variations has been observed to cause opposite current variations (verified for HCl vapours), thus being in principle discernible from the expected behaviour in response to NH_3. Nonetheless, eventual tuning of the physical and chemical properties of the hydrogel could be, for example, a viable strategy to provide the present device with enhanced selectivity. Since the long-term and short-term NH_3 exposure limits are set by official dispositions on safety and prevention at 25 and 35 ppm, respectively,[93] and considering the wide concentration range (18 – 7899 ppm), the low detection limit (15 ppm) and the fast response time obtained, the developed gas sensor could be suited for NH_3 vapours detection in potentially hazardous workplaces. Indeed, thanks to the simple electronics required and the two-terminal configuration, it will be further implemented on textile supports and integrated in a wearable platform for gaseous threats detection.

Summarizing, a novel class of electrochemically gated, two-terminal devices inspired by the Organic Electrochemical Transistor has been developed for sensing applications. The core of this approach is the design of composite transducer materials that spontaneously

change their electrochemical potential in response to external stimuli. Such feature is hence exploited to modulate the conductivity of the polymer channel, thus realising a gating effect that is triggered by spontaneous electrochemical reactions. In this situation, application of an external bias to vary the doping state of the channel (such as the V_g in an OECT) is no longer necessary and the device can work as an electrochemical sensor in two-terminal geometry. In order to get a deeper insight into the working principle of the here discussed devices and provide a physicochemical model to interpret their behaviour, *in-operando* microscopic experiments are ongoing following the SECM approach introduced in Chapter II. Moreover, assessment of the real-life performance of all the implemented sensors is in progress, as well as the construction of textile-compatible electronic components with aim to realize fully wearable sensing platforms, configurated to send the output data wirelessly to a user-friendly interface in real-time.

7. References

1. L. H. Hess, M. Jansen, V. Maybeck, M. V. Hauf, M. Seifert, M. Stutzmann, I. D. Sharp, A. Offenhäusser, J. Garrido. *Adv. Mater*. **2011**, *23*, 5045–5049.
2. A. Noy. *Adv. Mater*. **2011**, *23*, 807–820.
3. T. Cramer, A. Campana, F. Leonardi, S. Casalini, A. Kyndiah, M. Murgia, F. Biscarini. *J. Mater. Chem. B* **2013**, *1*, 3728-3741.
4. A. J. Bandodkar, I. Jeerapan, J. Wang. *ACS Sens*. **2016**, *1*, 464−482.
5. J. Kim, E.-F. Chou, J. Le, S. Wong, M. Chu, M. Khine. *Adv. Healthc. Mater*. **2019**, *8*, e1900109.
6. R. Lazazzera, Y. Belhaj, G. Carrault. *Sensors* **2019**, *19*, 2557.
7. E. Nemati, M. J. Deen, T. Mondal. *IEEE Commun. Mag*. **2012**, *50*, 36-43.
8. D. Pani, A. Dessi, J. F. Saenz-Cogollo, G. Barabino, B. Fraboni, A. Bonfiglio. *IEEE Trans. Biomed. Eng*. **2016**, *63*, 540-9.
9. X. An, G. K. Stylios. *Materials* **2018**, *11*, 1887.
10. T. Yamada, Y. Hayamizu, Y. Yamamoto, Y. Yomogida, A. Izadi-Najafabadi, D. N. Futaba, K. Hata. *Nat. Nanotechnol*. **2011**, *6*, 296−301.
11. D. Son, J. Lee, S. Qiao, R. Ghaffari, J. Kim, J. E. Lee, C. Song, S. J. Kim, D. J. Lee, S. W. Jun, S. Yang, M. Park, J. Shin, K. Do, M. Lee, K. Kang, C. S. Hwang, N. Lu, T. Hyeon,

D.-H Kim. *Nat. Nanotechnol*. **2014**, *9*, 397−404.

12. D. Pani D, A. Achilli, A. Spanu, A. Bonfiglio, M. Gazzoni, A. Botter. *IEEE Trans. Neural. Syst. Rehabil. Eng.* **2019**, *27,* 1370-1377.
13. J. R. Windmiller, J. Wang. *Electroanalysis* **2013**, *25*, 29 – 46.
14. R. Byrne, D. Diamond. *Nat. Mater.* **2006**, *5*, 421-424.
15. N. De Giovanni, N. Fucci. *Curr. Med. Chem*. **2013**, *20*, 545–561.
16. D. A. Kidwell, J. C. Holland, S. Athanaselis. *J. Chromatogr. B* **1998**, *713*, 111–135.
17. P. M. Farrell, B. J. Rosenstein, T. B. White, F. J. Accurso, C. Castellani, G. R. Cutting, P. R. Durie, V. A. LeGrys, J. Massie, R. B. Parad, M. J. Rock, P. W. Campbell III. *J. Pediatr*. **2008**, *153,* S4–S14.
18. M. A. Raina, M. S. Khan, S. A. Malik, A. B. H. Raina, M. J. Makhdoomi, J. I. Bhat, S. Mudassar. *J. Clin. Diagn. Res*. **2016**, *10*, BC01–BC06.
19. M. Taghizadeh-Behbahani, B. Hemmateenejad, M. Shamsipur, A. Tavassoli. *Anal. Chim. Acta* **2019**, *1080,* 138-145.
20. T. Guinovart, A. J. Bandodkar, J. R. Windmiller, F. J. Andrade, J. Wang. *Analyst* **2013**, *138*, 5208 —5215.
21. A. J. Bandodkar, D. Molinnus, O. Mirza, T. Guinovart, J. R. Windmiller, G. Valdés-Ramírez, F. J. Andrade, M. J. Schöning, J. Wang. Biosens. Bioelectron. **2014**, *54*, 603-609.
22. S. Coyle, D. Morris, K. T. Lau, D. Diamond, F. Di Francesco, N. Taccini, M. G. Trivella, D. Costanzo, P. Salvo, J. A. Porchet, J. Luprano. *Proc. 3rd Int. Conf. Pervasive Computing Technologies for Healthcare*. IEEE, **2009**, 1–6.
23. N. Coppedè, G. Tarabella, M. Villani, D. Calestani, S. Iannotta, A. Zappettini. *J. Mater. Chem. B* **2014**, *2*, 5620-5626.
24. E. Battista, V. Lettera, M. Villani, D. Calestani, F. Gentile, P. A. Netti, S. Iannotta, A. Zappettini, N. Coppedè. *Org. Electron*. **2017**, *40*, 51-57.
25. Y. Kim, T. Lim, C.-H. Kim, C. S. Yeo, K. Seo, S.-M. Kim, J. Kim, S. Y. Park, S. Ju, M.-Han Yoon. *NPG Asia Mater*. **2018**, *10*, 1086–1095.
26. W. Gao, S. Emaminejad, H. Y. Y. Nyein, S. Challa, K. Chen, A. Peck, H. M. Fahad, H. Ota, H. Shiraki, D. Kiriya, D.-H. Lien, G. A. Brooks, R. W. Davis, A. Javey. *Nature* **2016**, *529*, 509–514.
27. Y. J. Hong, H. Lee, J. Kim, M. Lee, H. Jin Choi, T. Hyeon, D.-H. Kim. *Adv. Funct. Mater.* **2018**, *28*, 1805754.
28. H. Lee, C. Song, Y. S. Hong, M. S. Kim, H. R. Cho, T. Kang, K. Shin, S. H. Choi, T.

Hyeon, D.-H. Kim. *Sci. Adv*. **2017,** *3*, e1601314.

29. S. Anastasova, B. Crewther, P. Bembnowicz, V. Curto, H. M. D. Ip, B. Rosa, G.-Z. Yang. *Biosens. Bioelectron*. **2017**, *93*, 139-145.
30. A. J. Bandodkar, P. Gutruf, J. Choi, K. H. Lee, Y. Sekine, J. T. Reeder, W. J. Jeang, A. J. Aranyosi, S. P. Lee, J. B. Model, R. Ghaffari, C.-J. Su, J. P. Leshock, T. Ray, A. Verrillo, K. Thomas, V. Krishnamurthi, S. Han, J. Kim, S. Krishnan, T. Hang, J. A. Rogers. *Sci. Adv*. **2019**, *5*, eaav3294.
31. R. J. Maughan, S. M. Shirreffs. *Scand. J. Med. Sci. Sports* **2010**, *20*, 40-47.
32. L. B. Baker, K. A. Barnes, M. L. Anderson, D. H. Passe, J. R. Stofan. *J. Sports Sci.* **2016**, *34*, 358–68.
33. J. Moyer, D. Wilson, I. Finkelshtein, B. Wong, R. Potts. *Diabetes Technol. Ther*. **2012**, *14*, 398-402.
34. P. J. Derbyshire, H. Barr, F. Davis, S. P. J. Higson. *J. Physiol. Sci*. **2012**, *62*, 429–440.
35. D. R. Seshadri, R. T. Li, J. E. Voos, J. R. Rowbottom, C. M. Alfes, C. A. Zorman, C. K. Drummond. *npj Digit. Med*. **2019**, *2*, 72.
36. M. J. Patterson, S. D. Galloway, M. A. Nimmo. *Acta Physiol. Scand.* **2002,** *174*, 41-6.
37. M. J. Patterson, S. D. Galloway, M. A. Nimmo. *Exp. Physiol*. **2000**, *85*, 870-876.
38. A.C. Vimieiro-Gomes, F.C. Magalhães, F.T. Amorim, C.A. Machado-Moreira, M.S. Rosa, N.R.V. Lima, L.O.C. Rodrigues. *Braz. J. Med. Biol. Res.* **2005**, *38*, 1133-1139.
39. S. Fowkes Godek, A. R. Bartolozzi, J. J. Godek. Br. J. Sports Med. **2005**, *39*, 205–211.
40. Z. Sonner, E. Wilder, J. Heikenfeld, G. Kasting, F. Beyette, D. Swaile, F. Sherman, J. Joyce, J. Hagen, N. Kelley-Loughnane, R. Naik. *Biomicrofluidics* **2015**, *9*, 031301.
41. L. B. Baker. *Sports Med*. **2017**, *47*, S111–S128.
42. M. Ochoa, R. Rahimi, B. Ziaie. *IEEE Rev. Biomed. Eng*. **2014**, *7*, 73–86.
43. M. S. Brown, B. Ashley, A. Koh. *Front. Bioeng. Biotechnol*. **2018**, *6*, 47.
44. M. Qin, H. Guo, Z. Dai, X. Yan, X. Ning. *J. Semicond*. **2019**, *40*, in press.
45. H. Lambers, S. Piessens, A. Bloem, H. Pronk, P. Finkel. *Int. J. Cosmet. Sci*. **2006**, *28*, 359–370.
46. G. Gethin. *Wounds UK* **2007**, *3*, 52–56.
47. M. F. Farooqui, A. Shamim. *Sci. Rep*. **2016**, *6*, 28949.
48. T. Guinovart, G. Valdés-Ramìrez, J. R. Windmiller, F. J. Andrade, J. Wang. *Electroanalysis* **2014**, *26*, 1345–1353.
49. A. Tamayol, M. Akbari, Y. Zilberman, M. Comotto, E. Lesha, L. Serex, S. Bagherifard, Y. Chen, G. Fu, S. K. Ameri, W. Ruan, E. L. Miller, M. R. Dokmeci, S. Sonkusale, A.

Khademhosseini. *Adv. Healthc. Mater*. **2016**, *5*, 711–719.

50. L. Liu, X. Li, M. Nagao, A. L. Elias, R. Narain, H.-J. Chung. *Polymers* **2017**, *9*, 558.
51. R. Ozanich. *Pure Appl. Chem*. **2018**, 90, 1605–1613.
52. MicroPEM™ Sensor. https://www.rti.org/impact/micropem-sensor-measuring-exposure-air-pollution
53. CBEx handheld Raman analyzer. http://www.wysri.com/cbex/
54. J. R. Sempionatto, R. K. Mishra, A. Martín, G. Tang, T. Nakagawa, X. Lu, A. S. Campbell, K. M. Lyu, J. Wang. *ACS Sens*. **2017**, *210*, 1531-1538.
55. R. K. Mishra, A. Barfidokht, A. Karajic, J. R. Sempionatto, J. Wang, J. Wang. *Sens. Actuators B* **2018**, *273*, 966–972.
56. J. Qia, X. Xinxina, X. X. Liua, K. T. Lau. *Sens. Actuators B* **2014**, *202*, 732–740.
57. Dinesh K. Subbiah, G. K. Mani, K. J. Babu, A. Das, J. Bosco Balaguru Rayappan. *J. Clean. Prod.* **2018**, *194*, 372-382.
58. D. Maity, K. Rajavel, R. Thangavelu Rajendra Kumar. *Sens. Actuators B* **2018**, *261*, 297–306.
59. X. Wang, S. Meng, M. Tebyetekerwa, W. Weng, J. Pionteck, B. Sun, Z. Qin, M. Zhu. *Synth. Met*. **2017**, *233*, 86–93.
60. S. Wu, P. Liu, Y. Zhang, H. Zhang, X. Qin. *Sens. Actuators B* 2017, 252, 697–705.
61. D. Maity, R. Thangavelu Rajendra Kumar. *ACS Sens*. **2018**, *3*, 1822−1830.
62. P.-G. Su, Z.-H. Liao. *Mater. Chem. Phys.* **2019**, *224*, 349–356.
63. I. Gualandi, M. Tessarolo, F. Mariani, T. Cramer, D. Tonelli, E. Scavetta, B. Fraboni. *Sens. Actuators B* **2018**, *273*, 834-841.
64. A. J. Bard, L. R. Faulkner. “Electrochemical Methods - Fundamentals and Applications”. Wiley, New York, **2001**.
65. D. A. Bernards, D. J. Macaya, M. Nikolou, J. A. DeFranco, S. Takamatsu, G. G. Malliaras. *J. Mater. Chem.* **2008**, *18* , 116–120.
66. J. Rivnay, P. Leleux, M. Ferro, M. Sessolo, A. Williamson, D. A. Koutsouras, D. Khodagholy, M. Ramuz, X. Strakosas, R. M. Owens, C. Benar, J.-M. Badier, C. Bernard, G. G. Malliaras. *Sci. Adv*. **2015**, *1*, e1400251.
67. J. Rivnay, P. Leleux, M. Sessolo, D. Khodagholy, T. Hervé, M. Fiocchi, G. G. Malliaras. *Adv. Mater*. **2013**, *25*, 7010-4.
68. D. Khodagholy, J. Rivnay, M. Sessolo, M. Gurfinkel, P. Leleux, L. H. Jimison, E. Stavrinidou, T. Herve, G. G. Malliaras. *Nat. Commun*. **2013**, *4*, 2133.
69. M. Zhang, S. Hö, J. Czolk, A. Mertens, A. Colsmann. *Nanoscale* **2015**, *7*, 20009–20014.

70. X. Ma, Y. Dai, M. Guo, Y. Zhu, B. Huang. *Phys. Chem. Chem. Phys.* **2013**, *15*, 29–34.
71. H. B. Michaelson. *J. Appl. Phys*. **1977**, *4729*, 1–6.
72. B. Tribollet, M. E. Orazem. "Electrochemical Impedance Spectroscopy". John Wiley & Sons, New York, **2008**.
73. N. W. Ashcroft, N. D. Mermin. "Solid State Physics". Rinehart and Winston, Holt, **1976**.
74. C. M. Proctor, J. Rivnay, G. G. Malliaras. *J. Polym. Sci. PART B Polym. Phys*. **2016**, *54*, 1433–1436.
75. R. Seeber, L. Pigani, F. Terzi, C. Zanardi. *El. Acta* **2015**, *179*, 350–363.
76. D. A. Skoog, D. M. West, F. J. Holler. "Fundamentals of Analytical Chemistry". Saunders College Publishing, Philadelphia, **1992**, 6th edition.
77. Chloride Low Range Test Kit, Model 8-P. https://www.hach.com/chloride-low-range-test-kit-model-8-p/product-details?id=7640219502
78. Merck Chloride Test. http://www.merckmillipore.com/GB/en/product/Chloride-Test,MDA_CHEM-114401
79. A. Campana, T. Cramer, D. T. Simon, M. Berggren, F. Biscarini. *Adv. Mater*. **2014**, *26*, 3874–3878.
80. M. J. Tarlov, S. Semancik, K. G. Kreider. *Sens. Actuators B* **1990**, *1*, 293-297.
81. M. Wang, S. Yao, M. Madou. *Sens. Actuators B* **2002**, *81*, 313-315.
82. H. A. Elsen, C. F. Monson, M. Majda. *J. Electrochem. Soc*. **2009**, *156*, F1-F6.
83. M. L. Zamora, J. M. Dominguez, R. M. Trujillo, C. B. Goy, M. A. Sánchez, R. E. Madrid. *Sens. Actuators B* **2018**, *260*, 601–608.
84. G. Scheiblin, R. Coppard, R. M. Owens, P. Mailley, G. G. Malliaras. *Adv. Mater. Technol.* **2016**, 2, 1600141.
85. E. Prats-Alfonso, L. Abad, N. Casan˜-Pastor, J. Gonzalo-Ruiz, E. Baldrich. *Biosens. Bioelectron*. **2013**, *39*, 163–169.
86. M. Jović, J. C. Hidalgo-Acosta, A. Lesch, V. Costa Bassetto, E. Smirnov, F. Cortés-Salazar, H. H. Girault. *J. Electroanal. Chem*. **2018**, *819*, 384–390.
87. M. Khalil, S. Wang, J. Yu, R. L. Lee, N. Liu. *J. Electrochem. Soc.* **2016**, *163*, B485-B490.
88. M. Khalil, N. Liu, R. L. Lee. *Int. J. Technol.* **2018**, *9*, 446-454.
89. Y. Zhao, E. A. Hernandez-Pagan, N. M. Vargas-Barbosa, J. L. Dysart, T. E. Mallouk. *J. Phys. Chem. Lett.* **2011**, *2*, 402–406.
90. H. S. White, G. P. Kittlesen, M. S. Wrighton. *J. Am. Chem. Soc*. **1984**, *106*, 5375–5377.
91. G. P. Kittlesen, H. S. White, M. S. Wrighton. *J. Am. Chem. Soc*. **1984**, *106*, 7389-7396.
92. E. W. Paul, A. J. Ricco, M. S. Wrighton. *J. Phys. Chem*. **1985**, *89*, 1441-1447.

93. Ammonia, anhydrous. GESTIS Substance Database, **2019**, 1–25.
94. G. Cruz. *J. Chem. Educ*. **2013**, *90*, 1645–1648.

VI. Conclusion

OECTs are presently focus of extensive research and development in the field of bioelectronics. First developed in the 80s, these devices have experienced increasing application as hybrid, engineered interfaces that hold promise for the control and stimulation of biologic events as actuators, or their transduction into processable electronic outputs, thus gaining access to medically relevant information from our body. A potentially disruptive impact is often invoked in relation to such technologies, which could revolutionise both diagnostic and therapeutic practices in our everyday life, in view of a personalized medical care.

In this context, the portable and wearable sensor market is growing at steady rate with the advancement in sensor technology, expansion of Internet of Things and development of innovative power supply strategies. Electrochemical based methods already dominate the area of home glucose test kits and there is pressing demand in bringing to the market new technologies capable to monitor our body status in real time. Even though, in principle, performances and architectural features showed by many OECT-based sensors meet the requirements that a smart portable/wearable technology must address, no example of commercialized organic bioelectronic products is available at the moment.

Indeed, tangible challenges exist that profoundly hinder the achievement of a high technological readiness level and commercialization of OECT-based devices. First of all, the highly cross-disciplinary domain to which organic bioelectronics belongs. While multidisciplinary approaches are often the key to develop solutions of highly innovative content in complex target panoramas, the building concepts require multifaceted scientific backgrounds that should culminate in comprehensive interpretations. Such collective

research effort is sometimes limited by field-specific terminology and lack of univocally defined criteria, for instance, in device assessment. Possibly related to this aspect, the understanding of electrochemical and physical events originating signal transduction is mainly based on phenomenological studies, thus limiting further improvement of device performances based on material research or geometry modelling. Finally, the design of integrated platforms able to cope with real-life scenarios raises incredibly demanding tasks. For instance, finalization of wearable sensors must address great robustness in harsh operative conditions, which are very far from those of a laboratory for clinical tests, and suffer from still poorly correlated data between the non-invasively collected biofluids and blood samples that are employed for routine analyses.

As far as technological immaturity is concerned, it must be said that OECTs are still of recent discovery, if contextualized within the well-assessed, over-100-yers-old field of electrochemical sensors or the worldwide-driven Si-based electronics. Concurrently, a unique combination of chemical and physical features is paving the way for such devices to outperform consolidated sensing technologies, while inherent material and configuration versatility might be complementary to inorganic electronic components for the realization of smart bio-interfaces. Also, the major advantage of being placed in the landscape of electrochemical devices consists in the possibility to borrow and adapt a library of already explored techniques and transducers in the design and assessment of OECT-based sensors. Essentially, it has been the *leitmotif* of the work presented in this Thesis, motivated by the abovementioned constraints that limit a widespread applicability of OECT sensors in end-user scenarios. Here, for the first time a scanning electrochemical setup was adjusted to characterize in-operando devices, thus offering unprecedented insight into the electrochemical phenomena underlying the transistor operation and the detection mechanism at the semiconductor/electrolyte interface. Selectivity and sensitivity issues related to the determination of a medically relevant biomolecule such as Dopamine have been addressed by the development of a potentiodynamic protocol to operate the OECT sensor and the design of sub-micrometric devices for spatially resolved analysis of physiological amounts of analyte. Moreover, particular attention has been devoted to all-plastic devices that can be easily fabricated with high throughput onto a variety of supports. In this view, a flexible OECT pH sensor has been realized to overcome the performance of standard ion selective electrodes and does not require freestanding reference electrodes, reference solution or a dedicated architecture for differential measurements in order to reliably perform the analytical determination. Inspired by the OECT architecture and by

already known potentiometric transducers, innovative composite materials have been designed to allow further simplification of the sensor geometry, thus paving the way for the implementation of smart textiles based on thread-shaped, electrochemically gated sensors.

Acknowledgements

First, I must thank my supervisor Erika Scavetta, who gave me the chance to challenge myself with this unique experience, for always being source of inspiration and sincere enthusiasm. Right after her, I want to thank Dr. Isacco Gualandi for his great support and for sharing with me his bright point of view during these years. Thank you for always instilling in me the “right” doubts.

I am very grateful to all people from the Analytical Chemistry lab, Dept. of Industrial Chemistry in Bologna, in which I spent almost 1/3 of my life (already!), in particular Prof. Domenica Tonelli, Dr. Andreas Lesch and Dr. Elisa Musella. I would like to thank Dr. Silvia Ruggieri of the Group of Inorganic Chemistry, Dr. Arianna Rivalta and Dr. Andrea Giunchi of the Group of Physical Chemistry, and all the graduate and undergraduate students who passed by here, for both science and the good time together. Also, I must thank Prof. Beatrice Fraboni, Dr. Tobias Cramer, Dr. Marta Tessarolo, Dr. Marco Marzocchi, Dr. Francesco Decataldo and Dr. Luca Possanzini of the Semiconductor Physics group in Bologna for the fruitful discussions and collaboration on transistors and for providing the devices. Thanks to Prof. Francesco Basile and Dr. Andrea Fasolini of the Catalysis group for their support in the Electrocatalysis projects.

A special thank goes to Prof. Wolfgang Schuhmann, Prof. Corina Andronescu and the Electrochemistry group of the Ruhr-Universität Bochum, Germany. I have beautiful memories of the period that I spent in the ELAN group, where I found a bit of home in all the people that I had the pleasure to work with. The thank-you list is long, but I would like

to mention Dr. Thomas Quast, who patiently trained me on nanoelectrodes fabrication and German habits, Dr. Felipe Conzuelo for supporting all my SECM experiments and for his friendship, Dr. Carla Santana Santos and Dr. Olga Krysiak for making Bochum less boring.

I would like to acknowledge Plastod S.p.A. for providing the textiles to fabricate wearable sensors, Elements S.r.l. for the portable electronic components, Dr. Ciro Polizzi for his help in developing wearable readout electronics.

After all this science, I have some special friends to address. My closest friends Massimo and Giulia for their amazing friendship, and Dr. Cristina Grosu and Dr. Ilaria Zanoni for sharing and surviving together these bumpy years inside and outside the university. Lorenzo, to whom this thesis is dedicated: I know you did not love electrochemistry, but since *that* day I have spent most of my writing time thinking of you. Thank you for your belly laugh that still echoes with freedom in my mind.

Last, I would like to thank my family. Thank you, Mom and Dad, for always encouraging and supporting me so deeply, even if you don't have a clue what I have been doing during my PhD, just because you trust and love me. Thank you, Francesco, from the bottom of my heart, for your endless patience and love, for being such a generous and ambitious man by my side. Thank you for supporting my dreams, despite all the things that come up every day.